

REPORT DOCUMENTATION PAGE			Form Approved OMB No. 0704-0188		
<p>Public reporting burden for this collection of information is estimated to average 1 hour per response, including the time for reviewing instructions, searching existing data sources, gathering and maintaining the data needed, and completing and reviewing this collection of information. Send comments regarding this burden estimate or any other aspect of this collection of information, including suggestions for reducing this burden to Department of Defense, Washington Headquarters Services, Directorate for Information Operations and Reports (0704-0188), 1215 Jefferson Davis Highway, Suite 1204, Arlington, VA 22202-4302. Respondents should be aware that notwithstanding any other provision of law, no person shall be subject to any penalty for failing to comply with a collection of information if it does not display a currently valid OMB control number. PLEASE DO NOT RETURN YOUR FORM TO THE ABOVE ADDRESS.</p>					
1. REPORT DATE (DD-MM-YYYY) October 2012		2. REPORT TYPE Technical Paper		3. DATES COVERED (From - To) October 2012-December 2012	
4. TITLE AND SUBTITLE EXPERIMENTAL INVESTIGATION OF SHEAR DRIVEN LIQUID FILMS FOR FILM COOLING APPLICATIONS IN LIQUID ROCKET ENGINES			5a. CONTRACT NUMBER In-House		
			5b. GRANT NUMBER		
			5c. PROGRAM ELEMENT NUMBER		
6. AUTHOR(S) R. Miller			5d. PROJECT NUMBER		
			5e. TASK NUMBER		
			5f. WORK UNIT NUMBER Q0VZ		
7. PERFORMING ORGANIZATION NAME(S) AND ADDRESS(ES) Air Force Research Laboratory (AFMC) AFRL/RQRC 10 E. Saturn Blvd. Edwards AFB CA 93524-7680			8. PERFORMING ORGANIZATION REPORT NO.		
9. SPONSORING / MONITORING AGENCY NAME(S) AND ADDRESS(ES) Air Force Research Laboratory (AFMC) AFRL/RQR 5 Pollux Drive Edwards AFB CA 93524-7048			10. SPONSOR/MONITOR'S ACRONYM(S)		
			11. SPONSOR/MONITOR'S REPORT NUMBER(S) AFRL-RQ-ED-TP-2012-483		
12. DISTRIBUTION / AVAILABILITY STATEMENT Distribution A: Approved for Public Release; Distribution Unlimited. PA#13033					
13. SUPPLEMENTARY NOTES Thesis presented at Purdue University Graduate School					
14. ABSTRACT Liquid film cooling is an important method for cooling the walls of a liquid rocket engine. Mass transfer via entrainment decreases the effectiveness of the film coolant and it is therefore important to estimate the amount of film coolant that establishes itself along the wall of a combustion chamber if the coolant flow rate is to be optimized. However, film entrainment research is limited in regards to film cooling applications in rockets. The correlations and theories that have been published are often limited in scope and have only been tested at momentum fluxes that are an order of magnitude less than those typically experienced in rockets. Experimental research has been conducted in a cold-flow test article at AFRL in order to investigate the effects of the gas stream momentum flux on the coolant flow rate that remains attached to the wall. Specifically, the objective of this study was to investigate the establishment of a shear driven liquid film introduced into a rectangular test section by a .38 mm X 25.4 mm slot, perpendicular to the stream-wise direction of the gas phase. A secondary objective of this thesis was to investigate the ability of several diagnostics to measure the interfacial shear stress, mean film thickness, and the film mass flow rate of a liquid water film shear-driven by nitrogen gas in cold flow conditions. Ultimately, a film removal slot was chosen to measure the film mass flow rate, differential pressure taps were chosen to indirectly deduce the interfacial shear stress by measuring a stream-wise pressure drop, and a laser focus displacement meter was chosen to measure the liquid film thickness. Lastly, a high-speed video camera was used to obtain qualitative visual data of the surface of the shear driven liquid film.					
15. SUBJECT TERMS					
16. SECURITY CLASSIFICATION OF:			17. LIMITATION OF ABSTRACT	18. NUMBER OF PAGES	19a. NAME OF RESPONSIBLE PERSON Edward Coy
a. REPORT Unclassified	b. ABSTRACT Unclassified	c. THIS PAGE Unclassified			19b. TELEPHONE NO (include area code) 661-275-5219

EXPERIMENTAL INVESTIGATION OF SHEAR DRIVEN LIQUID FILMS FOR
FILM COOLING APPLICATIONS IN LIQUID ROCKET ENGINES

A Thesis
Submitted to the Faculty
of
Purdue University
by
Ryan P. Miller

In Partial Fulfillment of the
Requirements for the Degree
of
Master of Science

December 2012

Purdue University

West Lafayette, Indiana

For my parents, thanks for all you're guidance and support.

And, to those who requested/deserve a dedication:

For Sara, my conference karaoke buddy.

For Cassandra, you're all my engineer.

For Svetlana, you had me at "tell me something fascinating about the universe."

ACKNOWLEDGMENTS

Foremost, I would like to thank my boss, advisor, and mentor, Dr. Edward B. Coy of the Air Force Research Lab for his extensive contributions to my learning and the development of this thesis. He also been very generous, and offered some of his time on several of his days off to help me fabricate the initial test article. As a result of his efforts, guidance, and patience, I've learned many essential new skills and am now much more independent and self-disciplined. I'd also like to thank Dr. Steven Dancyk for all his help in teaching me how to machine and guidance in experimental techniques. I'd like to thank both Dr. Alex Schumaker and Dr. Malissa Lightfoot for their help in getting me set up in the lab. A special thanks goes out to Todd Newkirk for helping me resolve the noise issues with my instrumentation. Thank you to Dave Hill, John Hasier, and Edgar Felix for helping me machine and set up my test article. A special thanks goes out to Jeff Wegener, for giving me some much needed advice that only a fellow grad student can give. Finally, thanks to my friends Matt, Vivian, Kelly, Ryan, and Amanda for helping me maintain my sanity while working on this.

TABLE OF CONTENTS

	Page
LIST OF TABLES	vii
LIST OF FIGURES	ix
NOMENCLATURE	xiv
ABSTRACT	xix
CHAPTER 1. INTRODUCTION	1
1.1 Overview of Mechanics of Shear-driven Liquid Films in Cold-Flow	6
1.1.1 Differences Between Hot-Fire at Subcritical Conditions and Cold Flow	10
1.1.2 Differences at Supercritical Conditions	11
1.2 Chapter 1 Summary	12
CHAPTER 2: LITERATURE REVIEW	13
2.1 Review of Literature Specific to Liquid Film Cooling in Rocket Engines	13
2.1.1 Liquid Film Attachment investigations by Warner and Reese	14
2.1.2 Liquid Fuel Film Studies by Kinney, Sloop and Abramson	15
2.1.3 Studies Regarding Film Stability by Knuth	16
2.1.4 Film Cooling Entainment Studies by Gater and L'Ecuyer	16
2.1.5 Liquid Film Cooling Research and Modeling by Grissom	17
2.1.6 Liquid Fuel Film Cooling Studies by Volkmann et. al	18
2.1.7 Kirchberger's Studies	18
2.1.8 Fuel Film Cooling Review by Yu, Schuff and Anderson	19
2.1.9 Cold-Flow Liquid Film Establishment Experiments by Coy, Schumaker, and Lightfoot	20
2.2 Minor Literature Review of Two-Phase Annular Flow Experiments	20
2.2.1 Experimental Investigations by Sawant and Ishii	21
2.2.2 Annular Two-phase Flow Review and Analysis by Cioncolini and Thome ...	23
2.3 Review of Experiments of Shear-Driven Liquid Films in a Rectangular Channel	23
2.3.1 Shear Driven Liquid Film Studies by Schober and Ebner	24

	Page
2.3.2 Shear-Driven Liquid Film Experiments at a Sharp, Expanding Corner by Friedrich and Wegener.....	25
2.3.3 Inception Criteria for Droplet Entrainment in Two-Phase Concurrent Film Flow	26
2.4 Conclusions from the Literature and Applicabilty to the Current Study	26
CHAPTER 3: OVERVIEW OF DIAGNOSTIC TOOLS	29
3.1 Overview and Background of the Laser Focus Displacement Meter for Measurement of Shear Driven Liquid Films	30
3.2 Shear Stress Measrument Techniques	33
3.2.1 Determining the Shear Stress from Pressure Drop Measurements.....	33
3.2.2 Other Shear Stress Measurement Techniques	36
3.3 Film Mass Flow Rate Measurements.....	38
3.4 Film Visualization Tools.....	40
3.5 Chapter 3 Summary	40
CHAPTER 4: DESCRIPTION OF EXPERIMENT AND TEST ARTICLE.....	43
4.1 Test Article Description	43
4.2 Experimental Procedures	53
4.1.1 Experimental Procedure for the June 2011 Tests	54
4.1.2 Experimental Procedure for the November 2011 Tests.....	56
4.3 Experimental Description Summary	59
CHAPTER 5: EXPERIMENTAL RESULTS AND DISCUSSION	60
5.1 Film Attachment Discussion.....	60
5.2 Film Mass Flow Rate Results	62
5.2.1 Film Mass Flow Rate Measured Using the Film Removal Slot	63
5.2.2 Onset of Entrainment Discussion	66
5.2.3 Liquid Lost From Film Due to Evaporation	67
5.3 Pressure Drop Results	71
5.4 Film Thickness Results	72
5.4.1 Raw LFD Data	73
5.4.2 The Direct Method for Determing Liquid Film Thickness Using the LFD	75
5.3.2 The Index of Refraction Method for Determining Liquid Film Thickness Using an LFD.....	76
5.4.3 Comparison of the Direct Method with the Index of Refraction Method	81

	Page
5.4.4 Film Thickness Results Obtained Using the Index of Refraction Method During the November 2011 Tests	84
5.4.5 Comparison of Film Thickness Results	88
5.5 High Speed Video Results	92
CHAPTER 6: CONCLUDING REMARKS AND RECOMMENDATIONS FOR FUTURE WORK	98
LIST OF REFERENCES	103
APPENDIX	107
Appendix A: Dimensioned Drawings of Test Article	108
Appendix B: Supplementary Results	117
Appendix C: Derivation of Equation	169
Appendix D: Uncertainty in the Momentum Flux	176

LIST OF TABLES

Table	Page
Table 2-1: Comparison of the Momentum Flux of Several Experiments.....	28
Table 4-1: Variables Directly Measured by Test Article.....	45
Table 5-1: Comparison of the Critical Injected Liquid Flow Rate Determined by Different Equations. Surface Tension is Assumed to be .68 N/m.....	67
Table B-1: June 2011 Test Data, ILFR \approx .0034 kg/s	117
Table B-2: June 2011 Test Data, ILFR \approx .0034 kg/s, Continued.....	118
Table B-3: June 2011 Test Data, ILFR \approx .0046 kg/s.....	119
Table B-4: June 2011 Test Data, ILFR \approx .0046 kg/s, Continued.....	120
Table B-5: June 2011 Test Data ILFR \approx .0056 kg/s.....	121
Table B-6: June 2011 Test Data, ILFR \approx .0056 kg/s, Continued.....	122
Table B-7: June 2011 Test Data, ILFR \approx .0064 kg/s.....	123
Table B-8: June 2011 Test Data, ILFR \approx .0064 kg/s, Continued.....	124
Table B-9: June 2011 Test Data ILFR \approx .0070 kg/s.....	125
Table B-10: June 2011 Test Data, ILFR \approx .0070 kg/s, Continued.....	126
Table B-11: November 2011 Test Data, ILFR \approx .0034 kg/s.....	127
Table B-12: November 2011 Test Data, ILFR \approx .0034 kg/s, Continued.....	128
Table B-13: November 2011 Test Data, ILFR \approx .0034 kg/s, Continued.....	129
Table B-14: November 2011 Test Data, ILFR \approx .0034 kg/s, Continued.....	129
Table B-15: November 2011 Test Data, ILFR \approx .0070 kg/s.....	130
Table B-16: November 2011 Test Data, ILFR \approx .0070 kg/s, Continued.....	131
Table B-17: November 2011 Test Data, ILFR \approx .012 kg/s.....	132
Table B-18: November 2011 Test Data, ILFR \approx .012 kg/s, Continued.....	133
Table B-19: November 2011 Test Data, ILFR \approx .012 kg/s, Continued.....	134
Table B-20: November 2011 Test Data, ILFR \approx .012 kg/s, Continued.....	134
Table B-21: November 2011 Test Data ILFR \approx .018 kg/s.....	135
Table B-22: November 2011 Test Data, ILFR \approx .018 kg/s, Continued.....	136

Table	Page
Table B-23: November 2011 Test Data, ILFR \approx .018 kg/s, Continued.....	137
Table B-24: November 2011 Test Data, ILFR \approx .018 kg/s, Continued.....	137

LIST OF FIGURES

Figure	Page
Figure 1-1: Liquid Water Film Being Injected Through a Perpendicular Slot	2
Figure 1-2: Description of Experimental Apparatus.....	4
Figure 1-3: Diagram of Film Issuing from a Slot	7
Figure 1-4: Forces acting on waves in a shear-driven liquid film in cold flow	8
Figure 2-1: Illustration of of equation 2-8.	22
Figure 3-1: Diagram of LFD operation. Figure taken from Wegener [4].....	31
Figure 3-2: Different Configurations for measuring film thickness	32
Figure 3-3: Momentum balance on flow over an area of film.....	34
Figure 4-1: Plumbing and Instrumentation Diagram of Experiment	44
Figure 4-2: Assembled View of the Test Article (Left) and Cross-Sectional View of the Flow Area (Right)	45
Figure 4-3: Image of Cylindrical Plug at Test Section Exit.....	47
Figure 4-4: Fully Assembled Injector Piece	48
Figure 4-5: Upstream Piece of Injector Panel.....	49
Figure 4-6: Middle Piece of Injector Panel.....	49
Figure 4-7: Downstream Piece of Injector Panel	50
Figure 4-8: Underside View of Downstream Injector Piece.....	50
Figure 4-9: Injector Panel Assembly	51
Figure 4-10: Injector Panel Installed in Test Article	51
Figure 4-11: Close up of LFD.....	52
Figure 4-12: Close-up of Test Article Top	53
Figure 5-1: Comparison of the Injected Liquid Velocity with Critical Velocity of Injection for the June tests	61
Figure 5-2: Comparison of the Injected Liquid Velocity with the Critical Velocity of Injection for the November tests.....	61

Figure	Page
Figure 5-3: Images of the Film Removal Slot. Left: Removal Slot Valve is Closed. Right: Removal Slot Valve is Open.....	63
Figure 5-4: Liquid Film Removal Flow Rate vs Gas Momentum Flux.....	64
Figure 5-5: Fraction of Liquid Entrained into Gas Phase vs Gas Momentum Flux	66
Figure 5-6: Evaporative Mass Flow Rate from the Liquid Film as a percent of the Injected Liquid Flow Rate	70
Figure 5-7: Problem with pressure tap mid-experiment	72
Figure 5-8: Raw Position Data from the LFD during a typical test run	74
Figure 5-9: View of Aluminum Surface Estimate	76
Figure 5-10: Illustration of the LFD's Conical Laser Beam Passing Through the Surface of The Liquid Film and Reflecting off of the Aluminum Surface.....	77
Figure 5-11: Plot Showing how the Liquid Film Surface Angle Shifts the Focal Point of the LFD	79
Figure 5-12: Range of Possible Values for δ/f_{shift} Based on the Uncertainty of the Variables in Equation 5-12	80
Figure 5-13: Histogram of Film Thickness Estimates for Each Method with Momentum Flux = 2,970 Pa and Liquid Film flow rate = .007 kg/s.....	82
Figure 5-14: Histogram of Film Thickness Estimates for Each Method with Momentum Flux = 7,750 Pa and Liquid Film flow rate = .007 kg/s.....	83
Figure 5-15: Histogram of Film Thickness Estimates for Each Method with Momentum Flux = 38,300 Pa and Liquid Film flow rate = .007 kg/s.....	83
Figure 5-16: Raw LFD data for second series of tests.....	85
Figure 5-17: Example of a typical Frequency Histogram for the LFD data for the second round of testing	86
Figure 5-18: Film Thickness vs Momentum Flux	87
Figure 5-19: Results Compared with the Upper Bound Calculations and Coy et al [1]..	91
Figure 5-20: High Speed Video Images of the Film for Lowest Liquid Flow Rates.....	93
Figure 5-21: High Speed Video Images of the Liquid Film for .0154 kg/s Liquid Flow.	94
Figure 5-22: High-Speed Video Images of the Film for High Liquid Flow Rates	95
Figure A-1: Test Article Bottom.....	108
Figure A-2: Test Article Top	109
Figure A-3: Side Walls	110
Figure A-4: Cover Plate	111
Figure A-5: Upstream Injector Panel	112
Figure A-6: Injector Panel, Middle Piece	113

Figure	Page
Figure A-7: Downstream Injector Panel	114
Figure A-8: Rear Block.....	115
Figure A-9: Test Article Assembly Drawing.....	116
Figure B-1: Position of the Aluminum Substrate Stated by the LFD for Run 126.....	138
Figure B-2: LFD Histogram for Run 126	138
Figure B-3: Position of the Aluminum Substrate Stated by the LFD for Run 127.....	139
Figure B-4: LFD Histogram for Run 127	139
Figure B-5: Position of the Aluminum Substrate Stated by the LFD for Run 130.....	140
Figure B-6: LFD Histogram for Run 130	140
Figure B-7: Position of the Aluminum Substrate Stated by the LFD for Run 131.....	141
Figure B-8: LFD Histogram for Run 131	141
Figure B-9: Position of the Aluminum Substrate Stated by the LFD for Run 106.....	142
Figure B-10: LFD Histogram for Run 106	142
Figure B-11: Position of the Aluminum Substrate Stated by the LFD for Run 110.....	143
Figure B-12: LFD Histogram for Run 110	143
Figure B-13: Position of the Aluminum Substrate Stated by the LFD for Run 107.....	144
Figure B-14: LFD Histogram for Run 107	144
Figure B-15: Position of the Aluminum Substrate Stated by the LFD for Run 111.....	145
Figure B-16: LFD Histogram for Run 111	145
Figure B-17: Position of the Aluminum Substrate Stated by the LFD for Run 128.....	146
Figure B-18: LFD Histogram for Run 128	146
Figure B-19: Position of the Aluminum Substrate Stated by the LFD for Run 129.....	147
Figure B-20: LFD Histogram for Run 129	147
Figure B-21: Position of the Aluminum Substrate Stated by the LFD for Run 132.....	148
Figure B-22: LFD Histogram for Run 132	148
Figure B-23: Position of the Aluminum Substrate Stated by the LFD for Run 133.....	149
Figure B-24: LFD Histogram for Run 133	149
Figure B-25: Position of the Aluminum Substrate Stated by the LFD for Run 108.....	150
Figure B-26: LFD Histogram for Run 108	150
Figure B-27: Position of the Aluminum Substrate Stated by the LFD for Run 114.....	151
Figure B-28: LFD Histogram for Run 114	151

Figure	Page
Figure B-29: Position of the Aluminum Substrate Stated by the LFD for Run 113.....	152
Figure B-30: LFD Histogram for Run 113	152
Figure B-31: Position of the Aluminum Substrate Stated by the LFD for Run 126.....	153
Figure B-32: LFD Histogram for Run 126	153
Figure B-33: Position of the Aluminum Substrate Stated by the LFD for Run 125.....	154
Figure B-34: LFD Histogram for Run 125	154
Figure B-35: Position of the Aluminum Substrate Stated by the LFD for Run 134.....	155
Figure B-36: LFD Histogram for Run 134	155
Figure B-37: Position of the Aluminum Substrate Stated by the LFD for Run 135.....	156
Figure B-38: LFD Histogram for Run 135	156
Figure B-39: Position of the Aluminum Substrate Stated by the LFD for Run 99.....	157
Figure B-40: LFD Histogram for Run 99	157
Figure B-41: Position of the Aluminum Substrate Stated by the LFD for Run 115.....	158
Figure B-42: LFD Histogram for Run 115	158
Figure B-43: Position of the Aluminum Substrate Stated by the LFD for Run 103.....	159
Figure B-44: LFD Histogram for Run 103	159
Figure B-45: Position of the Aluminum Substrate Stated by the LFD for Run 116.....	160
Figure B-46: LFD Histogram for Run 116	160
Figure B-47: Position of the Aluminum Substrate Stated by the LFD for Run 121.....	161
Figure B-48: LFD Histogram for Run 121	161
Figure B-49: Position of the Aluminum Substrate Stated by the LFD for Run 122.....	162
Figure B-50: LFD Histogram for Run 122	162
Figure B-51: Position of the Aluminum Substrate Stated by the LFD for Run 136.....	163
Figure B-52: LFD Histogram for Run 136	163
Figure B-53: Position of the Aluminum Substrate Stated by the LFD for Run 137.....	164
Figure B-54: LFD Histogram for Run 137	164
Figure B-55: Position of the Aluminum Substrate Stated by the LFD for Run 101.....	165
Figure B-56: LFD Histogram for Run 101	165
Figure B-57: Position of the Aluminum Substrate Stated by the LFD for Run 120.....	166
Figure B-58: LFD Histogram for Run 120	166
Figure B-59: Position of the Aluminum Substrate Stated by the LFD for Run 105.....	167
Figure B-60: LFD Histogram for Run 105	167

Figure	Page
Figure B-61: Position of the Aluminum Substrate Stated by the LFD for Run 119.....	168
Figure B-62: LFD Histogram for Run 119	168
Figure C-1: Illustration of the LFD's Conical Laser Beam Passing Through the Surface of the Liquid Film and Reflecting off of the Aluminum Substrate.....	169

NOMENCLATURE

Symbol	Description
A	= defined by eq. 5-14
A_t	= Cross-sectional area of test section
a	= wave or disturbance height
B	= defined by eq. 5-15
b	= injection slot thickness
C	= defined by eq. 5-16
Con	= constant
C_D	= drag coefficient
C_L	= lift coefficient
D	= defined by eq. 5-17
D_h	= Hydraulic diameter
D_t	= Diameter
$D_{W,N}$	= diffusion coefficient of water into nitrogen
d	= derivative
∂	= partial derivative
$d_{sur,\#}$	= position stated by LFD, # depends on test run number
E	= defined by eq. 5-18
EF	= entrainment fraction
F	= defined by eq. 5-19
F_D	= Drag force
F_L	= Lift Force
Fr_f	= liquid film Froude number
f	= friction factor
f_l	= defined in Figure 5-8
f_r	= defined in Figure 5-8

Symbol	Description
f_{shift}	= shift in the liquid film focal point due to the presence of the liquid film
f_{smooth}	= friction factor in pipe/channel for perfectly smooth walls
G	= defined by eq. 5-20
g	= acceleration due to gravity
H	= height of a rectangular channel
h_m	= mass-transfer coefficient
ILFR	= injected liquid flow rate
ILFR'	= injected liquid flow rate per unit slot width in circumferential direction
ILFR _c	= critical injected liquid flow rate
J	= defined by eq. 5-21
j_f	= superficial velocity of the liquid film
j_g	= superficial velocity of the gas phase
j_l	= superficial velocity of the liquid phase
L_f	= Liquid film length
l	= stream-wise distance downstream of injection slot
MF _g	= Momentum Flux of the gas phase
\dot{m}	= mass flow rate
\dot{m}_L	= injected liquid flow rate
\dot{m}'_l	= film mass flow rate per unit width
\dot{m}''_{evap}	= mass flow rate per unit area due to evaporation
\dot{m}_{evap}	= mass flow rate due to evaporation
N_μ	= viscosity number
$N_{\mu f}$	= viscosity number, corresponding to the film
Oh	= Ohnesorge number
$P_{D,N}$	= pressure downstream of sonic nozzle
$P_{D,W}$	= pressure of water downstream of cavitating venture
P_{STP}	= pressure of sea-level standard atmosphere
P_T	= pressure in test section just upstream of film injection slot
$P_{U,N}$	= pressure upstream of sonic nozzle

Symbol	Description
$P_{U,W}$	= pressure of water upstream of cavitating venture
P_{vap}	= vapor pressure
P_1	= upstream pressure
P_2	= downstream pressure
ΔP	= pressure differential
Q_f	= volumetric flow rate within the liquid film
Q_g	= volumetric flow rate of the gas phase
Q_l	= volumetric flow rate of the liquid phase
Re_D	= hydraulic diameter based Reynolds number
$Re_{f,E}$	= film Reynolds number as defined by Ebner
$Re_{f,OE}$	= film Reynolds number at the onset of entrainment
$Re_{f,S}$	= film Reynolds number as defined by Sawant
$Re_{l,S}$	= liquid phase Reynolds number as defined by Sawant
Re_g	= gas-phase Reynolds number
Re_L	= length-averaged Reynolds number
R_N	= real gas constant of N_2
R_w	= real gas constant of H_2O
r_{1l}	= defined in Figure 5-8
r_{1r}	= defined in Figure 5-8
r_{2l}	= defined in Figure 5-8
r_{2r}	= defined in Figure 5-8
S	= perimeter
Sc	= Schmidt number
Sh_D	= hydraulic diameter based Sherwood number
\overline{Sh}_L	= length-average Sherwood number
T	= Temperature
T_g	= temperature of the gas phase
T_N	= temperature of nitrogen upstream of sonic nozzle
T_s	= liquid film surface temperature

Symbol	Description
T_{STP}	= temperature of sea-level standard temperature
T_T	= temperature of nitrogen entering test section
T_W	= temperature of water upstream of cavitating venture
t_l	= defined in Figure 5-8
t_r	= defined in Figure 5-8
U_1	= upstream velocity profile
U_2	= downstream velocity profile
u	= horizontal component of velocity
u_l	= horizontal component of velocity within established liquid film
V	= Velocity
V_g	= gas phase velocity
V_L^*	= critical velocity of injection
$V_{L,i}$	= injected liquid velocity
w	= width of test article
w^+	= dimensionless injected liquid flow rate
$We_{D,E}$	= Weber number based on hydraulic diameter as defined by Ebner
$We_{D,S}$	= Weber based on a hydraulic diameter number as defined by Sawant
X_e	= entrainment parameter
y	= coordinate denoting perpendicular distance to the wall
x	= coordinate denoting distance in the stream-wise direction
α	= liquid film surface angle
Γ_{cr}	= critical liquid flow rate per unit perimeter
γ	= ratio of specific heats
δ	= liquid film thickness
δ^+	= non-dimensional film thickness
δ_{ave}	= average liquid film thickness
δ_l	= film thickness on left
δ_r	= liquid film thickness on the right
θ_{hc}	= LFD laser cone half-angle

Symbol	Description
θ_l	= angle of the laser cone on the left in the presence of the liquid film
θ_r	= angle of the laser cone on the right in the presence of the liquid film
λ	= stream-wise distance downstream of film injection slot
ρ	= density
ρ_f	= density of the liquid film
ρ_g	= density of the gas phase
ρ_l	= density of the liquid phase
$\rho_{w,N}$	= partial density of H ₂ O in free-stream nitrogen far from the liquid surface
$\rho_{w,s}$	= partial density of H ₂ O at the surface of the liquid film
μ	= absolute viscosity
μ_g	= absolute viscosity of the gas phase
μ_f	= absolute viscosity of the liquid film
μ_l	= absolute viscosity of the liquid phase
ν	= kinematic viscosity
ν_f	= kinematic viscosity of the liquid film
σ	= surface tension
τ	= shear stress
τ_i	= interfacial shear stress acting on liquid film surface
τ_w	= wall shear stress
ϕ	= substrate surface angle
φ	= angle of flow direction with respect to the horizontal

ABSTRACT

Miller, Ryan P. M.S., Purdue University, December 2012. Experimental Investigation of Shear Driven Liquid Films for Film Cooling Applications in Liquid Rocket Engines. Major Professor: William E. Anderson.

Liquid film cooling is an important method for cooling the walls of a liquid rocket engine. Mass transfer via entrainment decreases the effectiveness of the film coolant and it is therefore important to estimate the amount of film coolant that establishes itself along the wall of a combustion chamber if the coolant flow rate is to be optimized. However, film entrainment research is limited in regards to film cooling applications in rockets. The correlations and theories that have been published are often limited in scope and have only been tested at momentum fluxes that are an order of magnitude less than those typically experienced in rockets. Experimental research has been conducted in a cold-flow test article at AFRL in order to investigate the effects of the gas stream momentum flux on the coolant flow rate that remains attached to the wall. Specifically, the objective of this study was to investigate the establishment of a shear driven liquid film introduced into a rectangular test section by a .38 mm X 25.4 mm slot, perpendicular to the stream-wise direction of the gas phase. A secondary objective of this thesis was to investigate the ability of several diagnostics to measure the interfacial shear stress, mean film thickness, and the film mass flow rate of a liquid water film shear-driven by nitrogen gas in cold flow conditions. Ultimately, a film removal slot was chosen to measure the film mass flow rate, differential pressure taps were chosen to indirectly deduce the interfacial shear stress by measuring a stream-wise pressure drop, and a laser focus displacement meter was chosen to measure the liquid film thickness. Lastly, a high-

speed video camera was used to obtain qualitative visual data of the surface of the shear-driven liquid film.

Experiments were conducted during June and November 2011 in order to accomplish the objectives of the thesis. The experimental apparatus consisted of a rectangular channel through which nitrogen gas flowed at momentum fluxes ranging from 2.5 to 110 kPa. A liquid water film was introduced into the test section at flow rates ranging from .0034 kg/s to .018 kg/s through a .38 X 25.4 mm slot that was perpendicular to the gas flow. In the experiments described herein, the film removal slot failed to completely remove the entire film, and, therefore, the results from the film removal slot were inaccurate. However, from the data that was obtained, it appears as though the liquid that becomes entrained into the gas phase increases with both increasing gas phase momentum flux and injected liquid flow rate. The amount of liquid entrained appears to vary from about 20 to 60 % of the injected liquid flow rate for the conditions studied. In addition, the correlations for entrainment proposed by several other authors did not agree well with the data that was obtained nor each other. The pressure drop data that was obtained was inaccurate due to problems with the flow, an electrical error, or leaks in pressure lines. Due to difficulties encountered with the differential pressure transducers, it is not recommended that the interfacial shear stress be estimated from pressure drop data. The thickness of the liquid film was shown to decrease with increasing gas phase momentum flux and increase with increasing liquid film flow rate. The film thicknesses measured ranged from 4 μm at the highest momentum fluxes and lowest liquid flow rates to 160 μm at the lowest gas phase momentum fluxes and highest liquid flow rates, with a 25 % relative uncertainty. The film thicknesses that were measured were of the same order of magnitude as estimated or measured for similar conditions by other researchers. A numerical model was used to determine an upper bound on the film thickness results, and the experimental results fell below and exhibited the same trends as the upper bound. It was also discovered that the turbulent surface of the liquid film and entrained liquid droplets at high momentum fluxes adversely affected the ability of the LFD to directly detect the surface of the liquid film. A new method for using the LFD to measure film

thicknesses based on geometric optics is proposed. However, the results obtained by this new method still require further validation.

CHAPTER 1. INTRODUCTION

Liquid film cooling is an effective means of protecting the wall of a combustion chamber and throat in liquid rocket engines. In addition, it may also serve to protect the wall from potentially damaging reactions with species in the core flow. A trade-off associated with liquid film cooling is that it reduces the temperature of the combustion gases, thereby resulting in a performance loss. Therefore, it is undesirable to inject more film coolant than what is needed and it is important to optimize the liquid film flow rate in order to achieve the best possible performance in liquid rockets.

Experimental research has been undertaken at the Air Force Research Lab to investigate liquid film cooling. Cold flow experiments have previously been conducted by Coy et al [1] to investigate the establishment of a liquid water film injected by a thin slot perpendicular to the stream-wise direction of gas flow. Their experiments consisted of a 25.4 mm X 25.4 mm rectangular duct through which dry nitrogen gas flowed. A liquid water film was injected through a thin slot, perpendicular to the stream-wise gas direction. Figure 1 illustrates a liquid film being injected by a perpendicular slot into the gas flow.

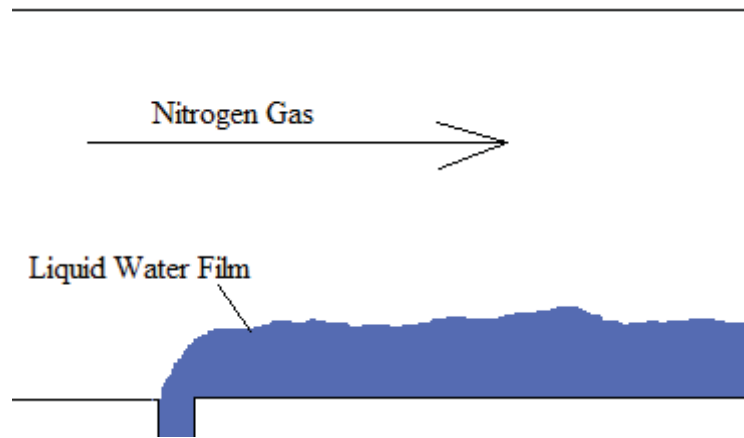


Figure 1-1: Liquid Water Film Being Injected Through a Perpendicular Slot

This thesis seeks to continue the work begun by Coy et al [1]. The main objective was to determine the mass flow rate of the liquid film that establishes itself along the wall and how much gets entrained into the gas phase right at the point of injection after being injected through a thin slot in the manner shown in Figure 1. To complete this objective, another experiment was designed and built to directly supplement the experiments of Coy et al. To separate the effects of mass transfer due to entrainment from evaporation, the experiments described in this thesis have been performed under cold-flow conditions, using nitrogen gas and water as simulants for the combustion gases and film coolant, respectively.

A schematic of the experimental apparatus used in this thesis is shown in Figure 1-2. The slot under investigation in this thesis was .38 mm across in the downstream direction, 25.4 mm in span across the test section, and 6.35 mm in depth. The rectangular channel through which dry nitrogen gas flowed had a 26.4 mm X 12.7 mm cross-section, with the film being injected 600 mm downstream of where the nitrogen was introduced. The flow rates of the nitrogen gas and liquid water were metered using a sonic nozzle and a cavitating venturi, respectively. The film was removed by means of a film removal slot placed 139 mm downstream of the injection slot where it was then passed to a gas liquid separator in order to measure the mass flow rate of liquid that remained within the film. The static pressure of the test section was monitored by a pressure tap located 25.4 mm upstream of the slot. Two differential pressure taps were located at 25.4 mm and 127 mm downstream of the injection slot in order to estimate the

pressure drop and shear stress associated with the liquid film. The Mach number in the test section was controlled by inserting cylindrical plugs of various diameters at the exit of the test section. Finally, the film thickness 50.4 mm downstream of the injection slot was measured using a laser focus displacement meter (LFD), which is represented by the red cone in Figure 1-2. The image on the right in figure 4 is a picture taken with a high speed video camera during a test through the side of the test article opposite of the film. Schematics of the film injector and test article components can be found in the appendix. Further details of the experimental apparatus can be found in chapter 4, a thorough description of the LFD can be found in chapter 3, and additional details of experimental procedures and results can be found in chapter 5.

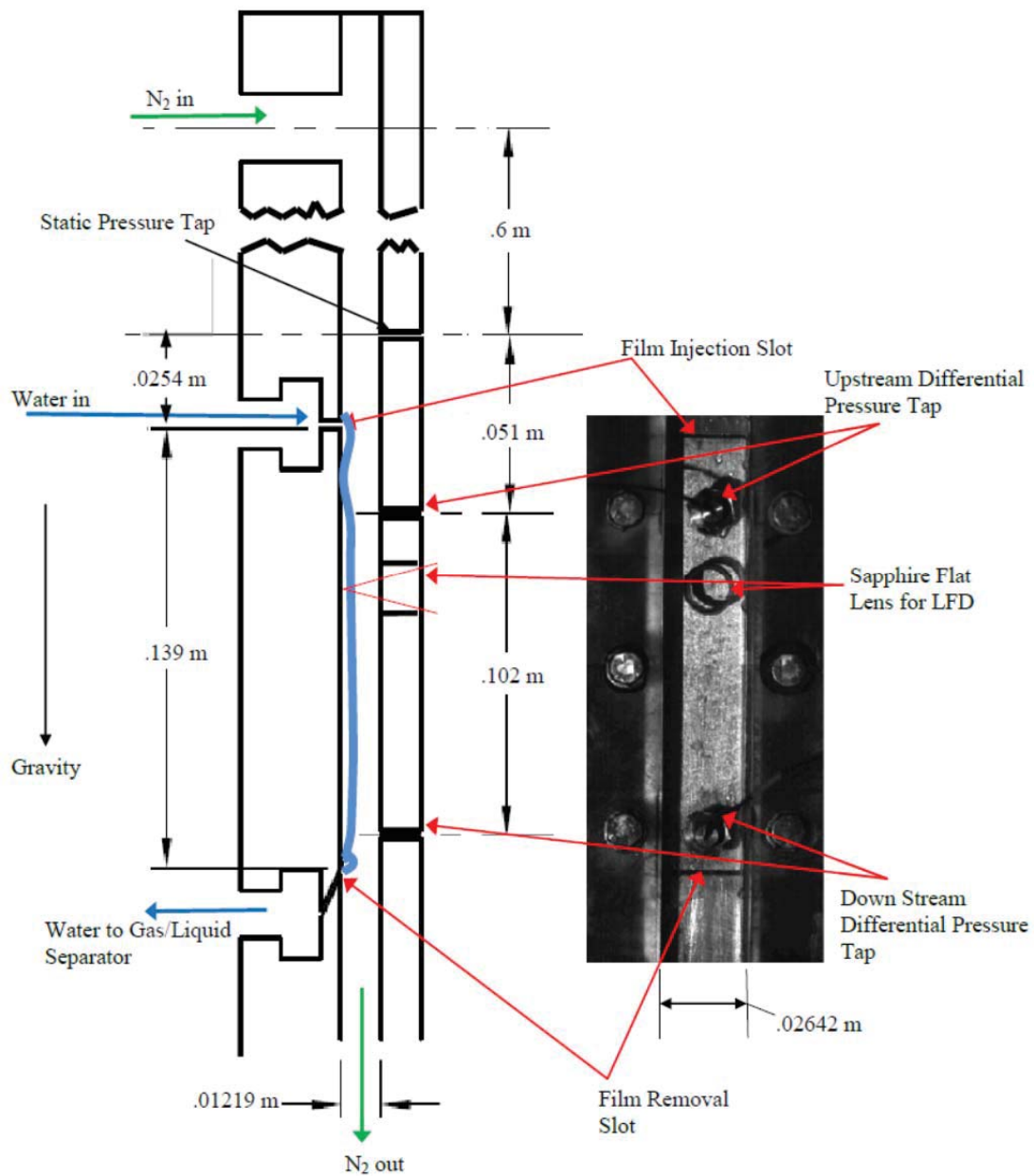


Figure 1-2: Description of Experimental Apparatus

A second objective of the experiments described in this thesis was to identify and evaluate techniques that could be used to determine the liquid film mass flow rate, the shear stress at the interface between the film and the gas, and the thickness of the liquid film. In the experiments described in this thesis, a thin slot was used to remove the film about 14 cm downstream of the injection slot in order to determine the film mass flow

rate. However, the slot failed to completely remove the film during any of the experiments. The pressure drop along a 10 cm span of the test article was measured. It was hoped that an estimate of the shear stress could be determined from the pressure drop data, however, the author was unable to get the differential pressure transducers to work correctly in the allotted time. Finally, qualitative studies of the film's surface were made using a Vision Research Phantom v7.3 high speed video camera.

While the second objective of this thesis was to evaluate several different liquid film diagnostics, most of the work focused on qualifying the ability of a laser focus displacement meter (LFD) to measure the thickness of a shear-driven liquid film. As will be discussed in section 1.2, the film thickness is a very important variable needed to characterize the phenomena of shear-driven liquid films. Coy et al did not measure the film thickness directly in their experiments, and directly measuring the film thicknesses for the conditions they studied was one of the primary interests in this thesis. The LFD is a fairly recent diagnostic that has shown an ability to measure film thicknesses in shear-driven liquid film experiments by other researchers [2],[3],[4],[5],[6]. However, it has not yet been used to measure the thickness of a shear-driven liquid film subjected to gas phase momentum fluxes exceeding 10,000 Pa. Qualifying the ability of an LFD to measure the film thickness at these conditions was a major focus of the experiment. In this thesis, the LFD was determined to be capable of measuring the thickness of a shear-driven liquid film to within a relative uncertainty of approximately 25%. Further analysis and experiments could potentially improve the LFD's ability to measure the thickness of shear-driven liquid films subjected to high momentum fluxes.

More work is needed before the objectives of this thesis are met, as most of the experimental results were inconclusive. The amount of liquid entrained into the gas phase after being injected appears to vary within 20%-60% of the injected liquid flow rate for gas phase momentum fluxes ranging from 34 kPa to 110 kPa and injected liquid flow rates ranging from .0034 kg/s to .0064 kg/s. However, these results are inconclusive as the film removal slot did not work effectively in this experiment. Accurate interfacial shear stress data was never obtained due to a failure to correctly measure the pressure drop. Finally, measurements obtained using the LFD demonstrated that the film

thickness varied between about 4 μm to 170 μm with a 25% relative uncertainty for gas phase momentum fluxes ranging from 5.2 kPa to 110 kPa and liquid flow rates ranging from .0034 kg/s to .018 kg/s, with film thickness decreasing as gas phase momentum flux increases and the injected liquid flow rate decreases.

1.1 Overview of Mechanics of Shear-driven Liquid Films in Cold-Flow

Due to the complex physical mechanisms governing the behavior of the liquid films around a corner and the atomization process, it is difficult to determine how much of the film remains attached to the wall after injection. To aid in CFD modeling and heat transfer and performance calculations, there is a need to determine the film thickness and velocity that the film assumes after being injected, and, it is also useful to determine the interfacial roughness and shear stress on the film. These parameters are important in CFD validation and heat transfer rates. Such knowledge could also potentially allow one to predict the film flow rate that becomes attached to the wall and how much becomes entrained into the gas phase.

While there are a significant number of variables that need to be understood in regards to liquid film cooling in liquid rocket engines, the experiments and objectives of this thesis are all associated with cold-flow phenomena. Consequently, this section provides an overview of the fluid mechanics associated with a shear-driven liquid film established by an injection slot that is perpendicular to the primary direction of gas flow, corresponding to geometry of the experiments described in this thesis. Specifically, this thesis is concerned with the mass flow rate of the liquid film that attaches to the wall and the amount that gets entrained into the gas phase. There are two main sources for entrainment of a shear-driven liquid film in cold-flow. The first is from inertial forces tending to throw the film outward into the gas phase as the liquid film attempts to navigate the corner at the slot. The second source of entrainment is from atomization of liquid after it has been established along the wall following injection, which is characterized by liquid droplets being stripped off the films surface and becoming entrained into the gas phase.

The first source where entrainment of the liquid phase into the gas phase can occur is at the injection slot. Figure 1-2 shows a diagram describing the injection of the film into the gas via a perpendicular slot.

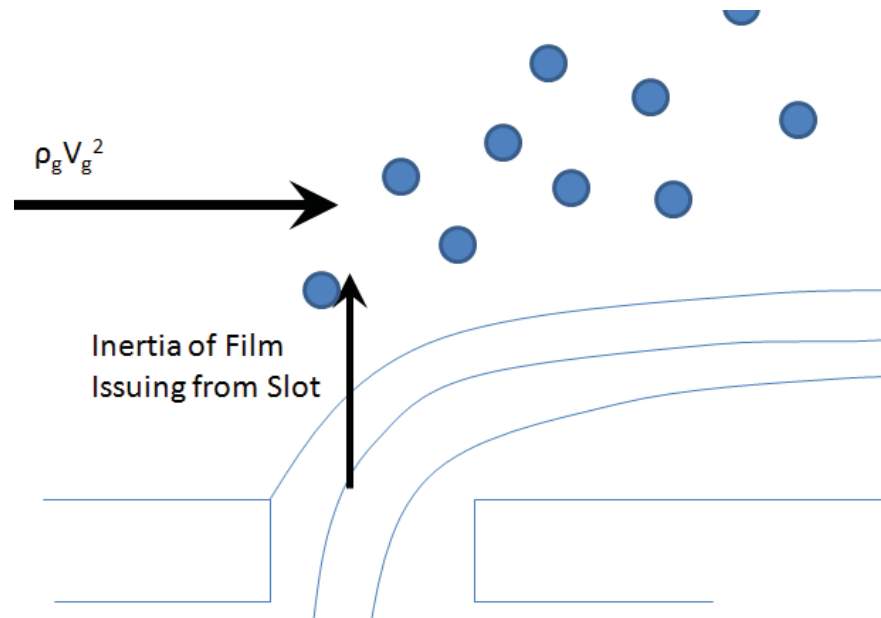


Figure 1-3: Diagram of Film Issuing from a Slot

The force required for the film to navigate the corner of the injection slot is dependent on the momentum flux of the gas and the injected liquid. Surface tension and viscous forces help maintain the injected liquid's integrity. The radius of the corner and the roughness of slot walls are also important. Finally, hydrodynamic instabilities must also be considered.

The second source of entrainment is from the atomization of the liquid film after it has been established along the wall. Atomization occurs from the interaction of two physical phenomena: growth of disturbances at the gas liquid interface, followed by their breakdown due to aerodynamic forces from the gas phase [7]. In shear-driven film flows, the growth of disturbances on the surface is propagated by hydrodynamic instabilities, turbulent gas structures deforming the surface of the film, and wall roughness [7]. As these disturbances continue to grow, the aerodynamic forces acting on them from the gas phase also become larger, depending on the size and shape of the disturbances. Once the aerodynamic forces acting on a disturbance overcome surface tension and viscous forces,

a part of the disturbance breaks off as a droplet and becomes entrained into the flow [7]. An extensive amount of literature has been devoted to analytical and numerical studies of the growth of the disturbances, however, the mathematics involved are very complex and beyond the scope of the current study. Figure 1-4 shows a free-body diagram of the forces acting on a typical wave crest.

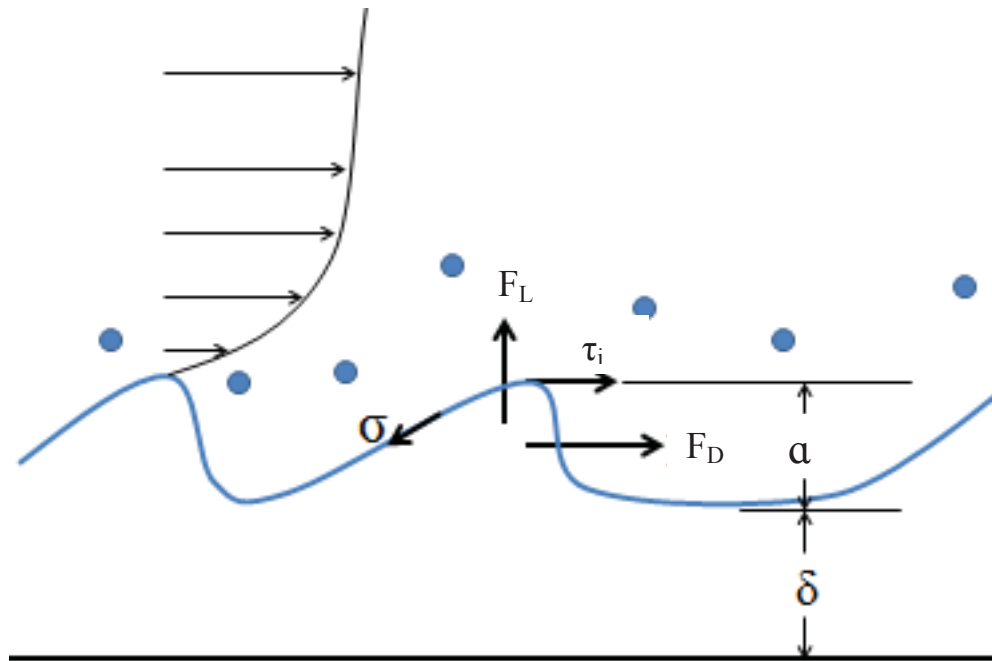


Figure 1-4: Forces acting on waves in a shear-driven liquid film in cold flow

The growth of disturbances in the liquid film is propagated by inertial forces in the film and in the gas phase just above the interface. The viscosity within the liquid film acts to dampen the disturbances and laminarize the flow. Close to the wall, viscous forces are expected to dominate over inertial forces and the flow is expected to be laminar, regardless of whether the bulk of the flow is turbulent. This region is referred to as the laminar sublayer [8]. Prior work[1],[9],[10] suggests that disturbances form on the surface of a liquid film when the film becomes thick enough such that “turbulent forces predominate over viscous forces” [9]. A common non-dimensional parameter that relates

the inertial forces which grow with distance from the wall to the viscous forces is a non-dimensional film thickness [1],[9], which is a type of Reynolds number:

$$\delta^+ = \frac{\delta}{\nu} \sqrt{\frac{\tau_i}{\rho_l}} \quad (eq\ 1 - 1)$$

Therefore, thinner films are generally more stable, and thus, more difficult to atomize. Indeed, entrainment has not been observed in cases where no waves are present on the surface [10],[11].

The atomization and breakdown of those disturbances, and thus entrainment into the gas phase, results when aerodynamic forces overcome viscous and surface tension forces in the film. These aerodynamic forces are represented in figure 1-4. The three forces are the bluff body drag force, F_d , the interfacial shear stress, τ_i , and the lift force, F_L . Once the resultant of these forces on a disturbance overcomes the surface tension, inertial, and viscous forces, a droplet breaks off and becomes entrained into the gas phase, where it may undergo additional atomization [7]. Each of the aerodynamic forces is proportional to the momentum flux of the gas phase. The lift, drag and surface tension forces are all also dependent on the height of the disturbance. Therefore, it is proposed that a Weber number relating the momentum flux of the gas, the disturbance height, and the surface tension is an important non-dimensional number governing the entrainment rate due to atomization:

$$We = \frac{\rho_g V_g^2 a}{\sigma} \quad (eq\ 1 - 2)$$

The two non-dimensional numbers described by equations 1-1 and 1-2 are expected to be the most important variables characterizing the atomization of a liquid film. References [10] and [12] provide some experimental evidence for this. However, there are many other non-dimensional variables and groups that are also expected to be important. They are:

$$\frac{\mu_g}{\mu_l} \quad (eq\ 1 - 3)$$

$$\frac{\rho_g}{\rho_l} \quad (eq\ 1 - 4)$$

$$\frac{a}{\delta} \quad (eq\ 1 - 5)$$

$$Oh = \frac{\mu_l}{\sqrt{\rho_l \sigma D_h}} \quad (eq\ 1 - 6)$$

$$C_D = \frac{F_D}{\rho_g V_g^2 a w} \quad (eq\ 1 - 7)$$

$$C_L = \frac{F_L}{\rho_g V_g^2 a w} \quad (eq\ 1 - 8)$$

$$C_F = \frac{\tau_i}{\rho_g V_g^2} \quad (eq\ 1 - 9)$$

From analysis above, the most important variables associated with shear-driven liquid films in cold flow are the film thickness, the interfacial shear stress, the drag force, an average film velocity, the momentum flux of the gas phase, and the mass flow rate of the liquid film that establishes itself along the wall. After a literature review, it was determined to not be feasible to measure the velocity profile within the liquid film or the drag forces acting on the waves with available resources. Rather, the drag forces acting on the surface of the liquid film are likely to be reflected in an average shear stress in the gas phase just above the film, or the wall shear stress below the film. Therefore, the experiments in this thesis attempted to measure the film thickness, interfacial shear stress and the film mass flow rate as a function of the momentum flux of the gas and the liquid flow rate that is initially injected through the slot, herein referred to as the injected liquid flow rate (ILFR).

1.1.1 Differences Between Hot-Fire at Subcritical Conditions and Cold Flow

The results described in this thesis and the results described above are limited in their applicability to situations where the core gas flow is hot. For one, the rate of heat transfer to the liquid film will reduce both the surface tension and viscosity of the liquid. More significantly, the interaction of the gas phase at the interface of the film will be

affected by the evaporation of the film into the gas phase. Rapid evaporation at high heat flux conditions will cause a secondary flow off of the liquid surface called Stefan flow [1]. This secondary flow rate from the surface of the film will affect the ability of the gas phase to interact with the surface of the liquid film. Additionally, the evaporation is expected to have a tendency to make the film thinner as it progresses downstream [9]. This thinning effect is expected to make the film more stable, depending on heat transfer and evaporation rates [9].

Finally, another significant effect on film cooling in hot-fire is from heat transfer from the wall itself. In a rocket engine, heat can be transferred from other parts of the engine to the wall underneath the film via conduction. The hot wall can boil the film, creating gas bubbles along the wall [13]. The presence of the fuel vapor bubbles along the wall can significantly reduce the effectiveness of film cooling.

1.1.2 Differences at Supercritical Conditions

Liquid film cooling is expected to behave even more differently at supercritical conditions. If the liquid film is injected at subcritical temperatures into a gas phase where pressures are near or above the critical point of the film, then the film will not undergo a discrete phase change as its temperature increases. Surface tension disappears, and therefore the Weber number goes to infinity. Near the critical point, the heat capacity of the high-density film goes to infinity [14]. As a result, it is expected that the film will behave more like a very high density gas [14]. It will still remain and flow along the wall, however, the entrainment of the fuel into the gas phase will behave more like the mixing of two gases of dissimilar densities. Once enough heat is imparted into the supercritical fuel film, it suddenly undergoes a rapid expansion process and diffuses into the gas phase much more rapidly [14].

In the instance where a liquid at a subcritical temperature is injected into a gas phase of a different species or composition than the liquid where the temperature and pressure are above the critical point, part of the gas phase diffuses into the liquid phase, which can significantly increase the critical pressure of the liquid phase [14]. When this

happens surface tension is small, but still significant, and there is still a discrete boundary between the gas and liquid phases [14].

1.2 Chapter 1 Summary

The objective of this thesis was to investigate establishment of a shear-driven liquid film after being injected into gas flow through a perpendicular slot. Based on the mechanics of shear driven liquid films, the independent variables in the experiments of this thesis were chosen to be the momentum flux of the gas phase and the injected liquid flow rate. The dependent variables being investigated in this experiment were chosen to be the liquid film mass flow rate, the interfacial shear stress, and the liquid film thickness. The secondary objective of this thesis was to investigate the ability of several test diagnostics to measure the dependent variables. Specifically, the ability of a film removal slot to measure the film flow rate, the ability to deduce the interfacial shear stress from pressure drop measurements, and the ability of an LFD to measure the film thickness were all investigated. However, the focus of the experiments and this thesis was biased toward using the LFD to obtain film thickness measurements.

A literature review of previous film liquid film cooling and shear-driven film studies is presented in Chapter 2. A brief overview of the experimental diagnostics used in this thesis, with a brief description of other diagnostics is presented in Chapter 3. Chapter 4 discusses and explains the test article. The results of the experiment are presented in chapter 5. This thesis ends with a summary and concluding remarks in Chapter 6.

CHAPTER 2: LITERATURE REVIEW

The amount of experimental work that has been done to characterize the mechanisms of entrainment and film stability for liquid film cooling applications in rockets is limited [15]. Most of the literature regarding film stability and entrainment for liquid film cooling in rockets occurred prior to 1970. Kinney [9], Knuth [16], and Coy [1] all concluded that the establishment of the liquid film is dominated by a maximum stable liquid film Reynolds number, though the definitions of that Reynolds are different for each researcher. On the other hand, Gater [17] observed that the amount of film entrained into the gas flow is entirely dependent on the momentum flux of the gas phase and surface tension of the film coolant. Ebner [6] conducted experiments on the entrainment fraction of thin oil films at much lower momentum fluxes than the others, but observed that entrainment fraction from a liquid film is dependent on both a Weber number and liquid film Reynolds number. Finally, Sawant [10] observed that the entrainment fraction in annular flows is primarily dependent on a Weber number at low Weber numbers and primarily dependent on a liquid film Reynolds number at high Weber numbers. Tests that have investigated the phenomena of entrainment from thin liquid films have been limited to momentum fluxes of less than 200,000 Pa, whereas momentum fluxes characteristic of high performance liquid rocket engines are generally above 1,000,000 Pa in the combustion chamber to 10,000,000 Pa at the throat.

2.1 Review of Literature Specific to Liquid Film Cooling in Rocket Engines

This section provides an overview of the literature concerning experimental investigations of liquid film cooling in rocket engines. The literature discussed in this section did not necessarily focus on entrainment from liquid films. Rather, much of the

literature discussed in this section focused on all aspects of liquid film cooling. This literature review is not comprehensive, but it covers much of the experimental work involving liquid film cooling from the mid 1950's to present.

2.1.1 Liquid Film Attachment investigations by Warner and Reese

Warner and Reese [18] were among the first to investigate the establishment of a liquid film injected by means of a slot for the purposes of cooling liquid rocket engines. They investigated the effects that slot geometry, gas velocity, gas density, injected liquid velocity, and liquid properties have on the film's ability to attach to the wall just after being injected. In their experiments, for a particular configuration, they increased the velocity of the liquid film being injected until the film just failed to attach to the wall directly after the injection slot. The velocity at which the film failed to attach to the wall was termed the "critical velocity of injection." Warner and Reese observed that increasing the gas velocity increases the critical velocity of injection. Changing the viscosity and surface tension appeared to have no effect. Increasing the density of the liquid decreased the critical velocity of injection. However, the surface tensions were varied by using aqueous solutions of different concentrations, and, therefore, the surface tensions they reported may not have been the surface tensions at the injection point, as it takes time for surfactants to diffuse to the surface to effect surface tension [19]. Finally, it was observed that the geometry of the injection slot had a significant effect on the critical velocity of injection. In general, thinner slots had a higher critical velocity of injection, suggesting that the film establishes itself better with thinner slot designs. Finally, angling the slot with respect to the gas stream also affected the critical velocity of injection. Slots perpendicular to the gas stream had the lowest critical velocities, with the critical velocity of injection increasing as the slot became more tangential with the gas flow. Warner and Reese were unable to get the film to separate if the injection angle was greater than 75 degrees (an injection angle of 0 degrees is defined as perpendicular to the gas flow and 90 degrees is defined as tangential). The authors also proposed a correlation

predicting the critical velocity of injection based on film and gas properties and slot width.

$$\frac{V_L^*}{V_g} \sqrt{\frac{\rho_L}{\rho_g}} \left(\frac{b}{D_h} \right)^{f'(Re_g)} = 0.153 [Re_g \times 10^{-5}]^{.65} \quad (eq\ 2 - 1)$$

for $Re_g = .5 \times 10^5$ to 2.5×10^5

$$\frac{V_L^*}{V_g} \sqrt{\frac{\rho_L}{\rho_g}} \left(\frac{b}{D_h} \right)^{f'(Re_g)} = .085 \quad (eq\ 2 - 2)$$

for $Re_g = 2.5 \times 10^5$ to 12×10^5

where

$$f'(Re_g) = .404 - 0.012 Re_g \times 10^{-5} \quad (eq\ 2 - 3)$$

and

$$Re_g = \frac{\rho_g V_g D_h}{\mu_g} \quad (eq\ 2 - 4)$$

2.1.2 Liquid Fuel Film Studies by Kinney, Sloop and Abramson

Kinney et al [9] performed extensive experimental heat transfer and cold flow studies on liquid film cooling in the 1950's. Heated air was used to simulate the combustion gases and liquid water was used as the coolant simulant in the heat transfer experiments, while water, aqueous ethylene glycol solutions, and water-detergent solutions were used as coolants to vary surface tension and viscosity in the cold flow experiments. In the heat transfer experiments, it was observed that the film cooling effectiveness began to decrease when the injected non-dimensional coolant flow rate, w^+ exceeded about 360. Equation 2-5 shows the definition of w^+ . Kinney et al [9] concluded that this nonlinearity was due to the formation of disturbance waves on the film surface that subsequently lead to droplets being sheared off of the wave crests. It was hypothesized that the surface of the liquid film becomes unstable and waves begin to

form once the liquid film is thick enough such that turbulent forces in the gas phase overcome viscous forces in the liquid phase. In their cold-flow experiments, they observed that waves formed on the surface of the liquid film at a non-dimensional coolant flow rate of 90. Kinney et al [9] concluded that heat transfer to and evaporation from the liquid film had a stabilizing effect, which allowed more coolant to be injected before the effectiveness began to decrease in the heat transfer experiments than what was predicted by the cold-flow experiments. Kinney et al [9] also observed that the liquid flow rate at which disturbances were first observed increased with increasing viscosity, increased slightly with increased surface tension, and was relatively independent of the gas stream mass velocity.

$$w^+ = \frac{ILFR'}{\mu_l} \quad (eq\ 2 - 5)$$

2.1.3 Studies Regarding Film Stability by Knuth

Later, Knuth [16] extended the results of Kinney's experiments on film stability. Knuth [16] also performed similar cold-flow visualization tests and heat transfer tests to Kinney. Knuth [16] concluded that the maximum stable coolant flow rate per unit length around the test section perimeter, ie. the maximum flow rate before waves are formed, follows the following equation [15],[20]:

$$\Gamma_{cr} = 1.01 \times 10^5 \left(\frac{\mu_g^2}{\mu_l} \right) \quad (eq\ 2 - 6)$$

Again, both Kinney and Knuth observed that the stable liquid film flow rate seems to be independent of the gas phase momentum flux.

2.1.4 Film Cooling Entrainment Studies by Gater and L'Ecuyer

Gater and L'Ecuyer [17] attempted to distinguish the mass transfer by entrainment from the mass transfer by evaporation in their experiments. Gater and

L'Ecuyer [17] conducted their experiments with a flat film, as opposed to annular flow, and measured the amount of liquid that remained attached to the wall with a knife-edge capture slot. The film coolants studied were water, methanol, butanol, and RP-1, and the gas was heated air. Contrary to the observations of Kinney et al and Knuth, Gater and L'Ecuyer [17] observed that the wave structure and instabilities on the surface of the film were dependent only on the momentum flux of the gas stream and surface tension of the liquid film. No dependence on the viscosity of the liquid film was observed. Secondly, it was observed that the fraction of the liquid film entrained into the gas flow was also only a function of the momentum flux of the gas and surface tension of the liquid film. They proposed the following dimensional, empirical correlation for the entrainment fraction [17]:

$$EF = 1.0 - \exp(-5 \times 10^{-5}(X_e - 1000)) \quad (eq\ 2 - 7)$$

Where X_e is a dimensional entrainment parameter defined by:

$$X_e = \frac{MF_g^{1/2}}{\sigma} \left(\frac{T_g}{T_s} \right)^{1/2} (\text{lb}_f)^{-1/2} \quad (eq\ 2 - 8)$$

Note that the units of equation 2-7 and 2-8 are simply those given in Gater and L'Ecuyer. No attempt has been made to convert them to S.I. in this thesis. This correlation is only truly applicable to flat films running through a rectangular duct due to its dimensionality. However, Gater and L'Ecuyer [17] did suggest that X_e could be recast as a Weber number with the wave height on the liquid film taken as the characteristic length.

2.1.5 Liquid Film Cooling Research and Modeling by Grissom

Grissom [20] performed a review of both liquid and gas film cooling literature. From the literature, Grissom proposed a liquid film cooling model and compared it with prior experiments. Grissom also suggested that the work of Kinney et al, Knuth, Gater

and L'Ecuyer, and Warner and Emmons be improved, due to the uncertainties and discrepancies associated with each experiment. The models and equations used are not repeated here, as the one's relevant to this thesis were reviewed in prior paragraphs. For further details, the reader is directed to the work of either Yu et al [15] or Grissom [20] work.

2.1.6 Liquid Fuel Film Cooling Studies by Volkmann et. al

Volkmann et al [21] studied the effectiveness of using liquid film cooling to reduce the heat flux in rocket combustors. Their experiments consisted of hot-fire combustion experiments in a sub-scale LOX/CH₄ and LOX/RP-1 combustor. Film coolant was introduced at the injector face in some of the experiments, and 112 mm upstream of the throat in other experiments [21]. The heat flux through the wall was measured as a function of distance from the throat. The results of the wall and throat experiments were compared to each other and to the control case in which no film coolant was used. Volkmann et al [21] demonstrated that applying film coolant near the injector face significantly reduced the heat flux for most of the chamber but was much less effective near the throat, where heat fluxes are highest. Injecting the coolant 112 mm upstream of the throat was found to significantly reduce the heat flux at the throat. The authors recommended that film cooling be applied at throat and not just at the injector face, contrary to what has been done in the past. Secondly, they recommended applying film cooling only where it was needed, as applying the coolant at a single axial location was much simpler from a design perspective than to apply the the coolant at multiple locations, as would be done in the case of transpiration cooling. Finally, they proposed several design concepts for incorporating liquid film cooling in flight hardware.

2.1.7 Kirchberger's Studies

Kirchberger et al conducted several experiments investigating film cooling in Kerosene/GOX combustion chambers [22], [23]. The combustion chamber used in their

experiments was put together in modular segments, allowing for the cylindrical section of the chamber to be varied in length between 206-396 mm. The diameter of the cylindrical section of the chamber was 37.00 mm and the throat diameter was 16.53 mm. Nitrogen or kerosene could be introduced as a film coolant through a film applicator about 200 mm downstream of the injector face. Wall heat fluxes through different sections were measured using calorimeters and temperatures within the wall were measured using thermocouples. Kirchberger et al. observed that kerosene was a more effective film coolant than nitrogen. They also compared several film cooling numerical models to the data they collected. They observed that the numerical film cooling models agreed with the data when no film cooling was used or when nitrogen was used as a film coolant. However, the numerical simulation differed significantly from the test results in the region close to the film injector when kerosene was used as a film coolant.

2.1.8 Fuel Film Cooling Review by Yu, Schuff and Anderson

Yu et al. [15] performed a critical literature review of all gaseous and liquid film cooling rocket literature. They emphasized the lack of literature related to the subject and the need for further experiments. They compared models and experiments from various researchers and highlighted the discrepancies, indicating a need for further research. Finally, they proposed that swirling the liquid film after injection might provide for more efficient film cooling, as the centrifugal force of the swirling film would help hold the film to the wall and reduce entrainment. After performing an order of magnitude analysis on the forces acting on a liquid film, they concluded that wall shear stress, surface tension, liquid inertia and centrifugal force were the most dominant forces acting on the film.

2.1.9 Cold-Flow Liquid Film Establishment Experiments by Coy, Schumaker, and Lightfoot

More recently, Coy et al [1] estimated the entrainment fraction from a slot injector. Gas momentum fluxes were 33 kPa, 66 kPa, and 99 kPa and the liquid film was injected at .155, .219, and .268 kg/s-mm (per mm of slot width). The pressures and temperatures were about ambient and the Mach number in the test section was estimated to be approximately .6. The authors used high speed video to track the velocities of the disturbances on the liquid film [1]. Assuming couette flow and an empirical correlation for surface roughness, Coy et al [1] were able to estimate the thickness of the liquid film. Reducing this thickness to wall coordinates, it was discovered that the δ^+ for all the experimental conditions collapsed to about 20. Coy et al [1] concluded that a δ^+ of 20 governed the maximum amount of liquid film that could remain attached to the wall before becoming entrained into the gas phase. It was hypothesized that any additional liquid injected as a film that would tend to push δ^+ above 20 would become entrained into the gas phase [1].

2.2 Minor Literature Review of Two-Phase Annular Flow Experiments

The literature reviewed in this section concerns annular two-phase flow experiments. The objective behind most of the research regarding annular two-phase flow experiments was to develop annular flow models for cooling applications in nuclear reactors. The results and small geometries of these experiments are not directly applicable to modeling the establishment of a liquid film for liquid film cooling in rocket engines. However, these experiments nonetheless involve a shear driven liquid film flowing around the internal annulus of a pipe. Therefore, the underlying physical phenomena and experimental results associated with the entrainment of the annular liquid films described in the following experiments provide insights into the behavior and trends associated with the establishment of a liquid film for liquid film cooling in rockets. This review is not at all comprehensive. However, the literature discussed here includes both reviews and data from numerous researchers.

2.2.1 Experimental Investigations by Sawant and Ishii

Sawant et al [10] investigated the entrainment fraction in co-current vertical air-water and Freon-113 annular flows. The experiments were conducted for $We_{D,S}$ from 0-25000 and for $Re_{l,S}$ ranging from 150-5000 (definitions in equation 2-11 and 2-12). Sawant et al [10] suggested two correlations to estimate the entrainment fraction in vertical upward annular flows for diameters up to 32.0 mm. The simpler of the two (a good approximation of the other) is:

$$EF = \left(1 - \frac{13N_{\mu f}^{-.5} + .3(Re_{l,S} - 13N_{\mu f}^{-.5})^{.95}}{Re_{l,S}} \right) \times \tanh(2.31 \times 10^{-4} Re_{l,S}^{-.35} We_{D,S}^{1.25}) \quad (eq\ 2 - 9)$$

where:

$$N_{\mu f} = \frac{\mu_f}{\left(\rho_f \sigma \sqrt{\frac{\sigma}{g(\rho_f - \rho_g)}} \right)^{1/2}} \quad (eq\ 2 - 10)$$

$$Re_{l,S} = \frac{\rho_l j_l D_t}{\mu_l} \quad (eq\ 2 - 11)$$

$$We_{D,S} = \frac{\rho_g j_g^2 D_t}{\sigma} \left(\frac{\rho_L - \rho_g}{\rho_g} \right)^{1/4} \quad (eq\ 2 - 12)$$

$$j_l = \frac{Q_l}{A_t} \quad (eq\ 2 - 13)$$

$$j_g = \frac{Q_g}{A_t} \quad (eq\ 2 - 14)$$

This correlation is illustrated in figure 1 for $N_{\mu f} = .00266$:

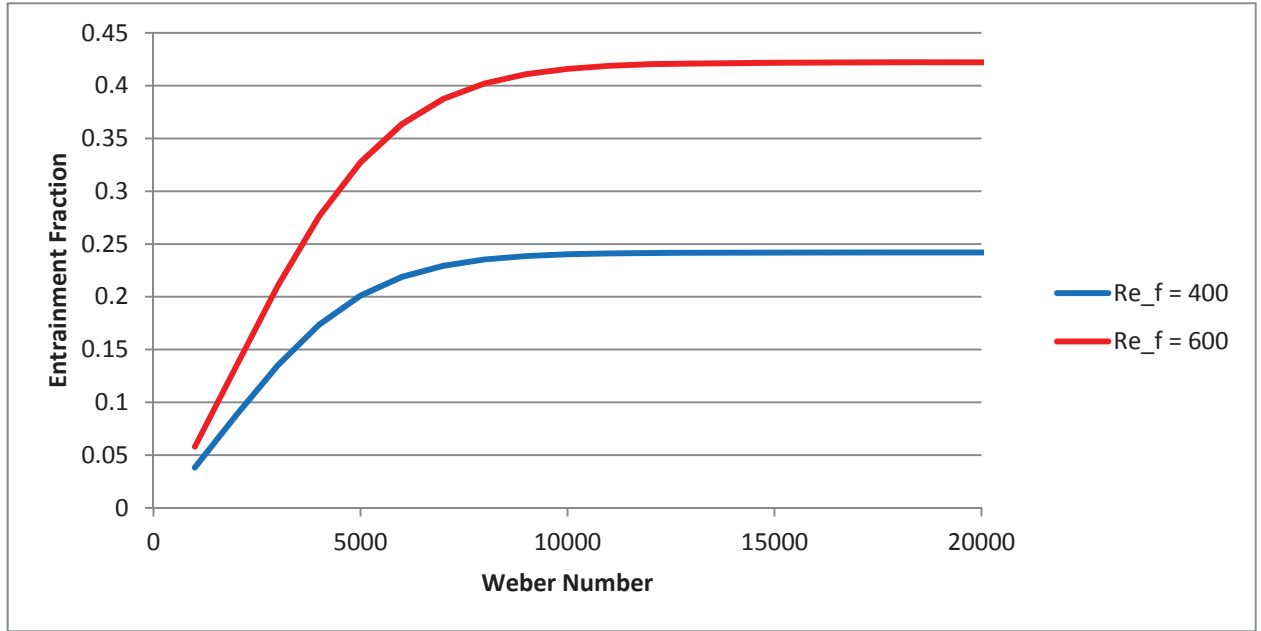


Figure 2-1: Illustration of of equation 2-8.

Figure 2-1 shows that the entrainment fraction in annular pipe flows is mostly dependent on $We_{D,S}$ at low $We_{D,S}$ and then becomes virtually independent of $We_{D,S}$ at increasing values of $We_{D,S}$. Sawant et al [10] suggested that the change in behavior was due to small entrained droplets decreasing the turbulence intensity in the gas phase, which laminarized the flow above the liquid film, thus shielding the film from the gas. Note that this equation is only valid for fully developed, annular pipe flows of pipe diameters less than 25.4 mm. Sawant et al [10] obtained all of his entrainment fraction data at 400 pipe diameters downstream of where the film was injected in his experiments. Thus, equation 2-9 is not valid for the geometry and conditions of the experiments in this thesis. However, equation 2-8 is illustrated in Figure 2-1 to illustrate the expected trends of the dependence of entrainment fraction on some of the two-phase flow variables. For instance, Figure 2-1 suggests that a Weber number based on the momentum flux of the gas phase is expected to dominate entrainment at low Weber numbers, and that a liquid film Reynolds number is expected to dominate entrainment at high Weber numbers.

Sawant et al also developed an expression to predict the onset of entrainment. Sawant et al suggested that entrainment occurs when the liquid film Reynolds number is equal to:

$$Re_{f,OE} = 13(N_{\mu f})^{-.5} \quad (eq\ 2 - 15)$$

where

$$Re_{f,OE} = \frac{\rho_f j_f D_t}{\mu_f} \quad (eq\ 2 - 16)$$

$$j_f = \frac{Q_f}{A_t} \quad (eq\ 2 - 17)$$

It is important to note that the fluid properties and variables used to calculate equations 2 through 2 correspond to the film, and not necessarily the liquid phase as a whole. This is especially important to note when calculating the superficial velocity.

2.2.2 Annular Two-phase Flow Review and Analysis by Cioncolini and Thome

Cioncolini and Thome [12] performed a thorough review of vertical annular two-phase flow experiments. They constructed a database of all the literature that they reviewed and evaluated the correlations proposed by various researchers. They concluded that the entrainment correlations proposed by Sawant et al [10] and Oliemans et al [24] were the most accurate correlations. They further concluded that a Weber number based on the core gas flow was the dominant non-dimensional number for predicting the entrained liquid fraction in such flows and proposed their own correlation which fit the data from all the experiments reviewed better than any other correlation. Finally, they performed a dimensional analysis and suggested alternative non-dimensional numbers that may be used to model the entrainment process.

2.3 Review of Experiments of Shear-Driven Liquid Films in a Rectangular Channel

This subsection provides an overview of some experimental research on shear driven liquid films driven by air flows in a horizontal rectangular duct. The objectives of the studies described in the following paragraphs were primarily to identify variables, such as film thickness and interfacial shear stress, that could be input into CFD models of atomizers. While the gas phase momentum fluxes of the experiments described here

were considerably less than those typically found in liquid rocket engines, the objectives, scope, diagnostic techniques, and experimental setup of the literature summarized here were very similar to the ones of this thesis. Some of the data and trends discovered and proposed by these researchers provide a comparison to the data presented later in Chapter 5.

2.3.1 Shear Driven Liquid Film Studies by Schober and Ebner

Schober et al [25] performed experiments on shear-driven liquid films along one wall of a horizontal duct. The goal of the studies was to develop a model to predict the two-phase flow field in prefilming airblast atomisers. Air was used as the gas and a kerosene-like liquid was used for the film. A movable nozzle was located on the wall opposite the film. The objective was to experimentally determine how the film thickness and interfacial shear stress are affected by the injected liquid flow rate, the initial air velocity, the acceleration of the air flow, and the strong negative pressure gradient imposed by the presence of the nozzle.

The results of the experiments in Schober et al were used to help develop and validate a CFD model for shear-driven liquid films described by Ebner et al [26]. A distinguishing feature of the model presented in by Ebner et al [26], was that it used the experimental results to determine an equivalent sand-grain roughness at the surface of the liquid film. This equivalent sand grain roughness was then used to determine the velocity profiles in the liquid and gas phases. The CFD model described by Ebner et al [26] correlated with the data obtained by Schober et al [25] very well.

Ebner et al [6] researched droplet entrainment from flat, shear-driven oil films at several inclination angles. Ebner et al [6] performed experiments in an unheated 30 mm X 50 mm rectangular duct. The oil films were injected by means of a tangential slot and terminated using a knife-edge capture slot at 10, 20, and 30 duct heights away from the injection point. Ebner et al [6] used an LFD to measure film thickness. The following correlations for film thickness and entrainment fraction were proposed:

$$EF = 1.042 \cdot 10^{-7} We_{D,E}^{1.2} Re_{f,E}^4 \lambda^{0.8} \left(1 + 2.061 \cdot 10^{-4} \frac{Re_{f,E}^2}{We_{D,E} Fr_f} \right)^{2.25} \quad (eq\ 2 - 18)$$

$$\delta = 1.714 We^{-0.36} Re_f^{0.457} \cdot \left(1 - 1.096 \cdot 10^{-14} \frac{Re_f^4}{Fr_f^2} \right)^{0.375} \quad (eq\ 2 - 19)$$

where:

$$We_{D,E} = \frac{\rho_f V_g^2 D_h}{\sigma} \quad (eq\ 2 - 20)$$

$$Re_{f,E} = \frac{j_f H}{\nu_f} \quad (eq\ 2 - 21)$$

$$Fr_f = \frac{j_f}{Hg \sin \varphi} \quad (eq\ 2 - 22)$$

$$\lambda = \frac{l}{H} \quad (eq\ 2 - 23)$$

2.3.2 Shear-Driven Liquid Film Experiments at a Sharp, Expanding Corner by Friedrich and Wegener

Friedrich et al [27] studied the behavior of shear-driven liquid films at a sharp expanding corner. Their objective was to determine conditions necessary to cause a shear-driven liquid film to separate from the surface after being driven over a sharp, expanding corner. Film thicknesses and air velocities were important variables in these experiments. Friedrich et al compared their results with computational models.

Wegner [5] extended the results of Friedrich et al One of the major contributions of Wegener [4], [5] was a qualification of the LFD as a shear-driven liquid film thickness measurement diagnostic, which will be discussed in section 3.1. Wegener repeated the experiments of Friedrich et al for different fluids. The thickness of the liquid film was measured just prior to the separation point. Film thickness and film velocity data were compared with computational models. The momentum flux of the gas phase in Wegener's experiments were all less than 2,000 Pa. The film thicknesses that were measured were on the order of 150 μm .

2.3.3 Inception Criteria for Droplet Entrainment in Two-Phase Concurrent Film Flow

Ishii and Grolmes [11] attempted to experimentally determine the gas velocities and injected liquid flow rates at which entrainment just begins in two-phase concurrent film flow. The experimental test article was a 2.54 cm X .317 cm rectangular tube that was 76.2 cm long through which both nitrogen and helium gas flowed. Water was injected through a slot at the entrance to the test section. The pressure drop across the test section was measured. For each test, the liquid flow rate was set and the gas velocity was increased and the pressure drop vs gas velocity curve was recorded for each liquid flow rate. For each liquid flow rate, the pressure drop vs gas velocity curve was determined. The point at which the slope in the pressure drop vs gas velocity curve changed was thought to correspond with the gas velocity at which entrainment from the liquid film just began to occur. It was observed that the onset of entrainment occurred with the formation of disturbance or roll waves on the surface of the liquid film. The analysis they performed suggested that entrainment occurs when the aerodynamic forces acting a disturbance overcome surface tension forces.

2.4 Conclusions from the Literature and Applicabilty to the Current Study

Studies available in the literature have thus far presented inconclusive observations regarding the entrainment and stability of shear driven liquid films. Many of the authors reviewed had different observations regarding the behavior and mechanics of shear-driven liquid films. The differences in the different researchers' observations can perhaps be explained by examining the experimental conditions of each study. The literature and experiments at AFRL have indicated that the momentum flux of the core gases in a rocket is a dominant variable affecting liquid film stability, entrainment, and overall film cooling effectiveness. Table 1 shows a comparison of the observations and gas momentum fluxes of the experiments described in references 1, 6, 9, 10, 16, and 17. Upon examination of Figure 2-1 and Table 2-1, it is suggested that gas momentum flux and liquid film surface tension are the dominant flow properties governing the establishment of the liquid film when momentum fluxes are low. It appears as though

liquid flow rate and coolant viscosity dominate entrainment and liquid film stability at higher momentum fluxes, suggesting a dependence on a liquid film Reynolds number.

Table 2-1 also shows that the momentum fluxes in all the experiments thus far are about an order of magnitude less than the conditions in liquid rockets. It is eventually planned to study the establishment of the liquid films in the presence of gas flows with momentum fluxes up to and exceeding 1 MPa. The experiment described in this paper was intended to study the entrainment fraction for momentum fluxes from 38 -110 kPa and qualify the LFD's ability to measure film thickness under these conditions. The results of the current study will be used to design a new test article capable of higher momentum fluxes. The eventual goal of the research at AFRL is to determine a correlation or criterion that accurately predicts the optimum liquid flow rate to be injected through a slot for the purposes of film cooling.

Table 2-1: Comparison of the Momentum Flux of Several Experiments.

Researcher	Gas Momentum Flux (kPa)	General Observations
Kinney [9]	40- 200 ¹	Cooling Effectiveness dependent on coolant viscosity and coolant flow rate. Little dependence on gas momentum flux and surface tension
Knuth [16]	40- 200	Cooling Effectiveness dependent on coolant viscosity and coolant flow rate. Little dependence on gas momentum flux and surface tension
Gater [17]	1 - 30 with one case at 54	Entrainment fraction dependent on gas momentum flux and surface tension. Little dependence on coolant viscosity and coolant flow rate
Coy [1]	33- 99	Maximum amount of coolant that remained attached to the wall seemed to be governed by $\delta^+ = 20$
Ebner [6]	.850 – 4.5	Entrainment fraction dependent on both a $We_{D,E}$ and $Re_{f,E}$
Sawant [10]	1-50	Entrainment fraction dependent on both a $We_{D,S}$ and $Re_{f,S}$
Current Experiment	2.5- 110	
Proposed Experiment	10– 1,000	
High Pressure Liquid Rockets (combustion chamber)	>1,000	
High Pressure Liquid Rockets (throat)	approx. 10,000	

¹ Due to a limitation in the data provided in the reference, these momentum fluxes are only rough estimates

CHAPTER 3: OVERVIEW OF DIAGNOSTIC TOOLS

It is difficult to experimentally elucidate the phenomena associated with liquid film cooling due to the extreme nature of the conditions in a rocket combustion chamber. First of all, in a hot-fire test, the high temperatures and pressures can damage or destroy most diagnostics. Secondly, the high density combustion gases and soot formation on windows make visualization of the flows inside of a rocket engine difficult. Even in cold-flow, the parameters of interest for shear-driven liquid films are very difficult measure. First, the films under the gas conditions of interest are very thin, on the order of $100\text{ }\mu\text{m}$ or less, dictating the need for precise, non-intrusive measurements, as even the smallest disturbance on the liquid film can render the results inaccurate. Secondly, the turbulent, unstable surface at the interface and rapid atomization makes surface roughness and interfacial shear stress measurements difficult as well. The culmination of these effects has obscured a complete understanding of shear-driven film flows relevant to liquid film cooling to date.

This chapter reviews potential diagnostic techniques for measuring the film thickness, interfacial shear stress, and the mass flow rate of a shear-driven liquid film in the absence of heat transfer, which, as stated in chapter 1, are the variables of interest in this thesis. For each measurement technique, diagnostics that have already been used in the literature are identified and the ones used in this current experiment are explained. Suggestions for which diagnostics techniques should be used in future experiments are also stated in some cases. For the shear stress and film thickness measurement techniques, other authors have already completed a comprehensive review and analysis of each of these methods, and the reader is referred to those papers for further details.

3.1 Overview and Background of the Laser Focus Displacement Meter for Measurement of Shear Driven Liquid Films

In the experiments described in this thesis, the thickness of the liquid film coolant was chosen to be measured by a Keyence LT-9030 Laser Focus Displacement Meter (LFD). While a variety of other techniques are available for measuring liquid film thicknesses, this instrument was chosen due to its off the shelf nature. In other words, an LFD can be bought, set-up and be ready for use very quickly, while other techniques are more complicated, take longer to set up, and are more difficult to work with. This instrument is intended for product testing and quality control whenever small dimensions or thicknesses are important. Common applications for the LFD are measuring the thickness of a contact lens, detecting surface scratches, or measuring surface profiles. If the reader is interested, a thorough review of film thickness diagnostics for very thin films is provided by Tibirica [2].

The LFD uses a converging laser beam with an oscillating focal point to detect the location of a surface. When the focal point of the beam is located directly on a surface, the amount of light reflected back to the instrument is at a maximum. Thus, the position of a surface can be determined by correlating peaks in the light intensity being reflected back to the LFD with the position of the focal point. Multiple surfaces can be detected with the LFD, provided that they fall within the range of the focal point's oscillations. For example, if a transparent film falls within the range of the focal point, then both surfaces of the film would be detected, as each surface would reflect its own light intensity peak back to the LFD. The oscillation range of the focal point for the LFD used in the experiments in this thesis is 2 mm. The half-cone angle of the laser beam is 11.5 degrees and the spatial resolution of the instrument is .2 μm in air. A schematic of the operating principle of the LFD is shown in figure 3-1.

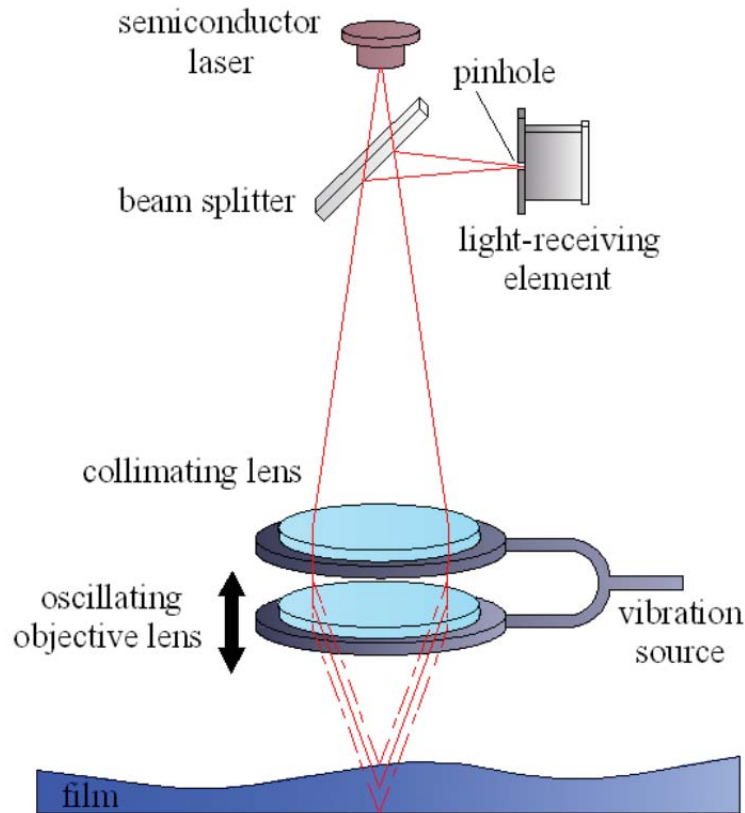


Figure 3-1: Diagram of LFD operation. Figure taken from Wegener [4].

While the LFD was not intended to be used to measure the surface of thin, wavy, shear-driven films, the LFD has been qualified and used to measure the thickness of liquid films in several experiments [3], [4], [6]. Wegener [4] evaluated the surface angle limitations of the LFD and demonstrated that the LFD is unable to detect the surface of a liquid film if the surface angle exceeds 8 degrees. Additionally, the frequency response of the LFD (about 550 Hz) is too slow to obtain time-resolved surface profiles of shear-driven liquid films for most applications [4], [6]. Despite these limitations, it was concluded that the LFD was capable of giving time-averaged film thicknesses for the experimental conditions studied thus far (generally much lower gas velocities than the ones in our experiment).

The LFD can be set up to measure liquid film thickness in one of two configurations, as shown in figure 3-2. Thus far, most techniques measured the liquid film thickness by orientating the LFD such that the laser beam passed behind the

substrate upon which a liquid film ran, as shown in left-hand side of figure 3-2. The other technique is to orient the LFD such that the laser passes through the liquid film before contacting the substrate (see the right image in Figure 3-2). The advantage with the former technique is that it avoids entrained droplets from interfering with the laser beam. However, Hazuku [3] observed that this limits the minimum film thickness that the LFD can detect. The minimum detectable film thickness depends on wall inclination angle and surface roughness [3]. Hazuku [3] was unable to detect film thicknesses less than 20-50 μm for this configuration. It is expected that the liquid films encountered in our experiment may be on the same order as or smaller than this [1]. Therefore, the latter orientation was chosen for measuring film thickness with the LFD. In addition, measuring the film thickness from the latter orientation makes design and selection of the substrate materials easier. Note that this is the first time that an attempt has been made to measure the thickness of a shear-driven liquid film using the latter configuration in a high momentum flux, high entrainment environment.

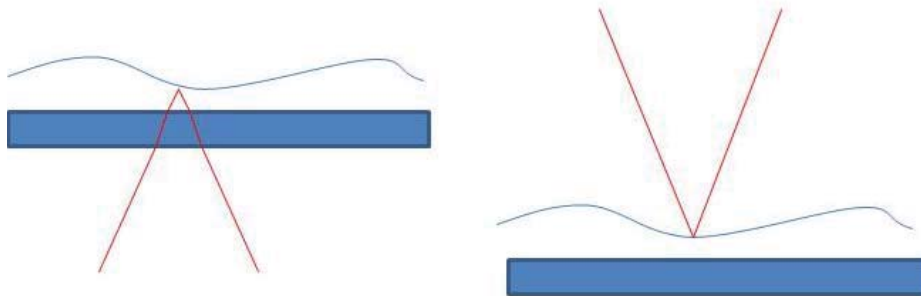


Figure 3-2: Different Configurations for measuring film thickness

Finally, it is important to discuss that while other techniques are temporally more capable than the laser focus displacement meter, this measurement technique was selected due to its simplicity. Techniques such as light attenuation, fluorescence intensity, and interferometry are non-intrusive, as spatially capable as the LFD, and they can produce continuous instantaneous measurements of the film thickness, which can be

useful for fourier analysis of the interface and determination of the film surface roughness [2]. However, these four techniques are complex and require significant effort and time to set up. The conductance technique used with flush mounted electrodes as described in reference [28] also have excellent spatial and temporal resolutions and has a relatively straight-forward calibration procedure. The downside to this technique is that it requires very precise machining and is limited to electrically conductive fluids. Thus, while the LFD is less temporally capable than the other techniques, it was selected due to it's off the shelf nature, as time was a tight constraint for the research in this thesis. While it is incapable of providing frequency content of the film surface, its ability to provide time-average film thickness values was considered adequate for the purposes of the present investigation.

3.2 Shear Stress Measurement Techniques

The interfacial shear stress on a shear-driven liquid film driven by the momentum fluxes in this experiment is perhaps the most difficult variable to measure. Section 3.2.1 describes the method used to determine the shear stress for the experiments in this thesis, which involved determining the interfacial shear stress from pressure drop measurements. Unfortunately, as discussed in section 5.3, accurate pressure drop measurements were not obtained in the experiments. Due to the difficulties encountered in this experiment and the broad assumptions employed in using pressure drop measurements to determine the interfacial shear stress, several more capable interfacial shear stress measurement techniques are discussed in section 3.2.2. Recommendations are also made regarding which measurement techniques should be used in future experiments.

3.2.1 Determining the Shear Stress from Pressure Drop Measurements

In this experiment, we attempted to determine the interfacial shear stress from pressure drop measurements. An average shear stress on a liquid film can theoretically be estimated by applying a momentum balance to the control volume between the

pressure taps. Figure 3-3 shows the forces and velocity profiles on a control volume applied to the gas phase above the film between two locations where the pressures and velocities profiles are assumed to be known. Therefore, the two unknowns in figure 3-3 are the shear stresses on the walls of the channel and the also on the liquid film. Note that the shear stress acts on all 4 walls of a rectangular channel, as opposed to just the two that are depicted in figure 3-3. In this analysis, the liquid film is assumed to be of negligible and constant thickness.

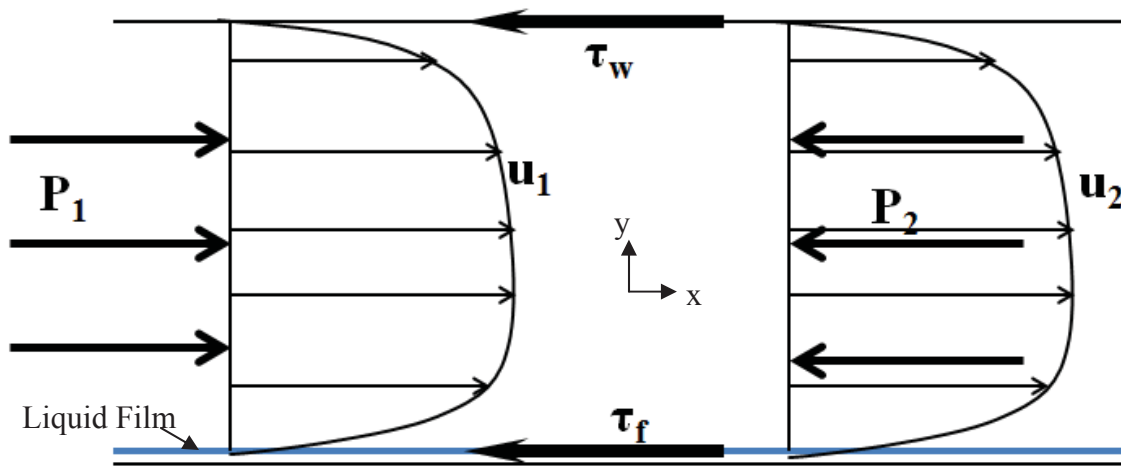


Figure 3-3: Momentum balance on flow over an area of film

To estimate the interfacial shear stress, τ_f , the following assumptions are employed:

- 1) Steady-state, fully developed flow
- 2) The gas phase velocity profile $u_1 = u_2$ regardless of whether the film is present or not
- 3) When the film is off, the shear stresses on all four walls of the rectangular channel are equal
- 4) The shear stresses on the dry walls of the channel do not change when the film is introduced.
- 5) The dry walls of the channel are all smooth

In the presence of no liquid film, then $\tau_f = \tau_w$. Under the these assumptions, the shear stress on each wall of the rectangular test section in the presence of no film can be found via a momentum balance:

$$\tau_w = \frac{(P_2 - P_1) \cdot A_t}{S \cdot L} \quad (eq\ 3 - 2)$$

With knowledge of the shear stress on the walls of the test article, the shear stress on the liquid film can be determined. When the liquid film is turned on, the net shear force on the control volume is the sum of the shear forces from the film surface and from the side walls. Under the assumption that the velocity profiles are equal, the sum of the shear stress forces should balance the pressure forces acting on the control volume:

$$\tau_f \cdot b \cdot L + \tau_w \cdot L \cdot (b + 2H) = (P_2 - P_1) \cdot A_t \quad (eq\ 3 - 3)$$

Thus, under the assumption that the shear stress on the walls of the test section does not change when the film is applied, then the shear stress on the liquid film can be estimated by:

$$\tau_f = \frac{(P_2 - P_1) \cdot A_t - \tau_w \cdot L \cdot (b + 2H)}{b \cdot L} \quad (eq\ 3 - 4)$$

Note that there is inherent error in this equation due to the rather broad assumptions employed, and it therefore only gives an estimate of the shear stress on the liquid film. The pressure drop and change in velocity profiles that could arise due to slight test section curvature are not accounted for. Additionally, the small drops that might be entrained from the liquid film between the pressure taps have an effect on the velocity profile of the gas, which would therefore affect the momentum flux of the gas, and, therefore, the shear stress on the surface. Finally, the shear stresses on the dry walls of the test section are likely to change slightly due to the expected redistribution of the velocity profiles with the introduction of the liquid film. Knowledge of the droplet distribution or entrainment fraction could improve the relationship between shear stress and pressure drop.

As will be discussed in section 5.3, a variety of problems were encountered in the experiments, and the author never managed to obtain accurate pressure drop data in the

time allotted for the experiments in this thesis. Due to the difficulties encountered in using the experiments, the level of precision required from the pressure drop measurements, and the broad assumptions associated with this method, it is not recommended to attempt to determine the interfacial shear stress from pressure drop measurements. The methods discussed in section 3.2.2 can potentially provide more accurate shear stress measurements. However, as knowledge of shear-driven liquid films improves, determining the interfacial shear stress from pressure drop measurements could be a reliable method in the future.

3.2.2 Other Shear Stress Measurement Techniques

Chapter Nine by Hanratty and Campbell of *Fluid Mechanics Measurements* by Goldstein [29] provides a comprehensive overview of methods that can be used to determine the wall shear stress in a flow. Seven methods that can be used to measure the wall shear stress are direct measurements using a movable plate and a force balance, extrapolation from measurements of the velocity field, the Stanton tube, Preston tube, the sublayer fence, heat transfer method, and the mass transfer method. The Stanton tube, direct measurement, Preston tubes, and sublayer fence methods were all found to be far too invasive to use for measuring the wall shear stress accurately in films of thicknesses expected in this experiment. Therefore, only the advantages and disadvantages associated with the velocity extrapolation, heat transfer, and electrochemical methods will be discussed in this section. The review of the heat and mass transfer methods by Hanratty and Campbell [29] is quite extensive, and the discussion here is very brief in comparison. The reader is referred to reference 29 for further details.

Heat and mass transfer methods both work on the principle that the temperature and species profiles, and therefore heat or mass transfer rates, above a surface subjected to a convecting fluid are related to the velocity profile at the surface. For the heat transfer method, a flush mounted probe or film is held at a constant temperature, and the electric current required to maintain the probe's temperature is measured. Knowledge of the electric current and voltage indicates how much power is being transferred from the

probe, which can then be used to determine the heat flux from the probe. Mass transfer methods employ an electrodiffusion technique. With this technique, a voltage is applied to an electrode that is used to drive a chemical reaction, which causes species to diffuse from the electrode into the flow. Just downstream is another electrode, at which the counterreaction occurs. The diffusion of the species and reactions at each electrode results in a current that flows within the fluid between the electrodes. This current is measured and used to determine the mass flux of the probe. Provided that either the heat or mass transfer probes are small enough, the temperature or mass boundary layers will fall entirely within the laminar sublayer of the flowing fluid, ie, the region of the flow where the velocity is directly proportional to the distance from the wall. If this condition is satisfied, then the heat or mass transfer from the hot-film or electrolyte probe can be used to determine the velocity gradient just above the probe. This relationship can be determined through a calibration procedure. Once the velocity gradient at the wall is known, then the shear stress can be estimated according to:

$$\tau = \mu \frac{du}{dy} \quad (eq\ 3 - 1)$$

The advantage that the hot-film probe has over the electrochemical method is that hot film probes can be used to measure the wall shear stress in gaseous flows, where the electrochemical diffusion method is generally limited to liquid flows. The disadvantages associated with the heat transfer technique are that the heat flux to the substrate surrounding the probe can be significantly greater than the heat flux to fluid and can be a source of error if it is not properly accounted for [29]. Because the heat transfer coefficient for gases is generally orders of magnitude less than that of a liquid, this problem is less important for liquid flows than gaseous flows.

The mass transfer technique by electrochemical diffusion has advantages over the heat transfer method as it is potentially more accurate, as there is no worry about the electrolyte diffusing into the substrate. In addition, it is possible to calibrate the mass transfer probe analytically or numerically, whereas it is recommended that the heat transfer probe be calibrated experimentally. Some limitations to the mass transfer

probes are that they are limited to liquid flows, and, secondly, the materials, fluids, and facility instruments must be compatible with the electrolytes used.

Another way to measure determine the interfacial shear stress is through extrapolation of the velocity profile in the gas phase above the liquid film. If the velocity profile in the gas phase is known, the interfacial shear stress can be deduced by using applicable turbulence models. Laser Doppler Velocimetry or Particle Image Velocimetry [30] are two non-intrusive techniques that can be used to determine the velocity profile in a flow. For shear-driven liquid film experiments, a Phase Doppler Particle Analyzer (PDPA) can be used to determine the velocity of the droplets entrained into the gas phase. Provided that the droplets are moving at a velocity that is characteristic of the gas phase, the velocity profile in the gas phase can be estimated.

Due to time and resource constraints, none of the methods described in this section were used in this experiment. A hot-film approach and measuring the velocity profile in the gas phase above the film with a PDPA to extrapolate the shear stress were considered; however, the simpler approach involving the pressure drop measurements was used instead. Future experiments should consider employing one of the methods described in this section to measure the interfacial shear stress.

3.3 Film Mass Flow Rate Measurements

One of the primary objectives of this thesis was to determine the mass flow rate of the liquid film that attaches itself to the wall immediately downstream of the slot. Unfortunately, this is another difficult variable to measure. Many of the techniques that previous researchers [10], [5], [31], have used to measure film mass flow rates are intrusive. The non-intrusive techniques can be time consuming and suffer limitations of their own. For the experiments in this thesis, a slot was used to remove the film via suction.

The most commonly used film mass flow rate measurement techniques involve the removal of the film via suction through a slot or a porous wall. A porous wall has been used for the determination of the void fraction in a variety of two phase flow

experiments [10], [5], [31]. As previously explained, Ebner et al [6] and Gater and L'Ecuyer [17] used a slot for the removal to remove the shear driven films in their experiments. For each technique, the backpressure behind the slot or the porous wall is continually lowered, which increases the amount of liquid removed from the film. Eventually, a plateau is reached at which the flow rate of the removed liquid becomes mostly independent of further decreases in back pressure. At this point, it is generally assumed that the entire film has been removed, with a negligible effect on the droplets [10], [17], [31]. Typically, the effectiveness of the porous walls and removal slots is accompanied by some sort of visual confirmation.

An isokinetic probe has been used by previous researchers to determine the entrained liquid fraction and the film flow rate in two-phase flow experiments [31]. With this technique, a small tube is used to suck the liquid entrained as droplets out of the gas phase at specific points. The probe is then traversed across a cross-section of the flow to determine the entrained liquid flux at a sufficient number of points. The entrained liquid flux measured at each point is then integrated across the flow cross-section of interest to determine the total entrained liquid flow rate. The film flow rate can then be determined by subtracting the entrained flow rate from the injected liquid flow rate.

Lastly, a PDPA can be potentially be used to determine the amount of liquid in a film. With this technique, the droplet size probability density function can be determined at the point in a flow [30]. With knowledge of the droplet size probability density function at adequate number of positions across a certain flow cross-section, the mass flow rate of the liquid phase that has been entrained into the gas phase as droplets can be determined by integrating the droplet size probability density functions at each point across the flow's cross-sectional area. The liquid film flow rate can then be determined by subtracting the entrained liquid flow rate from the injected liquid flow rate. While this technique is non-intrusive, it can be rendered inaccurate if the size of the entrained droplets are beyond the range of detection, if the droplets are not spherical, or if the droplet concentration passing through the control volume is too large [30]. Another disadvantage with using this technique is that it is time consuming and more complex than the film removal techniques.

In this thesis, the slot removal technique was used to measure the mass flow of the liquid film that remained attached to the wall due to its simplicity over the other techniques. Eventually, the film flow rate measurement was abandoned due to reasons described in section 5.2. Originally, it was desired to use the PDPA technique, but opted not to due to its complexity and the time constraints facing this thesis. It is recommended that a PDPA system be used in future experiments to determine both the interfacial shear stress and liquid film flow rate.

3.4 Film Visualization Tools

Previous researchers [9], [14] obtained useful insights into the behavior and mechanics of shear-driven liquid films from qualitative photographic and video images. In this experiment, a Vision Research Phantom v7.3 high-speed video camera was used to visualize the behavior of the liquid film in order to obtain qualitative data. Useful quantitative data, such as surface disturbance sizes and velocities could also have been obtained from high-speed video images. However, due to time constraints, only qualitative data for only a handful of test-runs was obtained.

3.5 Chapter 3 Summary

Investigating potential diagnostics that can be used to elucidate the phenomena of shear driven liquid films is an important part of this thesis. Originally, the 3 main variables to be measured in this thesis were the liquid film thickness, the interfacial shear stress, and the film mass flow rate. An LFD, differential pressure measurements, and a film removal slot were the main diagnostics employed in this thesis to measure these variables. However, the differential pressure measurements and the film removal slot both failed to yield conclusive results thus far. A high speed video camera was also employed to qualitatively study the surface of shear-driven liquid films.

There are numerous techniques that can be used to measure the film thickness of a thin, shear driven liquid film. For this thesis, a Keyence LT-9030 Laser Focus

Displacement Meter was chosen to measure the liquid film thickness. Previous authors have demonstrated that this instrument is a viable way to measure the thickness of a liquid film at gas phase momentum fluxes much lower than typically encountered in liquid rocket engines. One of the objectives of this thesis was to investigate the LFD's ability to measure the thickness of thin liquid films under flow conditions for which it has not yet been used to measure film thickness. Orienting the LFD differently may improve its ability to measure film thickness in future experiments as the measurements would not be affected by droplets interfering with the path of the laser.

Knowledge of the interfacial shear stress is critical for understanding the mechanics of shear-driven liquid films. Unfortunately, this is also one of the most difficult variables to measure. Reference [29] provides a thorough description of several diagnostics that could be used to measure the interfacial shear stress. Of these, the heat and mass transfer methods or extrapolating the shear stress from knowledge of the velocity profile are best suited to measure the interfacial shear stress in the types of shear-driven liquid films encountered in the experiments in this thesis. Due to time and resource constraints, these methods were ultimately not chosen to be used to measure the interfacial shear stress in this thesis. Instead, it was hoped that information related to the shear stress could be deduced by measuring the pressure drop in the stream-wise direction of the film. However, problems were encountered and accurate pressure drop data was never achieved in the allotted time. In addition, this is not the recommended way to measure the interfacial stress. Therefore, the interfacial shear stress was not deduced in this thesis. It would be more effective to determine the shear stress from heat or mass transfer or velocity extrapolation methods.

The mass flow rate within the liquid film in previous shear-driven film experiments has been measured by film removal techniques or by measuring the mass flow rate entrained via an isokinetic probe or a PDPA. In this thesis, the mass flow rate within the liquid film was measured using a film removal slot. As will be shown in section 5.2, the film mass flow rate results that were obtained by using this method were inconclusive, as the author was unable to make this method completely remove the liquid film.

Lastly, a high speed video camera was used to observe the surface of the liquid film. From this, qualitative information was obtained regarding the film's surface structure. High speed video could be used to gather quantitative information in future experiments, such as wave speeds or disturbance sizes.

CHAPTER 4: DESCRIPTION OF EXPERIMENT AND TEST ARTICLE

This chapter describes the test article and how the experiments were conducted at AFRL in order to determine the film thickness, interfacial shear stress and film flow rate for a liquid water film injected by a slot injector into a nitrogen gas cross-flow. Section 4.1 describes the test article, the experimental setup, the variables measured, and provides an overview of how the tests were conducted. Section 4.2 describes the experimental procedures.

4.1 Test Article Description

To study the mechanics of shear driven liquid films, a test article was constructed which consisted of a rectangular channel through which nitrogen gas flowed and a film was introduced onto one wall through a thin slot. The test article was made primarily of acrylic to provide maximum visual access to the test section. A plumbing and instrumentation diagram of the test article is shown in Figure 4-1. Table 4-1 relates figure 4-1 to the variables measured in the experiments and the uncertainties of the measurements. Note that the “Uncertainty in Measurement” column in Table 4-1 does not describe the instrument uncertainty, but the uncertainty in the averages for each variable measured for the test run. For example, the thermocouples used could measure the temperature more precisely than ± 1 K, but an average temperature over a time period of interest during a test might have been accurate to within ± 1 K. These uncertainties were used to estimate the uncertainties in the gas phase momentum flux. The error analysis for the uncertainty in the gas phase momentum flux is in Appendix D. Figure 4-2 shows 2 different views of the test article its overall dimensions.

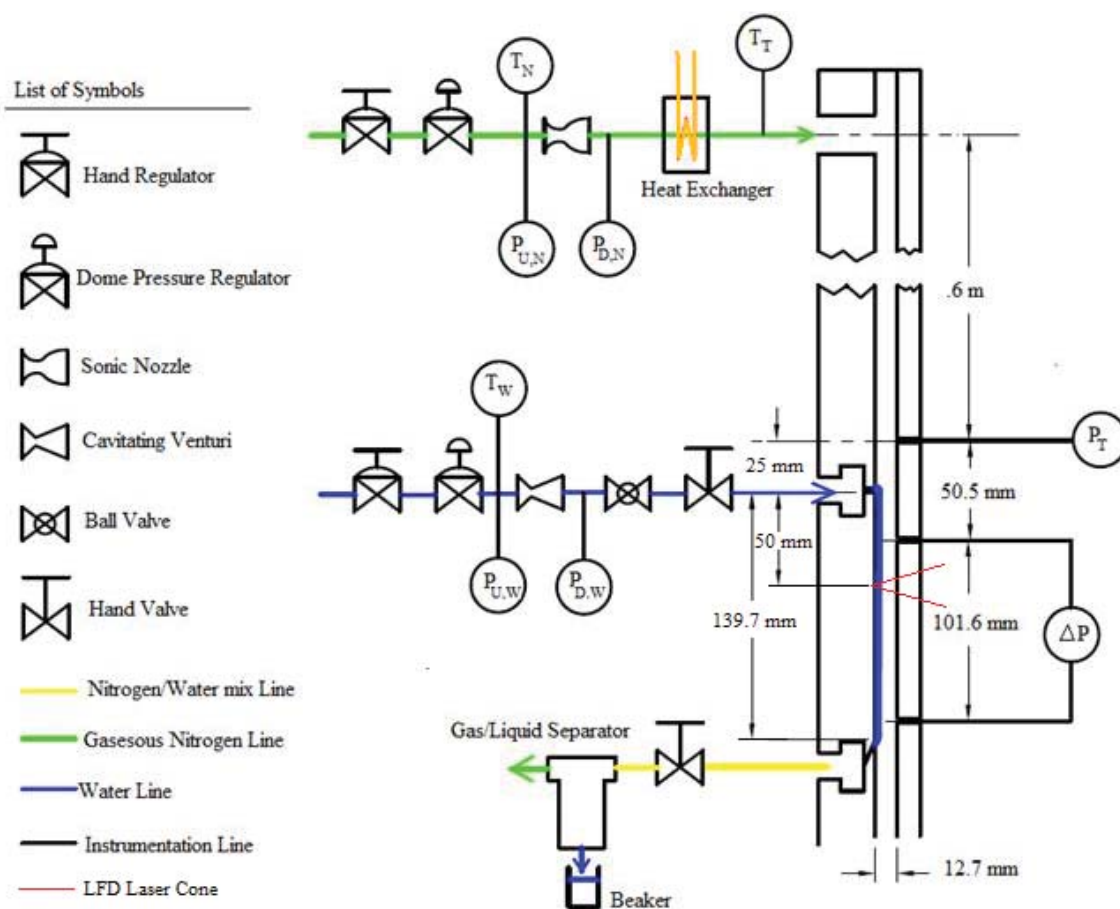


Figure 4-1: Plumbing and Instrumentation Diagram of Experiment

Figure 4-1 Label	Variable Measured	Tranducer/Instrument/Technique Used	Uncertainty in Measurement
$P_{U,N}$	Pressure Upstream of Cavitating Venturi	Diaphragm Pressure Transducer	1 psi
$P_{D,N}$	Pressure Upstream of Cavitating Venturi	Diaphragm Pressure Transducer	1 psi
T_N	Temperature Upstream of Cavitating Venturi	Type-K thermocouple	1 K
$P_{U,W}$	Pressure Upstream of Sonic Nozzle	Diaphragm Pressure Transducer	1 psi
$P_{D,W}$	Pressure Upstream of Sonic Nozzle	Diaphragm Pressure Transducer	1 psi
T_W	Temperature Upstream of Sonic Nozzle	Type-K thermocouple	1 K
T_T	Temperature of Nitrogen Entering Test Article	Type-K thermocouple	1 K
P_T	Static Pressure in Test Article	Piezoelectric Pressure Transducer	.1 psi
ΔP	Pressure Drop Across Distance in Figure 4-1	Diaphragm Pressure Transducer	.001 psi
LFD Laser Cone	Liquid Film Thickness	Keyence LT-9030 LFD	.2 μm
N/A	Liquid Film Flow Rate	Film Removal Slot, Beaker and Stop Watch	N/A

Table 4-1: Variables Directly Measured by Test Article

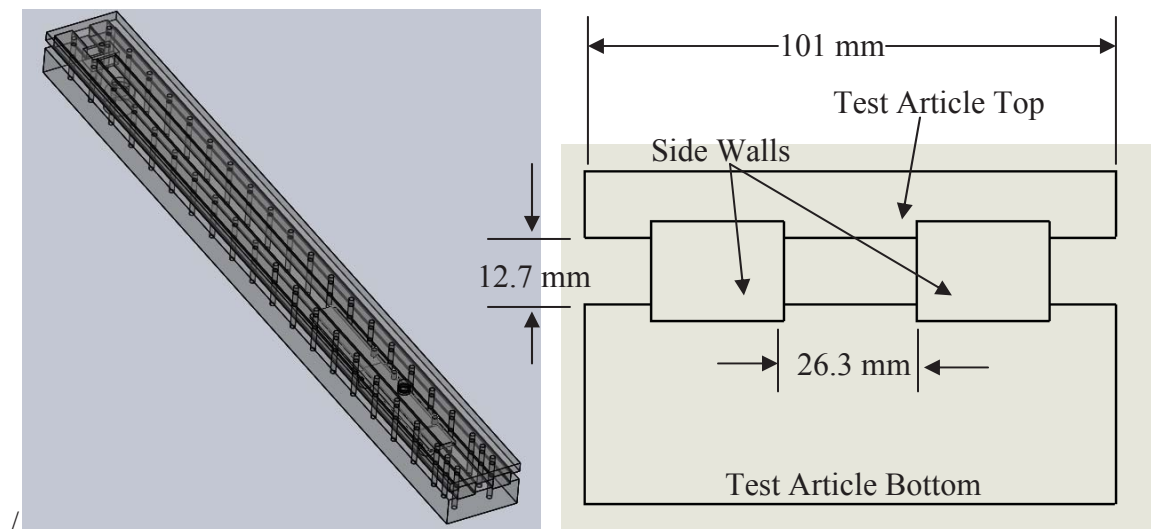


Figure 4-2: Assembled View of the Test Article (Left) and Cross-Sectional View of the Flow Area (Right)

During the experiments, gaseous nitrogen was supplied to the test article using AFRL's 13.8 MPa nitrogen supply. A hand regulator and dome pressure regulator were used to control the nitrogen pressure upstream of the sonic nozzle, which metered the nitrogen mass flow rate. The thermocouple just upstream of the sonic nozzle and the pressure transducers located just upstream and downstream of the sonic nozzle could be used to calculate the nitrogen flow rate based on a facility calibration code. Prior to entering the test article, incoming nitrogen was passed through a heat exchanger in order to recover some of the temperature lost due to the expansion from the sonic nozzle. The temperature of the nitrogen entering the test article was monitored with a thermocouple. The nitrogen then flowed through the test article and was vented to the atmosphere at the end.

Not shown in figure 4-1 are the cylindrical plugs that were used to create back-pressure in the test section and control the Mach number of the gas phase. An example of one of these plugs is shown in figure 4-3. The test section pressure and the Mach number set by the cylindrical plugs were used to control the momentum flux of the gas phase, as illustrated by equation 4-5. The standard definition of momentum flux is shown by equation 4-1. Equations 4-2, 4-3, and 4-4 are versions of the ideal gas law, ideal gas speed of sound, and definition of Mach number, respectively.

$$MF_g = \rho_g V_g^2 \quad (eq\ 4 - 1)$$

$$\rho_g = \frac{P_g}{R \cdot T_g} \quad (eq\ 4 - 2)$$

$$V_{s,g} = \sqrt{\gamma R T_g} \quad (eq\ 4 - 3)$$

$$V_g = M_g V_{s,g} \quad (eq\ 4 - 4)$$

Substituting and rearranging, the definition of momentum flux can also be expressed by equation 4-5.

$$MF_g = \gamma P_g M_g^2 \quad (eq\ 4 - 5)$$

Therefore, in order to control the momentum flux in the test article, it is only necessary to set the test section pressure and the gas phase Mach number. Assuming ideal gas behavior, the Mach number in the test section is governed solely by the ratio of the test

section area to the exit area created by the insertion of the cylindrical plug. Note that 6 plugs were used for the experiments which allowed for Mach numbers of 0.072, 0.095, 0.144, 0.195, 0.262, and 0.320, corresponding to velocities of approximately 25 m/s, 34 m/s, 51 m/s, 70 m/s, 90 m/s, and 113 m/s, respectively. The pressures achieved during the tests ranged from approximately 275 kPa to 800 kPa.

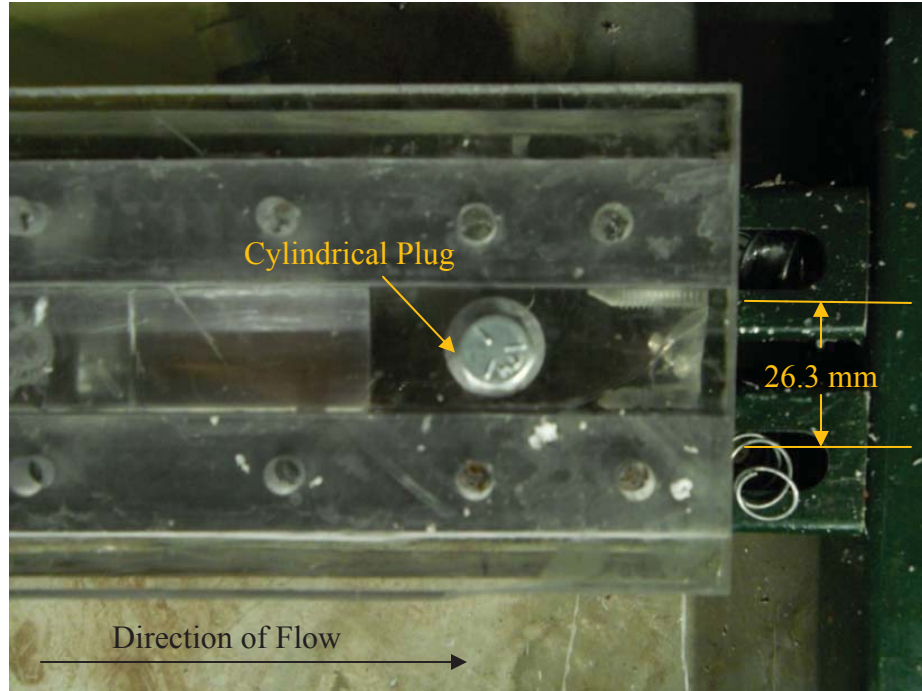


Figure 4-3: Image of Cylindrical Plug at Test Section Exit

The water to the film injection slot was supplied using the facility's water supply. A hand regulator and a dome pressure regulator were used to control the water pressure upstream of the cavitating venturi. The thermocouple upstream of and pressure transducers downstream and upstream of the cavitating venturi were used to calculate the flow rate of water using a facility calibration equation. The liquid flow rate through the injection slot could be controlled or turned on or off with the ball valve and hand valve leading into the test article.

While the tests were running, the pressure transducer labeled as P_T in figure 4-1 was used to measure the static pressure in the test article. The differential pressure transducer labeled as ΔP in figure 4-1 was used to measure the pressure drop across a 101.6 mm length, starting 25.4 mm downstream of the injection slot. Part of the both the

gas and film flow entered the film removal slot, where it was passed to a gas/liquid separator. The liquid removed via the slot was drained into a beaker and the nitrogen that passed through the removal slot was vented to the atmosphere.

An image of the injection slot and the film removal slot assembly is shown in Figure 4-4. The assembly was made of three different pieces: the upstream piece, the middle piece, and the downstream piece. A flat groove .38 mm deep was cut into downstream end of the upstream piece, such that the mate between the upstream piece and the middle piece formed the film injection slot. The upstream piece is shown in Figure 4-5. An angle of 25 degrees was cut onto the downstream end of the middle piece and the upstream end of the downstream piece such that the film removal slot was formed by a flat, angled groove cut into the middle piece when the two pieces were mated together. The middle piece is shown in Figure 4-6, and the downstream piece is shown in Figures 4-7 and Figure 4-8. All 3 pieces were 6.4 mm thick and dimensioned drawings can be found in the appendix.



Figure 4-4: Fully Assembled Injector Piece

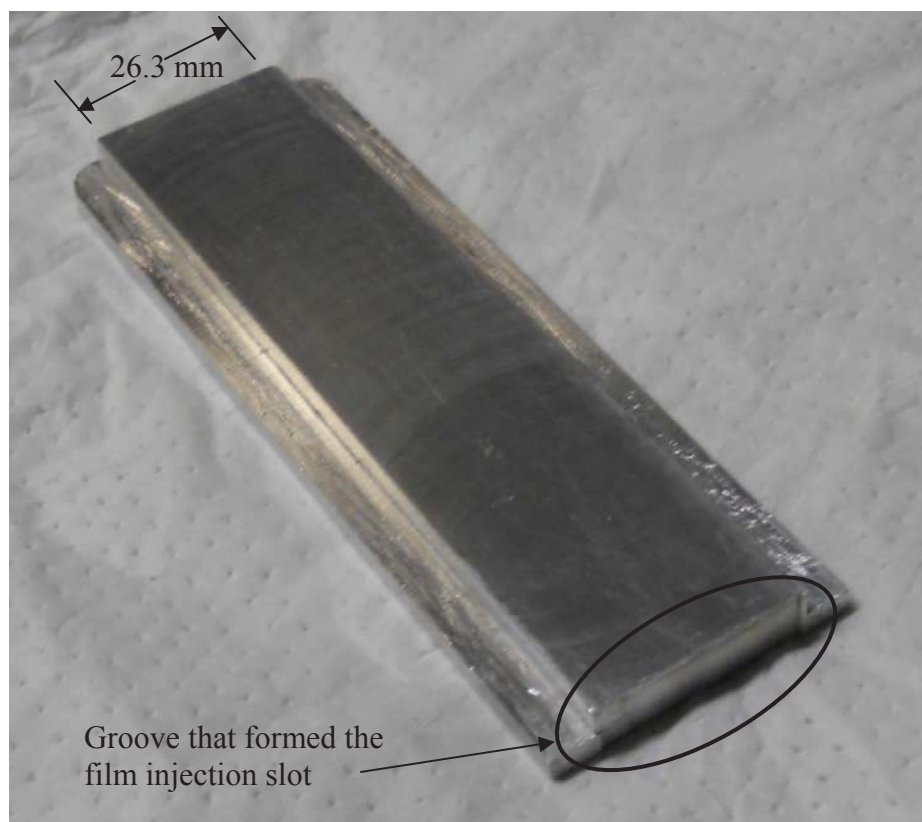


Figure 4-5: Upstream Piece of Injector Panel



Figure 4-6: Middle Piece of Injector Panel

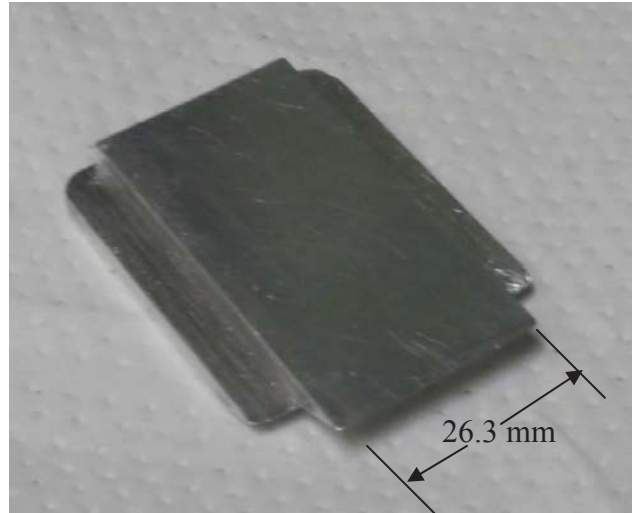


Figure 4-7: Downstream Piece of Injector Panel

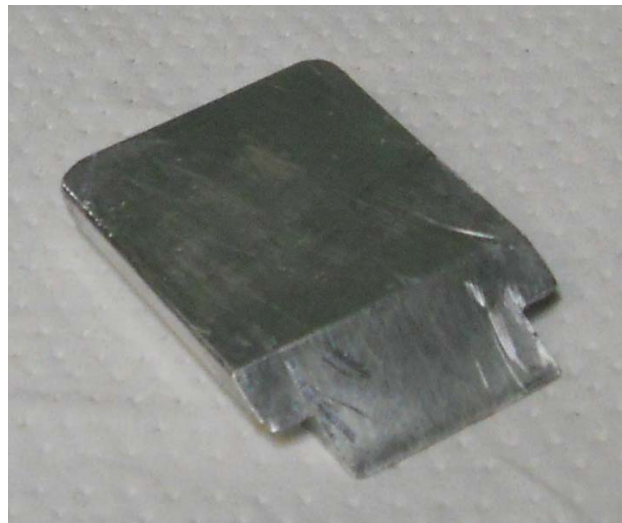


Figure 4-8: Underside View of Downstream Injector Piece

The film injector panel was installed into the test article bottom in the manner shown in Figure 4-9. The film injection slot sat centered over the film injection reservoir, a 25.4 mm by 25.4 mm by 12.7 mm deep cavity. Before the incoming water passed through the film injection slot, it first entered this cavity, where the flow was distributed by a metal disk, cloth, and a foam sponge. A cavity was also located beneath the film removal slot, denoted as the film removal reservoir in Figure 4-8. The film removal reservoir was left completely open. Figure 4-10 shows a picture of the film injector panel installed into the test article bottom with the side walls also installed.

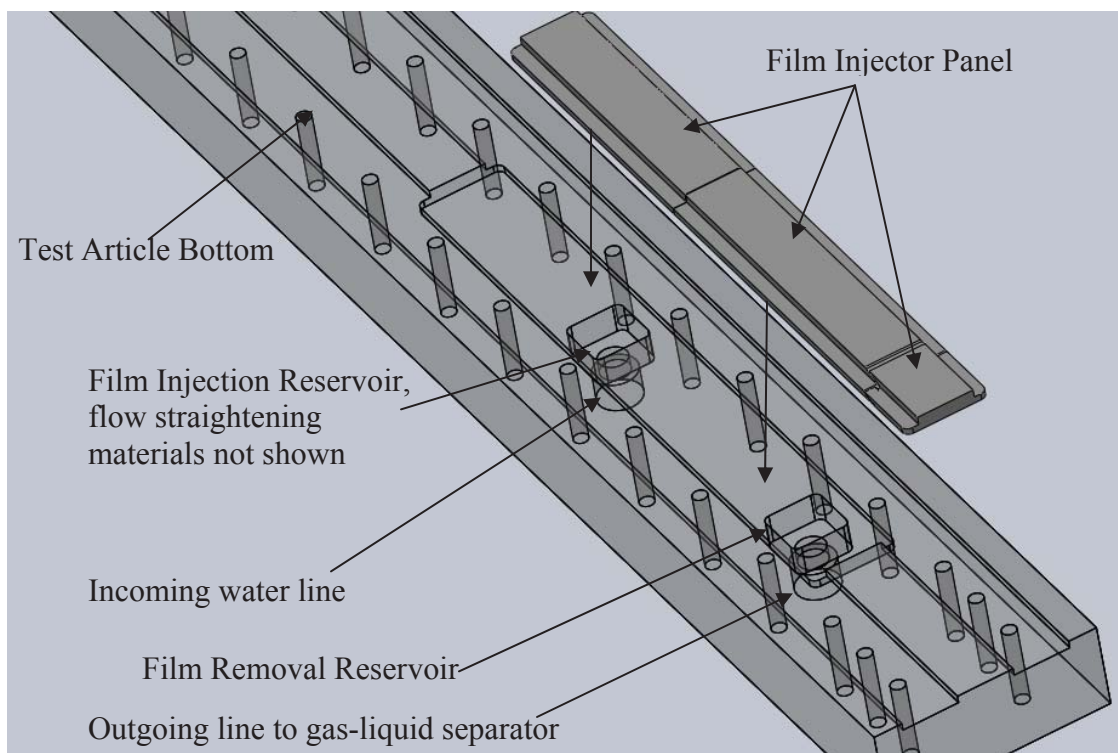


Figure 4-9: Injector Panel Assembly

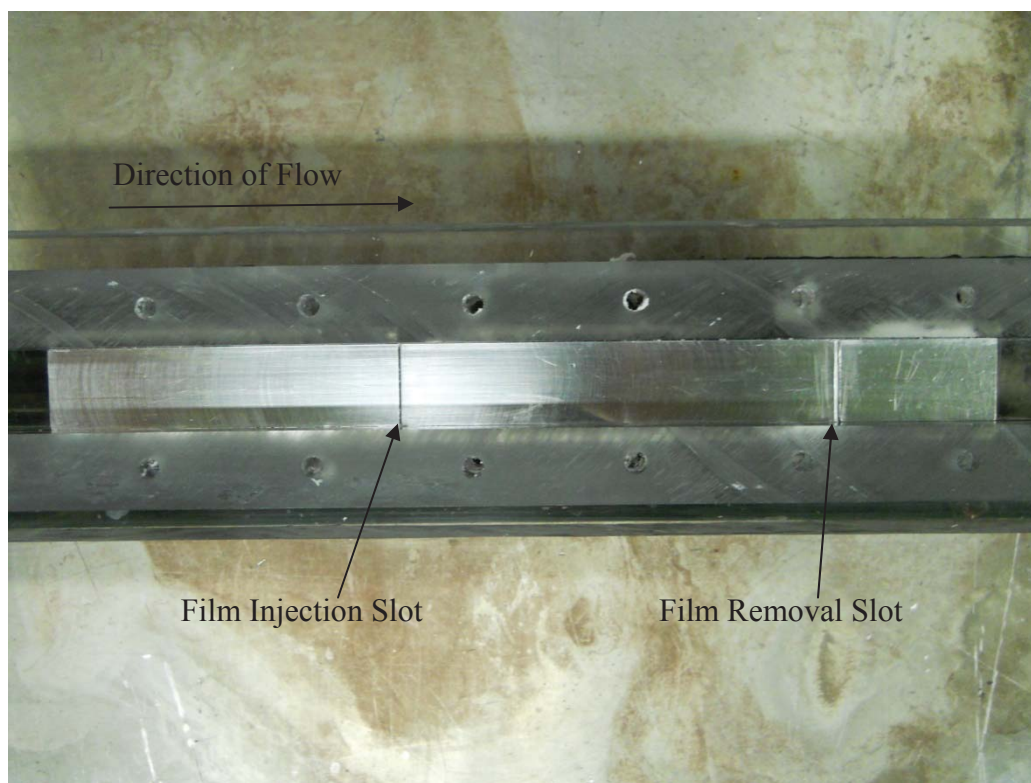


Figure 4-10: Injector Panel Installed in Test Article

In order to measure the film thickness, the LFD was mounted to the test article as shown in Figure 4-11. The operation of the LFD has already been described in section 3.1. A sapphire window was installed into the test article beneath the laser of the LFD. While both the sapphire window and the acrylic wall of the test article were transparent, the acrylic was found to attenuate an unacceptable amount of the light being returned to the LFD, which lead to inaccurate results. Having the laser pass through the sapphire window was found to yield much better results. Care was taken during the fabrication of the test article and installation of the window to make sure that flow was minimally affected by the window's presence. The test section side of the window was flush mounted with the test article wall to within .03 mm. A close-up of the test article top is shown in Figure 4-12, which shows the pressure taps and the port for the sapphire window.

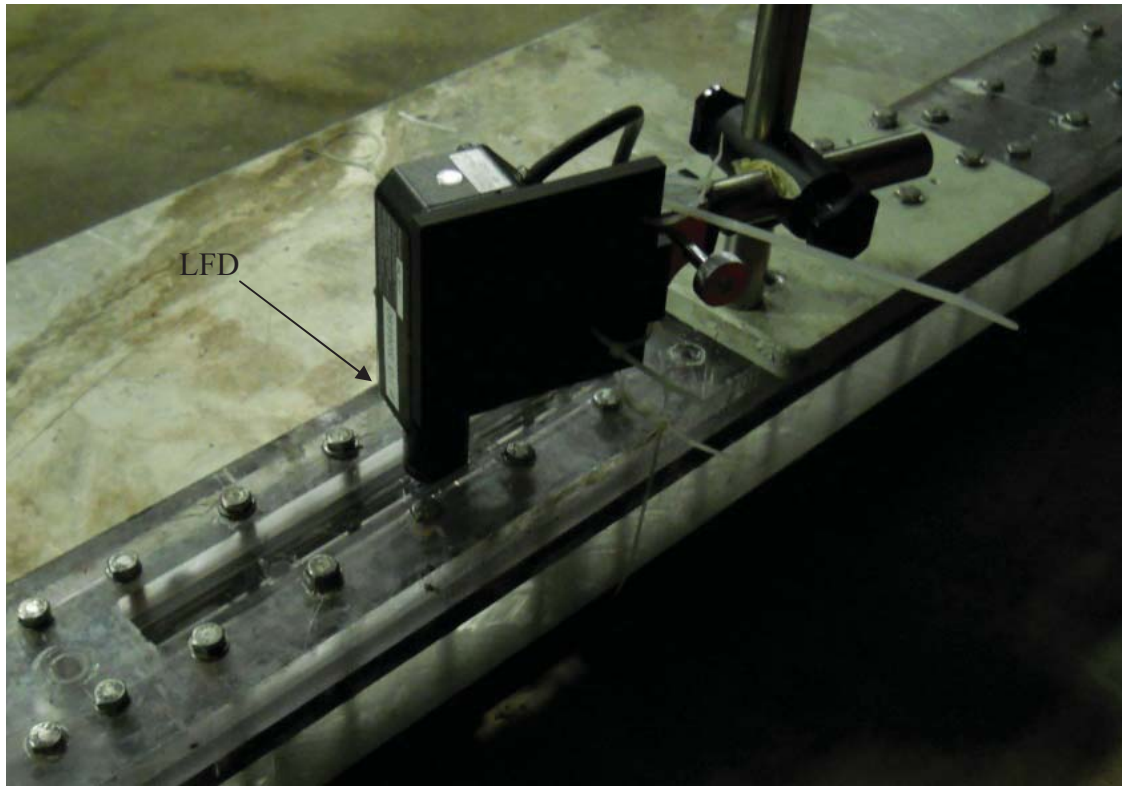


Figure 4-11: Close up of LFD

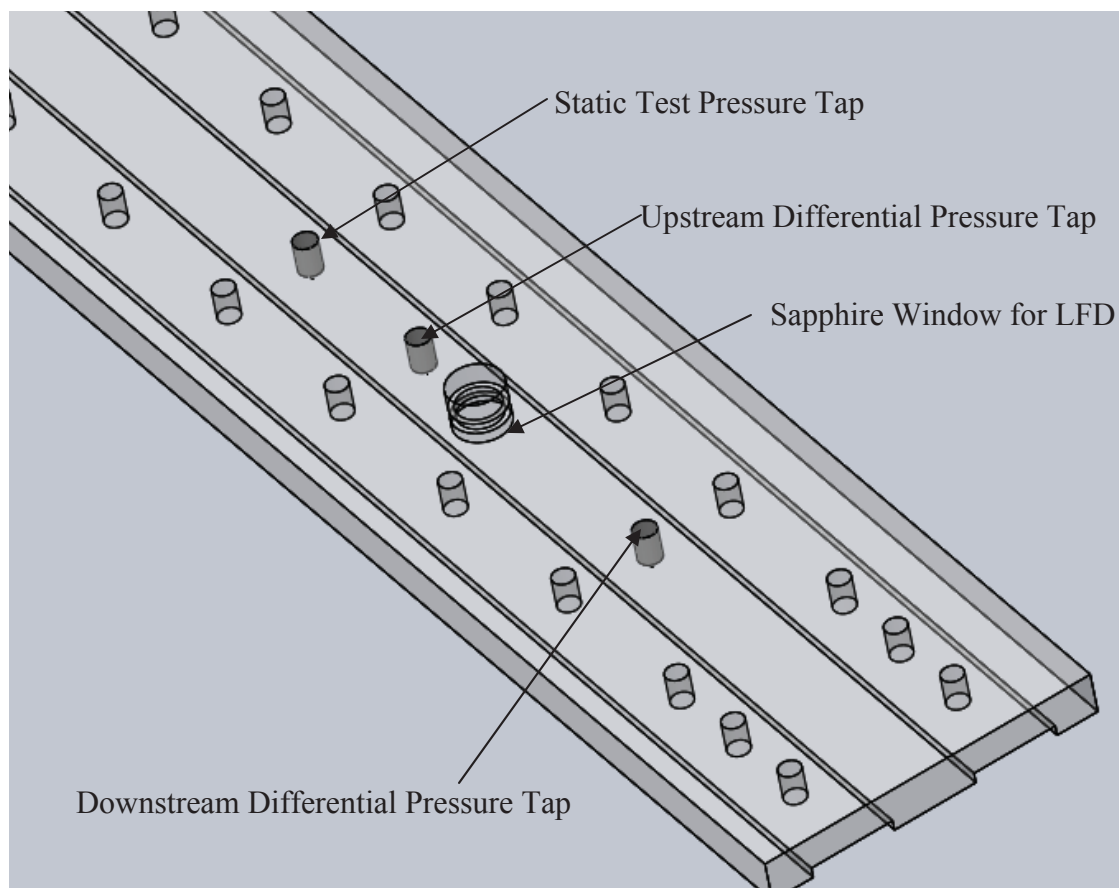


Figure 4-12: Close-up of Test Article Top

4.2 Experimental Procedures

A series of 37 experiments were initially conducted during June 2011. After analyzing the data from the June experiments, the test article and test procedures were improved and a second series of experiments were conducted during November 2011. The experimental procedures for both tests are described here.

During the June 2011 tests, measurements of the interfacial shear stress, liquid film thickness, and the film mass flow rate that remained attached to the wall as a function of momentum flux and injected liquid flow rate were attempted. The four injected liquid flow rates that were investigated were .0034 kg/s, .0046 kg/s, and .0064 kg/s, .0070 kg/s. For the majority of the tests, momentum fluxes ranging from 38,000 Pa to 110,000 Pa were studied. A few additional experiments were run in which only the

film thickness was measured. The momentum fluxes for these experiments were 2,500 Pa, 8,000 Pa, and 15,000 Pa, respectively. High speed video was used to evaluate the performance of the film removal slot. Unfortunately, the pressure transducer being used in these experiments failed to measure correct pressure drops and the film removal slot was observed to under-predict the film mass flow rate. Finally, the LFD was found to be unable to adequately detect the surface of the liquid film at the momentum fluxes studied in these experiments. To remedy this problem, a new method for using the LFD to measure film thickness was proposed. Even with the new method, complications associated with expansion and contraction of the test article due to temperature and pressure changes prevented accurate film thickness measurements during the first round of testing.

Due to the problems encountered in the June 2011 tests, a second round of testing was conducted in November 2011. In these tests, a greater range of momentum fluxes and liquid flow rates was also studied. This time, the momentum fluxes ranged from 5,800 Pa to 110,000 Pa, and the four injected liquid flow rates studied were .0034 kg/s, .0070 kg/s, .012 kg/s, and .018 kg/s. The slot used to measure the flow rate within the liquid film was abandoned, as it did not appear to be yielding conclusive results. Attempts were also made to accurately measure the pressure drop across the film, however, new problems arose which rendered those results inaccurate as well. Changes in the experimental procedure allowed for more accurate measurements of the film thickness to be made using the new method proposed in section 5.1.4. Finally, a high speed video camera was used to qualitatively study the surface of the liquid film.

4.1.1 Experimental Procedure for the June 2011 Tests

The experimental procedure for the first round of tests is as follows:

- 1) Verify that a plug of the correct diameter was installed in the test section in order to achieve the desired Mach number in the test article.
- 2) Verify that the cavitating venturi that was in place could achieve the desired liquid flow rates for the test.

- 3) The upstream pressure to achieve the desired liquid flow rate was then set using a regulator valve. The pressure was monitored with a diaphragm, strain-gauge type pressure transducer.
- 4) The flow of nitrogen into the test article was controlled using a regulator valve and sonic nozzle. The flow through the sonic nozzle could be determined using pressure transducers located upstream and downstream of the sonic nozzle. The flow rate of nitrogen was increased until the desired pressure within the test article was achieved.
- 5) Once the nitrogen was flowing through the test article, data acquisition using the LFD was initiated. Turning the LFD on before liquid was flowed into the test article allowed the surface of the dry substrate to be detected.
- 6) The static pressure, differential pressure, and gas temperature were recorded using a pencil and a spreadsheet.
- 7) The ball valve leading into the test article was then opened to allow the liquid film to begin flowing.
- 8) The switch valve connecting the film removal slot to the gas liquid separator was opened to begin the removal of the liquid film. A stop watch was simultaneously started. The liquid removed through the gas liquid separator was drained into a plastic beaker.
- 9) After about 1 minute, the pressures upstream and downstream of the sonic nozzle and cavitating venturi and the inlet temperature of the nitrogen gas were recorded onto a spreadsheet using a pencil. The static pressure and differential pressure within the test article with the film on was also recorded.
- 10) After about 3 minutes, the switch valve was closed, stopping the extraction of the liquid film. The stop watched was stopped simultaneously with the closing of the valve.
- 11) The ball valve controlling the liquid film flow rate into the test article was closed.
- 12) After sufficient time had passed (about 10 seconds) to allow the LFD to record the location of the aluminum substrate after the film was turned off, data acquisition from the LFD was stopped.

13) The regulator valve controlling the nitrogen flow rate was then closed and the test ended.

14) After each test run, the weight of the beaker with the collected water was measured using a scale and the mass was recorded.

For every third test, a high speed video camera was used to monitor the performance of the slot. The video images were taken at step 9 when the high speed video camera was used. The high speed video was not used for every test, because the flow conditions for a third of the tests were identical, in order to determine repeatability of the measurements.

4.1.2 Experimental Procedure for the November 2011 Tests

As previously discussed, the problems encountered during the June 2011 tests necessitated a need for a second series of tests to be conducted during November 2011. The data collected during the June 2011 tests indicated that the differences between the liquid flow rates studied were too small to be detectable. As a result, the range of the injected liquid flow rates was doubled for the November 2011 tests. Fewer flow rates were studied, and the difference between each injected liquid flow rate used was increased. A new pressure transducer was used to measure the pressure differential, as the one used during the June 2011 tests proved to be inaccurate for the differential pressures being measured. It was observed that the pressure and temperatures during each of the tests tended to change slightly. To capture these transient effects, the data was recorded using a Pacific Instruments data acquisition system instead of being handwritten for each test. Analysis of the high speed video images during the June 2011 tests indicated that the film removal slot was ineffective at completely removing the liquid film. Therefore, it was decided to abandon use of the film removal slot during the November 2011 tests. High speed video images from were also taken during the November 2011 tests to qualitatively evaluate the surface behavior of the liquid films during a few of the tests. Unfortunately, there was not enough time to take high speed video for all of the test conditions. Finally, the uncertain location of the aluminum substrate below the liquid film during the June 2011 tests resulted in inaccurate film

thickness measurements. Changes were made to the testing procedure in order to remedy this issue. Rather than leave the film on for 3 full minutes, it was decided to intermittently turn the film off and on at intervals of 20-30 seconds, i.e., the film was turned on for 30 seconds, then turned off, then on again, etc. This procedure allowed for the LFD to directly detect the location of the aluminum substrate fairly frequently during the test runs. This allowed changes in the measured location of the substrate to be accurately tracked during the tests.

The experimental procedure for the November 2011 tests is as follows:

- 1) Verify that a plug of the correct diameter was installed in the test section in order to achieve the desired Mach number in the test article.
- 2) Verify that the cavitating venturi that was in place could achieve the desired liquid flow rates for the test.
- 3) The upstream pressure required to achieve the desired liquid flow rate was then set using a regulator valve. The pressure was monitored with a diaphragm, strain gauge type pressure transducer.
- 4) The flow of nitrogen into the test article was controlled using a regulator valve and sonic nozzle. The flow through the sonic nozzle could be determined using pressure transducers located upstream and downstream of the sonic nozzle. The flow rate of nitrogen was increased until the desired pressure within the test article was achieved.
- 5) Once the nitrogen was flowing through the test article, data acquisition using the LFD was initiated. Turning the LFD on before liquid was flowed into the test article allowed the surface of the dry substrate to be detected. Data acquisition from the pressure transducers and thermocouple also began at this time.
- 6) The ball valve leading into the test article was then opened to allow the liquid film to begin flowing.
- 7) The switch valve added to the test article to control the liquid flow rate was turned on, and the liquid film instantly began to flow. After about 20 to 30 seconds, the switch valve was closed and the liquid film was turned off. The valve was left

closed for about 15-30 seconds, after it was visually determined that the test article was completely dry. This step was repeated 5 to 6 times per test.

- 8) Data acquisition from the LFD, the pressure transducers and the thermocouple were stopped.
- 9) The regulator valve controlling the nitrogen flow rate was then closed and the test ended.

The LFD obscured the view of the high-speed video camera, and it therefore had to be removed when the visual data was being recorded. Because the only qualitative observations were being made with the high-speed videos, it was unnecessary to record the pressures and temperatures as a function of time to a file. While experiments using the high speed video camera were being conducted, the readings from each transducer were simply recorded with a pencil from the data acquisition screen. The procedure for the flow visualization tests is as follows:

- 1) Verify that a plug of the correct diameter was installed in the test section in order to achieve the desired Mach number in the test article.
- 2) Verify that the cavitating venturi that was in place could achieve the desired liquid flow rates for the test.
- 3) The upstream pressure to achieve the desired liquid flow rate was then set using a regulator valve. The pressure was monitored with a differential pressure transducer.
- 4) The flow of nitrogen into the test article was controlled using a regulator valve and sonic nozzle. The flow through the sonic nozzle could be determined using pressure transducers located upstream and downstream of the sonic nozzle. The flow rate of nitrogen was increased until the desired pressure within the test article was achieved.
- 5) The static pressure and differential pressure was recorded onto a spreadsheet with a pencil.
- 6) The ball valve leading into the test article was then opened to allow the liquid film to begin flowing.

- 7) The static pressure and temperature within the test article, as well as the differential pressure, and the pressures upstream and downstream of the cavitating venturi and sonic nozzle were recorded onto a spreadsheet using a pencil.
- 8) A short high speed video file was recorded.
- 9) The ball valve controlling the liquid flow rate was closed.
- 10) The regulator valve controlling the nitrogen flow rate was closed and the test ended.

4.3 Experimental Description Summary

An acrylic test article was constructed at AFRL to study the mechanics of shear-driven liquid films, using liquid water and nitrogen gas as stimulants. Due to difficulties encountered with the experiments run in June 2011, the experimental procedures were modified to improve the tests, and a new set of experiments was run in November 2011. Chapter 5 will now discuss the results of those experiments.

CHAPTER 5: EXPERIMENTAL RESULTS AND DISCUSSION

This chapter presents the experimental results regarding how the film mass flow rate and liquid film thickness vary as a function of gas phase momentum flux and injected liquid flow rate. Section 5.1 discusses a concern regarding whether or not the film would immediately attach itself to the wall or separate upon injection. Section 5.2 discusses the results obtained using the film removal slot. An attempt was made to estimate the mass flow rate lost from the film due to evaporation in section 5.2.2. The problems with the pressure drop data are briefly addressed in Section 5.3. Section 5.4 discusses the results obtained using the LFD, the film thickness results, and the method used to obtain the film thickness results. Finally, section 5.5 discusses the results obtained using the high speed video camera.

5.1 Film Attachment Discussion

One concern in this experiment was that the film would not immediately attach itself to the wall and separate upon injection. As explained in section 2.2.1, Warner and Reese [18] already studied this problem in detail. For all of the tests studied, the velocity at which the water was injected (equation 5-1) was compared with the critical velocity of injection, defined by equations 2-1 through 2-3. The test conditions (Reynolds numbers, mass flow rates, momentum fluxes, size of the test article, etc) under which equations 2-1 through 2-3 were derived were all very similar to test conditions in this experiment, and it should therefore be applicable [18]. The injected liquid velocities from the June tests are displayed in Figure 5-1 and the injected velocities from the November tests are displayed in Figure 5-2. The symbols in figures 5-1 and 5-2 show the critical velocities of injection and the straight lines show the calculated injected liquid flow rates. Note that the injected liquid velocity was calculated according to:

$$V_{L,i} = \frac{ILFR}{\rho_l bw} \quad (eq\ 5 - 1)$$

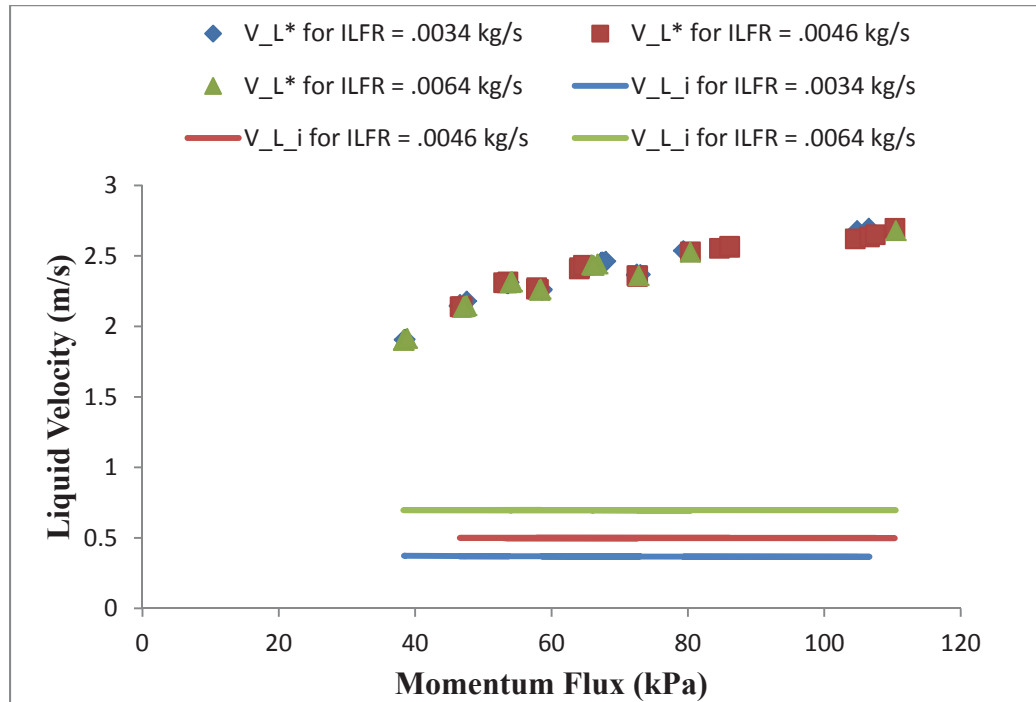


Figure 5-1: Comparison of the Injected Liquid Velocity with Critical Velocity of Injection for the June tests

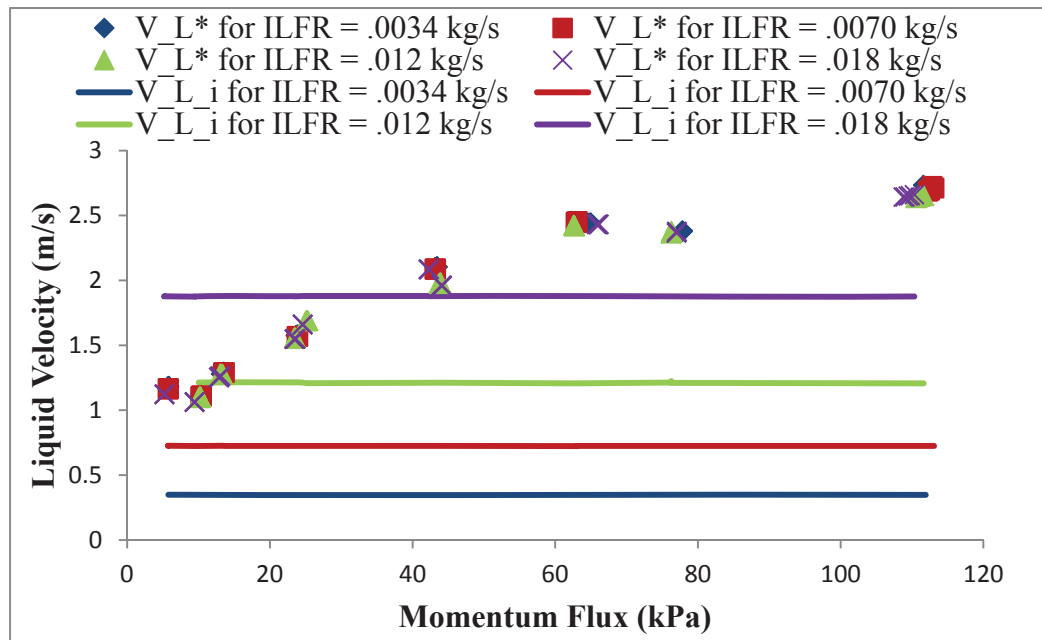


Figure 5-2: Comparison of the Injected Liquid Velocity with the Critical Velocity of Injection for the November tests.

As shown in figures 5-1 and 5-2, the injected liquid velocities were lower than the critical velocity of injection in every experiment except for those in which the mass flow rate was equal to or exceeded .12 kg/s and the momentum flux was less than 40 kPa. For most experiments, the injected liquid velocity was less than half of the critical velocity of injection, and, therefore, it is likely that film attached to the aluminum substrate immediately after injection. However, for the cases in which the injected liquid velocity was close to or greater than the critical velocity of injection, it is possible that some separation occurred or that the injected liquid did not immediately attach to the surface after being injected. However, neither the experimental data nor visual observations during the tests confirmed if the flow did indeed separate. In future experiments, the differential pressure should be measured across the slot, as a greater pressure drop should result from cases in which the injected liquid velocity exceeds the critical velocity of injection.

5.2 Film Mass Flow Rate Results

The mass flow rate results presented in this section only pertain to the June 2011 tests, as the film removal slot was used to measure the liquid film only during those tests, and not during the November 2011 tests. Section 5.4.1 covers the data collected by the film removal slot to determine the amount of liquid that remained attached to the wall. Several authors reviewed in Chapter 2 suggested that entrainment from a liquid film is impossible if the liquid flow rate, film thickness, or Reynolds number is below some threshold. Section 5.4.2 compares the injected liquid flow rates used in the experiments in this thesis with the onset of entrainment criteria established by these authors. Finally, section 5.4.3 discusses how much of the film flow rate may have been lost due to evaporation rather than pure entrainment.

5.2.1 Film Mass Flow Rate Measured Using the Film Removal Slot

The mass flow rate that remained in the liquid film was measured using the film removal slot. For the June 2011 tests, the liquid that was extracted with the film removal slot was emptied into a beaker for a period of about 3 minutes. The mass of liquid in the beaker divided by the time that it took the beaker to fill gave an estimate of the film mass flow rate. The film flow rate as a function of momentum flux and injected liquid flow rate is shown in Figure 5-4.

A high speed video camera was used to determine whether the film removal slot was effective at removing the entire liquid film. Unfortunately, the film removal slot was not entirely effective in removing all of the liquid film, as shown by the images in Figure 5-3. In figure 5-3, it appears that a small amount of film is escaping over the removal slot. The images of the removal slot are similar for all test conditions. Therefore, the removal slot was not completely effective in removing the film during any of the experiments.

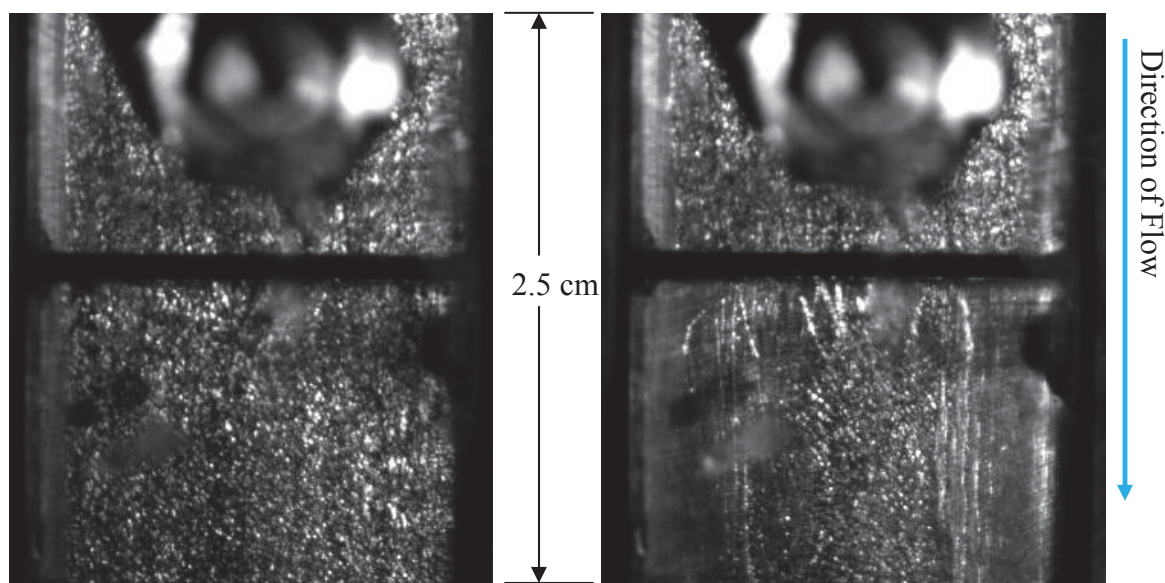


Figure 5-3: Images of the Film Removal Slot. Left: Removal Slot Valve is Closed. Right: Removal Slot Valve is Open.

Figure 5-4 shows the mass flow rate removed from the removal slot, which would ideally be the amount of liquid that remained in the liquid film and did not become

separated from the wall. As stated previously, Figure 5-3 showed that not all of the liquid was captured by the removal slot in the experiments. Thus, the raw data underpredicts the actual amount of liquid that remained in the liquid film after being injected through the upstream slot. It is very difficult to determine exactly how much liquid skimmed over the slot in all cases from the high speed video images alone. However, the removal flow rate seems to follow a trend in figure 5-4. Thus, it appears as though the amount of film that ran over the slot in the experiments introduced some sort of bias error to all the conditions studied.

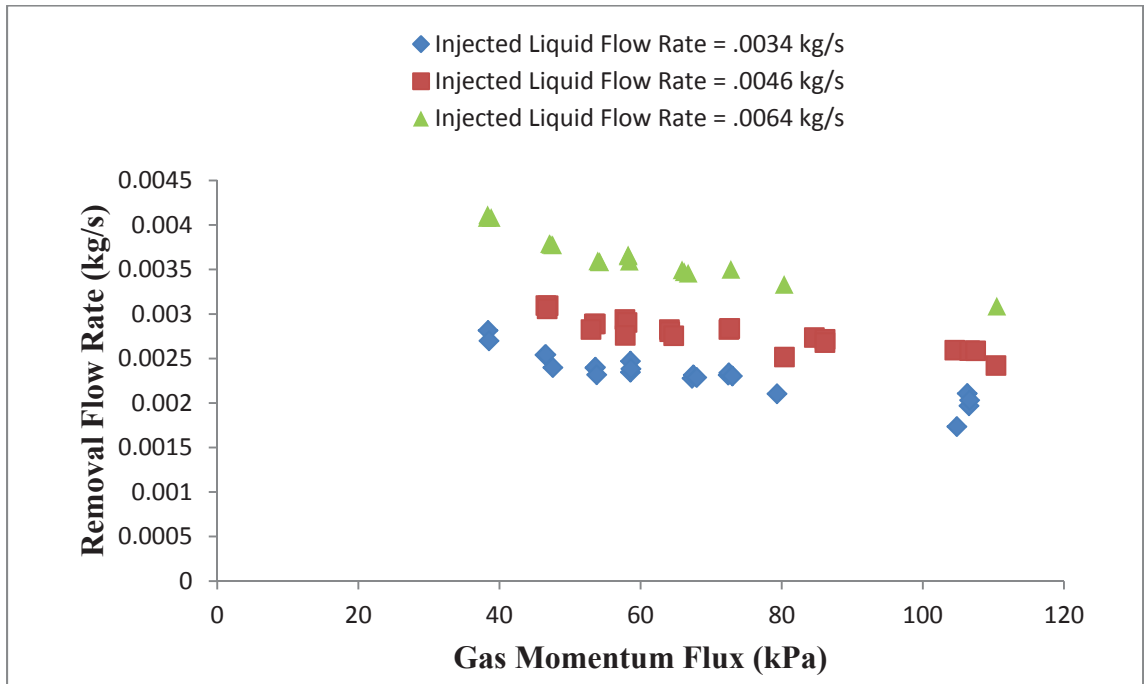


Figure 5-4: Liquid Film Removal Flow Rate vs Gas Momentum Flux

Figure 5-5 shows the fraction of liquid entrained into the gas phase as a function of gas momentum flux for several different injected liquid flow rates. The results are compared with the entrainment fraction correlations proposed by Gater [17], Ebner [6], and Sawant [10] (eqs. 2-7, 2-18, 2-9, respectively). Note that the hydraulic diameter for our experiment (.0167 m) was substituted for D_h in Sawant's correlation. While the data probably overpredicts the true entrainment fraction, the data does seem to follow the general trend of Gater's correlation. However, Gater's correlation for the entrainment fraction does not account for effect of the injected film flow rate on the entrainment

fraction. Ebner's correlation seems to overpredict the data from this experiment. Discrepancies between Ebner's correlation and the data may result from a number of reasons. First, Ebner only applied equation 2-18 to oil films and did not investigate other fluids [6]. Second, Ebner's films were also about an order of magnitude thicker than our films [6]. Third, the momentum fluxes in Ebner's experiment did not exceed 4,500 Pa [6]. While Sawant's correlation was not intended to be applied to the geometry of our experiment [10], it is interesting to note that Sawant's correlation predicts that virtually no entrainment should have occurred for liquid flow rates less than about .0059 kg/s. Therefore it is also possible that results from the removal slot may be indicating an entrainment fraction when there should not be one. However, it is not possible to confirm this until the removal slot has been modified. Despite the problems with the removal slot, the fact that correlations shown in Figure 5-5 do not correspond with the data nor each other indicates that there is a need for additional research on the establishment of a liquid film for film cooling in rockets.

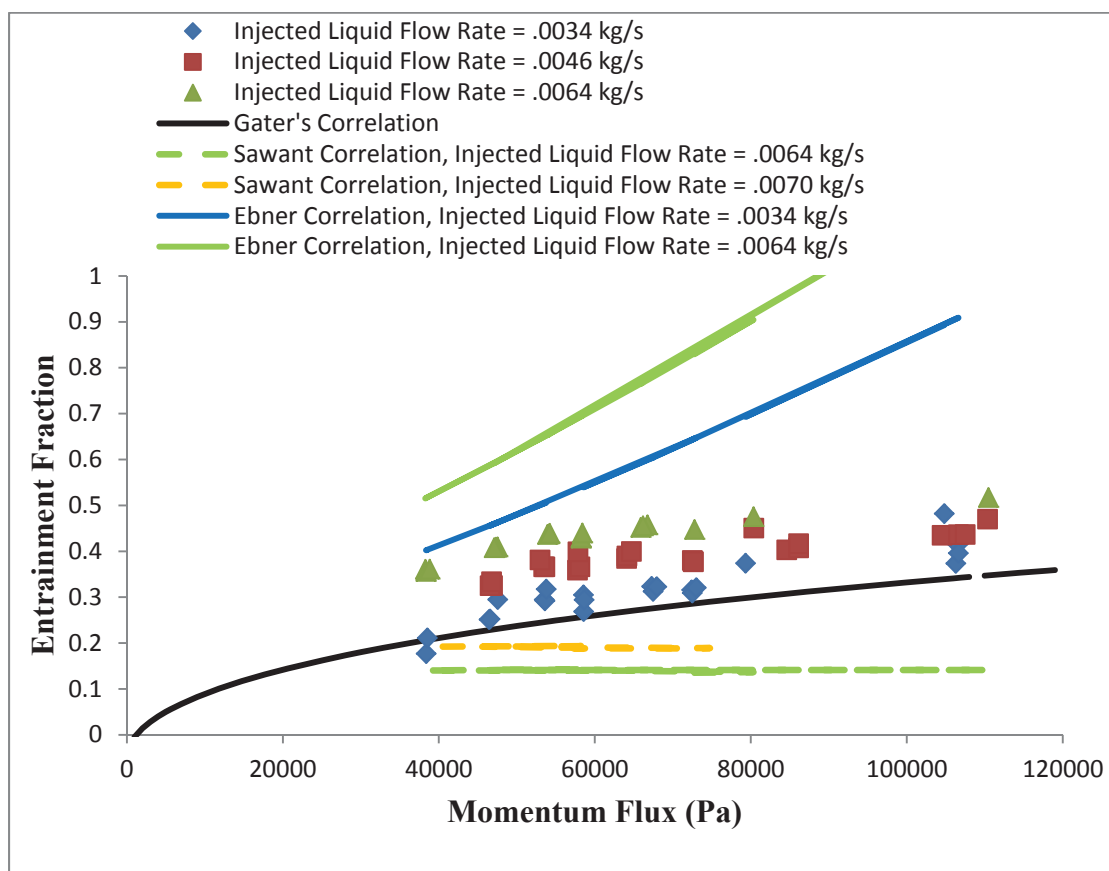


Figure 5-5: Fraction of Liquid Entrained into Gas Phase vs Gas Momentum Flux

It must also be noted that additional discrepancies between the data and the correlations could also be due to the geometry of the injection slot. Gater, Ebner, and Sawant introduced their films either tangentially with the gas flow or through a large porous medium [17], [6], [10]. However, the films in this thesis were injected through a thin slot perpendicular to the gas flow. This configuration may have resulted in additional mass loss at the point of injection that is not accounted for by the correlations shown in Figure 5-5. Note again that the mechanism for removing the liquid film needs to be modified before any definitive conclusions are drawn from this data.

5.2.2 Onset of Entrainment Discussion

Kinney et al, Knuth, Sawant et al, and Ishii and Grolmes all suggested that entrainment could not occur when no waves for present on the surface of the liquid film. Each author established criteria to determine whether or not entrainment from the liquid film was possible. Kinney et al suggested that no entrainment occurred for values of w^+ below 90, with w^+ defined by equation 2-5. Using Knuth's data, Grissom suggested that no entrainment could occur for values of Γ_{cr} less than that calculated by equation 2-6. The entrainment criterion for Sawant et al and Ishii and Grolmes is represented by equation 2-15. Each of these criteria are dependent on fluid properties only. Herein, the injected liquid flow rate below which no entrainment can occur will be defined as the critical injected liquid flow rate.

The critical injected liquid flow rate for the experiments in this thesis was calculated using each of the different entrainment criteria and the results are compared in Table 5-1. The temperatures and viscosities in the experiments varied. In addition, the film temperatures in the experiments were not measured and are not known. In order to bound the critical injected liquid flow rate calculated by each equation, film and gas properties were determined from the maximum and minimum temperatures recorded in the experiments. The reader is referred to Appendix B for further details. The fluid properties for nitrogen and water were determined from "Table A.4: Thermophysical

Properties of Gases at Atmospheric Pressure” in *Fundamentals of Heat and Mass Transfer* by Incopera et al [32] and “Table A.6: Thermophysical Properties of Saturated Water” in *Fundamentals of Heat and Mass Transfer* by Incopera et al [33], respectively.

Table 5-1: Comparison of the Critical Injected Liquid Flow Rate Determined by Different Equations. Surface Tension is Assumed to be .68 N/m

Assumed Gas Phase Temperature (K)	Assumed Liquid Film temperature (K)	Assumed Gaseous Nitrogen Viscosity (N·s/m ²)	Assumed Liquid Water Viscosity (N·s/m ²)	ILFR _c predicted by eq 2-5 (kg/s)	ILFR _c predicted by eq 2-6 (kg/s)	ILFR _c predicted by eq 2-17 (kg/s)
311	283	1.72E-05	1.30E-03	0.00298	0.00058	0.00588
311	311	1.85E-05	6.83E-04	0.00156	0.00128	0.00425
283	283	1.72E-05	1.30E-03	0.00298	0.00058	0.00588
283	311	1.85E-05	6.83E-04	0.00156	0.00128	0.00425

As shown by Table 5-1, the critical injected liquid flow rates predicted by equation 2-5 and 2-6 are both less than the lowest injected liquid flow rates used in this experiment, .0034 kg/s. Therefore, based on the predictions of equations 2-5 and 2-6, entrainment for all gas phase momentum fluxes and injected liquid flow rates used in this experiment is expected. Running additional experiments with injected liquid flow rates less than the critical injected liquid flow rates predicted by equation 2-5 and 2-6 were desired. However, this was infeasible with the resources available to the author. It is recommended that lower injected liquid flow rates be used in future experiments in order to evaluate the applicability of equations 2-5 and 2-6. The critical injected liquid flow rate predicted by equation 2-17 is higher than some of the injected liquid flow rates in this thesis, suggesting that entrainment should not have occurred at these values. The discrepancies between the data in this thesis and predictions from the correlations of Sawant et al have already been discussed in section 5.2.1.

5.2.3 Liquid Lost From Film Due to Evaporation

The film may have lost mass through evaporation and diffusion of the liquid in the film into the gas phase in addition to mass lost through entrainment. The mass lost

from the film via evaporation processes is addressed in this section. The evaporation rate was estimated for the June 2011 tests by using the methods in *Fundamentals of Heat and Mass Transfer* by Incopera et al [34]. The analysis described in this section attempts to estimate an upper bound on the evaporation rate in an attempt to determine how important the evaporation rate is in comparison to the entrainment rate. To aid in this endeavor, assumptions are employed in the following analysis that would tend to yield higher estimates of the evaporation mass flow rate.

Assuming fully developed, turbulent flow in the gas phase, the Sherwood number can be estimated according to:

$$Sh_D = .023Re_D^{4/5}Sc^{.4} \quad (eq\ 5 - 2)$$

where,

$$Re_D = \frac{\rho_g V_g D_H}{\mu} \quad (eq\ 5 - 3)$$

and

$$Sc = \frac{\nu}{D_{w,N}} \quad (eq\ 5 - 4)$$

The molecular diffusivity of water into nitrogen, $D_{w,N}$ was calculated according to [35]:

$$D_{w,N} = .2178 \left(\frac{P_{STP}}{P_T} \right) \left(\frac{T_T}{T_{STP}} \right)^{1.81} \quad (eq\ 5 - 5)$$

With the Sherwood number and molecular diffusivity for each test known, the mass transfer coefficient, h_m , can be calculated with

$$Sh_D = \frac{h_m D_h}{D_{w,N}} \quad (eq\ 5 - 6)$$

The evaporative mass flux can then be calculating according to:

$$\dot{m}_{evap}' = h_m (\rho_{w,s} - \rho_{w,N}) \quad (eq\ 5 - 7)$$

The nitrogen for all experiments was perfectly dry, and, therefore,

$$\rho_{w,N} = 0 \quad (eq\ 5 - 8)$$

The density of the water at the interface between the film and the gas is related to the vapor pressure of water. The temperature of the liquid in the film was unknown in

these experiments. However, the temperature of both the nitrogen and the water was known before entering the test article. To be conservative, the temperature at which the film vapor pressure was calculated used the larger of inlet temperature of nitrogen or water. The vapor pressure was determined using “Table A.6: Thermophysical Properties of Saturated Water” in *Fundamentals of Heat and Mass Transfer* by Incopera et al [33]. With the vapor pressure known, the density of water at the interface can be calculated with the ideal gas law:

$$\rho_{w,s} = \frac{P_{vap}}{R_w T} \quad (eq\ 5 - 9)$$

Assuming that h_m is uniform across the surface of the film, the evaporative mass flow can be calculated according to:

$$\dot{m}_{evap} = \dot{m}_{evap}'' w L_f \quad (eq\ 5 - 10)$$

where w is the width of channel (26.4 mm) and L_f is the length of the film in the stream-wise direction (137 mm according to Figure 4-1).

Equation 5-10 should provide a close estimate for the mass flow rate due to evaporation. However, this equation might underpredict the Sherwood number at the start of the film because it assumes that the gas flow is fully-developed turbulent. The Sherwood number and therefore the mass transfer coefficient are expected to be highest at the start of the film, where the boundary layer is just beginning to develop. To account for this affect, the film itself was modeled as flat plate and an equation for the average Sherwood number corresponding to a developed turbulent boundary over a flat plate, with the boundary layer tripped at the film’s start, was also used to estimate the evaporation rate. The average Sherwood and Reynolds numbers for flow over a flat plate is calculated by equation 5-11 and equation 5-12, respectively. The evaporative mass flow rates as a fraction of the injected liquid flow rate for all the June 2011 Tests is shown the figure 5-6. The results obtained using both the pipe flow and flat plate Sherwood numbers are compared to each other.

$$\overline{Sh}_L = .037 Re_L^{4/5} Sc^{1/3} \quad (eq\ 5 - 11)$$

where:

$$Re_L = \frac{\rho_g V_g L_f}{\mu_g} \quad (eq\ 5 - 12)$$

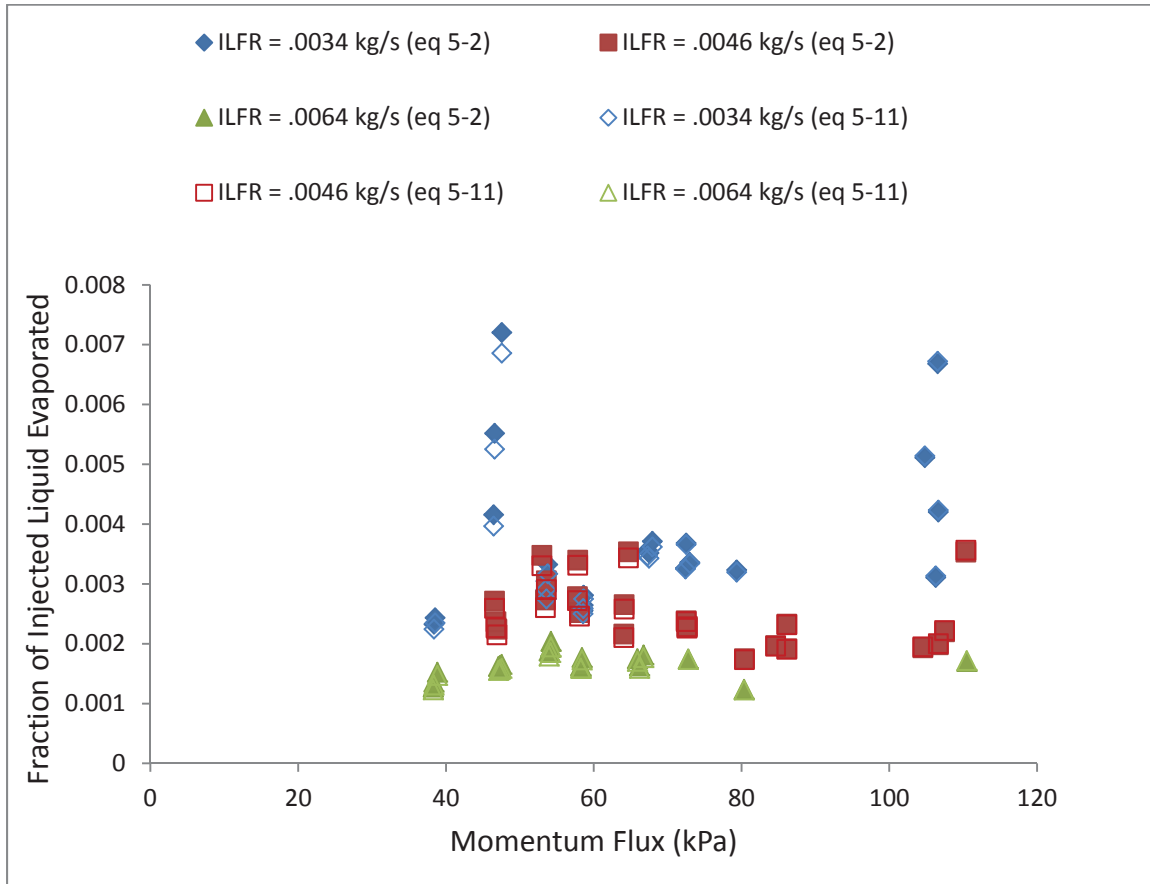


Figure 5-6: Evaporative Mass Flow Rate from the Liquid Film as a percent of the Injected Liquid Flow Rate

Figure 5-6 shows that the evaporative mass flow rate is less than 1% of the injected liquid flow rate for all of the June 2011 tests. The results shown in figure 5-6 should be an upper bound on the evaporative mass flow rate for a number of reasons. First, the entrained droplets above the film would also be evaporating during an experiment, which increase the concentration of water vapor in the gas flow above the film. This effect, which is not accounted for in the above analysis, would tend to reduce the concentration gradient at the interface and therefore reduce the mass transfer coefficient. Secondly, the flat plate model accounts for a developing turbulent boundary

layer starting at the film's edge, which would account for a higher mass transfer coefficient at the start of the film. Figure 5-6 shows that the evaporation estimates obtained from each model are almost identical to each other. On the other hand, the film surface roughness would tend to increase the surface area of the film, which would tend to increase the evaporation rate from the film. This effect is not accounted for in this analysis. In any event, the mass flow rates due to evaporation are negligible.

5.3 Pressure Drop Results

The pressure drop across the distance depicted in Figure 4-1 was also measured during both the June and November 2011 tests. It was hoped that this data would provide information according to the method described in section 3.2.1. However, accurate pressure drop data was not obtained during either the June or November 2011 Tests due to problems with the instrumentation.

During several of the test runs, it was observed that the measured pressure drop in the test section suddenly jumped up by a few hundred to a thousand Pascal. In subsequent tests, a higher differential pressure was recorded than what was previously recorded at similar gas phase momentum fluxes. An example of a test run during which the measured pressure drop jumped is shown in Figure 5-7. The source of these jumps was never discovered, though it is suspected that the lines connecting the pressure transducer to the test article were poorly sealed or that there was an electrical problem with the transducers used. Secondly, in order to try to obtain a better seal on the pressure taps, the author attempted to tighten the fittings on pressure taps during a test run. This was observed to change the measured value of the pressure drop. Since the measured pressure drop should not be dependent on how tight the fittings were if the lines were properly sealed, a leak check was performed with leak check fluid to make sure that the lines were fully sealed. However, regardless of the fact that the leak check showed no leak, the recorded pressure drop still seem to vary with the torque applied to the fittings. Finally, the test article was disassembled and then reassembled and tests were repeated. However the pressure drop data was not found to be repeatable.

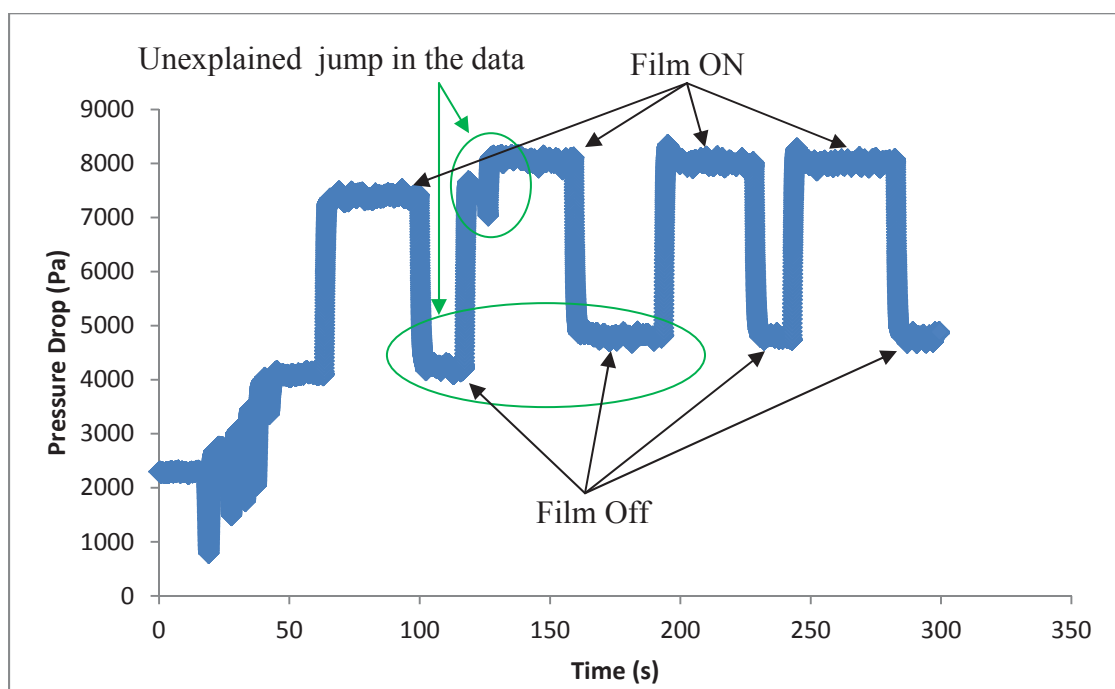


Figure 5-7: Problem with pressure tap mid-experiment

Due to the precision required for measurements associated with shear-driven liquid films, it is suggested that the shear stress be directly measured. There are three approaches to this. One approach would be to use a PDPA in order to estimate the velocity profile of the gas phase by measure the velocity of the entrained droplets. The second approach is to use a hot film anemometer flush mounted to the wall in order to directly measure the shear stress at the wall of the thin liquid film. The third approach to measuring the shear stress in the liquid film is an electrochemical diffusion technique.

5.4 Film Thickness Results

This section describes the how the film thickness was measured using the LFD and the film thickness results that were obtained with that method. First, the raw data collected from the LFD is discussed in section 5.4.1. Then, in sections 5.4.2 and 5.4.3, two different approaches for determining the film thickness from the LFD data are discussed. The first approach, discussed in section 5.4.2, is referred to as the “direct

method,” and the second approach, discussed in section 5.4.3, is referred to as the “index of refraction method.” Section 5.4.4, compares the two methods using data collected during the June 2011 tests. Ultimately, the “index of refraction method” was found to be the better method for determining the film thickness. Section 5.4.5 discusses the film thickness results that were obtained during the November 2011 tests using the “index of refraction method.” Finally, section 5.4.6 compares the film thickness data collected in this thesis to a mathematical model and to film thickness data obtained by Coy et al [1].

5.4.1 Raw LFD Data

Figure 5-8 displays the raw data of the position of the film surface taken by the LFD during a typical test run. In addition to the position of a surface, the LFD also records the intensity of the light intensity peak on a scale of 1-255. Different surfaces that fall within the range of the focal point of the LFD usually reflect light intensities of different strengths. Thus, the LFD can be used to discriminate between two different surfaces based on the strengths of the light intensities that correspond to each surface. This can be very important for deciphering which surface is which in dynamic applications, such as when measuring the thickness of shear-driven film flows. For example, during the tests, it was observed that the intensity of light reflected to the LFD from the surface of still water did not exceed 70, and that the intensity of the light intensity peaks typically varied between 30-70 when the surface was disturbed. The intensity of the light reflected from the dry aluminum substrate upon which the film ran during test runs was typically about 180. With a turbulent liquid film running over the aluminum surface, the strongest signal reflected back to the LFD was observed to never drop below 135. Based on this knowledge, the strongest light intensity peak received by the LFD during measurements was assumed to correspond with the aluminum surface and the second strongest light intensity was assumed to correspond with the surface of the liquid film.

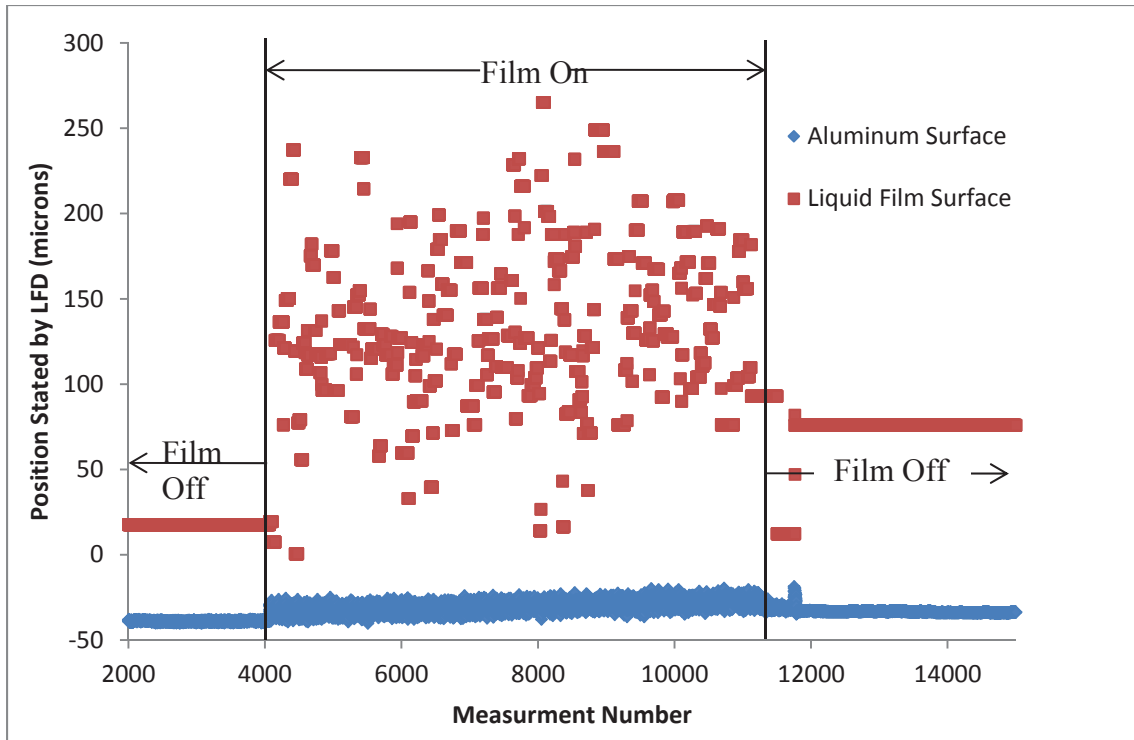


Figure 5-8: Raw Position Data from the LFD during a typical test run

Much of the data that was believed to correspond with the surface of the liquid film in Figure 5-8 is repeated several times in a row. In the event that the LFD is unable to detect a second highest intensity light peak, then the LFD simply outputs the previously measured value. Similarly, in the event that the LFD is unable to detect any light intensity peak, then the previous value for both signals will simply be repeated. Before the film flow is initiated, there is no second highest light intensity to be received by the LFD, as only the aluminum surface is present to reflect a signal. Therefore, the LFD continues to output the last measurable value from what was assumed to be the film surface from the previous run. This explains the straight line from the “Liquid Film Surface” data in Figure 5-8. Once the film is turned on, the “Liquid Film Surface” data becomes very scattered. As demonstrated by Wegener [4], the LFD is incapable of detecting the surface of the liquid film if the surface angle exceeds 8 degrees. Since the film surfaces were highly turbulent in all experiments, it was expected that the LFD would not always be able to detect the location of the surface of the liquid film. Thus,

much of the “Liquid Film Surface” data is repeated, due to the LFD not receiving a reflection of sufficient intensity.

The intensity of light reflected from the aluminum surface was not observed to fall below a value of 130 during any of the experiments. Thus, none of the data from the aluminum surface was repeated due to a failure of the LFD to detect a reflection of sufficient intensity. In addition, when the film is turned on, the surface of the aluminum seems to jump up to a new position. This jump results from the fact the laser being reflected off of the aluminum surface now has to pass through the liquid film, which shifts the focal point of the LFD due to the film’s index of refraction.

5.4.2 The Direct Method for Determining Liquid Film Thickness Using the LFD

Two methods can be used to estimate the thickness of the liquid film. The first method, hereafter referred to as the “direct method,” involves estimating the thickness of the liquid film by taking the difference between the “Liquid Film Surface” data and the position of the aluminum substrate. Note, that the position of the aluminum substrate is unknown when the film is running along the surface because the liquid film interferes with the laser beam. Secondly, the nitrogen air flow was usually at a different temperature than the test article, which would cause the entire test article to contract or expand due to temperature changes. This effect changes the location of the aluminum surface relative to the LFD. Figure 5-9 presents a close up view of the signal being returned from the aluminum surface, which shows that the position of the aluminum surface is higher after the test run than it is before the test run. To account for this, a linear trend line was applied to the data in order to estimate the position of the aluminum surface during a test run. Thus, in the “direct method,” the film thickness can be estimated by finding the difference between “Liquid Film Surface” data and this trend line.

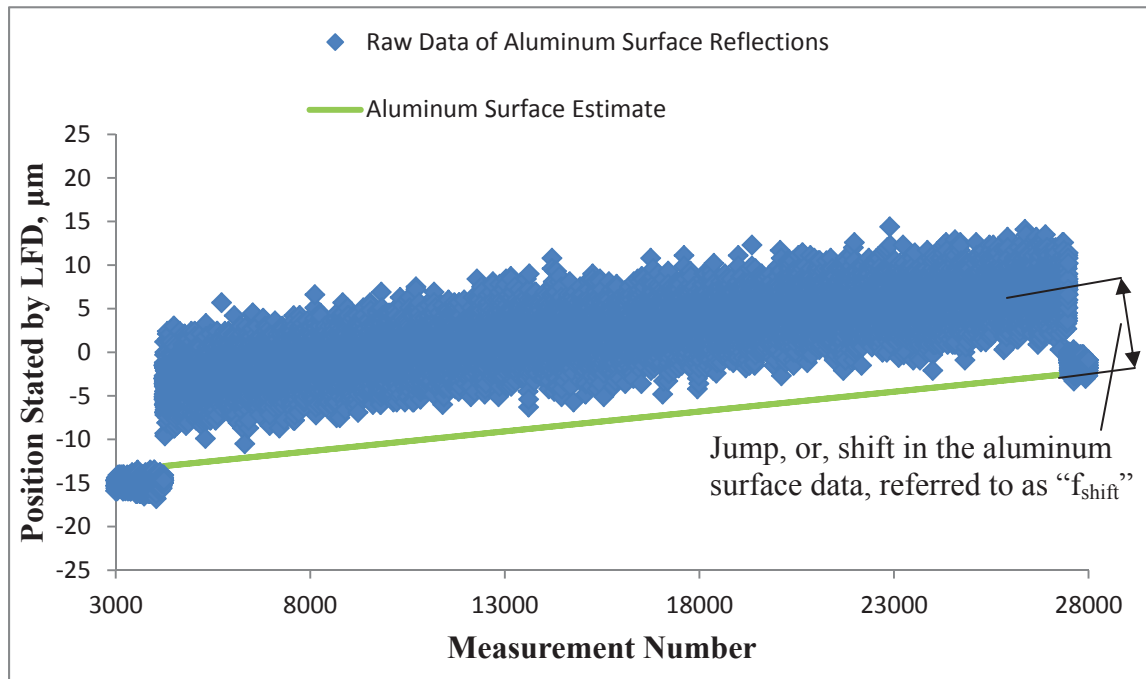


Figure 5-9: View of Aluminum Surface Estimate

5.3.2 The Index of Refraction Method for Determining Liquid Film Thickness Using an LFD

The “index of refraction method” involved determining the film thickness from the shift in the aluminum surface data in the presence of a liquid film. The shift in the “Aluminum Surface” data is related to the film thickness, and, therefore, the thickness of the liquid film can also be estimated from the shift observed in the “Aluminum Surface” data by tracking the path of the beam as it passes through a liquid film. Figure 5-10 shows an illustration of this problem. The dotted red line in the figure represents where the focal point of the LFD would be in the presence of no film. The solid red line represents the actual beam that is reflecting off of the aluminum surface.

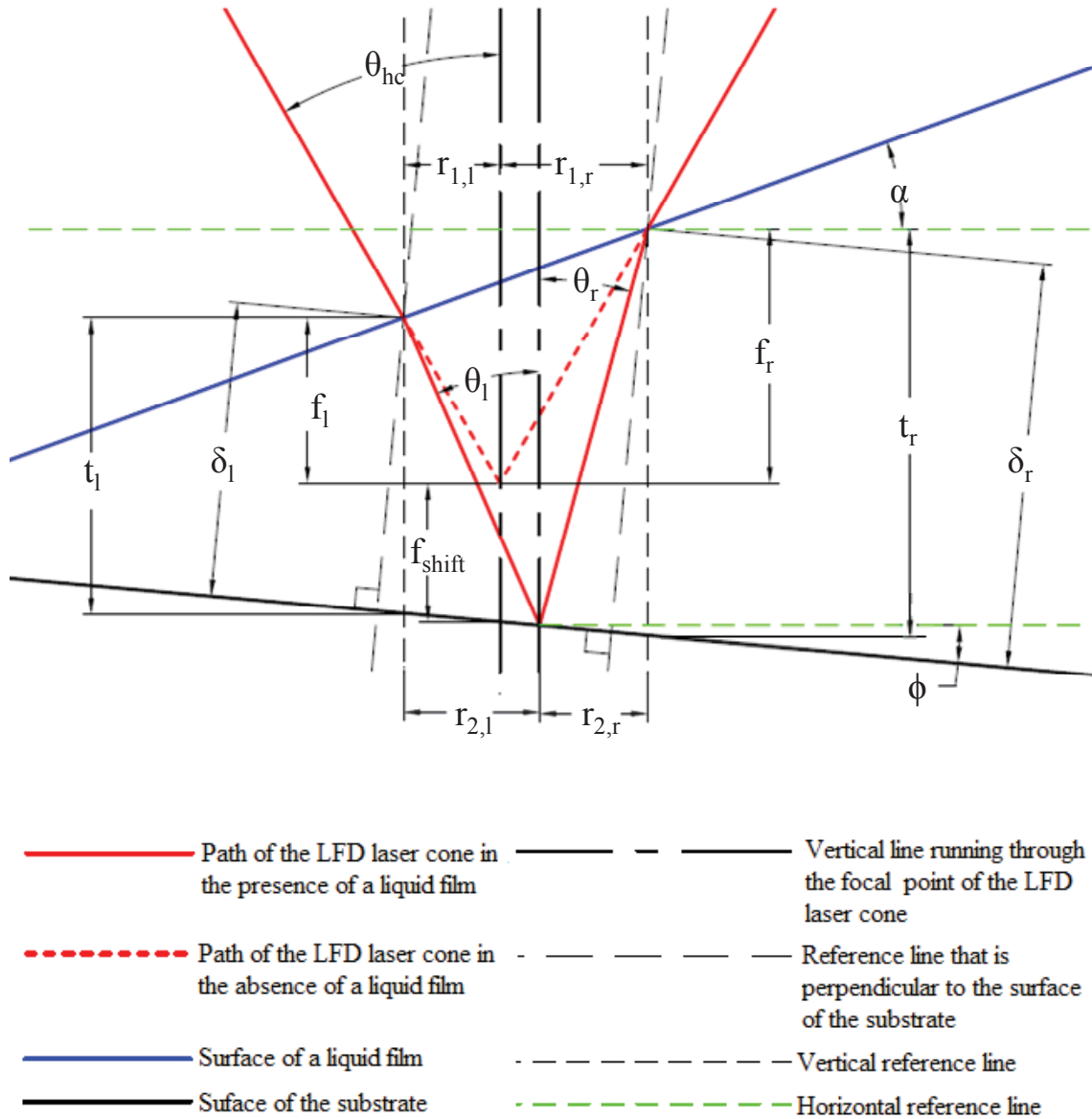


Figure 5-10: Illustration of the LFD's Conical Laser Beam Passing Through the Surface of The Liquid Film and Reflecting off of the Aluminum Surface.

The variables that need to be taken into account when calculating the film thickness based on the shift seen in the data in Figure 5-9 are the half-cone angle, the surface angle of the liquid film, and also the angle that the substrate forms with the centerline of the LFD laser cone. While every effort was made to ensure that the LFD was perpendicular with aluminum surface, there was still an uncertainty in the angle of $\pm 5^\circ$, and, therefore, the angle that the substrate forms with the centerline of the LFD

laster cone needs to be considered. Based on the variables defined by Figure 5-10, the ratio of the average film thickness, δ_{ave} , to f_{shift} can be calculated according to equation 5-12. A full derivation can be found in Appendix C. Note that the film thickness is defined as a distance perpendicular to the substrate and that f_{shift} is the distance between an “aluminum surface” data point and the best fit line in Figure 5-9.

$$\frac{\delta_{ave}}{f_{shift}} = \frac{\cos \phi}{2} \cdot \left(\frac{A + B}{A + B - C - D} + \frac{E + F}{E + F - G - J} \right) \quad (eq\ 5 - 13)$$

where:

$$A = \frac{\tan \theta_{hc}}{1 - \tan \theta_{hc} \tan \phi} \quad (eq\ 5 - 14)$$

$$B = \frac{\tan \theta_{hc} (1 + \tan \alpha \tan \theta_{hc})}{(1 - \tan \theta_{hc} \tan \phi)(1 - \tan \theta_{hc} \tan \alpha)} \quad (eq\ 5 - 15)$$

$$C = \frac{\tan \theta_l}{1 - \tan \theta_l \tan \phi} \quad (eq\ 5 - 16)$$

$$D = \frac{\tan \theta_r (1 + \tan \theta_l \tan \alpha)}{(1 - \tan \theta_l \tan \phi)(1 - \tan \theta_r \tan \alpha)} \quad (eq\ 5 - 17)$$

$$E = \frac{\tan \theta_{hc}}{1 + \tan \theta_{hc} \tan \phi} \quad (eq\ 5 - 18)$$

$$F = \frac{\tan \theta_{hc} (1 - \tan \alpha \tan \theta_{hc})}{(1 + \tan \theta_{hc} \tan \phi)(1 + \tan \theta_{hc} \tan \alpha)} \quad (eq\ 5 - 19)$$

$$G = \frac{\tan \theta_r}{1 + \tan \theta_r \tan \phi} \quad (eq\ 5 - 20)$$

$$J = \frac{\tan \theta_l (1 - \tan \theta_r \tan \alpha)}{(1 + \tan \theta_r \tan \phi)(1 + \tan \theta_l \tan \alpha)} \quad (eq\ 5 - 21)$$

Figure 5-11 shows how δ_{ave}/f_{shift} varies with the surface angle of the liquid film and the surface of the substrate relative to the LFD. This figure demonstrates that δ_{ave}/f_{shift} is a strong function of the surface angle of the liquid film, and, therefore, in order to obtain an accurate estimate of the average film thickness by tracking the beam as it passes through the film, an estimate of the surface angle on the liquid film must be known. In addition, in reality, the film surface will have some curvature to it; this could also shift the focal point due to a lensing effect. Finally, the above analysis is based only on geometric optics. The effects of the wave nature of light are not accounted for.

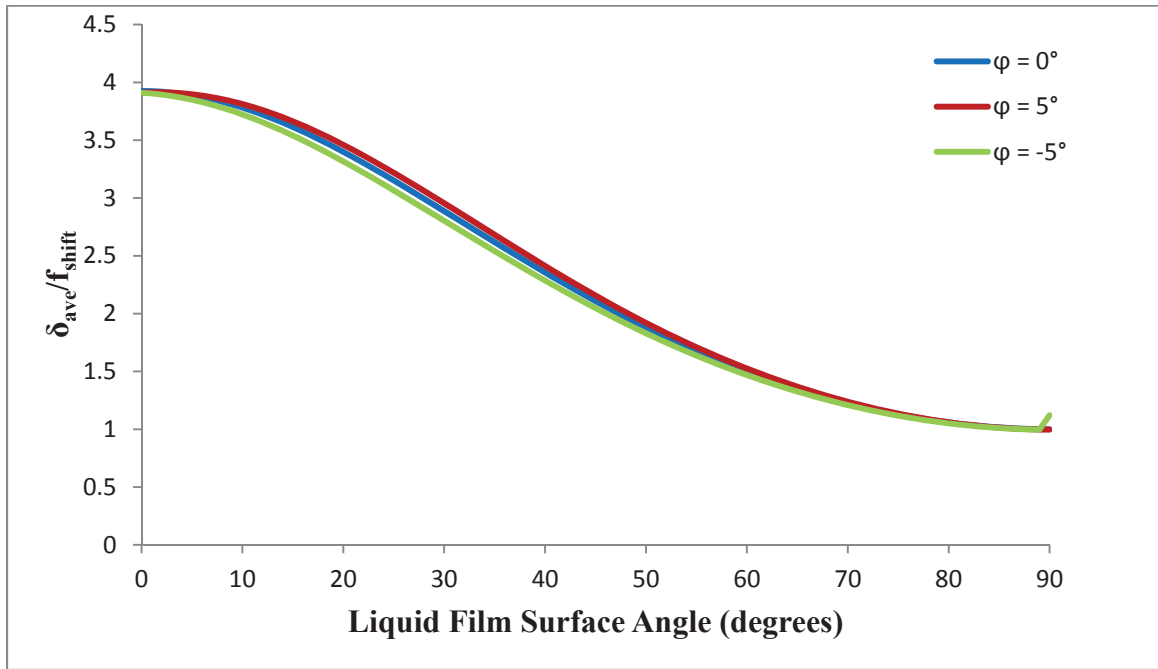


Figure 5-11: Plot Showing how the Liquid Film Surface Angle Shifts the Focal Point of the LFD

As shown by Figure 5-11, knowledge of the surface angle of the liquid film is necessary in order to accurately determine the film thickness using the index of refraction method. Wegener experimentally observed that the surface angle of the liquid water film must be less than 28° in order for the LFD to detect the polished aluminum substrate beneath it [4]. As previously noted, the LFD signal corresponding to the aluminum surface always seemed to return valid measurements. Therefore, the surface angle of the liquid film must have been less than 28 degrees for every LFD measurement that

corresponded to the aluminum surface, otherwise, no signal would have been returned to the LFD.

With knowledge that the surface angle of the liquid film never exceeded 28 degrees, and with the uncertainty in the angle of the substrate estimated to be $\pm 5^\circ$, the range of δ_{ave}/f_{shift} can be determined. In determining the range of δ_{ave}/f_{shift} , the index of refraction of water was taken to be 1.33 [36], the index of refraction of the nitrogen was assumed to be the same as that of air at 1.000335 [36], with a negligible uncertainty, and the half-cone angle of the LFD was stated by the manufacturer at 11.5° . The author never found the uncertainty in the index of refraction of water and estimated it to be ± 0.01 . Microsoft EXCEL's random number generator was used to create 10,000 combinations of numbers that fell within uncertainty for each variable in equations 5-13 through 5-21. Equation 5-13 was then used to calculate δ_{ave}/f_{shift} for those 10,000 combinations of numbers. A histogram of the data is shown in Figure 5-12. As shown by the histogram, a value for δ_{ave}/f_{shift} of approximately 3.9 is the most common result. The range of δ_{ave}/f_{shift} is 3.05 to 4.05.

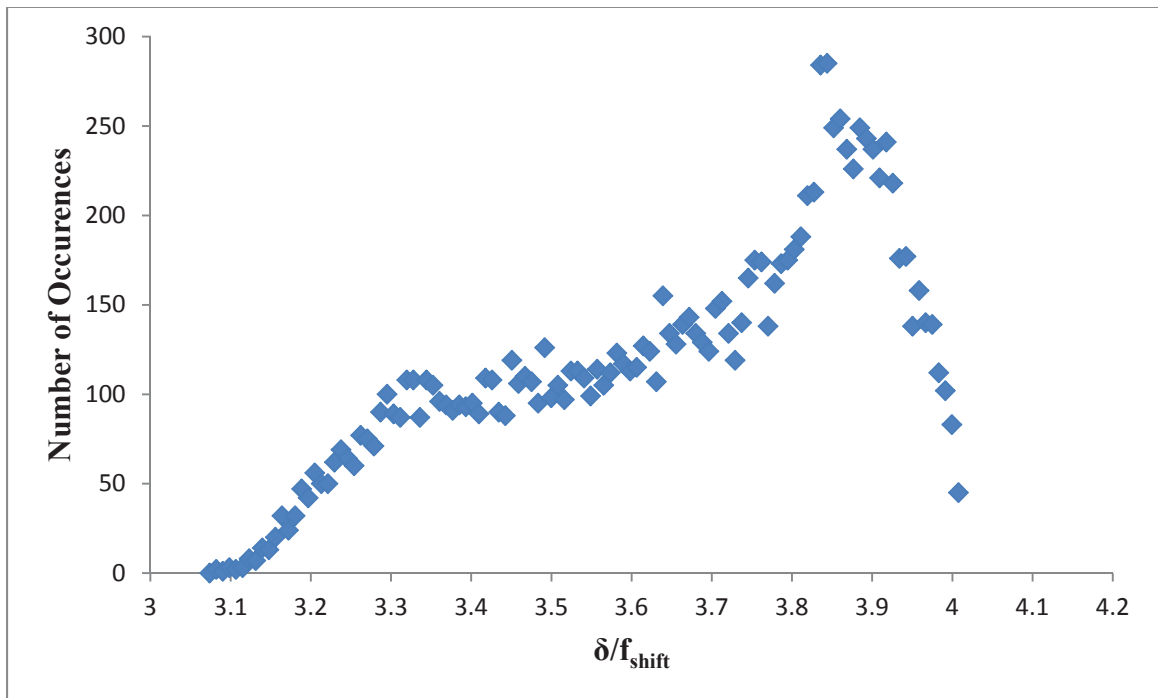


Figure 5-12: Range of Possible Values for δ/f_{shift} Based on the Uncertainty of the Variables in Equation 5-12

Assuming that the surface angle of the liquid film is randomly distributed between -28 and 28 degrees, the ratio between the average film thickness and f_{shift} is expected to 3.9 most of the time, with the range being 3.05 to 4.05. Therefore, the average film thickness in an experiment is most likely to be 3.9 times the value of f_{shift} , although it possible for the film thickness to be anywhere between 3.05 and 4.05 times the value of f_{shift} , depending on the surface angles of the liquid film.

5.4.3 Comparison of the Direct Method with the Index of Refraction Method

During the June 2011 tests, it was observed that film thicknesses determined using the “direct method” for momentum fluxes exceeding 38 kPa were inconclusive, noisy, and did not follow expected trends. It was suspected that turbulence of the film’s surface and the number droplets entrained into the gas flow were of sufficient magnitude at gas momentum fluxes exceeding 38 kPa such that they interfered with the direct detection of the film surface by the LFD. In order qualify and compare the two methods, several low momentum flux, low liquid flow rate experiments were run in June 2011. It was observed that the surface of the liquid films run during these cases was much more stable and that there was much less liquid entrained into the gas phase. Note that the raw LFD data for each of these additional test conditions was similar to what is depicted in Figure 5-8, and that a film thickness can be computed for each data point recorded by the LFD. A histogram was made for each test run for all the film thicknesses measured during a test run using each method.

Figures 5-13 through 5-15 show histogram plots of the film thickness estimates obtained using the “direct method” and the “index of refraction method” for several test conditions during the June 2011 tests. The plots are not normalized. For the film thickness estimates determined using “direct method,” the repeated data points are removed for the generation of the histogram. For the film thickness estimates determined using the “index of refraction method,” the value of $\delta_{\text{ave}}/f_{\text{shift}}$ was taken to be 3.9. The histogram plots determined using each method resemble a normal distribution. Thus, an

estimate of the average film thickness for a test condition can be obtained from the peak of each histogram.

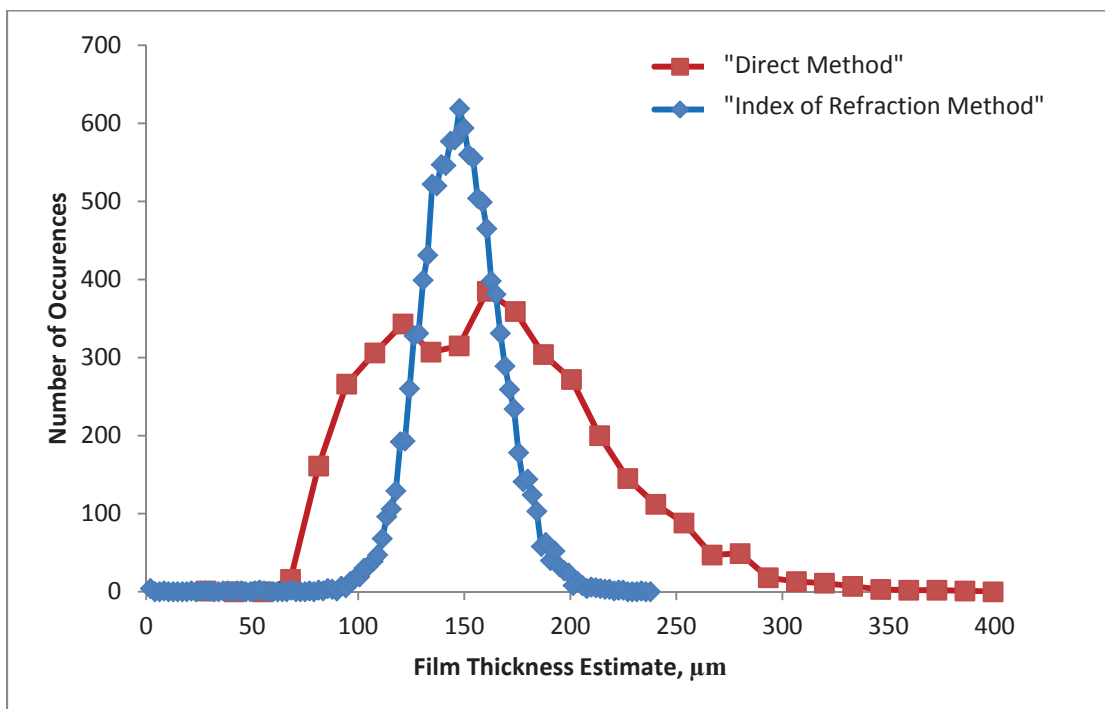


Figure 5-13: Histogram of Film Thickness Estimates for Each Method with Momentum Flux = 2,970 Pa and Liquid Film flow rate = .007 kg/s

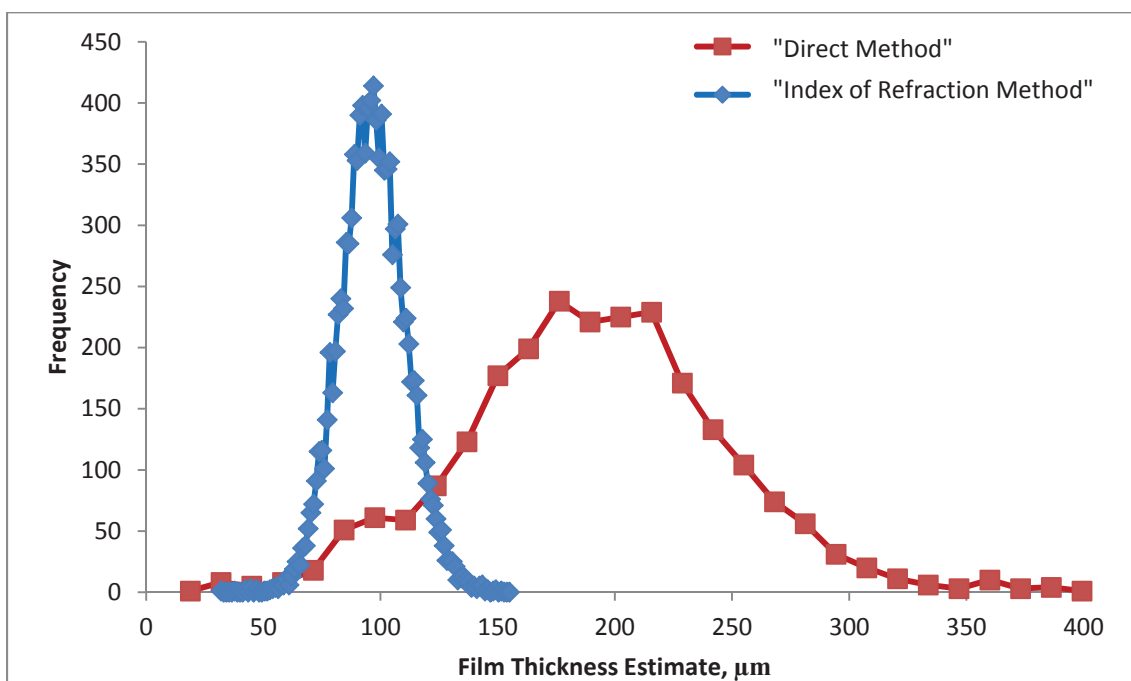


Figure 5-14: Histogram of Film Thickness Estimates for Each Method with Momentum Flux = 7,750 Pa and Liquid Film flow rate = .007 kg/s

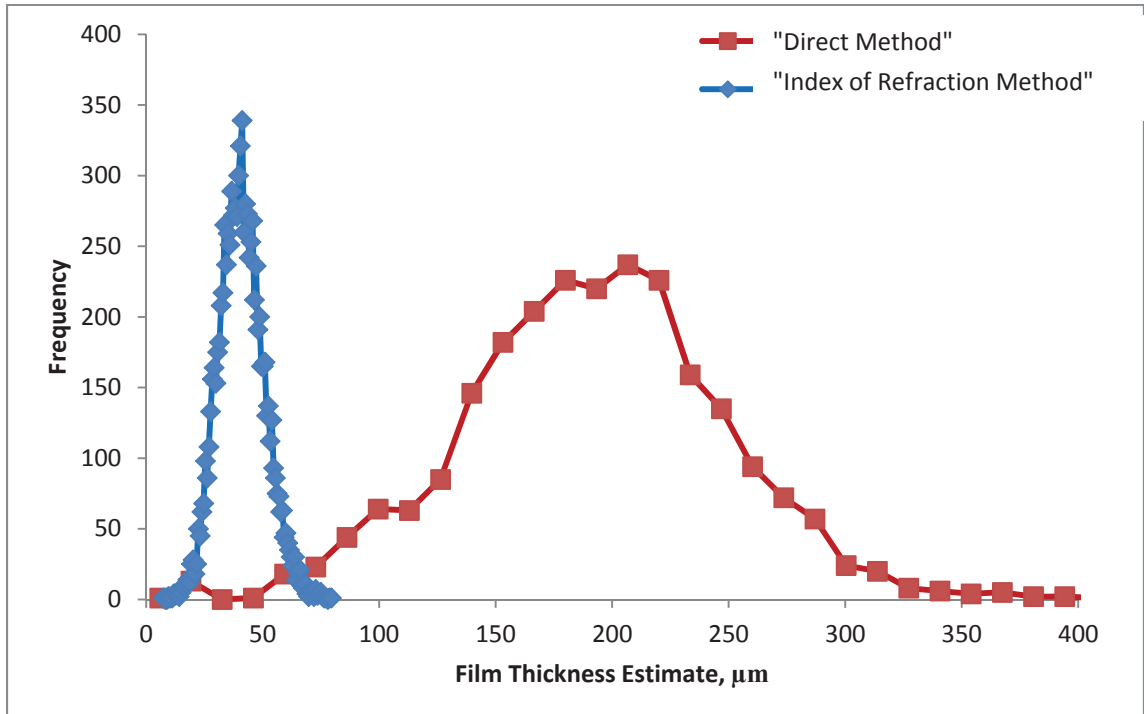


Figure 5-15: Histogram of Film Thickness Estimates for Each Method with Momentum Flux = 38,300 Pa and Liquid Film flow rate = .007 kg/s

Figure 5-13 shows that the average film thickness estimated from both methods are generally in very good agreement with each other at very low momentum fluxes, when the amount of entrained liquid is low. The peaks of the histograms for each method correspond very well with each other. However, “the index of refraction method” is not able to account for the wide variations in film thickness that the “direct method” was able to resolve. This is expected because in order for the “index of refraction method” to account for all the variations in film thickness, all the variations in surface angle and curvature would need to be accounted for when calculating δ_{ave}/f_{shift} . Yet, the average film thickness estimates obtained using both methods do agree very well with each other at low momentum fluxes. Therefore, it does appear as though the “index of refraction method” gives a valid approximation of the average film thickness for a test run, at least when momentum fluxes are low.

Figures 5-14 and 5-15 show that the film thickness estimates obtained from each method begin to deviate substantially from each other once the momentum flux of the gas phase, and therefore the entrained fraction, increases. The estimate of the average film thickness obtained using the “direct method” increases when the momentum flux is increased from 2,970 Pa in figure 5-13 to 7,750 Pa in figure 5-14. Then, there doesn’t seem to be a significant change in the histograms pertaining to the “direct method” between figures 5-14 and 5-15, yet the momentum flux is nearly tripled. On the other hand, the average film thickness predicted by the “index of refraction method” is seen to decrease with increasing momentum flux as one would expect. Thus, it appears as though the “index of refraction method” might be a more valid way to estimate the film thickness when the LFD is oriented such that the laser passes through the film before reflecting off the substrate.

From analysis of the LFD data, it appears as though the “Liquid Film Surface” data shown in Figure 5-8 does not actually correspond with the surface of the liquid film in most of the experiments as was assumed. Rather, it is speculated that the droplets that were stripped off the film seem to form a droplet heavy layer just above the film that scattered more light back to the LFD than what was reflected off of the liquid film surface. Therefore, orienting the LFD such that it measures the thickness of the liquid film by passing the laser beam through a transparent substrate, as shown in the left hand side of Figure 2-2, might be a better way to measure film thickness. This would avoid the issue of entrained droplets interfering with the laser beam.

5.4.4 Film Thickness Results Obtained Using the Index of Refraction Method During the November 2011 Tests

During the June 2011 tests, the film thickness data was too noisy to be useful due to the uncertain location of the substrate due to thermal expansion and pressure effects. In order to remedy this problem, it was decided to turn the film flow on for 30 seconds, then turn it off for 15-20 seconds, and then turn it back on again. This was repeated 5 times per test. By keeping the times during which the film thickness was measured

shorter, it was possible to accurately track the location of the substrate. This allowed for more accurate film thickness measurements and a substantial reduction in uncertainty. The 30 second time interval that the film was left on was found to be sufficient for data gathering purposes, and the 15-20 seconds that the film was left off was found to be a sufficient length of time to allow the substrate to dry and allow the LFD to obtain an accurate position of the substrate.

Figure 5-16 shows the raw LFD data during a typical run during the November 2011 tests. A comparison of the data shown in Figure 5-16 with the data shown in Figure 5-9 showed that position of the substrate was much more accurately known during the November 2011 tests than during the June 2011 tests. A best fit line was applied to the LFD position measurements that corresponded to a dry substrate. The difference between the raw LFD data and the best fit line was then found in order to determine f_{shift} . The position of a dry substrate is represented by the red data points in Figure 5-16.

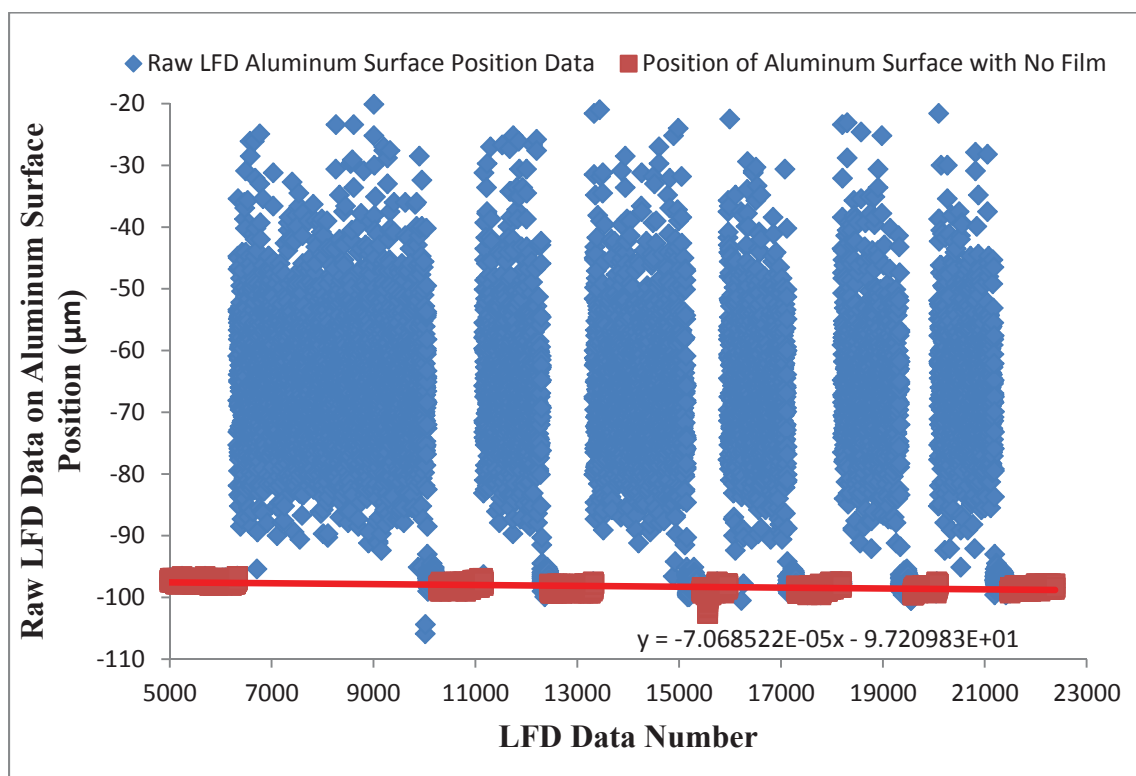


Figure 5-16: Raw LFD data for second series of tests

A histogram was then created for the difference between the LFD data and the best fit line for each test run. An example of such a frequency histogram is displayed in

figure 5-17. The histogram peaks around two positions. The first peak, around 0, corresponds to the position of the aluminum substrate. The second peak is the mean value for f_{shift} . The Raw LFD data and Frequency Histograms can be found for every test run in Appendix B.

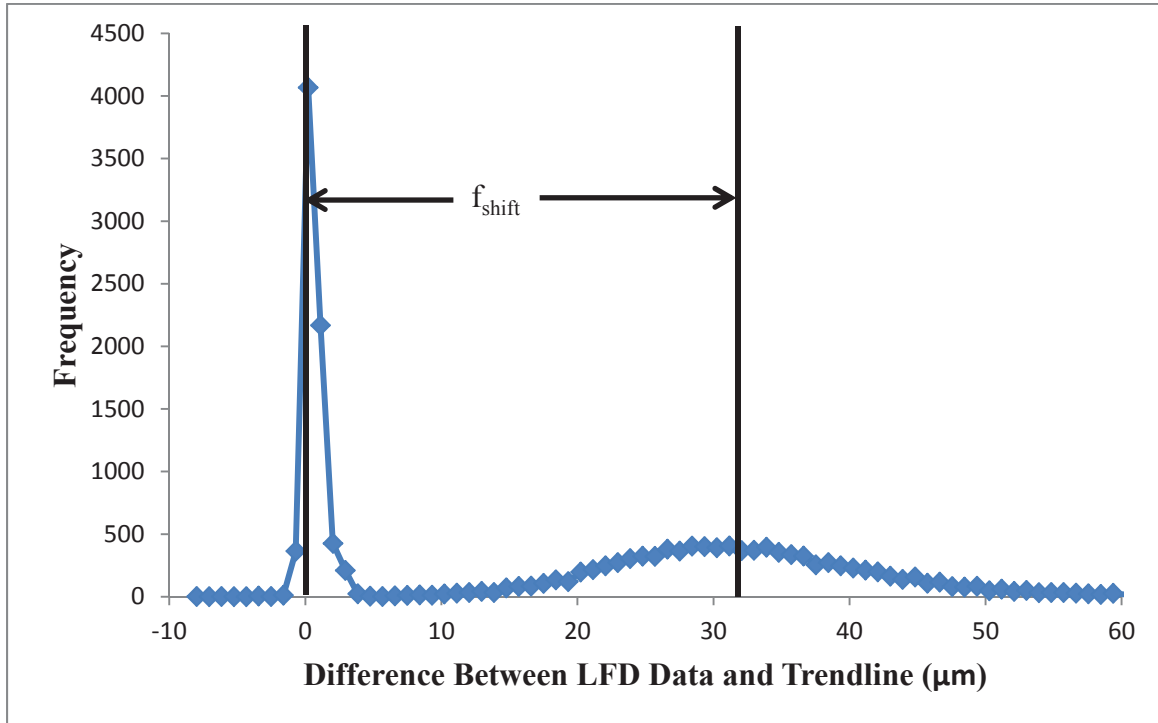


Figure 5-17: Example of a typical Frequency Histogram for the LFD data for the second round of testing

Using the procedure in the previous two paragraphs, the mean value of f_{shift} was determined for each gas phase momentum flux and injected liquid flow rate. The uncertainty in the mean value of f_{shift} was estimated to be $\pm 1.25 \mu\text{m}$ for each test run. For every experiment, the average film thickness was then calculated using the “index of refraction method” by multiplying f_{shift} by 3.9, which was the most common value for $\delta_{\text{ave}}/f_{\text{shift}}$. Upper and lower bounds for the film thickness were also calculated using the extremes of $\delta_{\text{ave}}/f_{\text{shift}}$, which was shown to vary from 3.0 to 4.05. The uncertainty in f_{shift} was taken into account when determining the upper and lower bounds.

Figure 5-18 shows a plot of the film thickness data as a function of the gas phase momentum flux and injected liquid flow rate. As previously mentioned, the upper and lower error bars for the film thickness data were determined using the extremes of

δ_{ave}/f_{shift} , with the uncertainty in f_{shift} taken into account. The film thickness is a function of both the injected liquid flow rate and the gas phase momentum flux. As momentum flux increases, the film thickness decreases. As the injected liquid flow rate increases, the film thickness also increases. It appears as though the film thickness approaches an asymptote as the momentum flux increases. The uncertainty in the film thickness is largely a result of the uncertainty in the film surface angle. The uncertainty in the momentum flux increases as momentum flux increases because the velocity was indirectly determined from knowledge of the mass flow rate, and this uncertainty increases with increasing momentum flux. The reader is referred to Appendix D for how the uncertainty in the gas phase momentum flux is derived. The uncertainty in the momentum flux could be reduced by either directly measuring the velocity of the gas phase, or through reducing the uncertainty in the cross-sectional area of the test section.

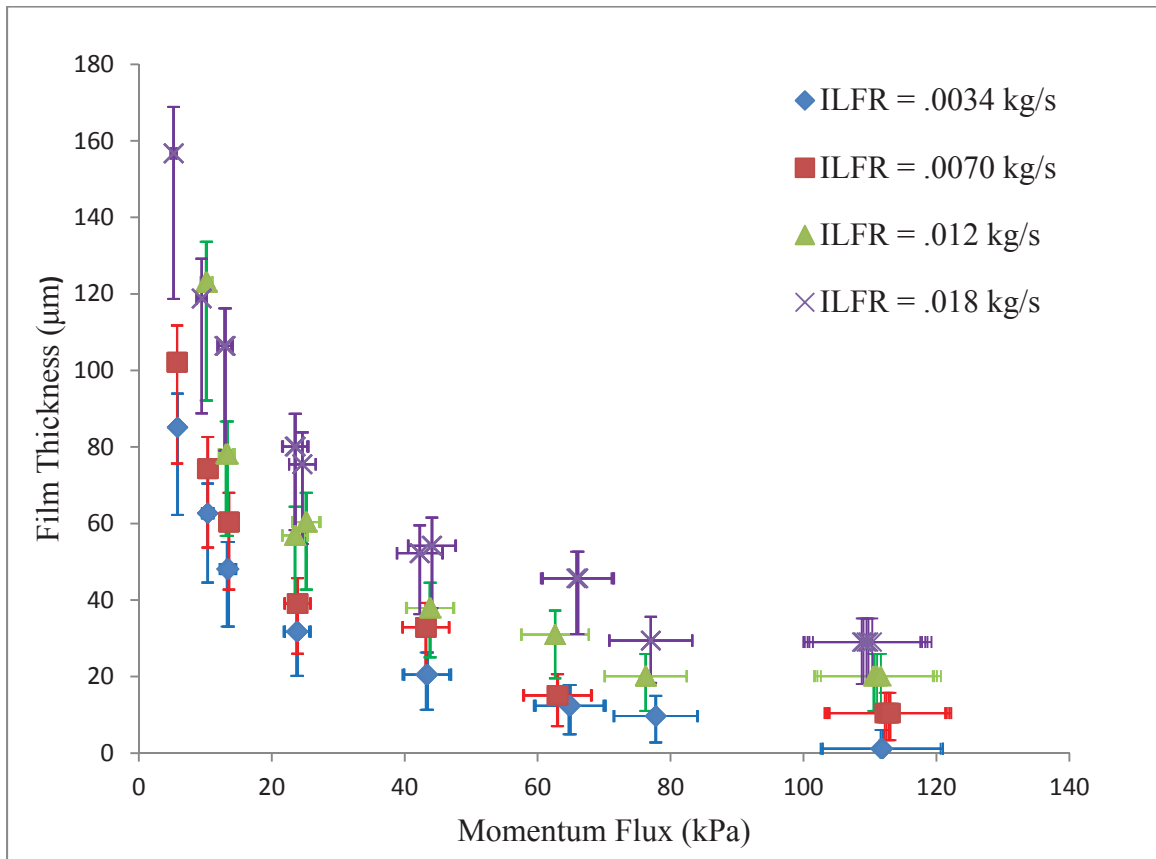


Figure 5-18: Film Thickness vs Momentum Flux

5.4.5 Comparison of Film Thickness Results

As a first attempt at validating the film thickness results, a film thickness model was created in Matlab. In order to place an upper bound on what the expected results should be, the film thickness estimated by equations 5-21 through 5-29 assumes that none of the film becomes entrained into the gas phase, and all of the film attaches itself to the wall. Thus, this film thickness model should provide an estimate of the maximum film thickness. The following assumptions were implemented in deriving the film thickness model described by equations 5-21 through 5-29:

- 1) Laminar flow within liquid film
- 2) Liquid film flow driven by interfacial shear stress
- 3) No waves on the surface of the film. To account for the roughness caused by the waves, a friction factor correlation was implemented using equation 5-22.
- 4) Gravity has a negligible influence on the flow
- 5) Steady, two-dimensional flow
- 6) The film is an incompressible fluid

In order to estimate the shear stress at the film's surface, which is the force that drives the film, an interfacial friction factor can be estimated according to [1]:

$$f = f_{smooth} \left(1 + 24 \left(\frac{\rho_l}{\rho_g} \right)^{1/3} \left(\frac{\delta}{D_H} \right) \right) \quad (eq\ 5 - 22)$$

where f_{smooth} is the friction factor corresponding to a smooth wall. This variable can be estimated with [37]:

$$f_{smooth} = .046 Re_D^{-1/5} \quad (eq\ 5 - 23)$$

The interfacial shear stress can then be calculated according to:

$$\tau_i = \frac{1}{8} f \rho_g V_g^2 \quad (eq\ 5 - 24)$$

In laminar flow, the velocity profile is:

$$u_l = Con \cdot y \quad (eq\ 5 - 25)$$

The shear stress is constant throughout the liquid film and equal to:

$$\tau = \mu \frac{du_l}{dy} \quad (eq\ 5 - 26)$$

The velocity gradient in the liquid film is also constant:

$$\frac{du_l}{dy} = Con \quad (eq\ 5 - 27)$$

Therefore, the unknown constant in equation 5-26 can be calculated according to:

$$\tau_i = \mu \cdot Con \quad (eq\ 5 - 28)$$

The mass flow rate per unit of film width can be calculated according to the following continuity equation:

$$\dot{m}'_l = \rho \int_0^\delta Con \cdot y \, dy \quad (eq\ 5 - 29)$$

Integrating, we can then derive an equation that can be used to relate the film thickness to the film mass flow rate per unit width:

$$\dot{m}'_l = \frac{1}{2} \rho_l \cdot Con \cdot \delta^2 \quad (eq\ 5 - 30)$$

For each test case, the film thickness was estimated assuming that none of the liquid was entrained into the gas phase. Because no entrainment was assumed in arriving at this estimate, this estimate should be greater than the results for the same conditions, and thus place an upper bound on the data.

In Figure 5-19 the film thickness estimates obtained from equations 5-22 through 5-30 are compared to the film thickness data gathered by the LFD using the “index of refraction method.” In all cases, the film thickness estimates are higher than the experimental data which is expected because no entrainment was assumed when calculating these estimates. Secondly, the estimates generally follow the same trend as the experimental data. This imparts confidence to the data collected by the LFD and the “index of refraction method.” In addition, if the interfacial shear stress and/or film mass flow rate measurements could be accurately measured in future experiments, then the model above could be modified to predict film thicknesses based on the gas momentum flux and injected liquid flow rate. The small amount of scatter in the simulation results from the fact the numerical code used to solve equations 5-22 through 5-30 occasionally converged on slightly different results for similar test conditions. This could be improved by choosing more selective convergence criteria. However, the convergence criteria that were chosen to solve those equations were convenient for the programs and computational power available to the author.

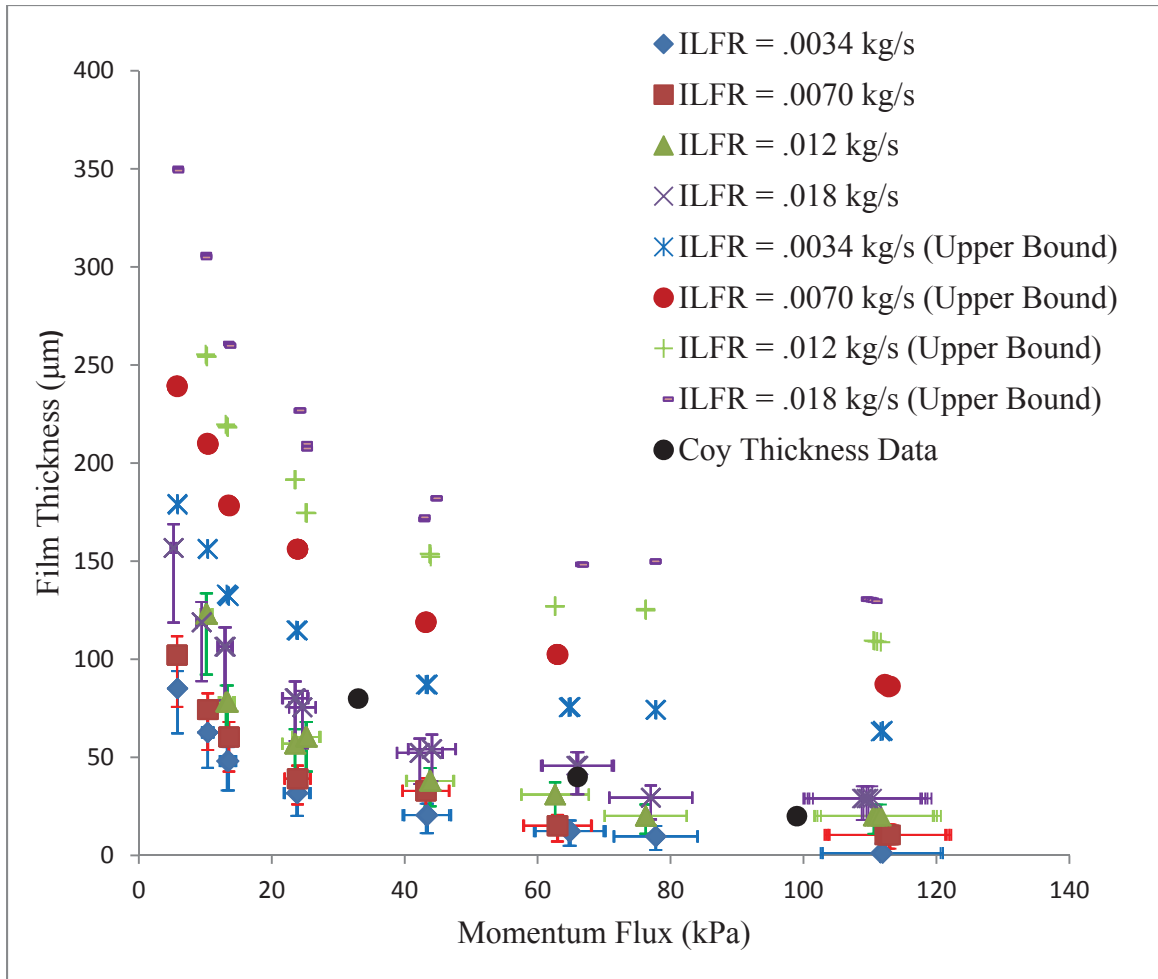


Figure 5-19: Results Compared with the Upper Bound Calculations and Coy et al [1]

Film thickness data obtained from Coy et al [1] is also compared to the experimental data in Figure 5-19. Wegener [5] also measured the film thickness of shear-driven liquid films using an LFD, but none of fluids in Wegener's experiments were liquid water. However, the film thicknesses measured by Wegener were of the same order of magnitude as the film thicknesses measured in this thesis for momentum fluxes less than 10 kPa. Finally, the data from Coy et al [1] matches the data in this thesis pertaining to the upper flow rates fairly closely. However, the data obtained from Coy et al [1], does not account for the dependence of the film thickness on the injected liquid flow rate, which results from the fact that Coy et al [1] did not observe a dependence of the velocity of the surface disturbances on the injected liquid flow rate. Nonetheless, the

method used for estimating the liquid film thickness in Coy et al [1] appears to offer a good order of magnitude approximation for estimating film thickness.

5.5 High Speed Video Results

During the November 2011 tests, 11 additional tests were run in which the film thickness was not measured, and a high speed video camera was the primary diagnostic. The objective of these tests was to observe how features or structures that form on the surface of a liquid film are related to the injected liquid flow rate and momentum flux of the gas phase. Several researchers have observed that the types of waves that form on a liquid film are related to the entrainment and the atomization rate. The film thickness was not measured during these tests because the LFD measuring unit would obstruct the view of the camera. Figures 5-20 through 5-22 show high speed video images of the surface of the liquid film at several different injected liquid flow rates and gas phase momentum fluxes. Unfortunately, due to time constraints, it was not possible to take high speed video images for every test condition. In particular, images corresponding to momentum fluxes greater than 30,000 Pa are lacking. However, from the 11 images that are represented here, it is still possible to draw qualitative conclusions regarding the behavior of shear-driven liquid films.

In all 11 images, there are 2 prominent surface features that can be observed on the liquid film. One of the surface features are the pebble like disturbances, or ripples, which are called out in figures 5-20 through 5-22 by the green arrows and circles. The other features, the disturbance waves, are called out by yellow arrows and circles.

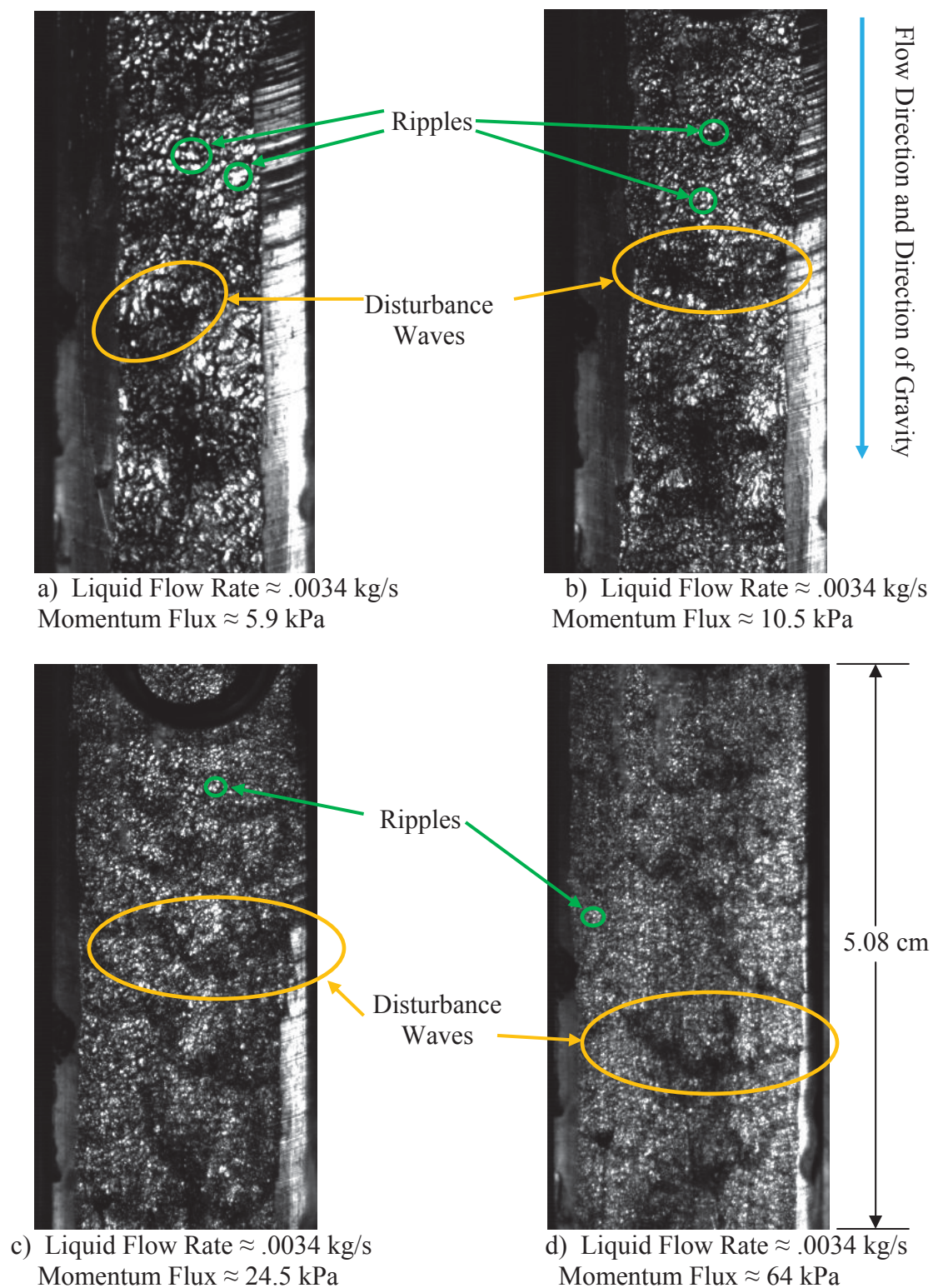


Figure 5-20: High Speed Video Images of the Film for Lowest Liquid Flow Rates.

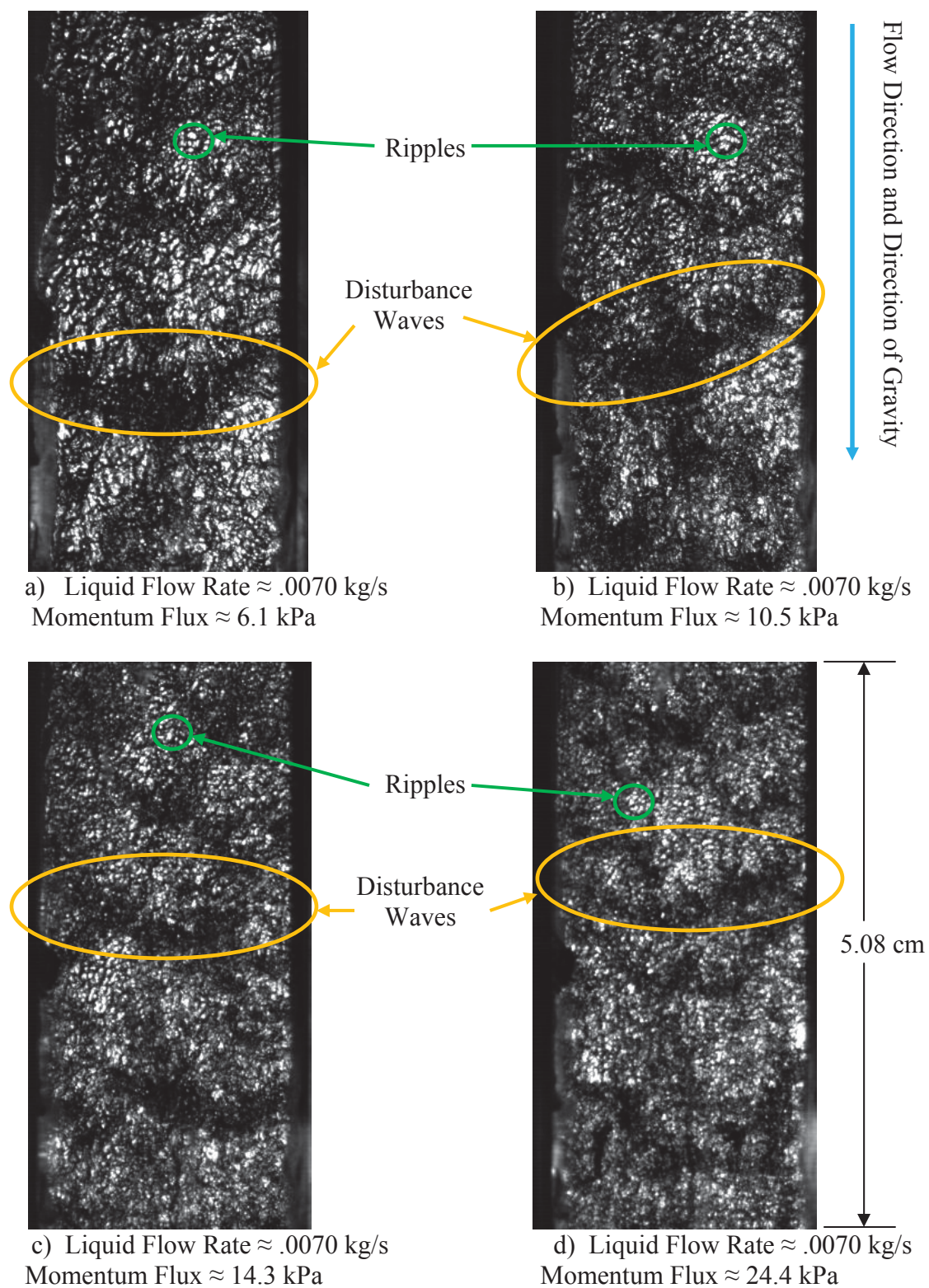


Figure 5-21: High Speed Video Images of the Liquid Film for .0154 kg/s Liquid Flow.

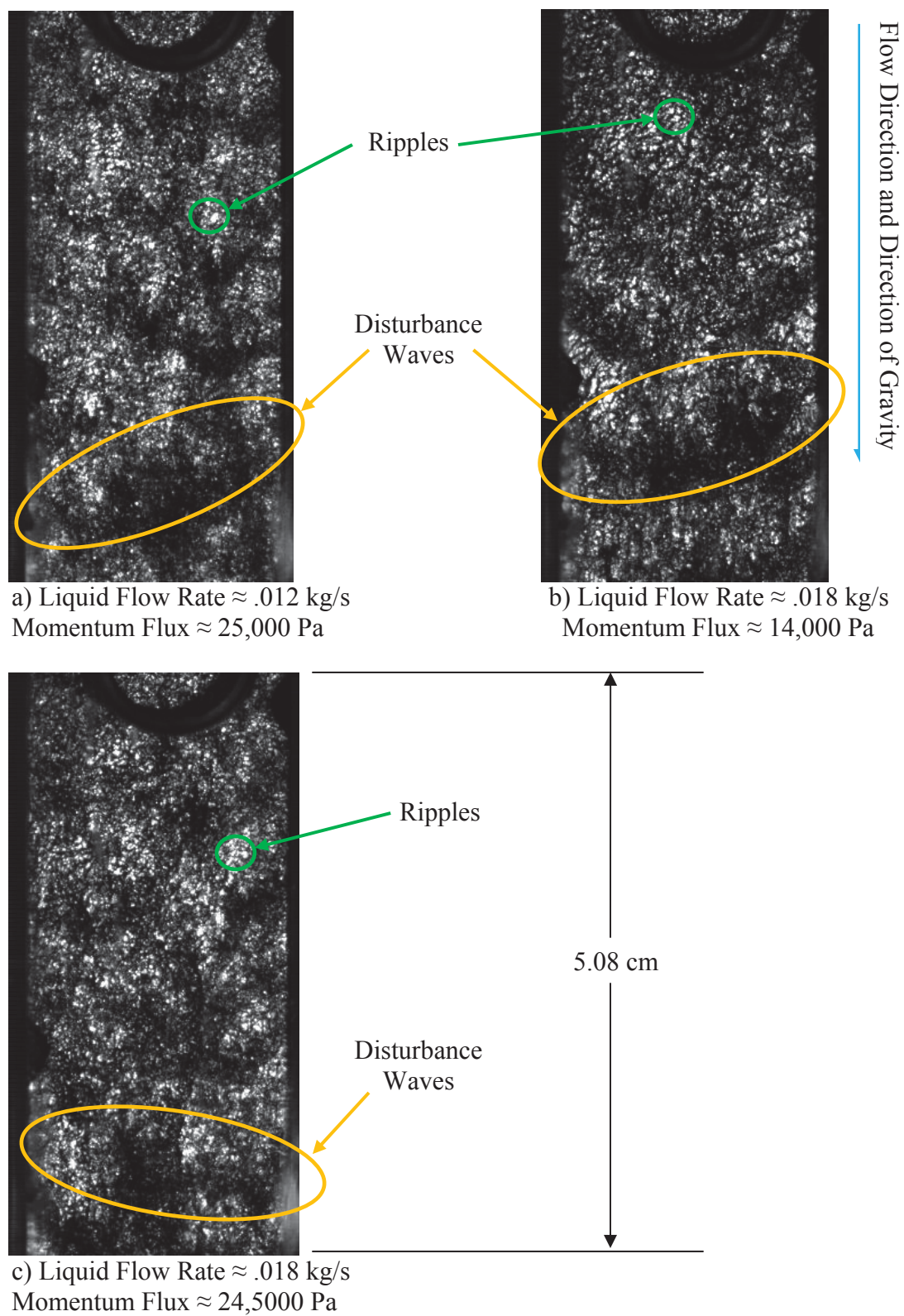


Figure 5-22: High-Speed Video Images of the Film for High Liquid Flow Rates

Figure 5-20 shows photographs for the lowest injected liquid flow rate and 4 different gas phase momentum fluxes. Inspection of the four images reveals that the granular surface ripples become smaller as the momentum flux increases. At low momentum fluxes, the surface tension in the film appears to be able to overcome the momentum forces in the gas and pull the film away from the sidewalls of the test article. As momentum flux increases, the film covers a greater portion of the bottom wall of the test article, indicating that the momentum forces of the gas phase overcome surface tension. In addition, by comparing Figure 5-20a with Figure 5-20d, the disturbance waves in figure 5-20d are darker, more well-defined, and easier to see than the disturbance waves in Figure 5-20a. Thus, as the momentum flux increases, the disturbance waves seem to grow and become more pronounced in relation to the ripples.

Figure 5-21 shows photographs for the second lowest liquid flow at .0070 kg/s. Again, it is observed that increasing the momentum flux decreases the size of the ripples and makes the disturbance waves more distinct, which can be observed by comparing the size of the ripples in Figure 5-21a with the size of the ripples in Figure 5-21d. The liquid flow rates for the images in figure 5-21 are all higher than the flow rates in figure 5-20. At these higher flow rates, the film is able to span most of the channel.

Figure 5-22 shows similar trends as observed in figures 5-20 and 5-21. Increasing the momentum flux decreases the size of the ripples and creates greater disturbance waves. At the flow rates in this figure, the film is observed to never pull away from the side walls.

The films in figures 5-20a and 5-21a are both exposed to the same momentum flux, but are at different liquid flow rates. The size of the ripples and the disturbance waves appear to be very similar in each image. Thus, it would appear as though the surface behavior of a shear driven liquid film is primarily dependent on the momentum flux of the gas phase. Comparing figure 5-20b with 5-21b and also comparing figures 5-20c, 5-21d, 5-22a, and 5-22c with each other supports this conclusion. These observations also agree with the observations in Gater's [17] experiments. A possible explanation for these phenomena is that the aerodynamic forces acting on the surface of

the liquid film are all proportional to the momentum flux of the gas phase, as explained in chapter 1.

While it is not possible to show the videos themselves here, one particular observation should be noted from the videos. In the videos, the large disturbance waves appear to coalesce with one another as they move downstream. This most likely results from a wake that forms downstream of the waves [38]. As explained earlier, the gas phase exerts a drag force on the wave crests, which results in a wake that forms downstream of the waves [38]. This wake creates a region of lower pressure downstream of the wave, which can potentially reduce the aerodynamic forces acting on downstream waves, slowing them down relative to the upstream waves [38]. As a result, the waves that form upstream are able to overtake the downstream waves and grow larger [38].

CHAPTER 6: CONCLUDING REMARKS AND RECOMMENDATIONS FOR FUTURE WORK

A study was made of shear driven liquid films injected by a thin perpendicular slot in order to better understand that factors that govern the establishment of a film along a wall for liquid film cooling applications in rocket engines. One of the main objectives of this study was to investigate the establishment of a shear driven liquid film introduced into a rectangular test section by a .38 mm X 25.4 mm perpendicular slot. The second objective of the study was to investigate the ability of different experimental techniques to elucidate the mechanics of shear-driven liquid films.

In pursuit of this endeavor, an acrylic test article consisting of a rectangular channel was constructed. Nitrogen gas was run through the rectangular section at momentum fluxes ranging from about 2,000 Pa to 110,000 Pa. Liquid water was injected through one wall into the test section by means of a perpendicular .38 mm X 25.4 mm slot. A second slot, .76 mm X 25.4 mm and angled at 25° with respect to the surface of the test article, placed 139.7 mm downstream of the first slot attempted to remove the film via suction. The mass flow rate of nitrogen was metered using a sonic nozzle and the mass flow rate of liquid water was metered by means of a cavitating venturi. The static pressure and temperature of nitrogen flowing into the test article was also measured using a pressure transducer and thermocouple, respectively. Measurements of the film mass flow rate were attempted using the film removal slot, measurements of the pressure drop were attempted using a differential pressure transducer, and measurements of the film thicknesses were attempted using an LFD. Finally, a Vision Research Phantom v7.3 high speed video camera was used to obtain qualitative images of the film's surface.

The results from this experiment suggest that the entrainment fraction increases with both increasing injected liquid flow rate and momentum flux of the gas phase. However, the film removal slot failed to completely remove the film. Therefore, more work needs to be done in order to determine the mass flow rate that remains attached to

the wall after being injected. In addition, the correlations for the entrainment fraction from a liquid film do not correlate well with the experimental data or each other at the momentum fluxes and liquid flow rates studied in this experiment. The correlation from Gater and L'Ecuyer agrees with the experimental data better than the other correlations, however, it fails to account for the observed dependence of the entrainment fraction on the injected liquid flow rate. Other researchers [15], [20] have noted that there might have been problems technique of using a film removal slot to measure the liquid flow rate that remained attached to the wall in Gater and L'Ecuyer. Therefore, due to the problems encountered in both this experiment and the experiments of Gater and L'Ecuyer, it appears as though using a slot is not the best method to measure the entrainment fraction from the liquid film and it appears to be very difficult to get it to work correctly. For future experiments, it might be more advantageous to remove the film via suction through a porous section of the substrate. It would be optimal if a non-intrusive technique could be used to film mass flow rate, however, such as a PDPA.

The liquid film thickness was shown to digressively decrease with increasing momentum flux and increase with increasing injected liquid flow rate. The trends from the experimental data of how the liquid film thickness varies with the momentum flux follow the same trends displayed by the computational estimates. The liquid film thicknesses were shown to vary between about 5 to 160 μm , with a relative uncertainty of approximately 25% for most of the measurements. More research is needed to find a way to reduce the uncertainty in the film thickness estimates.

One of the objectives of this experiment was to qualify the LFD as a means of measuring the thicknesses of shear driven liquid films driven by gas phase momentum fluxes exceeding 10,000 Pa. In previous experiments, the LFD was used to measure the thickness of the liquid film by directly detecting the thickness of the film surface. A new method for measuring the thickness of shear driven liquid films using the LFD was proposed because the original method did not work. During the experiments, the LFD was always able to receive a strong reflection off of the aluminum surface, even when there was a film between the substrate and the LFD. When the film was turned on, the location of the aluminum substrate appeared to change position due to refraction of

the laser beam as it passed through the film. With knowledge of the substrate's location when the film is dry, the film thickness could be estimated by relating the apparent change in position of the substrate to the film thickness. This method would be useful for situations in which an LFD is chosen to measure the film thickness and the substrate is opaque.

The film thicknesses determined using the "index of refraction method" are in the range predicted by previous experiments and appear to follow the trends predicted by models. Therefore, the technique does show promise for being able to measure time-averaged film thicknesses. However, this technique has several limitations. First, the technique is dependent on the shape of the film surface, which is difficult to determine. Second, droplets being stripped off and entrained from the film interfere with the beam and direct detection of the film surface. Third, it is very important that the location of the substrate over be known while the film thickness is being measured. This makes control of a test articles temperature very important and therefore makes experiments more difficult. Due to the uncertainty in the measurements that these limitations create, more experiments still need to be done in order to qualify the LFD's ability to measure liquid film thicknesses under highly turbulent flow conditions and verify the film thickness results.

The surface angle of the liquid film has an effect on the light intensity of the light intensity of reflection of the LFD laser off the aluminum substrate. As the surface angle of the liquid film increases, the light intensity decreases. Therefore, in future experiments, measures should be taken to record the light intensity of the LFD as well as the position measurements. The light intensity information may give information of the surface angle of the liquid film.

Due to time constraints, shear stress estimates were attempted by measuring the pressure drop. However, the author was not confident in the pressure drop results because there appeared to a problem with the plumbing and instrumentation used to measure the pressure drop. The source of the problems was never deduced. Due to the sensitivity of the pressure taps to imperfections in the flow and the fluid entrained, it is not recommended that they be used as the means to estimate the interfacial shear stress.

With more work, analysis, and better knowledge of the droplet size distribution and entrainment fraction, pressure drop measurements could eventually prove to be an effective way at determining the interfacial shear stress. However, other techniques, such as measuring the velocity profile above the film or using heat or mass transfer probes could provide more accurate results.

In future experiments, it is recommended that the velocity profile of the gas phase above the film be measured either with a PDPA or some other non-intrusive measurement technique. Knowledge of the velocity profile would not only allow the momentum flux to be more accurately known, but it would also show how well the flow has been straightened and if there are any other secondary flow structures that might be affecting the data. In addition, it would also allow the interfacial shear stress to be calculated using a turbulence model.

The film thickness was only measured at a single location in this experiment. As shown by Wegener [5], the average film thickness varies across the width of the film, which can result from surface tension effects, variations in the substrate, or secondary flow structures. While the experiments in this thesis were primarily concerned with how much film was entrained directly at the slot, it may be of interest to determine the film thickness at several downstream locations in order to achieve a better understanding of the mechanics of shear driven liquid films at rocket-level momentum fluxes. Therefore, in future experiments, it is recommended that film thickness be measured both across the width at the film and at several downstream locations.

To the best of the author's knowledge the gas phase momentum fluxes in all experiments that have investigated entrainment from shear driven liquid films have been an order of magnitude less than the momentum fluxes typically found in liquid rocket engines. It would be beneficial if the gas phase momentum fluxes in future experiments exceed 1 MPa, so that the results will be more applicable to film cooling in rocket engines.

Fluid properties, such as viscosity and surface tension need to be varied in future experiments. Nitrogen was the only gas used in this experiment and water the only liquid film. It was desired to vary the fluid properties more, however, time and facility

constraints made this infeasible. Although other experimenters have tried to vary the film properties in similar experiments [6], [9], [17], the data is thus far limited and inclusive.

More slot geometries need to be investigated in order to identify their effect on the entrainment from the liquid film. Efforts should be taken to decouple effects from droplet entrainment right at the injection point from additional entrainment due to atomization as the film progresses downstream. Finally, the test sections in future experiments should be long enough such that a steady state may be determined. In addition, the film thickness, shear stress and entrainment measurements should be taken at several different locations downstream of the slot in order to determine the evolution of the film.

LIST OF REFERENCES

1. Coy, E. B., Schumaker, S. A., Lightfoot, M. A., "Film Cooling of Liquid Hydrocarbon Engines for Operationally-Responsive Space Access," *JANNAF 5th Liquid Propulsion Subcommittee Meeting*, Colorado Springs, CO, May 2009
2. Tibirica, C. B, Nascimento, F. J., Ribatski, G., "Film Thickness Measurement Techniques Applied to Micro-Scale Two-Phase Flow Systems," *Experimental Thermal and Fluid Science*, Vol. 34, 2010, 463-473
3. Hazuku, T., Fukamachi, N., Takamasa, T., Hibiki, T., Ishii, M., "Measurement of Liquid Film in microchannels using a laser focus displacement meter," *Experiments in Fluids*, Vol. 38, No. 6, 2005, pp. 780-788
4. Wegener, J. L., Drallmeier, J. A., "Measurement of Thin Liquid Film Characteristics using Laser Focus Displacement Instruments for Atomization Applications," *ILASS-Americas 22nd Annual Conference on Liquid Atomization and Spray Systems*," Cincinnati, OH, May 2010
5. Wegener, J. L, *Experiments and Modeling of Shear-Driven Film Separation*, M.S. Thesis, Missouri University of Science and Technology, 2009
6. Ebner, J., Gerendás, M., Schäfer, O., Wittig, S., "Droplet Entrainment From a Shear-Driven Liquid Wall Film in Inclined Ducts: Experimental Study and Correlation Comparison," *Journal of Engineering for Gas Turbines and Power*, Vol. 124, No. 4, Oct. 2002, pp. 874-880
7. Lightfoot, M. D. A., "Fundamental Classification of Atomization Processes," *Atomization and Sprays*, Vol. 19, No. 11, 2009, pp. 1065 – 1104
8. Deissler, R. G., *Turbulent Fluid Motion*, Philadelphia, Taylor & Francis, 1998
9. Kinney, G. R., Abramson, A., E., Sloop, J. L. "Internal Liquid Film Cooling Experiments with Air-Stream Temperature to 2000°F in 2- and 4-Inch Diameter Horizontal Tubes," NACA Report 1087, 1952

10. Sawant, P., Ishii, M., Mori, M., "Prediction of amount of entrained droplets in vertical annular two-phase flow," *International Journal of Heat and Fluid Flow*, Vol. 30, No. 4, Aug. 2009, pp. 715-728
11. Ishii, M., Grolmes, M. A., "Inception Criteria for Droplet Entrainment in Two-Phase Concurrent Film Flow," *AIChE Journal*, Vol. 21, No. 2, Mar. 1975, pp. 308-318
12. Cioncolini, A., Thome, J. R., "Prediction of the Entrained Liquid Fraction in Vertical Annular Gas-Liquid Two-Phase Flow," *International Journal of Multiphase Flow*, Vol. 36, 2010, pp. 293-302
13. Ito, J., Aerojet, personal communication, January, 2012
14. Chehroudi, B., Talley, D., Coy, E., "Visual Characteristics and Initial Growth Rates of Round Cryogenic Jets at Subcritical and Supercritical Pressures," *Physics of Fluids*, Vol. 14, No. 2, Feb. 2002, pp. 850-861
15. Yu, Y. C., Schuff, R. Z., Anderson, W. E., "Liquid Film Cooling Using Swirl in Rocket Combustors," *40th AIAA/ASME/SAE/ASEE Joint Propulsion Conference and Exhibit*, American Institute of Aeronautics and Astronautics, July 2004, AIAA 2004-3360
16. Knuth, E. L., "The Mechanics of Film Cooling- Part 1," *Jet Propulsion*, Vol. 24, No. 6, 1954, pp. 359-365
17. Gater, R., A., L'Ecuyer, M. R., "A Fundamental Investigation of the Phenomena that Characterize Liquid Film Cooling," Jet Propulsion Center, TM-69-1, Jan. 1969
18. Warner, C. F., Reese, B. A., "Investigation of the Factors Affecting the Attachment of a Liquid Film to a Solid Surface," *Jet Propulsion*, Vol. 27, No. 8, pp. 877-881
19. Lightfoot, M. D. A., Air Force Research Laboratory, personal communication, September, 2010
20. Grissom, W., M., "Liquid Film Cooling in Rocket Engines," Arnold Engineering Development Center, AEDC-TR-91-1, Mar. 1991

21. Volkmann, J. C., McLeod, J. M., Claflin, S. E., "Investigation of Throat Film Coolant for Advanced LOX/RP-1 Thrust Chambers," *AIAA/SAE/ASME/ASEE 27th Joint Propulsion Conference*, Sacramento, CA, June 1991, AIAA 91-1979
22. Kirchberger, C., Schlieben, G., Hupfer, A., Kau, H., "Investigation on Film Cooling in a Kerosene/ GOX Combustion Chamber," *45th AIAA/ASME/SAE/ASEE Joint Propulsion Conference & Exhibit*, Dever, CO, August, 2009, AIAA 2009-5406
23. Kirchberger, C., Schlieben, G., Hupfer, A., Kau, H., "Film Cooling Investigations in a Kerosene/ GOX Combustion Chamber," *47th AIAA/ASME/SAE/ASEE Joint Propulsion Conference & Exhibit*, San Diego, CA, August 2011, AIAA 2011-5777
24. Olieman, R. V. A., Pots, B. F. M., Trompe, N., "Modelling of Annular Dispersed Two-Phase Flow in Vertical Pipes," *International Journal of Multiphase Flow*, Vol. 12, No. 5, pp. 711-732, 1986
25. Schober, P., Ebner, J., Schäfer, O., Wittig, S., "Experimental Study on the Effect of a Strong Negative Pressure Gradient on a Shear-driven Liquid Fuel Film,"
26. Ebner, J., Schober, P., Schäfer, O., Wittig, S., "Modelling of Shear-Driven Liquid Wall Films on Curved Surfaces: Effect of Accelerated Air Flow and Variable Film Load,"
27. Friedrich, M. A., Lan, H., Wegener, J. L., Drallmeier, J. A., Armaly, B. F., "A Separation Criterion With Experimental Validation for Shear-Driven Films in Separated Flow," *Journal of Fluids Engineering*, Vol. 130, May 2008, pp. 051301-1 to 051301-9
28. Sawant, P., Ishii, M., Hazuku, T., Takamasa, T., Mori, M., "Properties of Disturbance Waves in Vertical Annular Two-Phase Flow," *Nuclear Engineering and Design*, Vol. 238, 2008, pp. 3538-3541
29. Hanratty, T. J., Campbell, J. A., "Measurement of Wall Shear Stress," *Fluid Mechanics Measurements*, 2nd ed., edited by R. J. Goldstein, Philadelphia, Taylor & Francis, 1996, pp. 575-637

30. Coy, E. B., Air Force Research Laboratory, personal communication, September 2010 - May 2012
31. Hewitt, G. F., "Film Flow Rate and Entrainment," *Handbook of Multiphase Systems*, edited by G. Hestoni, New York, Hemisphere Publishing Corporation, 1982, pp. 10-61 to 10-67
32. Incropera, F. P., Dewitt, D. P., Bergman, T. L., Lavine, A. S., *Fundamentals of Heat and Mass Transfer*, 6th ed., Hoboken, NJ, John Wiley & Sons, 2007, pp. 941-945
33. Incropera, F. P., Dewitt, D. P., Bergman, T. L., Lavine, A. S., *Fundamentals of Heat and Mass Transfer*, 6th ed., Hoboken, NJ, John Wiley & Sons, 2007, pg. 949
34. Incropera, F. P., Dewitt, D. P., Bergman, T. L., Lavine, A. S., *Fundamentals of Heat and Mass Transfer*, 6th ed., Hoboken, NJ, John Wiley & Sons, 2007, pp. 376-377, 402-412, 528-529, 901
35. Massman, W. J., "A Review of the Molecular Diffusivities of H₂O, CO₂, CH₄, CO, O₃, SO₂, NH₃, N₂O, NO, and NO₂ in Air, O₂ and N₂ Near STP," *Atmospheric Environment*, Vol. 32, No. 6, 1998, pp. 1111-1127
36. Halliday, D., Resnick, R., Walker, J., *Fundamentals of Physics*, 7th ed., Hoboken, NJ, John Wiley & Sons, 2006, pg. 906.
37. Wilkie, D., Cowin, M., Burnett, P., Burgoyne, T., "Friction Factor Measurements in a Rectangular Channel with Walls of Identical and Non-Identical Roughness," *International Journal of Heat and Mass Transfer*, Vol. 10, 1967, pp. 661-621
38. Mudawwar, I., "Interfacial Instabilities of Air-Driven Liquid Films," *International Communications in Heat and Mass Transfer*, Vol. 13, 1986, pp. 535-543

APPENDIX

Appendix A: Dimensioned Drawings of Test Article

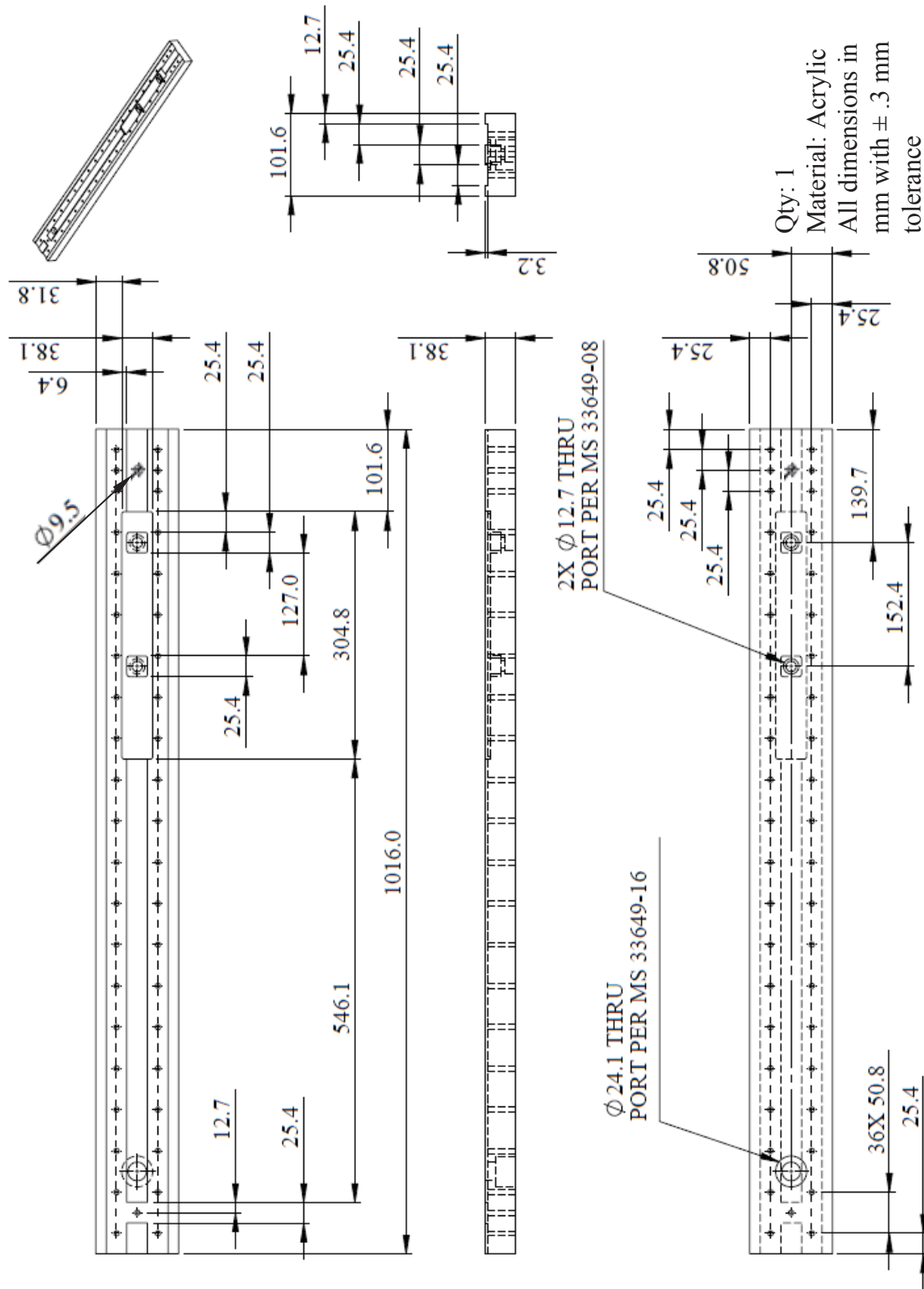
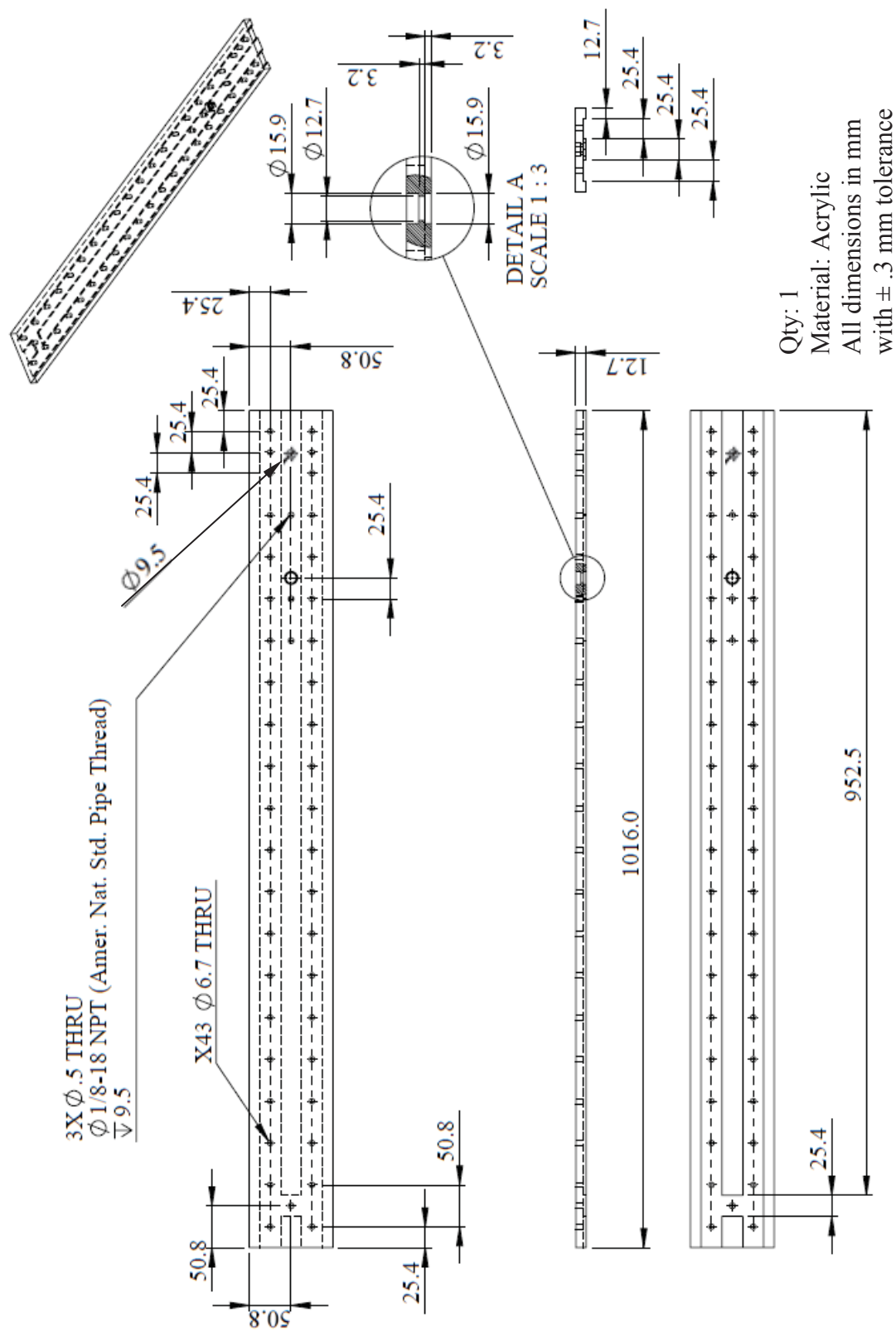
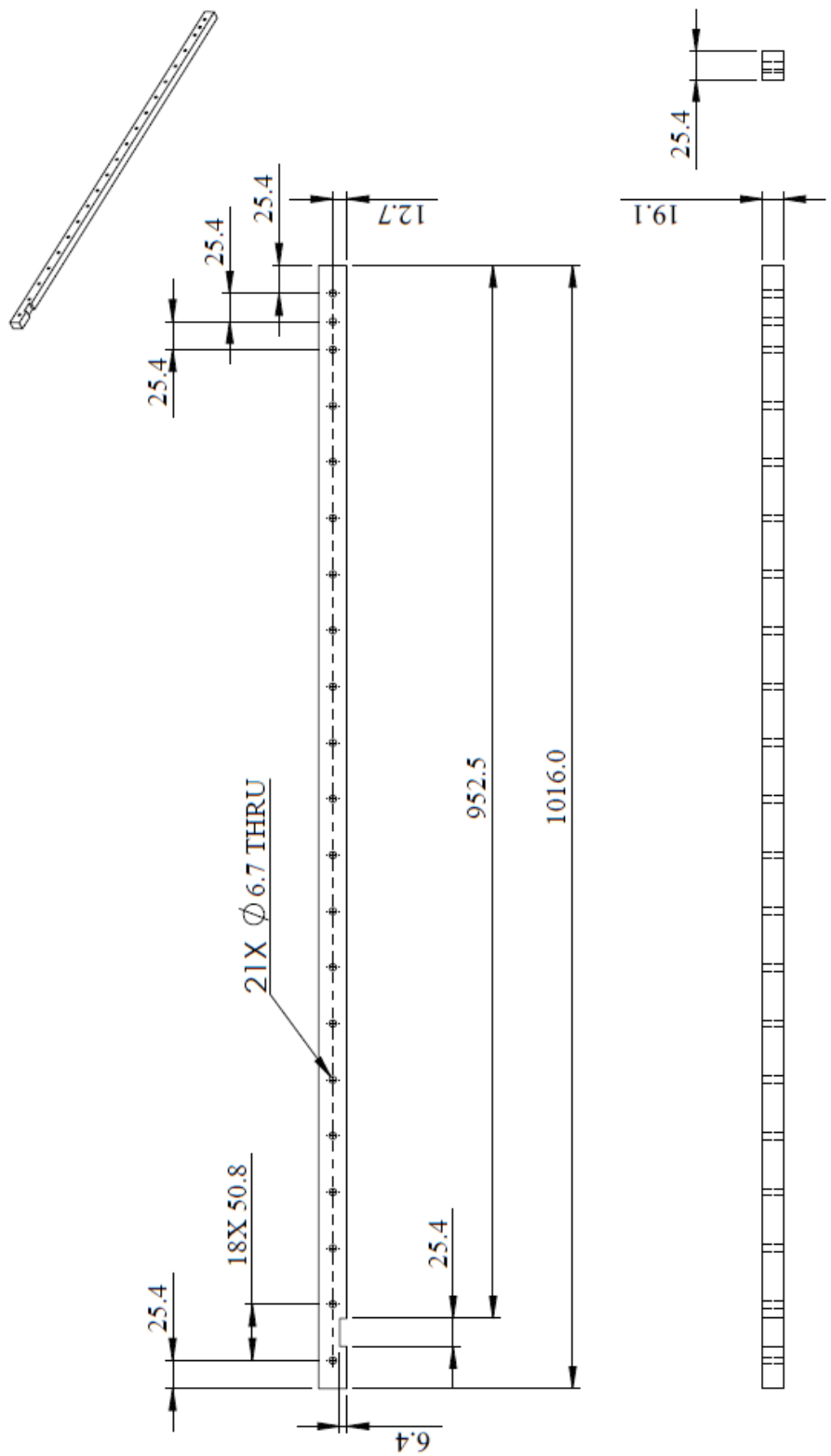


Figure A-1: Test Article Bottom

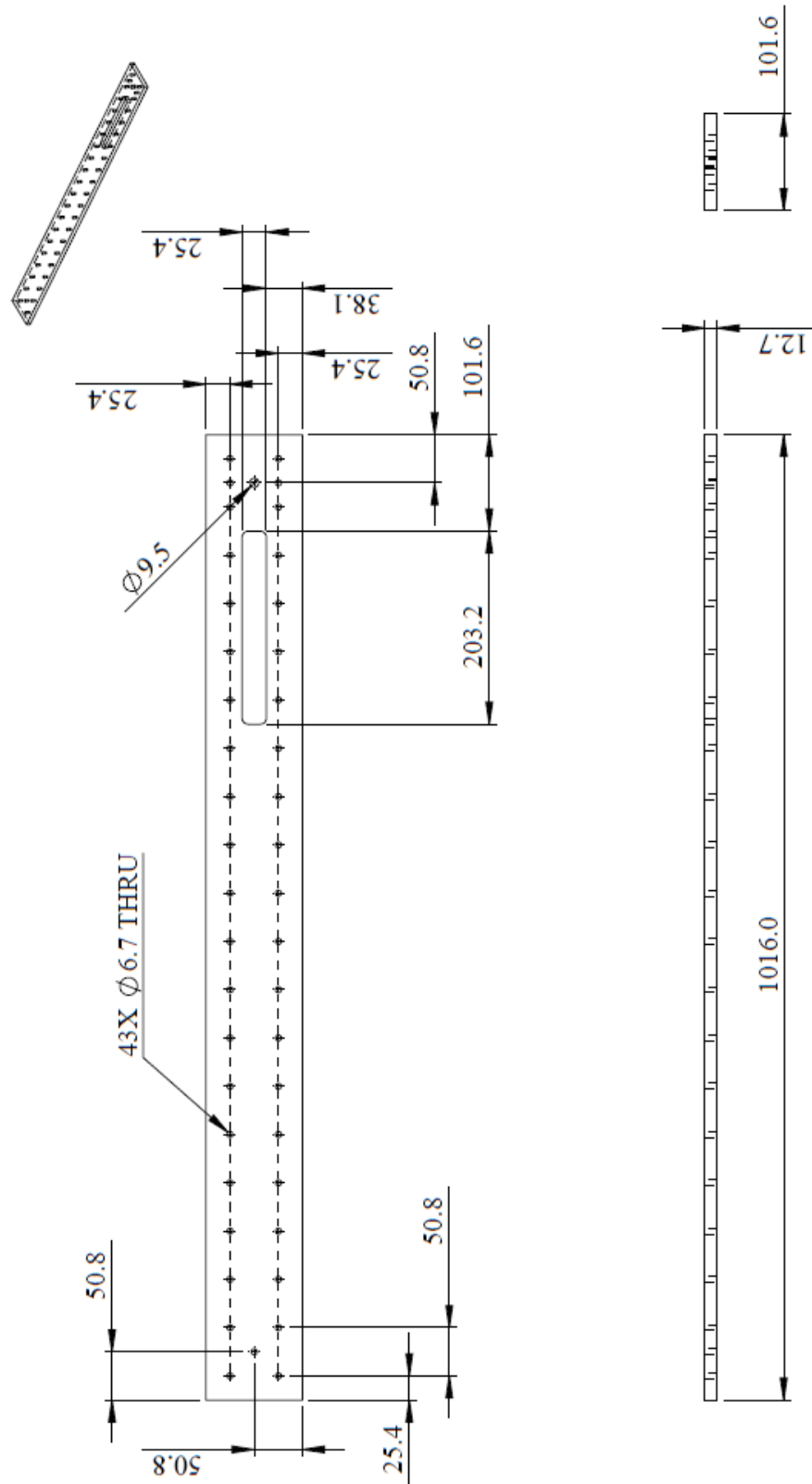


Qty: 1
Material: Acrylic
All dimensions in mm
with $\pm .3$ mm tolerance



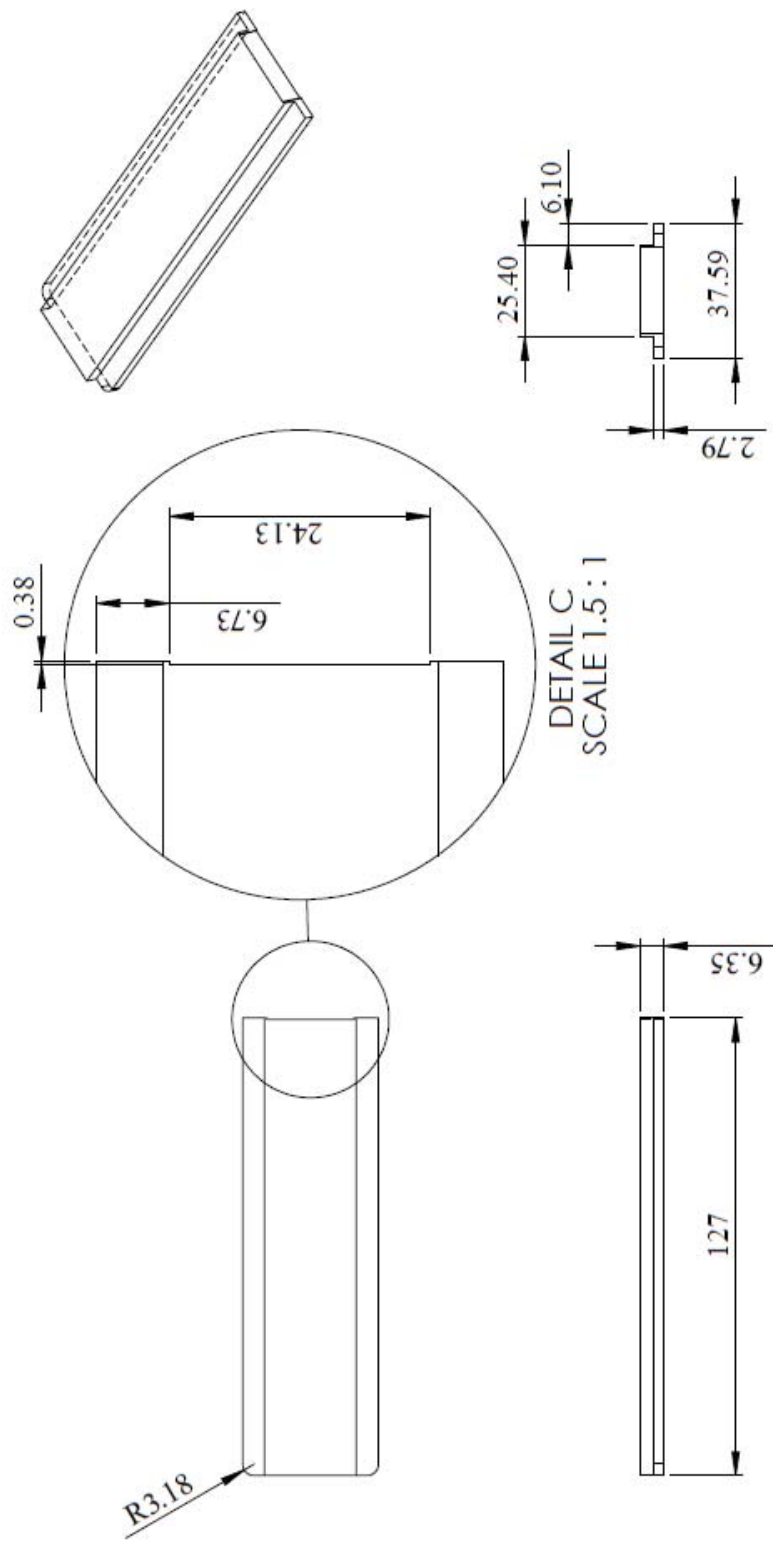
Qty: 2
Material: Acrylic
All dimensions in mm with
± .3 mm tolerance

Figure A-3: Side Walls



Qty: 1
Material: Acrylic
All dimensions in mm
with $\pm .3$ mm tolerance

Figure A-4: Cover Plate



Qty: 1
Material: Aluminum
All dimensions in mm
with $\pm .3$ mm tolerance

Figure A-5: Upstream Injector Panel

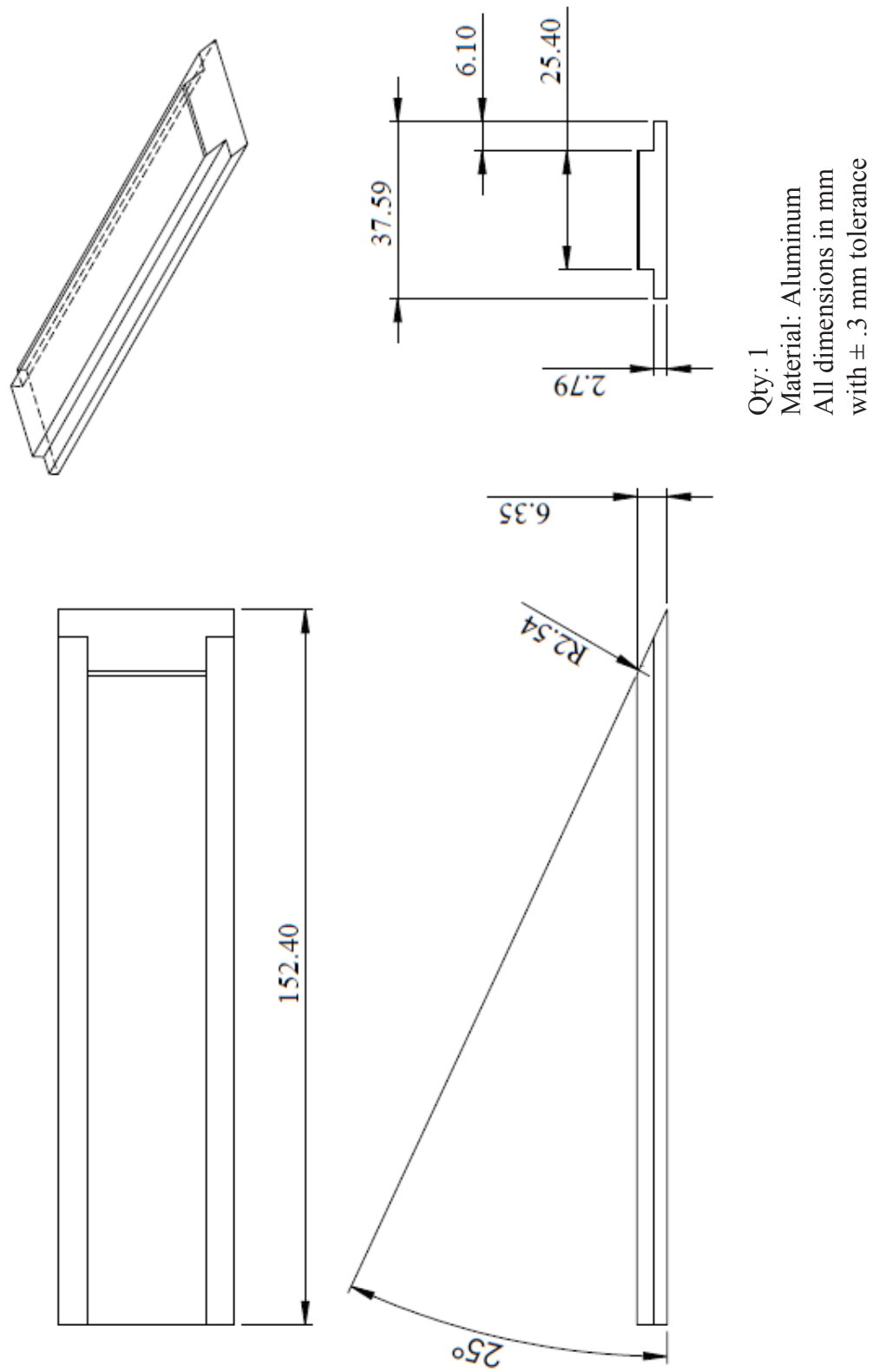


Figure A-6: Injector Panel, Middle Piece

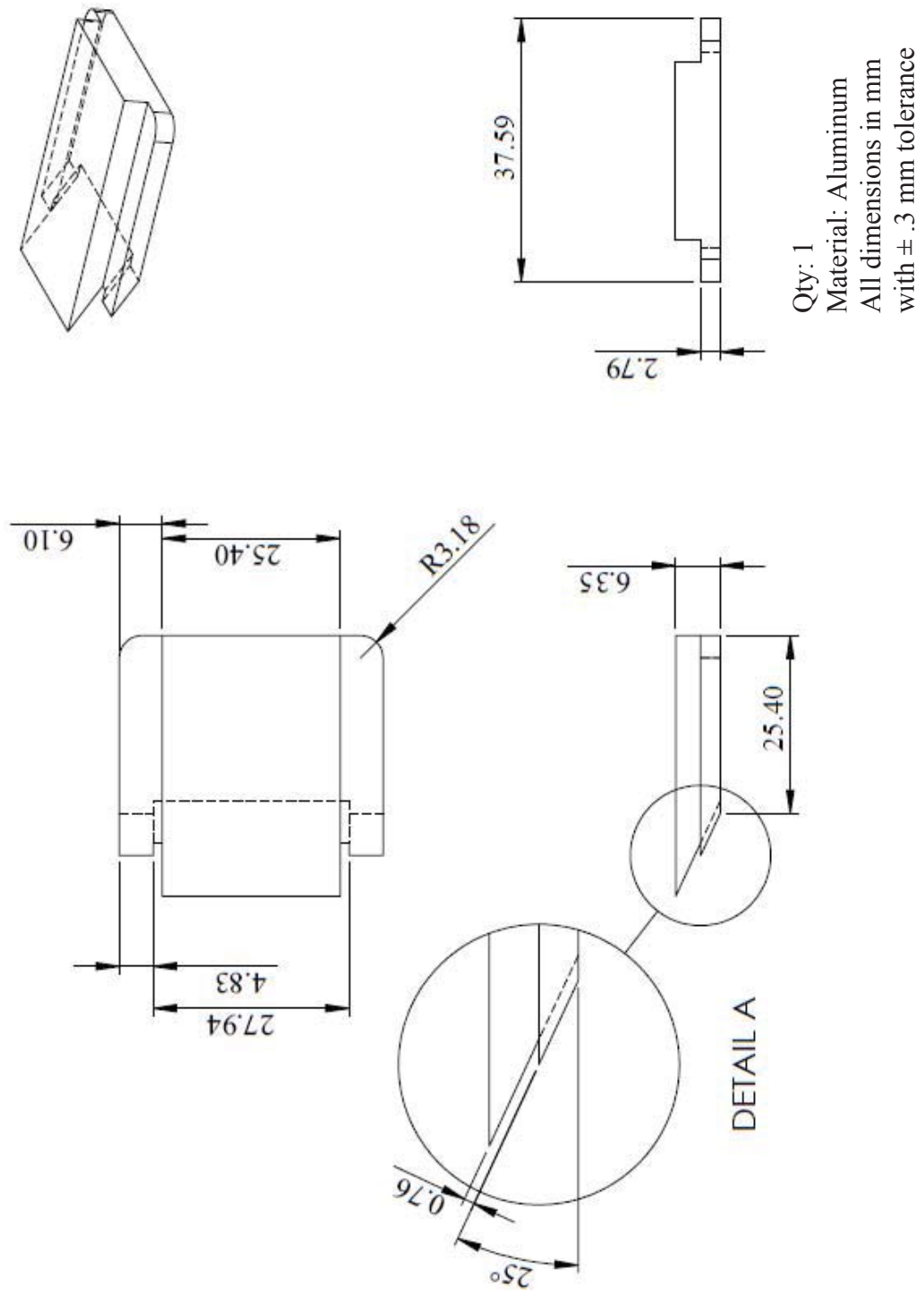
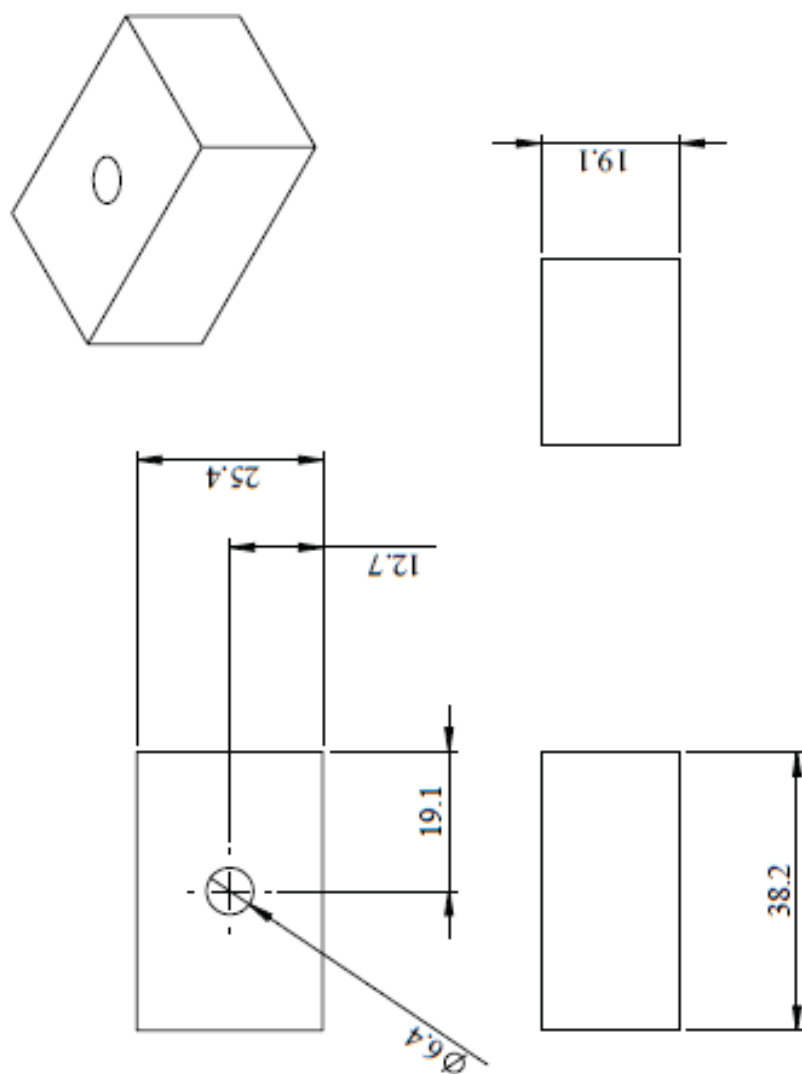


Figure A-7: Downstream Injector Panel



Qty: 1
Material: Aluminum
All dimensions in mm
with $\pm .3$ mm tolerance

Figure A-8: Rear Block

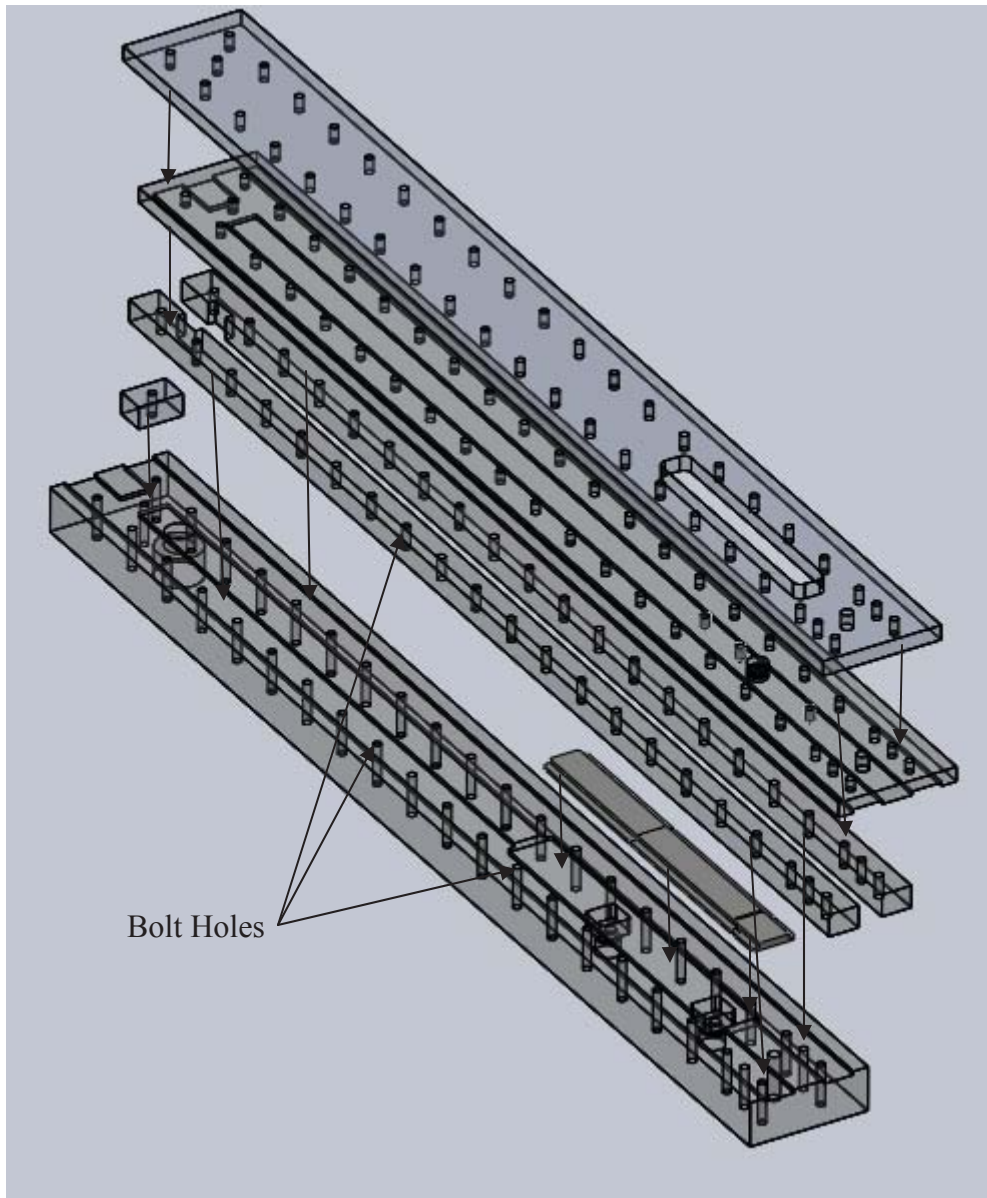


Figure A-9: Test Article Assembly Drawing.

Note that fasteners 6.3 mm in diameter were inserted through the bolt holes to hold the assembly together and silicone was used to seal the test article (not shown).

Appendix B: Supplementary Results

Table B-1: June 2011 Test Data, ILFR \approx .0034 kg/s

Test #	Barometric Pressure (kPa)	P _{U,W} (MPa)	P _{U,N} (MPa)	N ₂ Mass Flow Rate (kg/s)	P _T - film ON (kPa)	T _T - film ON (K)
T- 11	91.70	1.241	12.177	0.3022	649.5	297
T-19	91.70	1.248	9.474	0.2338	478.5	289
T-43	91.70	1.251	12.314	0.3097	655.0	289
T-41	91.70	1.251	12.225	0.3074	674.3	301
T-42	91.70	1.251	12.314	0.3097	665.4	294
T-89	91.70	1.255	7.915	0.1977	390.9	290
T-90	91.70	1.255	7.950	0.1985	393.0	289
T-116	91.70	1.262	8.364	0.2079	516.8	287
T-115	91.70	1.262	8.350	0.2078	516.8	288
T-114	91.70	1.262	8.308	0.2071	514.4	289
T-91	91.70	1.262	8.005	0.1998	397.5	290
T-99	91.70	1.265	10.411	0.2549	659.2	292
T-98	91.70	1.269	10.305	0.2538	657.1	294
T-100	91.70	1.272	10.479	0.2565	664.0	293
T-134	91.70	1.276	6.516	0.1631	392.2	295
T-69	91.70	1.276	6.337	0.1592	297.9	287
T-70	91.70	1.276	6.364	0.1599	299.2	286
T-68	91.70	1.276	6.330	0.1590	296.8	288
T-133	91.70	1.281	6.468	0.1622	393.0	299
T-132	91.70	1.281	6.509	0.1637	399.2	304
T-151	91.70	1.296	14.721	0.1780	595.0	290
T-150	91.70	1.296	14.742	0.1785	597.8	291
T-73	91.70	2.337	6.302	0.1584	298.6	290

Table B-2: June 2011 Test Data, ILFR \approx .0034 kg/s, Continued

Test #	Injected Liquid Flow Rate (kg/s)	MF _g - film ON (kPa)	Time to Collect Water in Beaker (s)	Weight of Water Collected (kg)	Calculated Removal Flow Rate (kg/s)
T- 11	0.00335	104.81	179	0.3105	0.00173
T-19	0.00336	79.34	180	0.3785	0.00210
T-43	0.00336	106.28	150	0.3160	0.00211
T-41	0.00336	106.54	181	0.3564	0.00197
T-42	0.00336	106.62	180	0.3656	0.00203
T-89	0.00337	67.28	180	0.4100	0.00228
T-90	0.00337	67.48	165	0.3820	0.00232
T-116	0.00338	58.55	182	0.4271	0.00235
T-115	0.00338	58.57	181	0.4470	0.00247
T-114	0.00338	58.63	180	0.4290	0.00238
T-91	0.00338	67.94	150	0.3430	0.00229
T-99	0.00338	72.42	180	0.4164	0.00231
T-98	0.00338	72.50	179	0.4186	0.00234
T-100	0.00339	73.01	180	0.4145	0.00230
T-134	0.00339	46.44	183.69	0.4667	0.00254
T-69	0.00339	53.53	180	0.4310	0.00239
T-70	0.00339	53.61	180	0.4324	0.00240
T-68	0.00339	53.77	180	0.4170	0.00232
T-133	0.00340	46.58	184.6	0.4694	0.00254
T-132	0.00340	47.56	183.44	0.4400	0.00240
T-151	0.00342	38.38	507	1.4273	0.00282
T-150	0.00342	38.52	181.66	0.4902	0.00270

Table B-3: June 2011 Test Data, ILFR \approx .0046 kg/s

Test #	Barometric Pressure (kPa)	P _{U,W} (MPa)	P _{U,N} (MPa)	N ₂ Mass Flow Rate (kg/s)	P _T - film ON (kPa)	T _T - film ON (K)
T-118	91.70	2.365	8.184	0.2035	512.3	294
T-119	91.70	2.365	8.308	0.2053	516.1	292
T-32	91.70	2.365	10.143	0.2507	517.1	286
T-33	91.70	2.365	10.301	0.2546	524.7	285
T-137	91.70	2.368	6.698	0.1667	400.8	290
T-135	91.70	2.369	6.599	0.1647	397.4	293
T-136	91.70	2.369	6.640	0.1656	397.2	290
T-117	91.70	2.372	8.095	0.2024	511.6	297
T-31	91.70	2.372	7.833	0.1927	385.1	287
T-30	91.70	2.372	7.805	0.1920	386.8	290
T-29	91.70	2.372	7.826	0.1925	393.0	295
T-34	91.70	2.372	10.301	0.2546	531.6	289
T-37	91.70	2.372	12.625	0.3091	658.5	286
T-36	91.70	2.372	12.590	0.3127	661.9	287
T-35	91.70	2.372	12.590	0.3128	660.5	288
T-72	91.70	2.337	6.268	0.1579	297.2	291
T-101	91.70	2.337	10.529	0.2559	664.0	292
T-103	91.70	2.337	10.667	0.2579	673.0	291
T-102	91.70	2.337	10.584	0.2564	664.0	291
T-71	91.70	2.344	6.240	0.1564	297.2	294
T-13	91.70	2.351	12.735	0.3165	677.8	296
T-22	91.70	2.362	9.625	0.2376	479.9	284

Table B-4: June 2011 Test Data, ILFR \approx .0046 kg/s, Continued

Test #	Injected Liquid Flow Rate (kg/s)	MF _g - film ON (kPa)	Time to Collect Water in Beaker (s)	Weight of Water Collected (kg)	Calculated Removal Flow Rate (kg/s)
T-118	0.00458	57.77	180.5	0.5305	0.00294
T-119	0.00458	58.07	182.5	0.5303	0.00291
T-32	0.00458	84.61	175	0.4787	0.00274
T-33	0.00458	86.12	150	0.4075	0.00272
T-137	0.00459	46.88	185.22	0.5731	0.00309
T-135	0.00459	46.57	181.32	0.5614	0.00310
T-136	0.00459	46.75	184.69	0.5646	0.00306
T-117	0.00459	57.82	189.78	0.5236	0.00276
T-31	0.00459	64.07	153	0.4324	0.00283
T-30	0.00459	64.11	153	0.4286	0.00280
T-29	0.00459	64.68	180	0.4960	0.00276
T-34	0.00459	86.12	180	0.4820	0.00268
T-37	0.00459	104.53	153	0.3970	0.00259
T-36	0.00459	106.63	150.16	0.3887	0.00259
T-35	0.00459	107.48	150	0.3880	0.00259
T-73	0.00456	53.44	180	0.5200	0.00289
T-72	0.00456	53.58	180	0.5200	0.00289
T-101	0.00456	72.50	180	0.5085	0.00283
T-103	0.00456	72.61	180	0.5105	0.00284
T-102	0.00456	72.63	180	0.5110	0.00284
T-71	0.00456	52.97	180	0.5085	0.00283
T-13	0.00457	110.35	180	0.4360	0.00242
T-22	0.00458	80.38	180	0.4530	0.00252

Table B-5: June 2011 Test Data, ILFR \approx .0056 kg/s

Test #	Barometric Pressure (kPa)	P _{U,W} (MPa)	P _{U,N} (MPa)	N ₂ Mass Flow Rate (kg/s)	P _T - film ON (kPa)	T _T - film ON (K)
T-96	91.70	3.448	7.957	0.1982	399.9	293
T-97	91.70	3.448	8.046	0.1996	402.7	292
T-24	91.70	3.448	9.639	0.2380	481.3	284
T-104	91.70	3.451	10.618	0.2565	668.1	292
T-95	91.70	3.454	7.950	0.1983	403.4	296
T-105	91.70	3.454	10.660	0.2575	668.8	292
T-49	91.70	3.461	12.232	0.3053	652.6	290
T-48	91.70	3.461	12.190	0.3046	653.0	295
T-47	91.70	3.461	12.197	0.3065	666.1	300
T-15	91.70	3.461	12.632	0.3138	666.7	291
T-140	91.70	3.481	6.716	0.1670	403.6	289
T-139	91.70	3.482	6.640	0.1656	399.9	289
T-122	91.70	3.482	8.433	0.2068	522.0	292
T-138	91.70	3.485	6.585	0.1641	399.6	291
T-121	91.70	3.489	8.371	0.2059	521.3	293
T-120	91.70	3.489	8.350	0.2071	526.1	296
T-78	91.70	3.558	6.457	0.1610	307.5	288
T-79	91.70	3.558	6.481	0.1614	306.1	288
T-77	91.70	3.558	6.447	0.1610	304.8	288
T-20	91.70	3.978	9.563	0.2361	481.3	285
T-16	91.70	3.999	12.673	0.3149	659.2	290

Table B-6: June 2011 Test Data, ILFR \approx .0056 kg/s, Continued

Test #	Injected Liquid Flow Rate (kg/s)	MF _g - film ON (kPa)	Time to Collect Water in Beaker (s)	Weight of water collected (kg)	Calculated Removal Flow Rate (approx)
T-96	0.00553	67.3	160	0.491	0.00307
T-97	0.00553	67.5	180	0.5555	0.00309
T-24	0.00553	80.5	181	0.5495	0.00304
T-104	0.00553	72.5	180	0.5877	0.00327
T-95	0.00554	67.5	180	0.555	0.00308
T-105	0.00554	72.9	367	1.18	0.00322
T-49	0.00554	104.0	150	0.434	0.00289
T-48	0.00554	105.2	125	0.359	0.00287
T-47	0.00554	106.5	180	0.501	0.00278
T-15	0.00554	108.4	196	0.5143	0.00262
T-140	0.00556	46.7	187.53	0.6502	0.00347
T-139	0.00556	46.3	186.25	0.6484	0.00348
T-122	0.00556	58.3	183.2	0.6138	0.00335
T-138	0.00556	45.8	182	0.626	0.00344
T-121	0.00556	58.1	182.6	0.6018	0.00330
T-120	0.00556	59.0	182.3	0.596	0.00327
T-78	0.00562	53.7	181	0.5962	0.00329
T-79	0.00562	54.0	182	0.6026	0.00331
T-77	0.00562	54.1	180	0.5968	0.00332
T-20	0.00594	79.6	180	0.5756	0.00320
T-16	0.00596	109.6	180	0.5264	0.00292

Table B-7: June 2011 Test Data, ILFR \approx .0064 kg/s

Test #	Barometric Pressure (kPa)	P _{U,W} (MPa)	P _{U,N} (MPa)	N ₂ Mass Flow Rate (kg/s)	P _T - film ON (kPa)	T _T - film ON (K)
T-107	91.70	4.527	10.742	0.2580	674.3	292
T-26	91.70	4.544	9.639	0.2380	481.3	283
T-85	91.70	4.578	7.991	0.1984	397.5	289
T-83	91.70	4.585	7.881	0.1955	388.2	289
T-84	91.70	4.585	7.964	0.1972	393.0	287
T-82	91.70	4.592	6.468	0.1611	307.5	289
T-81	91.70	4.592	6.461	0.1611	306.8	290
T-146	91.70	4.596	14.783	0.1791	606.8	291
T-145	91.70	4.599	14.776	0.1791	607.8	292
T-144	91.70	4.599	14.769	0.1804	613.0	293
T-143	91.70	4.606	6.854	0.1692	409.6	290
T-80	91.70	4.606	6.468	0.1614	308.9	290
T-17	91.70	4.606	12.714	0.3159	657.1	289
T-142	91.70	4.611	6.819	0.1686	408.0	290
T-141	91.70	4.613	6.785	0.1682	407.5	290
T-125	91.70	4.630	8.491	0.2075	524.0	291
T-124	91.70	4.633	8.481	0.2074	524.0	291
T-123	91.70	4.633	8.460	0.2070	522.6	292

Table B-8: June 2011 Test Data, ILFR \approx .0064 kg/s, Continued

Test #	Injected Liquid Flow Rate (kg/s)	MF _g - film ON (kPa)	Time to Collect Water in Beaker (s)	Weight of water collected (kg)	Calculated Removal Flow Rate (approx)
T-107	0.00634	72.8	481	1.6846	0.00350
T-26	0.00635	80.3	180.8	0.6025	0.00333
T-85	0.00638	66.7	180	0.6225	0.00346
T-83	0.00638	65.9	180	0.6293	0.00350
T-84	0.00638	66.2	180	0.6255	0.00348
T-82	0.00639	53.9	180	0.6475	0.00360
T-81	0.00639	54.1	180	0.646	0.00359
T-146	0.00639	38.3	185.38	0.757	0.00408
T-145	0.00639	38.3	188.1	0.774	0.00411
T-144	0.00639	38.8	184.15	0.7521	0.00408
T-143	0.00639	47.5	181.65	0.6859	0.00378
T-80	0.00639	54.2	180	0.6456	0.00359
T-17	0.00639	110.5	179	0.5527	0.00309
T-142	0.00640	47.3	181.96	0.6883	0.00378
T-141	0.00640	47.1	182.5	0.6918	0.00379
T-125	0.00641	58.2	181.65	0.6655	0.00366
T-124	0.00641	58.2	188.6	0.689	0.00365
T-123	0.00641	58.4	184.5	0.6629	0.00359

Table B-9: June 2011 Test Data, ILFR \approx .0070 kg/s

Test #	Barometric Pressure (kPa)	P _{U,W} (MPa)	P _{U,N} (MPa)	N ₂ Mass Flow Rate (kg/s)	P _T - film ON (kPa)	T _T - film ON (K)
T-113	91.70	5.468	8.302	0.2072	521.3	291
T-112	91.70	5.478	8.219	0.2051	514.4	290
T-111	91.70	5.482	8.129	0.2031	510.2	292
T-109	91.70	5.485	10.274	0.2568	673.3	297
T-110	91.70	5.485	10.322	0.2578	671.6	294
T-108	91.70	5.495	10.287	0.2580	681.9	303
T-87	91.70	5.509	8.019	0.1983	397.2	289
T-86	91.70	5.514	7.984	0.1979	395.1	289
T-76	91.70	5.516	6.412	0.1605	305.4	288
T-74	91.70	5.523	6.357	0.1595	302.0	289
T-75	91.70	5.523	6.412	0.1606	305.4	289
T-129	91.70	5.564	6.667	0.1636	396.8	290
T-128	91.70	5.571	8.477	0.2076	525.2	290
T-127	91.70	5.578	8.495	0.2079	526.1	290
T-126	91.70	5.589	8.491	0.2074	524.4	290
T-149	91.70	5.599	14.762	0.1787	606.4	290
T-148	91.70	5.606	14.776	0.1790	607.4	291
T-147	91.70	5.606	14.783	0.1791	608.8	291

Table B-10: June 2011 Test Data, ILFR \approx .0070 kg/s, Continued

Test #	Injected Liquid Flow Rate (kg/s)	MF _g - film ON (kPa)	Time to Collect Water in Beaker (s)	Weight of water collected (kg)	Calculated Removal Flow Rate (approx)
T-113	0.00697	58.4	180.5	0.7157	0.00397
T-112	0.00698	57.6	151	0.5938	0.00393
T-111	0.00698	57.3	180	0.697	0.00387
T-109	0.00698	73.3	180	0.6696	0.00372
T-110	0.00698	73.3	187	0.711	0.00380
T-108	0.00699	74.8	180	0.6573	0.00365
T-87	0.00700	66.6	268	0.99	0.00369
T-86	0.00700	66.7	180	0.662	0.00368
T-76	0.00700	53.6	183	0.6985	0.00382
T-74	0.00701	53.6	180	0.6907	0.00384
T-75	0.00701	53.9	180	0.6841	0.00380
T-129	0.00703	45.6	542.31	2.1842	0.00403
T-128	0.00704	58.1	191.81	0.7413	0.00386
T-127	0.00704	58.2	181.78	0.7135	0.00393
T-126	0.00705	58.1	187.6	0.7309	0.00390
T-149	0.00706	38.1	188.2	0.819	0.00435
T-148	0.00706	38.2	189.72	0.822	0.00433
T-147	0.00706	38.3	186.8	0.817	0.00437

Table B-11: November 2011 Test Data, ILFR $\approx .0034$ kg/s

Run	subrun	Cav venturi Diameter (mm)	Barometric Pressure (kPa)	P _{U,W} (kPa)	T _W (K)	P _{U,N} (MPa)	T _N (K)	P _T - film ON (kPa)	T _T - film ON (K)
126	4	0.323	90.81	1.251	296	2.179	247	465.6	310
126	5	0.323	90.81	1.251	296	2.175	247	464.5	310
126	3	0.323	90.81	1.251	296	2.182	247	465.9	310
126	2	0.323	90.81	1.251	296	2.189	248	466.6	310
126	1	0.323	90.81	1.251	296	2.213	250	467.6	310
127	1	0.323	90.81	1.251	296	3.875	245	813.7	309
127	2	0.323	90.81	1.251	296	3.889	245	815.5	308
127	3	0.323	90.81	1.251	296	3.896	245	816.5	308
127	4	0.323	90.81	1.251	296	3.903	245	817.2	308
127	5	0.323	90.81	1.251	296	3.909	244	817.2	307
130	1	0.323	90.81	1.234	297	3.337	254	459.0	310
130	2	0.323	90.81	1.234	297	3.351	251	462.4	311
130	3	0.323	90.81	1.234	297	3.358	250	463.8	311
130	4	0.323	90.81	1.234	297	3.365	249	464.5	311
130	5	0.323	90.81	1.234	297	3.368	249	464.5	311
131	1	0.323	90.81	1.231	296	5.854	247	798.9	308
131	2	0.323	90.81	1.231	296	5.895	247	803.1	307
131	3	0.323	90.81	1.231	296	5.909	247	803.8	306
131	5	0.323	90.81	1.231	296	5.923	247	803.8	305
131	4	0.323	90.81	1.231	296	5.919	247	804.1	305
106	1	0.323	91.15	1.245	297	6.081	249	452.4	296
106	3	0.323	91.15	1.245	297	6.078	247	451.8	295
106	2	0.323	91.15	1.245	297	6.081	247	451.8	295
106	4	0.323	91.15	1.245	297	6.074	246	451.1	294
106	5	0.323	91.15	1.245	297	6.071	246	450.4	294
110	1	0.323	91.01	1.248	297	7.522	251	450.9	290
110	2	0.323	91.01	1.248	296	7.533	250	451.3	289
110	4	0.323	91.01	1.248	296	7.540	250	450.9	289
110	3	0.323	91.01	1.248	296	7.536	250	450.9	289
110	5	0.323	91.01	1.248	296	7.543	250	450.2	288

Table B-12: November 2011 Test Data, ILFR ≈ 0.0034 kg/s, Continued

Run	Injected Liquid Flow Rate (kg/s)	N ₂ Mass Flow Rate (kg/s)	MF _g - film ON (kPa)
126	0.00336	0.05511	5.80
126	0.00336	0.05507	5.80
126	0.00336	0.05516	5.80
126	0.00336	0.05529	5.82
126	0.00336	0.05561	5.87
127	0.00336	0.09739	10.3
127	0.00336	0.09775	10.3
127	0.00336	0.09798	10.4
127	0.00336	0.09816	10.4
127	0.00336	0.09839	10.4
130	0.00334	0.08260	13.2
130	0.00334	0.08337	13.4
130	0.00334	0.08369	13.4
130	0.00334	0.08396	13.5
130	0.00334	0.08419	13.6
131	0.00334	0.14647	23.7
131	0.00334	0.14760	23.9
131	0.00334	0.14801	23.9
131	0.00334	0.14842	23.9
131	0.00334	0.14833	23.9
106	0.00335	0.15177	43.2
106	0.00335	0.15241	43.4
106	0.00335	0.15232	43.4
106	0.00335	0.15250	43.4
106	0.00335	0.15259	43.5
110	0.00336	0.18734	64.6
110	0.00336	0.18783	64.8
110	0.00336	0.18815	64.9
110	0.00336	0.18811	64.9
110	0.00336	0.18833	65.0

Table B-13: November 2011 Test Data, ILFR ≈ 0.0034 kg/s, Continued

Run	subrun	Cav venturi Diameter (mm)	Barometric Pressure (kPa)	P _{U,W} (kPa)	T _W (K)	P _{U,N} (MPa)	T _N (K)	P _T - film ON (kPa)	T _T - film ON (K)
107	5	0.323	91.15	1.243	296	10.963	253	795.1	287
107	4	0.323	91.15	1.243	296	10.949	252	795.1	287
107	2	0.323	91.15	1.243	296	10.911	252	794.4	289
107	3	0.323	91.15	1.243	296	10.935	252	794.4	288
107	1	0.323	91.15	1.243	296	10.887	251	793.8	289
111	1	0.323	91.01	1.248	298	12.673	257	768.8	302
111	2	0.323	91.01	1.248	297	12.676	255	769.5	300
111	3	0.323	91.01	1.248	297	12.680	254	769.1	298
111	4	0.323	91.01	1.245	297	12.683	253	768.1	296

Table B-14: November 2011 Test Data, ILFR ≈ 0.0034 kg/s, Continued

Run	Injected Liquid Flow Rate (kg/s)	N ₂ Mass Flow Rate (kg/s)	MF _g - film ON (kPa)
107	0.00335	0.27411	77.7
107	0.00335	0.27402	77.7
107	0.00335	0.27347	77.8
107	0.00335	0.27384	77.8
107	0.00335	0.27320	77.8
111	0.00336	0.31511	112
111	0.00336	0.31684	112
111	0.00336	0.31756	112
111	0.00335	0.31824	112

Table B-15: November 2011 Test Data, ILFR ≈ 0.0070 kg/s

Run	subrun	Cav venturi Diameter (mm)	Barometric Pressure (kPa)	P _{U,W} (kPa)	T _W (K)	P _{U,N} (MPa)	T _N (K)	P _T - film ON (kPa)	T _T - film ON (K)
128	4	0.323	90.81	5.519	296	2.193	247	473.8	308
128	5	0.572	90.81	5.519	296	2.193	246	473.1	308
128	3	0.323	90.81	5.519	296	2.200	247	474.5	308
128	2	0.323	90.81	5.523	296	2.210	248	475.9	308
128	1	0.323	90.81	5.523	296	2.224	250	475.2	307
129	1	0.323	90.81	5.518	296	3.923	245	831.3	307
129	2	0.323	90.81	5.517	296	3.954	245	834.8	306
129	4	0.323	90.81	5.516	296	3.972	245	837.5	306
129	3	0.323	90.81	5.516	296	3.965	245	836.5	307
129	5	0.323	90.81	5.515	296	3.978	245	838.4	305
132	1	0.323	90.81	5.530	296	3.392	247	470.7	306
132	2	0.323	90.81	5.526	296	3.406	246	471.4	305
132	3	0.323	90.81	5.523	296	3.413	246	473.1	305
132	4	0.323	90.81	5.521	296	3.416	246	473.5	305
132	5	0.323	90.81	5.519	296	3.420	246	473.8	305
133	1	0.323	90.81	5.516	296	5.985	247	814.8	301
133	2	0.323	90.81	5.516	296	6.016	248	816.9	301
133	3	0.323	90.81	5.516	296	6.030	248	817.9	300
133	4	0.323	90.81	5.513	296	6.040	248	818.6	300
133	5	0.323	90.81	5.513	296	6.047	248	818.2	300
108	3	0.323	91.15	5.516	296	6.171	248	459.7	291
108	1	0.323	91.15	5.519	296	6.171	248	459.7	291
108	2	0.323	91.15	5.516	296	6.171	248	459.7	291
108	4	0.323	91.15	5.516	296	6.174	247	459.3	290
108	5	0.323	91.15	5.513	296	6.174	247	459.0	290
114	4	0.323	91.01	5.502	296	7.188	246	446.1	300
114	3	0.323	91.01	5.502	296	7.188	246	446.8	301
114	5	0.323	91.01	5.499	296	7.191	246	445.8	299
114	2	0.323	91.01	5.506	296	7.185	246	447.5	301
114	6	0.323	91.01	5.499	296	7.191	246	444.7	299
114	1	0.323	91.01	5.506	296	7.178	247	447.5	303
113	5	0.323	91.01	5.516	297	12.825	252	780.2	293
113	4	0.323	91.01	5.516	297	12.825	252	781.9	295
113	2	0.323	91.01	5.516	298	12.814	253	783.3	298
113	1	0.323	91.01	5.516	298	12.811	254	784.0	300
113	3	0.323	91.01	5.516	298	12.818	252	781.5	297

Table B-16: November 2011 Test Data, ILFR ≈ 0.0070 kg/s, Continued

Run	Injected Liquid Flow Rate (kg/s)	N ₂ Mass Flow Rate (kg/s)	MF _g - film ON (kPa)
128	0.00701	0.05547	5.73
128	0.00701	0.05552	5.75
128	0.00701	0.05561	5.75
128	0.00701	0.05575	5.76
128	0.00701	0.05588	5.79
129	0.00701	0.09857	10.3
129	0.00701	0.09934	10.4
129	0.00700	0.09984	10.4
129	0.00700	0.09966	10.4
129	0.00700	0.10002	10.4
132	0.00701	0.08509	13.5
132	0.00701	0.08550	13.6
132	0.00701	0.08573	13.6
132	0.00701	0.08582	13.6
132	0.00701	0.08596	13.6
133	0.00700	0.14987	23.8
133	0.00700	0.15050	23.9
133	0.00700	0.15078	23.9
133	0.00700	0.15096	23.9
133	0.00700	0.15105	23.9
108	0.00700	0.15440	43.1
108	0.00701	0.15422	43.1
108	0.00700	0.15440	43.2
108	0.00700	0.15459	43.2
108	0.00700	0.15463	43.2
114	0.00700	0.18071	62.9
114	0.00700	0.18067	62.9
114	0.00699	0.18099	63.0
114	0.00700	0.18071	63.0
114	0.00699	0.18099	63.0
114	0.00700	0.18035	63.1
113	0.00700	0.32296	112
113	0.00700	0.32278	112
113	0.00700	0.32174	113
113	0.00700	0.32069	113
113	0.00700	0.32237	113

Table B-17: November 2011 Test Data, ILFR ≈ 0.012 kg/s

Run	subrun	Cav venturi Diameter (mm)	Barometric Pressure (kPa)	P _{U,W} (kPa)	T _W (K)	P _{U,N} (MPa)	T _N (K)	P _T - film ON (kPa)	T _T - film ON (K)
125	1	0.572	90.81	1.245	296	3.875	246	837.5	311
125	2	0.572	90.81	1.245	296	3.913	246	842.4	311
125	3	0.572	90.81	1.245	296	3.927	246	844.4	310
125	4	0.572	90.81	1.243	296	3.937	245	845.1	310
125	5	0.572	90.81	1.243	296	3.940	245	845.8	309
134	1	0.572	90.81	1.250	296	3.385	249	474.9	304
134	2	0.572	90.81	1.250	296	3.413	248	478.3	303
134	3	0.572	90.81	1.250	296	3.427	248	479.7	303
134	5	0.572	90.81	1.250	296	3.441	247	481.4	303
134	4	0.572	90.81	1.250	296	3.437	247	480.4	303
135	1	0.572	90.81	1.248	296	5.971	248	817.5	300
135	2	0.572	90.81	1.248	296	5.999	249	821.0	300
135	3	0.572	90.81	1.248	296	6.019	249	822.4	299
135	4	0.572	90.81	1.248	296	6.030	249	823.1	299
135	5	0.572	90.81	1.248	296	6.040	249	823.1	299
98	1	0.572	91.15	1.234	296	4.661	249	476.9	309
98	2	0.572	91.15	1.234	296	4.668	248	477.3	309
98	3	0.572	91.15	1.234	296	4.668	247	477.3	308
98	4	0.572	91.15	1.231	296	4.668	246	477.3	307
98	5	0.572	91.15	1.231	296	4.668	245	477.3	307
99	5	0.572	91.15	1.241	296	8.069	246	804.1	297
99	4	0.572	91.15	1.241	296	8.071	246	804.8	297
99	3	0.572	91.15	1.241	296	8.074	246	805.8	298
99	2	0.572	91.15	1.241	296	8.074	246	806.9	298
99	1	0.572	91.15	1.241	297	8.074	246	807.5	299
115	2	0.572	91.01	1.231	296	7.343	249	455.6	295
115	1	0.572	91.01	1.231	296	7.336	249	455.4	296
115	5	0.572	91.01	1.231	296	7.347	248	454.0	293
115	3	0.572	91.01	1.231	296	7.347	248	455.4	294
115	4	0.572	91.01	1.231	296	7.347	248	454.7	294

Table B-18: November 2011 Test Data, ILFR ≈ 0.012 kg/s, Continued

Run	Injected Liquid Flow Rate (kg/s)	N ₂ Mass Flow Rate (kg/s)	MF _g - film ON (kPa)
125	0.01172	0.09721	10.1
125	0.01172	0.09816	10.2
125	0.01172	0.09857	10.2
125	0.01172	0.09888	10.3
125	0.01172	0.09902	10.3
134	0.01175	0.08446	13.1
134	0.01175	0.08532	13.2
134	0.01175	0.08573	13.3
134	0.01175	0.08618	13.4
134	0.01175	0.08609	13.4
135	0.01174	0.14928	23.4
135	0.01174	0.14978	23.5
135	0.01174	0.15023	23.5
135	0.01174	0.15041	23.5
135	0.01174	0.15064	23.6
98	0.01168	0.11621	25.1
98	0.01168	0.11662	25.2
98	0.01168	0.11685	25.2
98	0.01167	0.11707	25.3
98	0.01167	0.11725	25.3
99	0.01171	0.20344	43.7
99	0.01171	0.20348	43.8
99	0.01171	0.20353	43.8
99	0.01171	0.20353	43.9
99	0.01171	0.20348	43.9
115	0.01167	0.18380	62.6
115	0.01167	0.18343	62.6
115	0.01167	0.18407	62.6
115	0.01167	0.18402	62.7
115	0.01167	0.18407	62.7

Table B-19: November 2011 Test Data, ILFR ≈ 0.012 kg/s, Continued

Run	subrun	Cav venturi Diameter (mm)	Barometric Pressure (kPa)	P _{U,W} (kPa)	T _W (K)	P _{U,N} (MPa)	T _N (K)	P _T - film ON (kPa)	T _T - film ON (K)
103	5	0.572	91.15	1.245	297	10.811	250	805.1	290
103	4	0.572	91.15	1.245	297	10.798	250	805.5	291
103	3	0.572	91.15	1.269	297	10.784	250	806.2	291
103	1	0.572	91.15	1.238	297	10.736	249	804.8	293
103	2	0.572	91.15	1.238	297	10.763	250	805.5	292
116	4	0.572	91.01	1.231	297	13.018	256	779.8	286
116	3	0.572	91.01	1.231	297	13.014	255	781.2	286
116	2	0.572	91.01	1.231	297	13.011	255	782.6	287
116	1	0.572	91.01	1.231	297	13.007	254	784.7	288

Table B-20: November 2011 Test Data, ILFR ≈ 0.012 kg/s, Continued

Run	Injected Liquid Flow Rate (kg/s)	N ₂ Mass Flow Rate (kg/s)	MF _g - film ON (kPa)
103	0.01173	0.27193	76.2
103	0.01173	0.27170	76.3
103	0.01183	0.27143	76.3
103	0.01170	0.27043	76.3
103	0.01170	0.27098	76.3
116	0.01167	0.32464	111
116	0.01167	0.32487	111
116	0.01167	0.32523	111
116	0.01167	0.32600	112

Table B-21: November 2011 Test Data, ILFR ≈ 0.018 kg/s

Run	subrun	Cav venturi Diameter (mm)	Barometric Pressure (kPa)	P _{U,W} (kPa)	T _W (K)	P _{U,N} (MPa)	T _N (K)	P _T - film ON (kPa)	T _T - film ON (K)
121	1	0.572	91.01	3.272	297	2.158	252	485.8	302
121	2	0.572	91.01	3.270	297	2.155	251	485.4	302
121	3	0.572	91.01	3.268	297	2.151	250	485.1	303
121	4	0.572	91.01	3.267	297	2.151	250	484.7	303
121	5	0.572	91.01	3.267	297	2.151	249	484.7	303
122	4	0.572	91.01	3.258	297	3.781	247	817.7	300
122	5	0.572	91.01	3.258	297	3.778	246	817.1	300
122	3	0.572	91.01	3.258	297	3.784	246	818.1	300
122	2	0.572	91.01	3.261	298	3.785	246	819.5	301
122	1	0.572	91.01	3.261	298	3.792	246	821.2	301
136	1	0.572	90.81	3.277	297	3.399	249	481.8	300
136	2	0.572	90.81	3.277	297	3.427	248	485.9	300
136	3	0.572	90.81	3.277	297	3.441	248	487.6	299
136	4	0.572	90.81	3.275	297	3.451	248	488.6	299
136	5	0.572	90.81	3.275	297	3.454	248	489.3	299
137	1	0.572	90.81	3.273	297	6.095	249	841.0	297
137	2	0.572	90.81	3.273	297	6.130	250	843.7	297
137	3	0.572	90.81	3.272	297	6.157	250	846.5	296
137	4	0.572	90.81	3.270	297	6.174	250	847.9	296
137	5	0.572	90.81	3.270	297	6.187	250	848.6	296
100	5	0.572	91.15	3.275	296	4.673	243	478.3	296
100	1	0.572	91.15	3.275	298	4.670	244	478.7	297
100	2	0.572	91.15	3.275	298	4.671	243	478.7	297
100	4	0.572	91.15	3.275	296	4.673	243	478.3	296
100	3	0.572	91.15	3.275	298	4.673	243	478.7	296
104	1	0.572	91.15	3.275	298	6.071	248	473.8	303
104	2	0.572	91.15	3.275	298	6.061	246	473.1	302
104	3	0.572	91.15	3.275	298	6.050	246	472.4	302
104	4	0.572	91.15	3.272	297	6.047	245	471.8	301
104	5	0.572	91.15	3.272	297	6.047	245	471.4	301
101	1	0.572	91.15	3.268	297	8.274	247	825.5	292
101	4	0.572	91.15	3.268	297	8.336	248	828.9	291
101	3	0.572	91.15	3.268	297	8.326	247	828.9	291
101	2	0.572	91.15	3.268	297	8.308	247	827.2	292
101	5	0.572	91.15	3.268	297	8.350	248	828.9	290

Table B-22: November 2011 Test Data, ILFR ≈ 0.018 kg/s, Continued

Run	Injected Liquid Flow Rate (kg/s)	N ₂ Mass Flow Rate (kg/s)	MF _g - film ON (kPa)
121	0.01816	0.05407	5.21
121	0.01815	0.05411	5.23
121	0.01815	0.05411	5.23
121	0.01814	0.05416	5.24
121	0.01814	0.05420	5.25
122	0.01812	0.09476	9.43
122	0.01812	0.09485	9.45
122	0.01812	0.09489	9.46
122	0.01813	0.09494	9.46
122	0.01813	0.09507	9.48
136	0.01817	0.08487	12.8
136	0.01817	0.08568	13.0
136	0.01817	0.08605	13.0
136	0.01816	0.08636	13.1
136	0.01816	0.08646	13.1
137	0.01816	0.15214	23.4
137	0.01816	0.15277	23.5
137	0.01815	0.15332	23.6
137	0.01815	0.15368	23.6
137	0.01815	0.15391	23.6
100	0.01816	0.11784	24.6
100	0.01816	0.11766	24.6
100	0.01816	0.11775	24.6
100	0.01816	0.11784	24.6
100	0.01816	0.11784	24.6
104	0.01816	0.15182	42.2
104	0.01816	0.15200	42.3
104	0.01816	0.15205	42.3
104	0.01816	0.15209	42.3
104	0.01816	0.15227	42.3
101	0.01815	0.20838	44.0
101	0.01815	0.20952	44.1
101	0.01815	0.20938	44.1
101	0.01815	0.20906	44.1
101	0.01815	0.20983	44.2

Table B-23: November 2011 Test Data, ILFR ≈ 0.018 kg/s, Continued

Run	subrun	Cav 137enture Diameter (mm)	Barometric Pressure (kPa)	P _{U,W} (kPa)	T _W (K)	P _{U,N} (MPa)	T _N (K)	P _T - film ON (kPa)	T _T - film ON (K)
120	1	0.572	91.01	3.275	298	7.971	254	493.2	291
120	2	0.572	91.01	3.275	298	7.988	254	493.2	290
120	3	0.572	91.01	3.275	298	7.998	254	493.3	290
120	4	0.572	91.01	3.275	298	8.005	254	493.5	290
120	5	0.572	91.01	3.275	298	8.015	254	493.5	289
105	5	0.572	91.15	3.265	297	10.991	250	828.6	291
105	4	0.572	91.15	3.265	297	10.977	250	828.9	292
105	1	0.572	91.15	3.265	296	10.901	249	828.2	295
105	3	0.572	91.15	3.265	296	10.963	250	829.3	293
105	2	0.572	91.15	3.265	296	10.935	249	828.9	294
119	5	0.572	91.01	3.261	297	12.942	258	785.0	290
119	4	0.572	91.01	3.261	297	12.942	257	787.1	290
119	3	0.572	91.01	3.261	297	12.942	257	789.1	291
119	2	0.572	91.01	3.261	297	12.942	256	791.5	291
119	1	0.572	91.01	3.261	298	12.942	255	793.6	292

Table B-24: November 2011 Test Data, ILFR ≈ 0.018 kg/s Continued

Run	Injected Liquid Flow Rate (kg/s)	N ₂ Mass Flow Rate (kg/s)	MF _g - film ON (kPa)
120	0.01816	0.19750	65.8
120	0.01816	0.19795	66.0
120	0.01816	0.19818	66.1
120	0.01816	0.19831	66.1
120	0.01816	0.19854	66.2
105	0.01814	0.27647	77.0
105	0.01814	0.27633	77.0
105	0.01814	0.27506	77.0
105	0.01814	0.27615	77.0
105	0.01814	0.27561	77.1
119	0.01813	0.32092	109
119	0.01813	0.32155	109
119	0.01813	0.32219	109
119	0.01813	0.32283	110
119	0.01813	0.32346	110

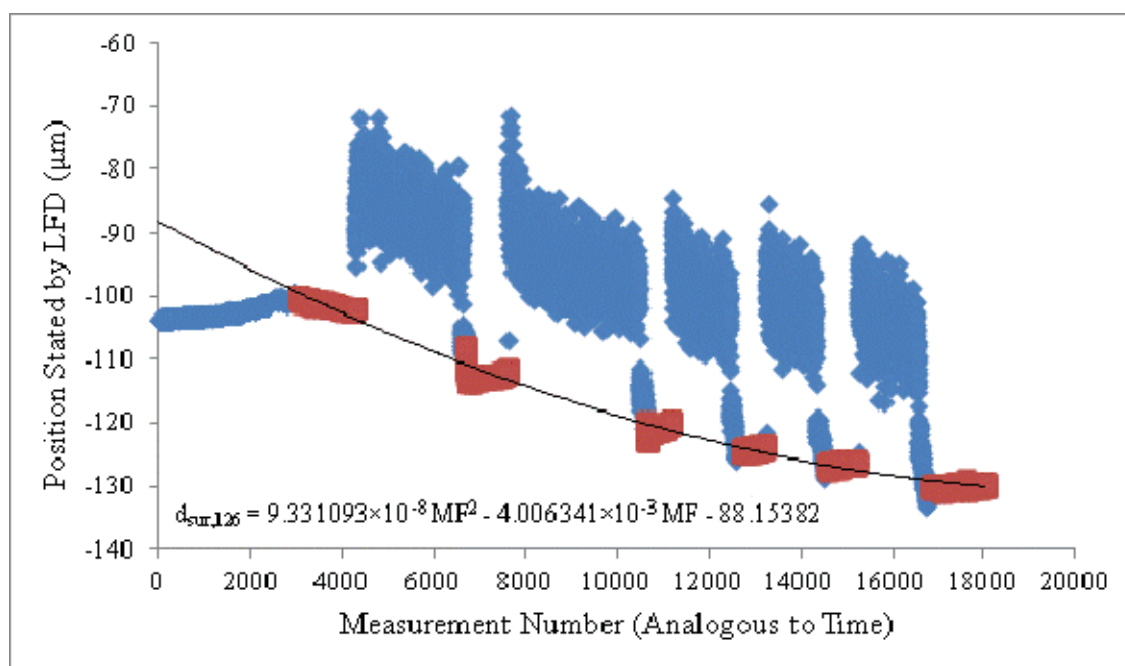


Figure B-1: Position of the Aluminum Substrate Stated by the LFD for Run 126

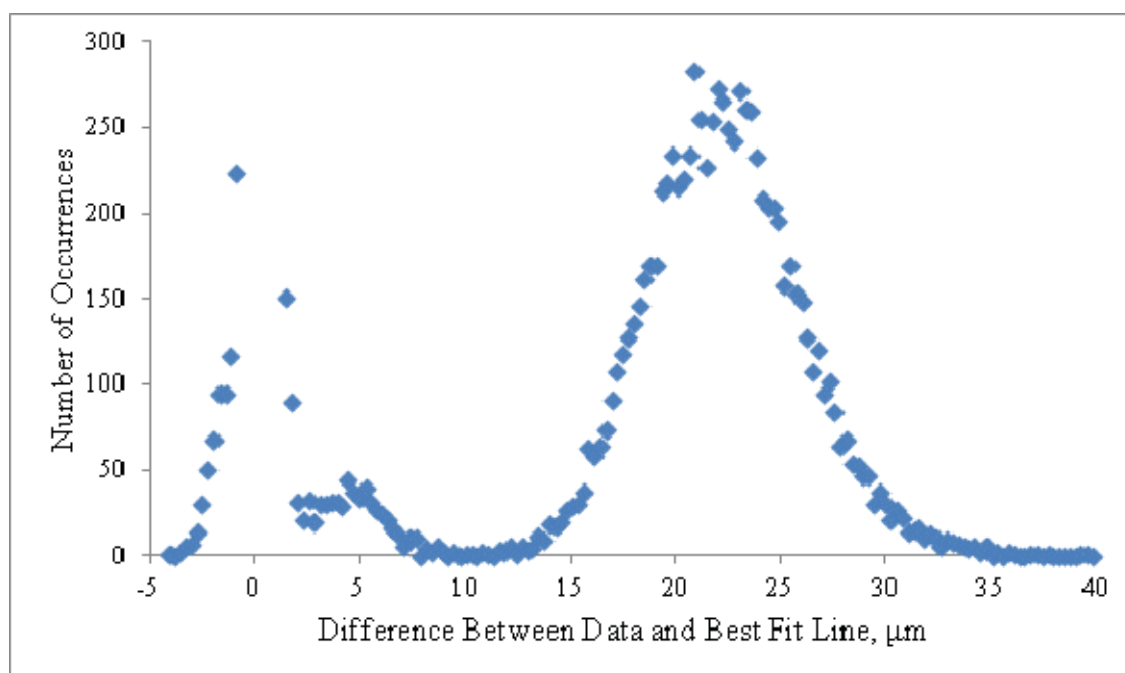


Figure B-2: LFD Histogram for Run 126

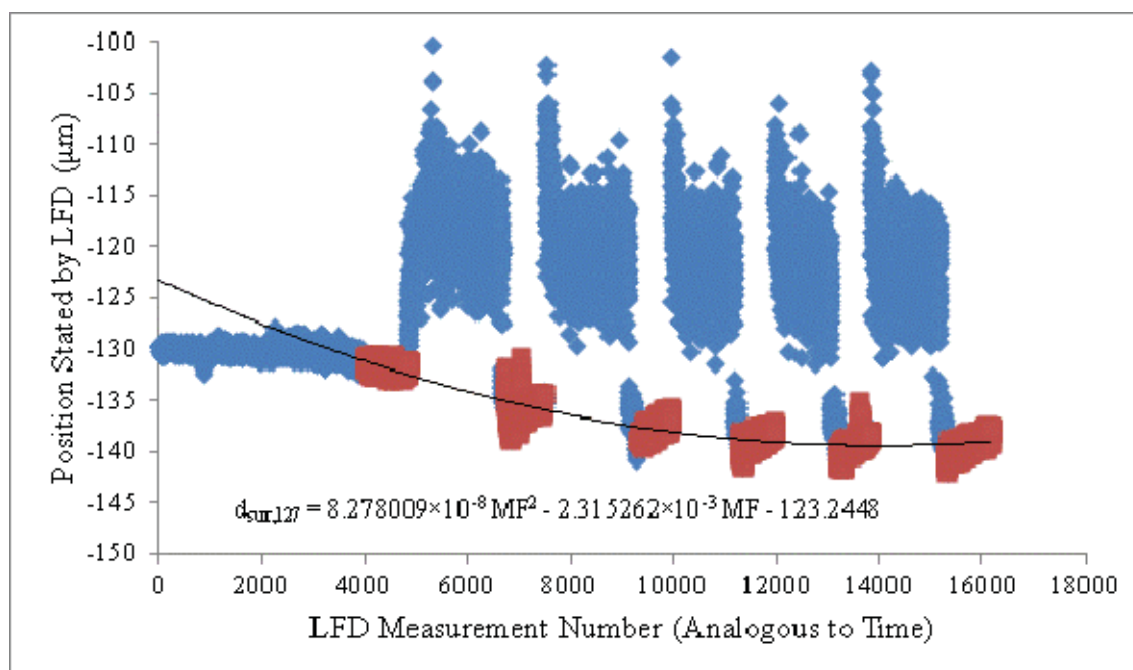


Figure B-3: Position of the Aluminum Substrate Stated by the LFD for Run 127

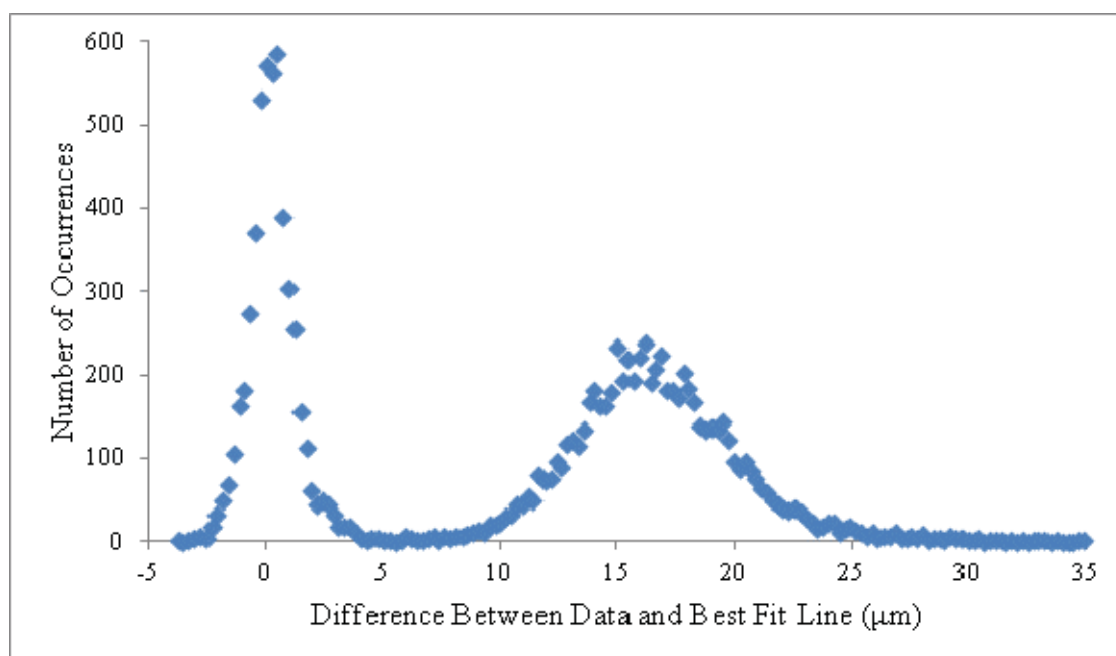


Figure B-4: LFD Histogram for Run 127

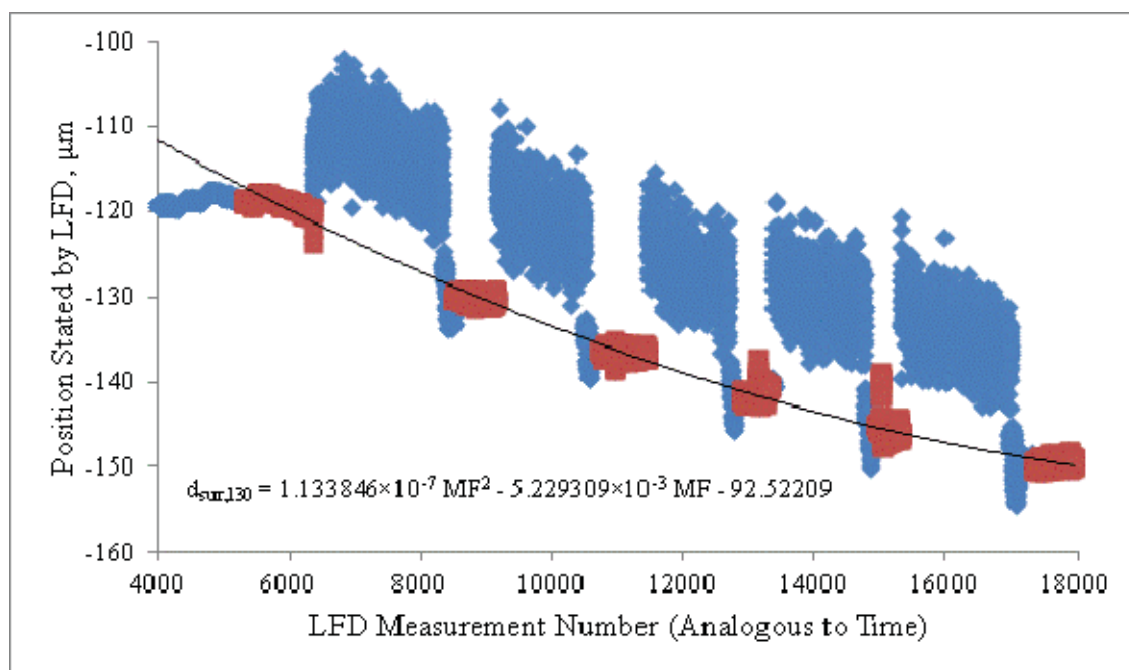


Figure B-5: Position of the Aluminum Substrate Stated by the LFD for Run 130

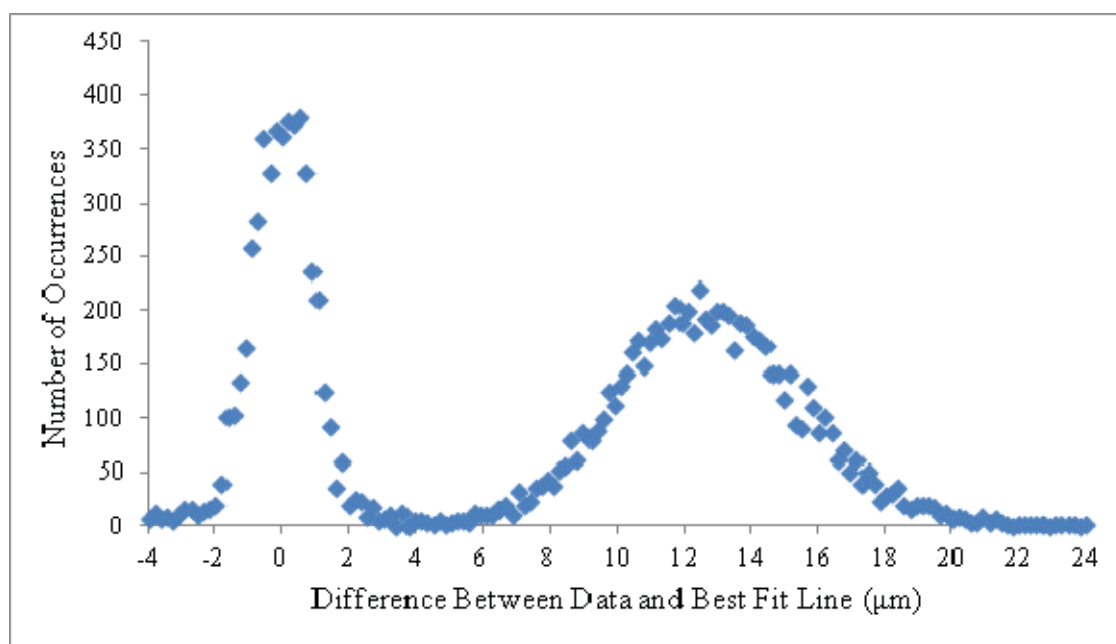


Figure B-6: LFD Histogram for Run 130

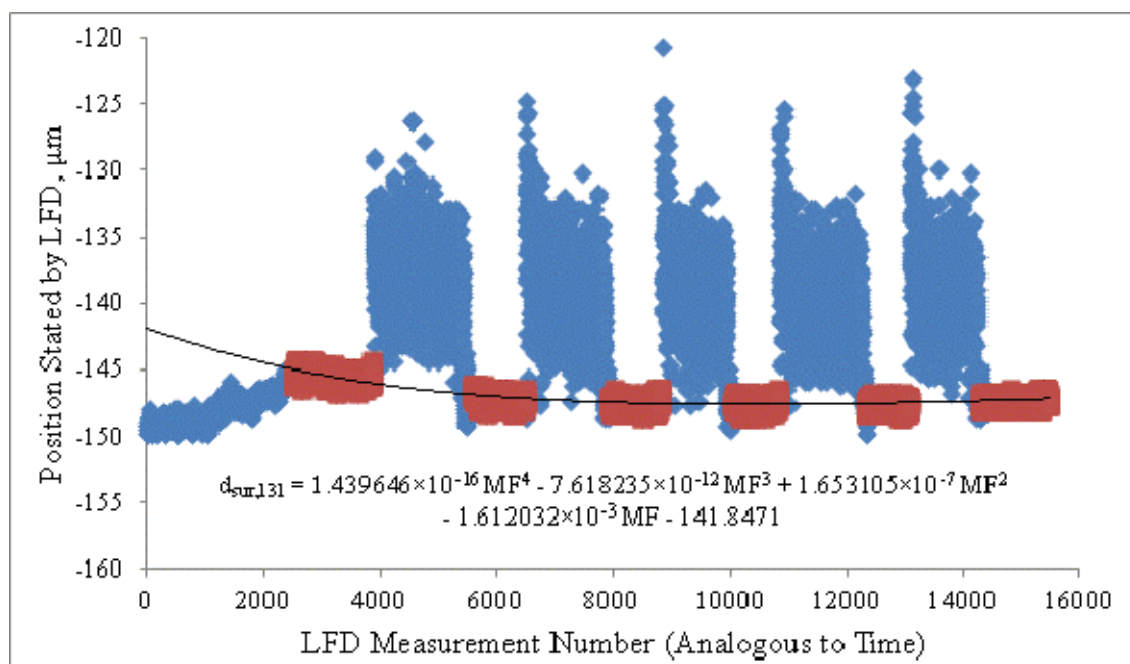


Figure B-7: Position of the Aluminum Substrate Stated by the LFD for Run 131

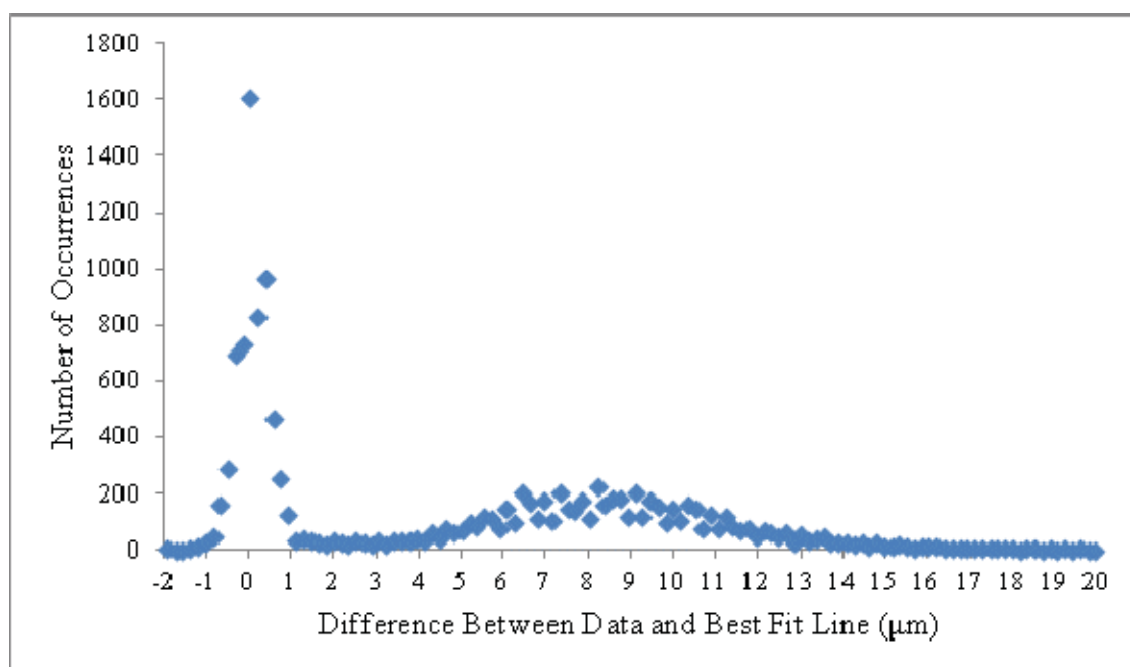


Figure B-8: LFD Histogram for Run 131

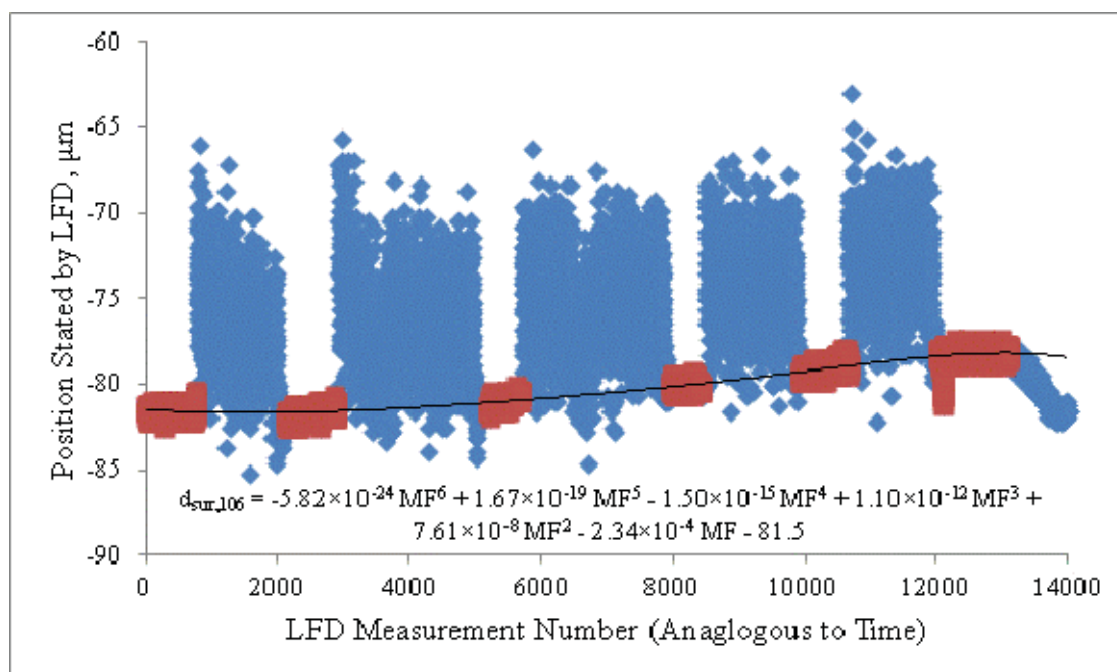


Figure B-9: Position of the Aluminum Substrate Stated by the LFD for Run 106

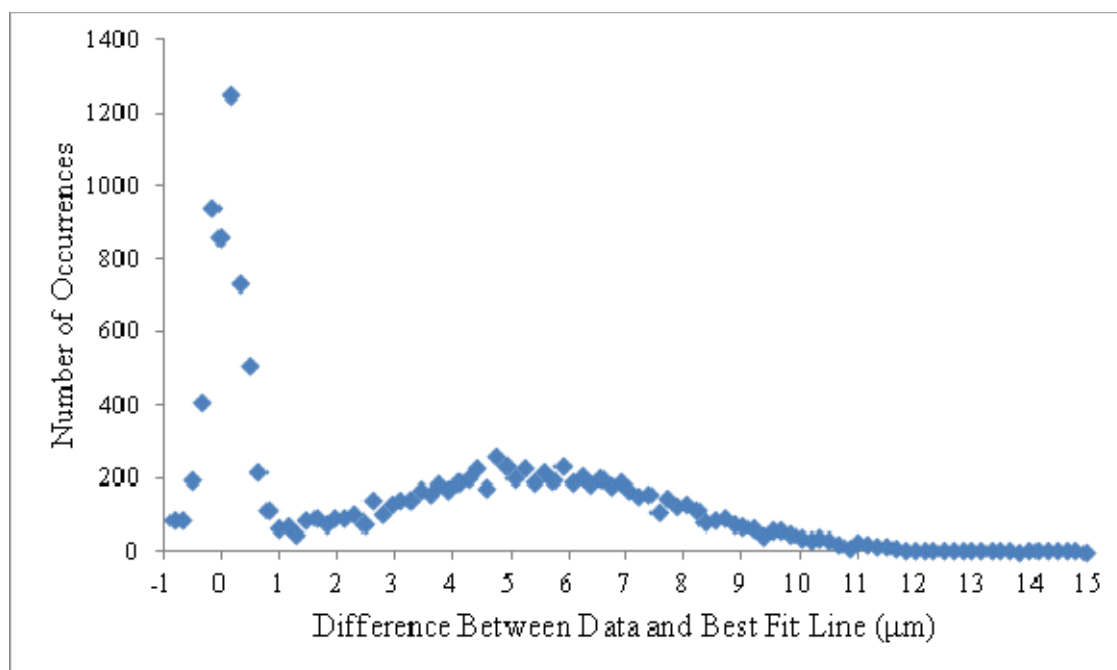


Figure B-10: LFD Histogram for Run 106

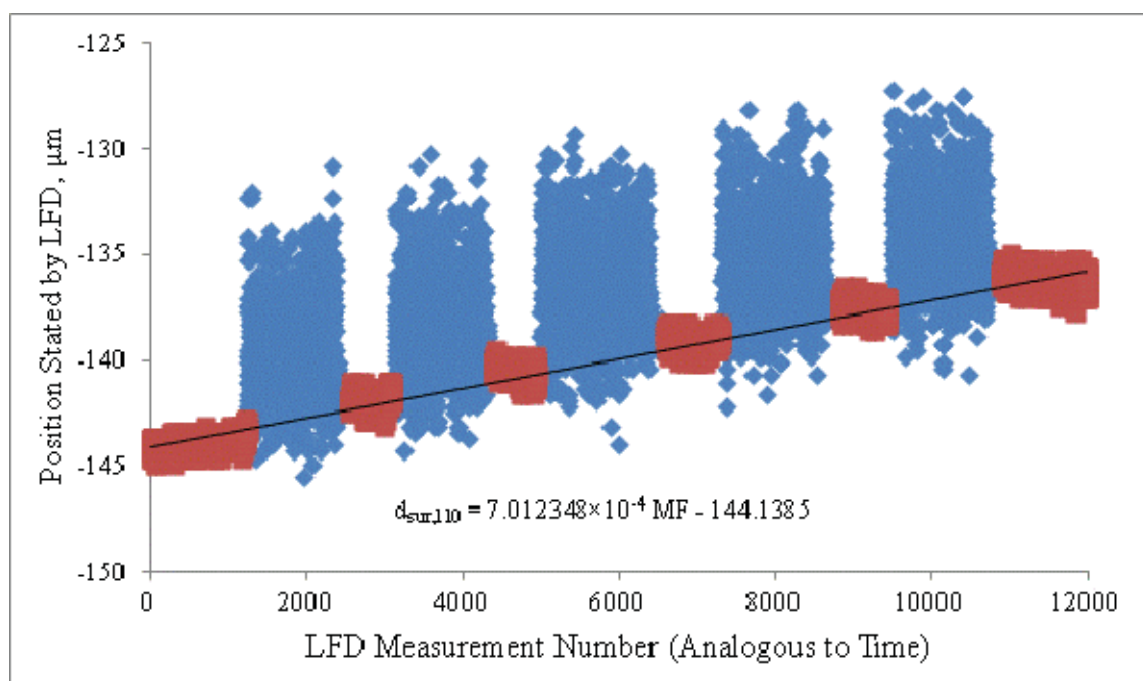


Figure B-11: Position of the Aluminum Substrate Stated by the LFD for Run 110

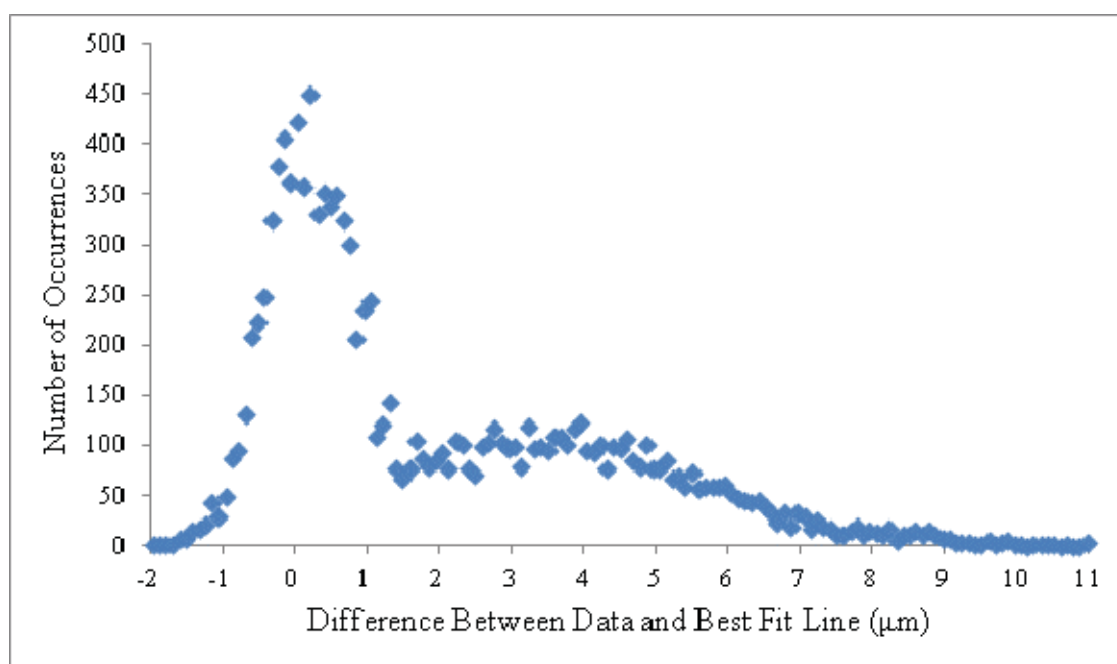


Figure B-12: LFD Histogram for Run 110

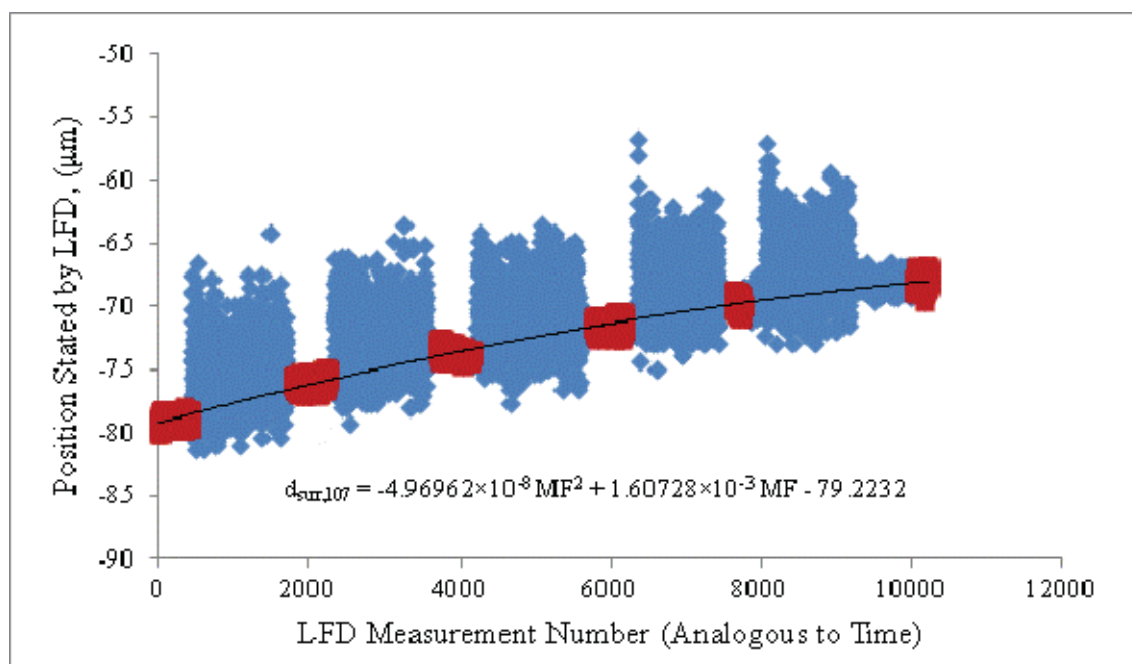


Figure B-13: Position of the Aluminum Substrate Stated by the LFD for Run 107

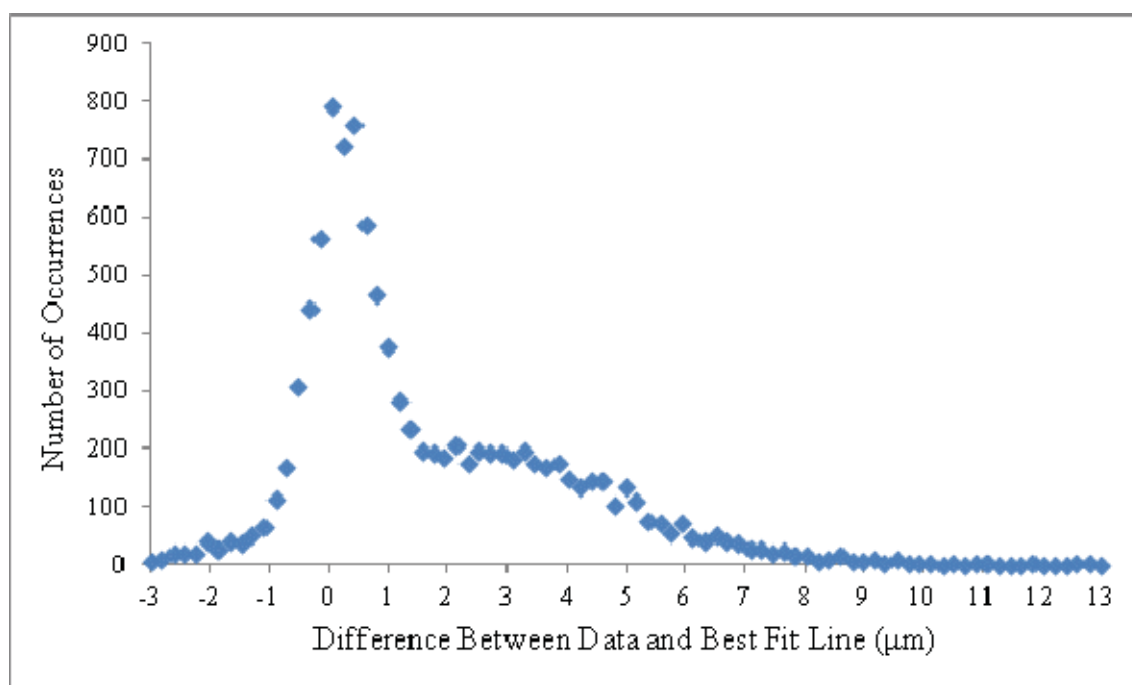


Figure B-14: LFD Histogram for Run 107

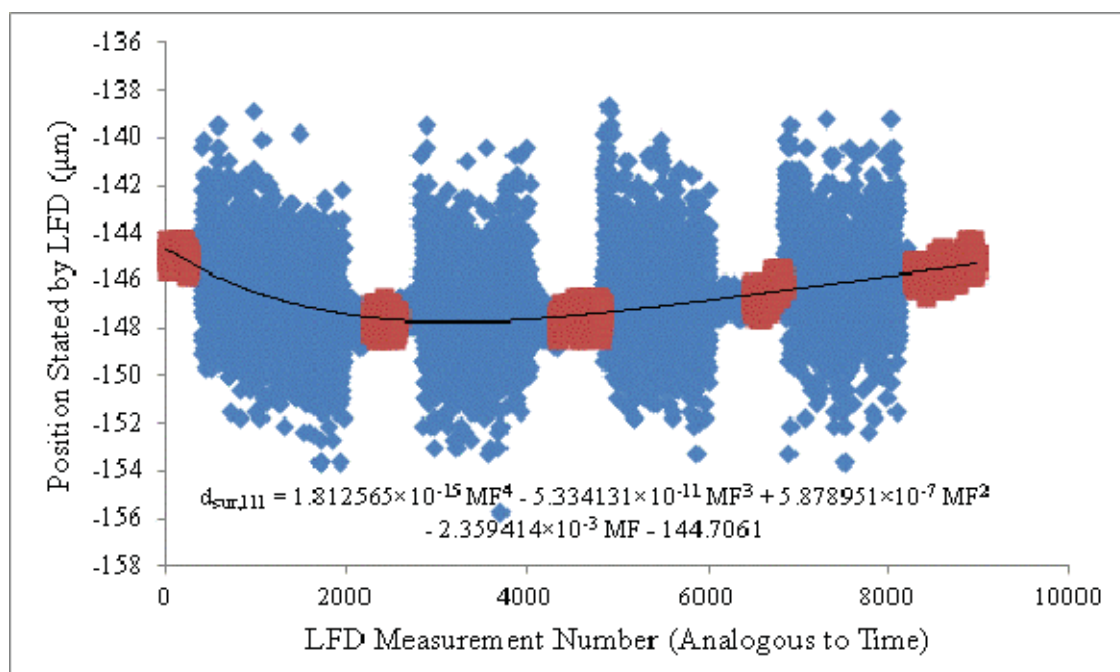


Figure B-15: Position of the Aluminum Substrate Stated by the LFD for Run 111

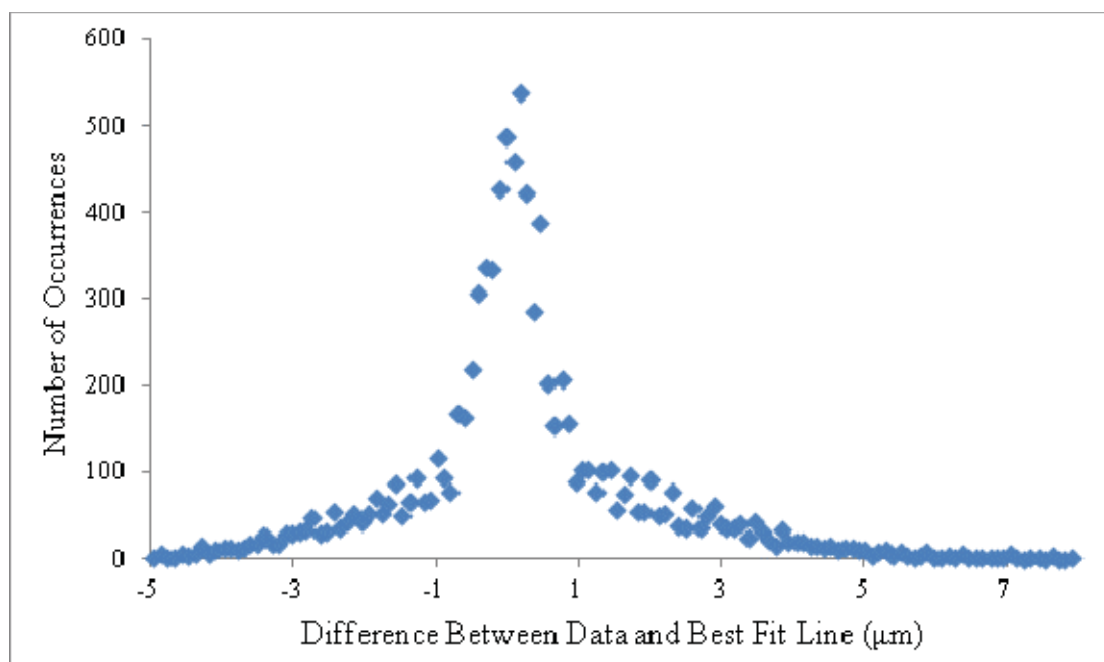


Figure B-16: LFD Histogram for Run 111

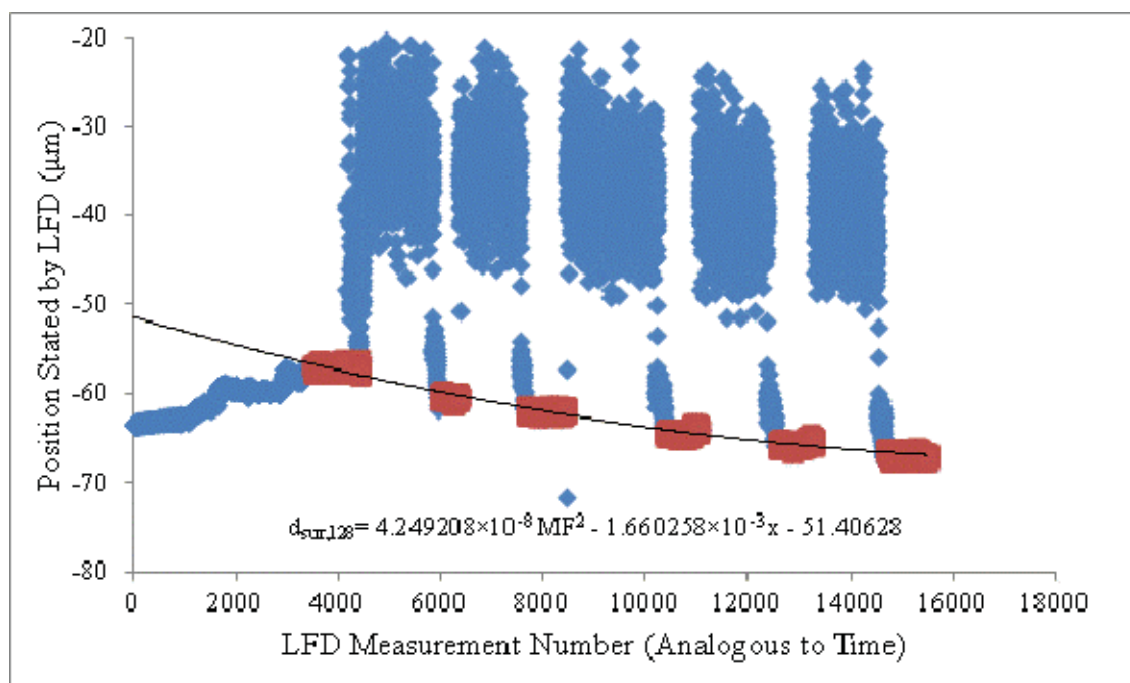


Figure B-17: Position of the Aluminum Substrate Stated by the LFD for Run 128

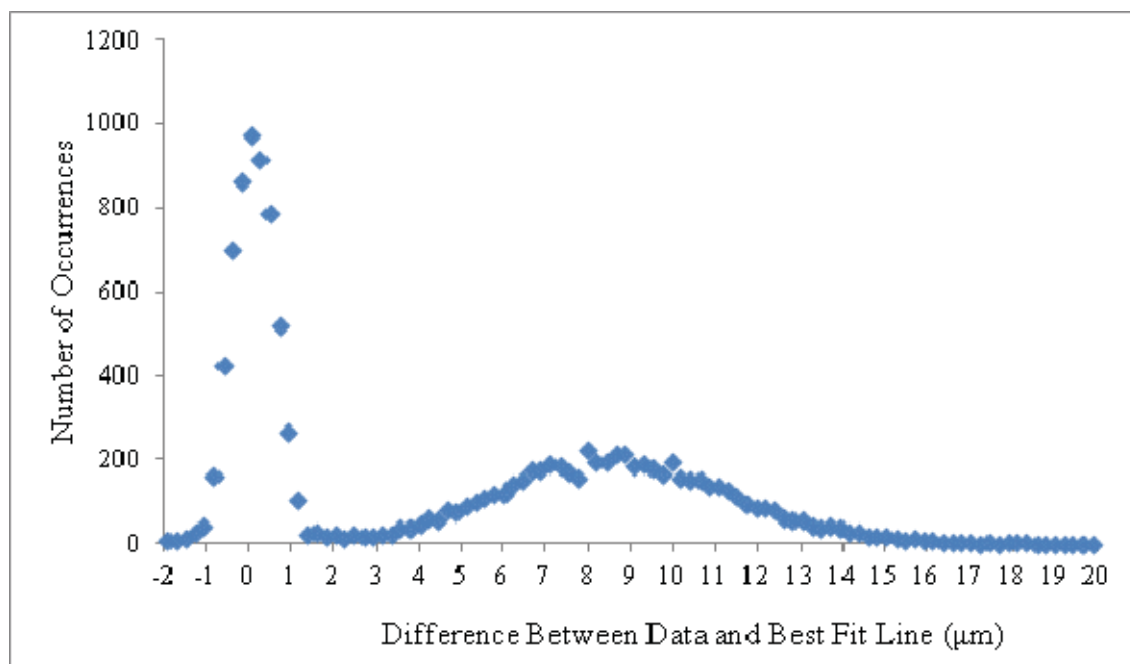


Figure B-18: LFD Histogram for Run 128

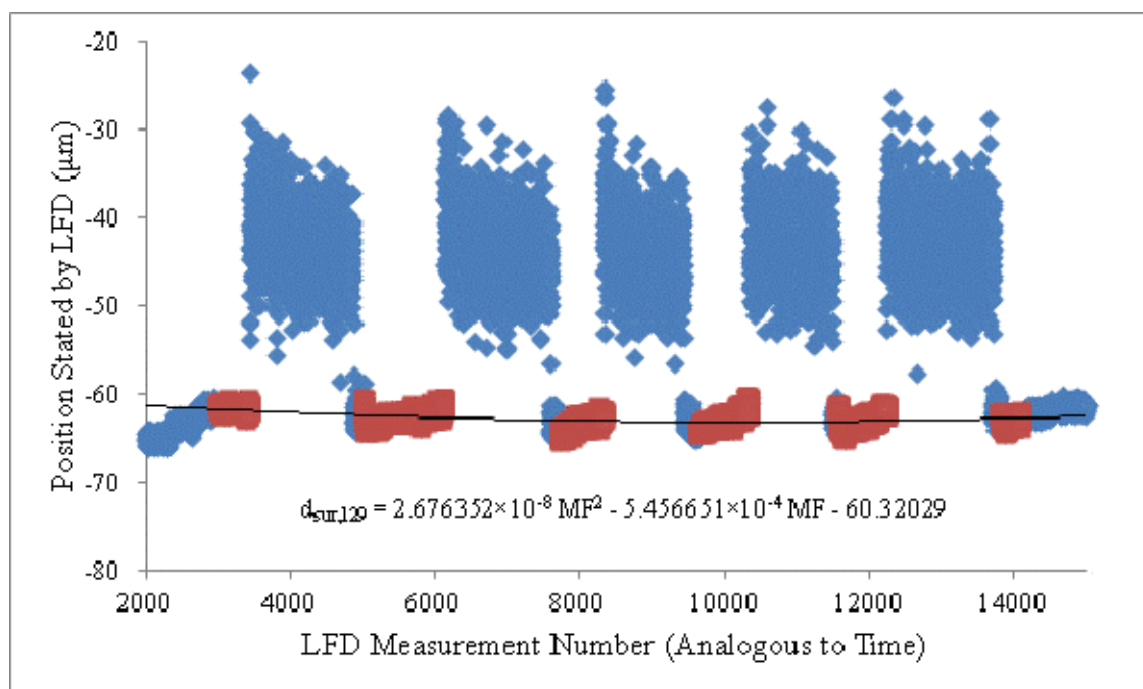


Figure B-19: Position of the Aluminum Substrate Stated by the LFD for Run 129

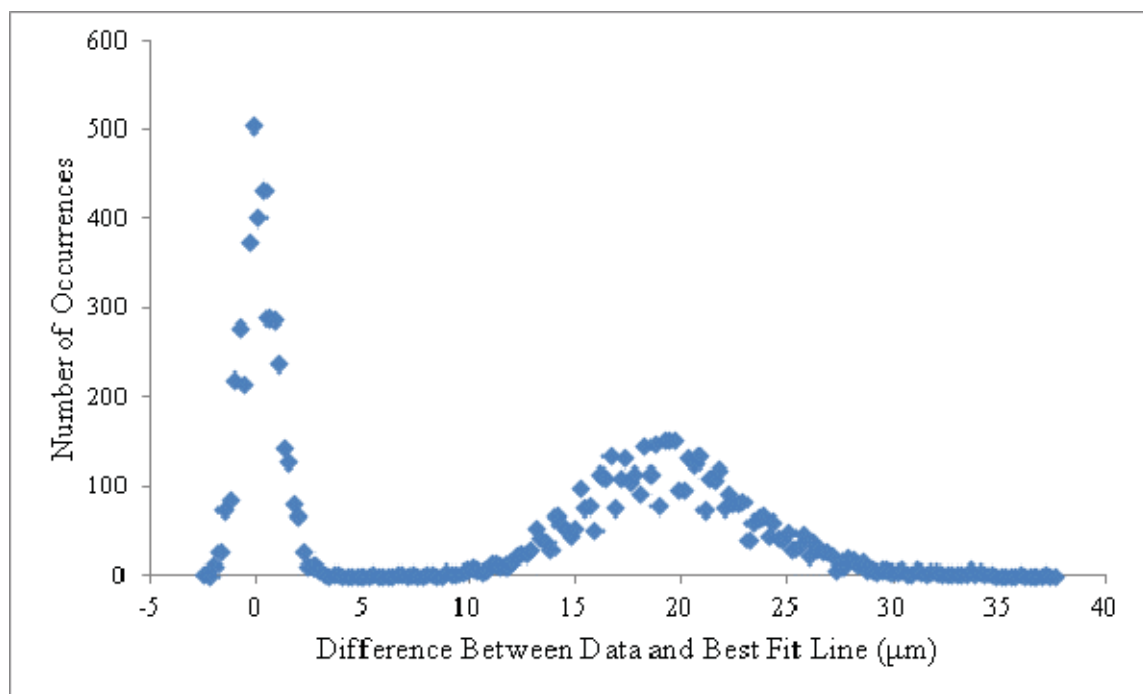


Figure B-20: LFD Histogram for Run 129

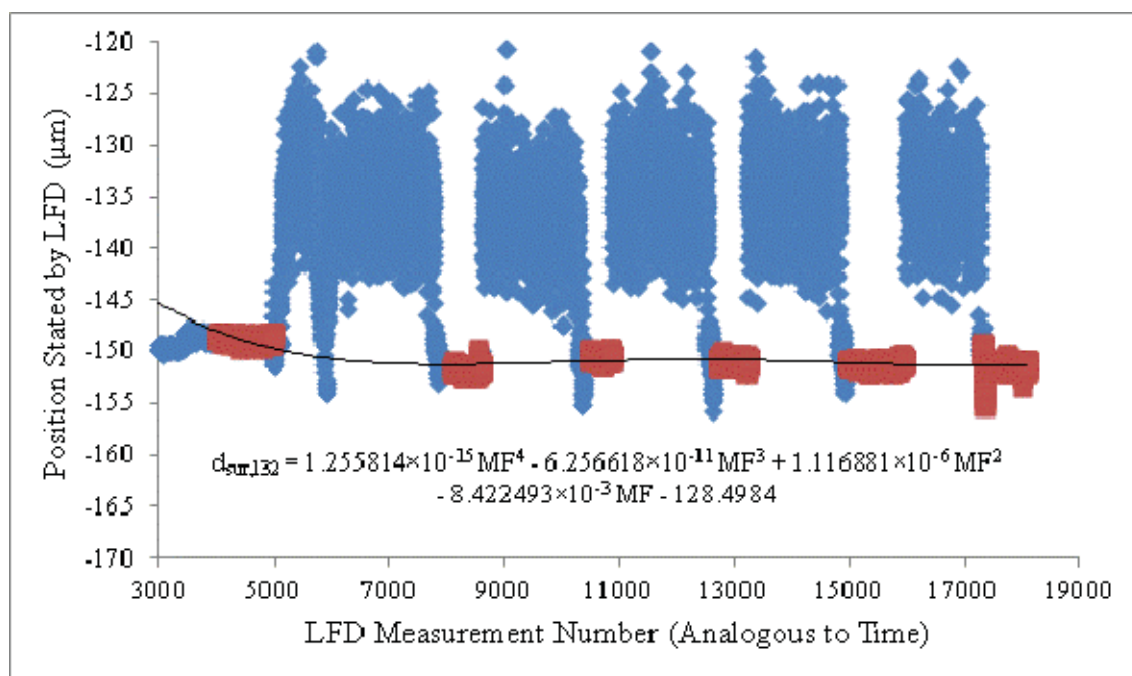


Figure B-21: Position of the Aluminum Substrate Stated by the LFD for Run 132

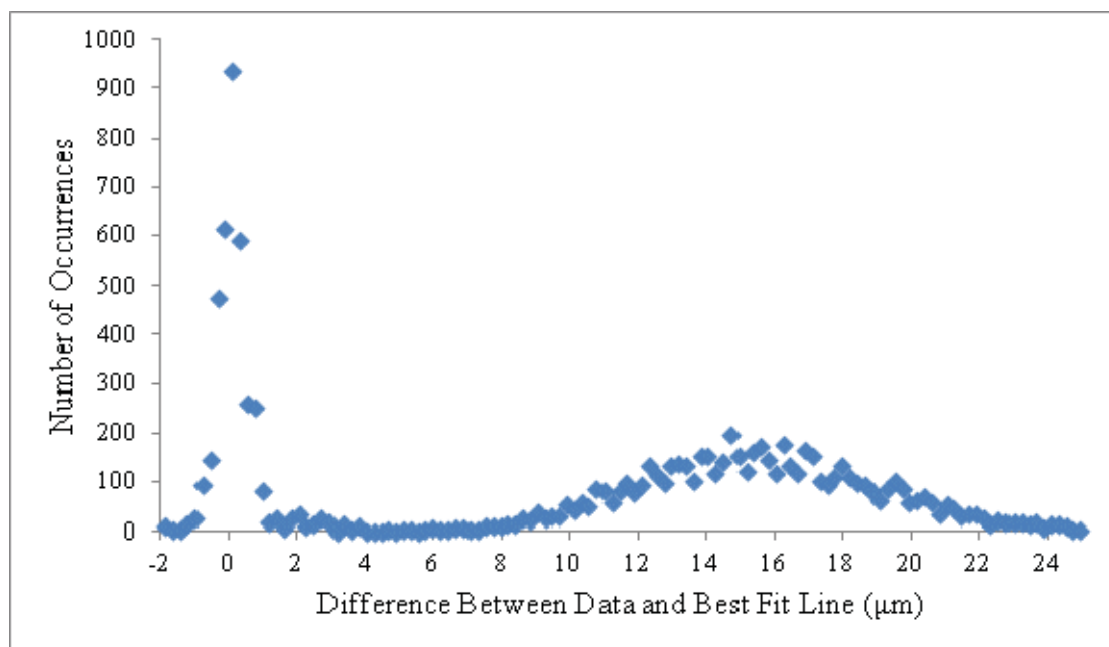


Figure B-22: LFD Histogram for Run 132

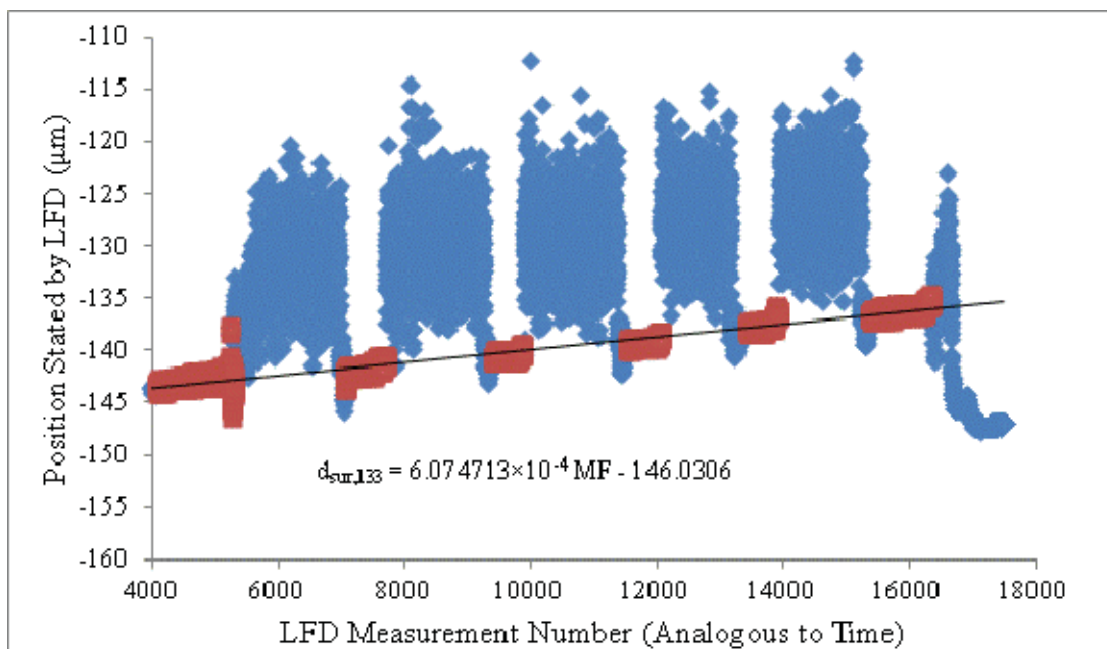


Figure B-23: Position of the Aluminum Substrate Stated by the LFD for Run 133

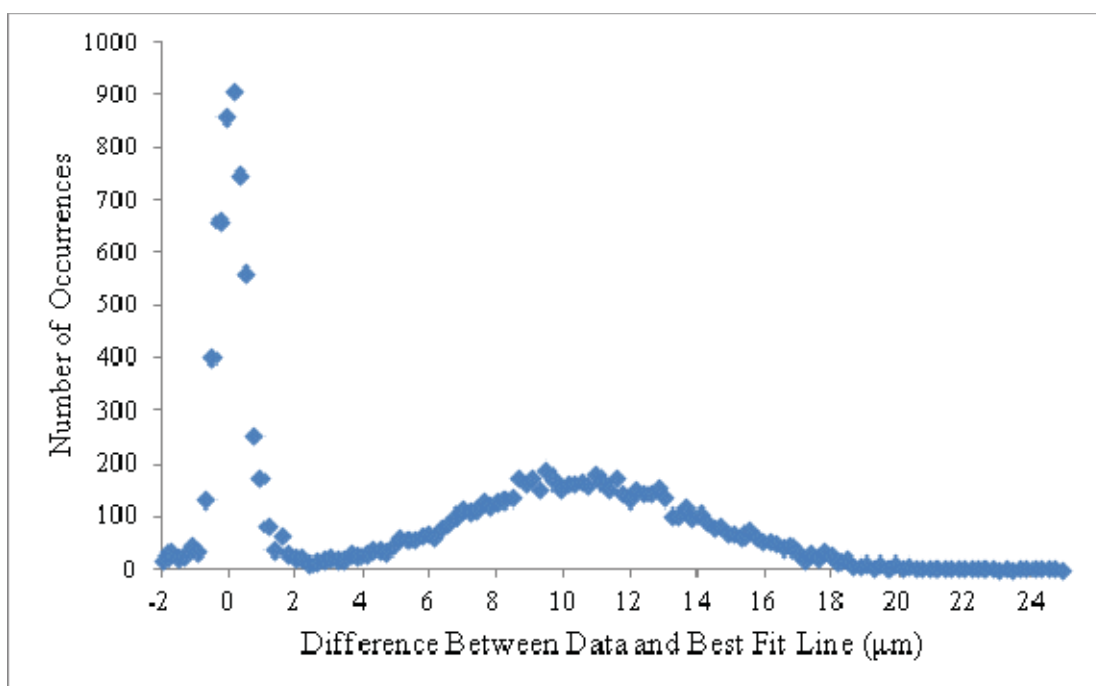


Figure B-24: LFD Histogram for Run 133

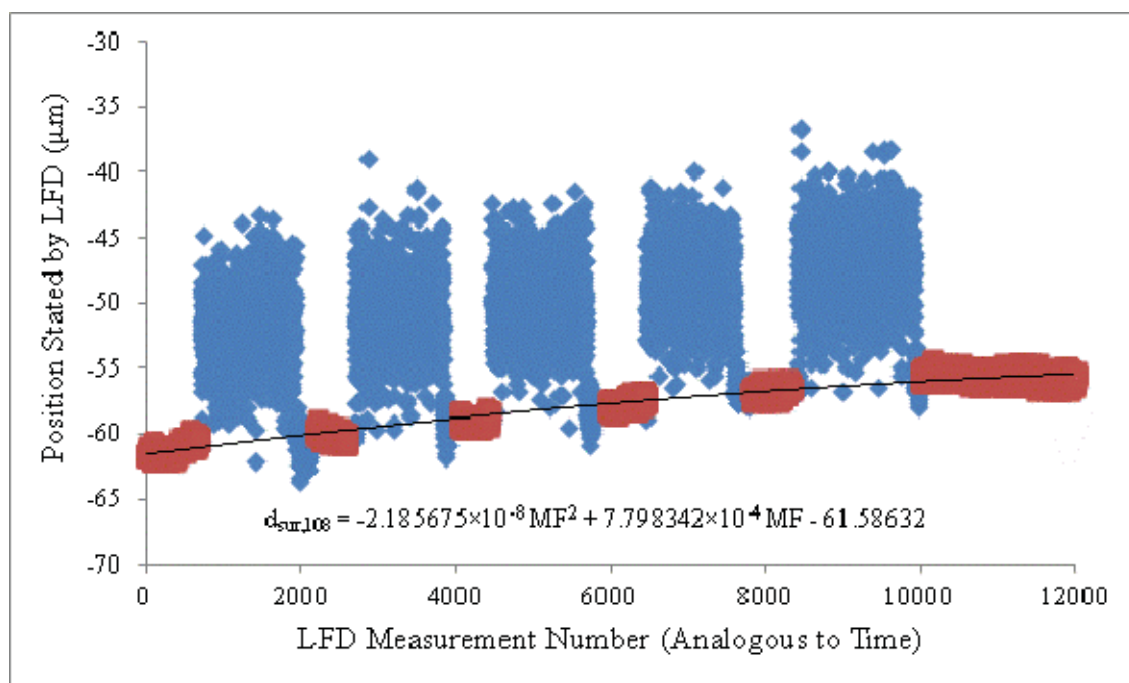


Figure B-25: Position of the Aluminum Substrate Stated by the LFD for Run 108

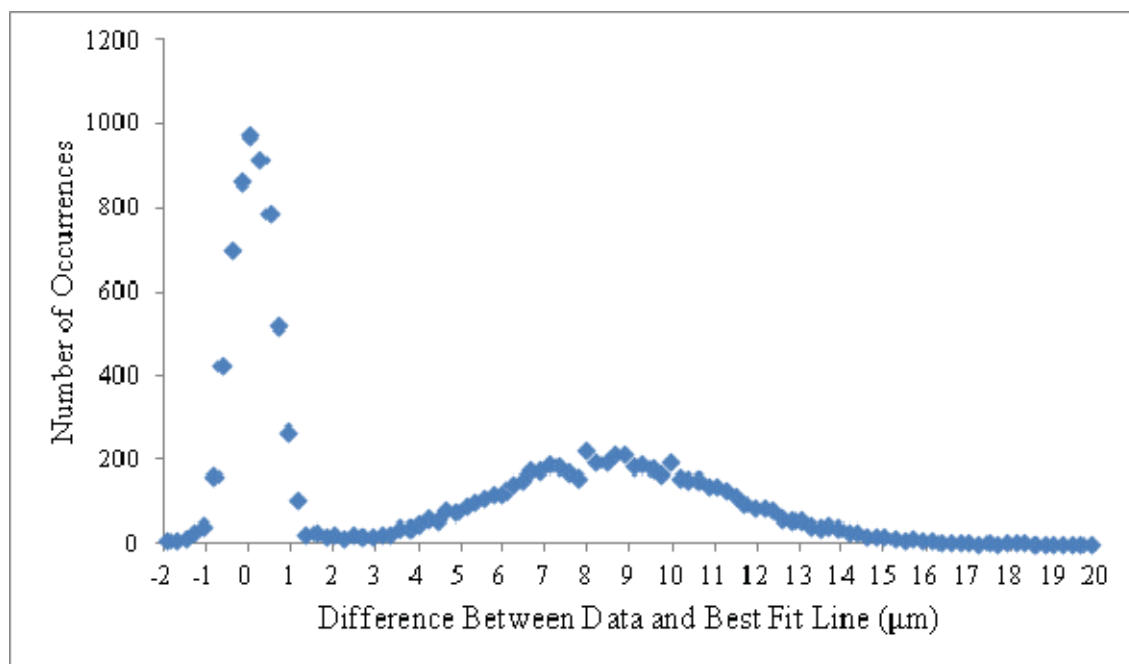


Figure B-26: LFD Histogram for Run 108

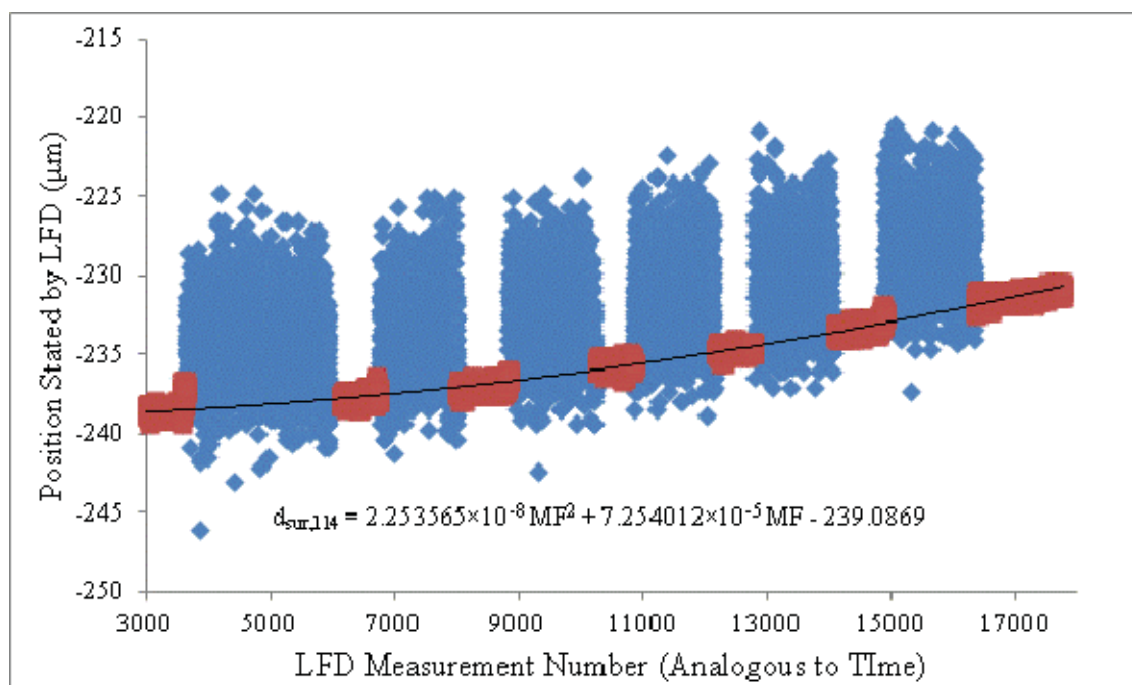


Figure B-27: Position of the Aluminum Substrate Stated by the LFD for Run 114

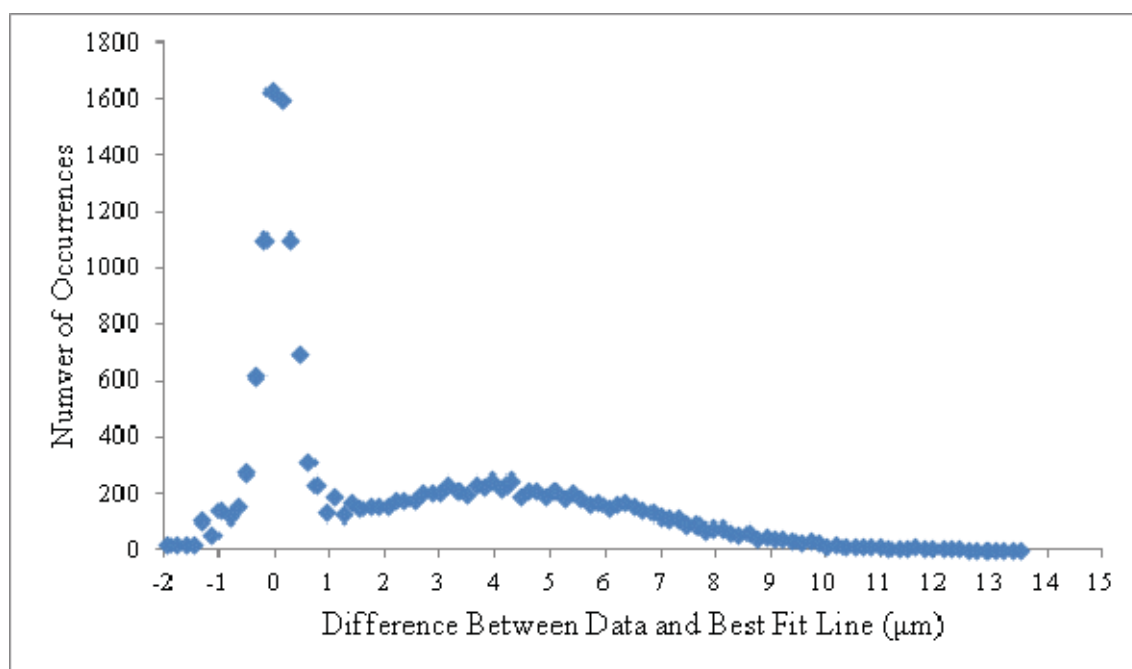


Figure B-28: LFD Histogram for Run 114

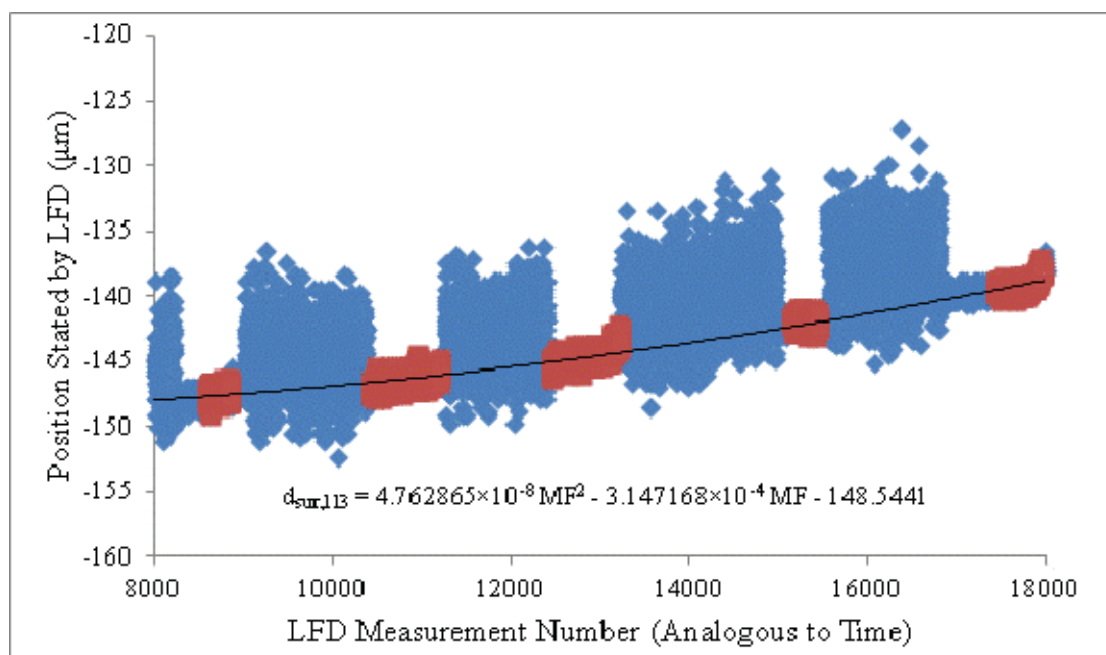


Figure B-29: Position of the Aluminum Substrate Stated by the LFD for Run 113

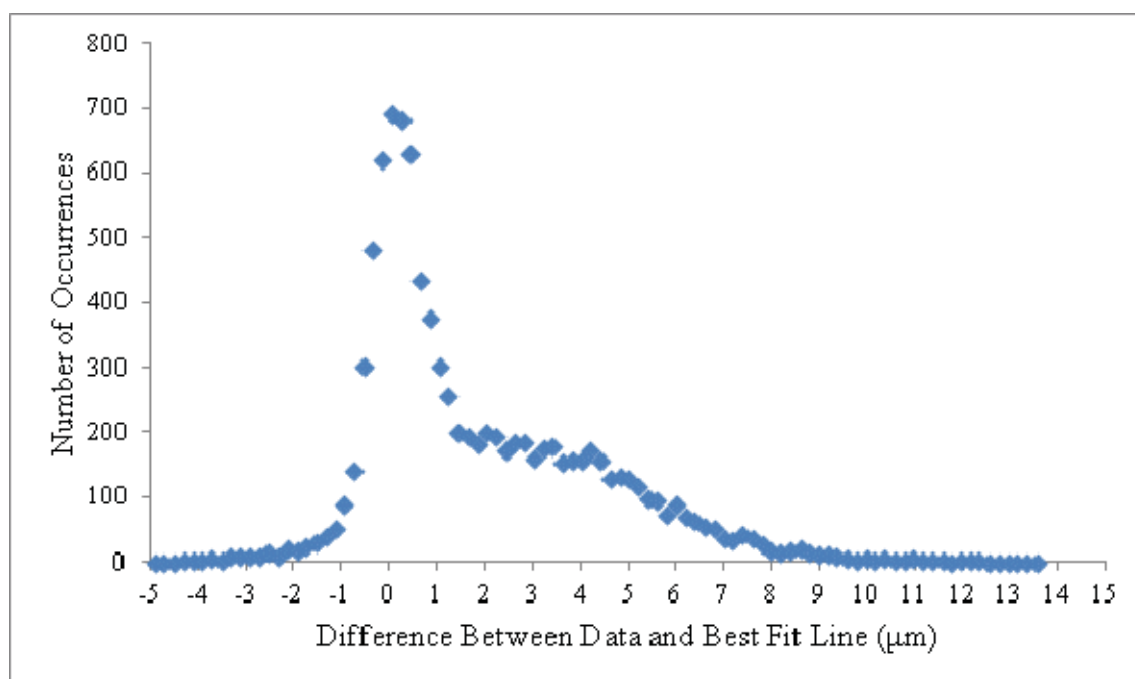


Figure B-30: LFD Histogram for Run 113

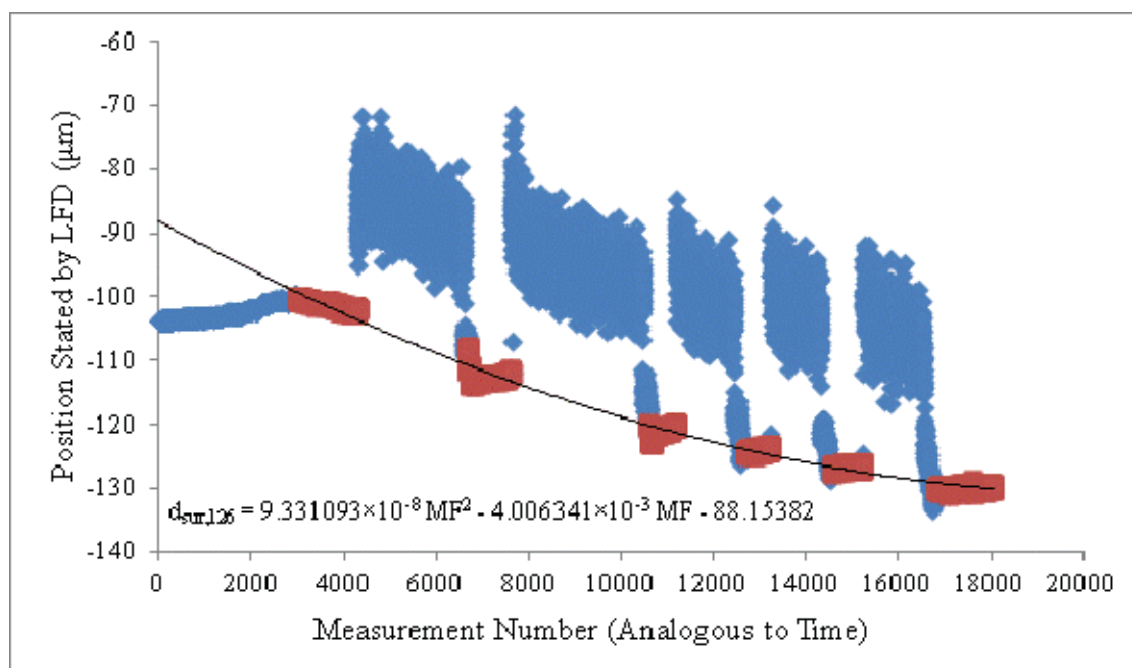


Figure B-31: Position of the Aluminum Substrate Stated by the LFD for Run 126

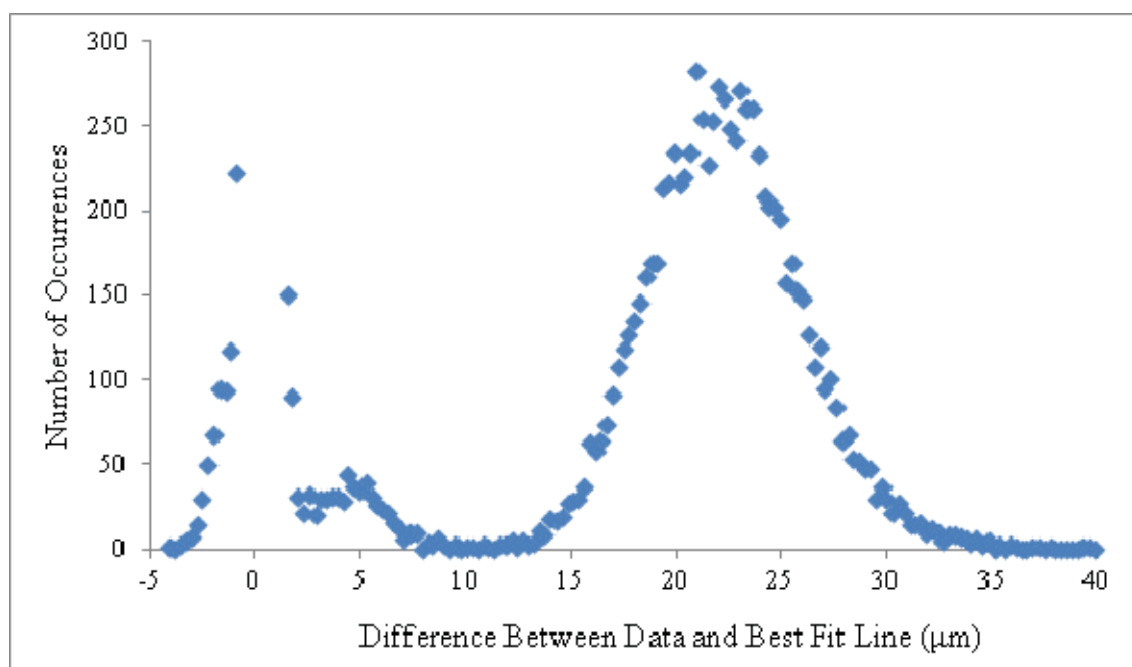


Figure B-32: LFD Histogram for Run 126

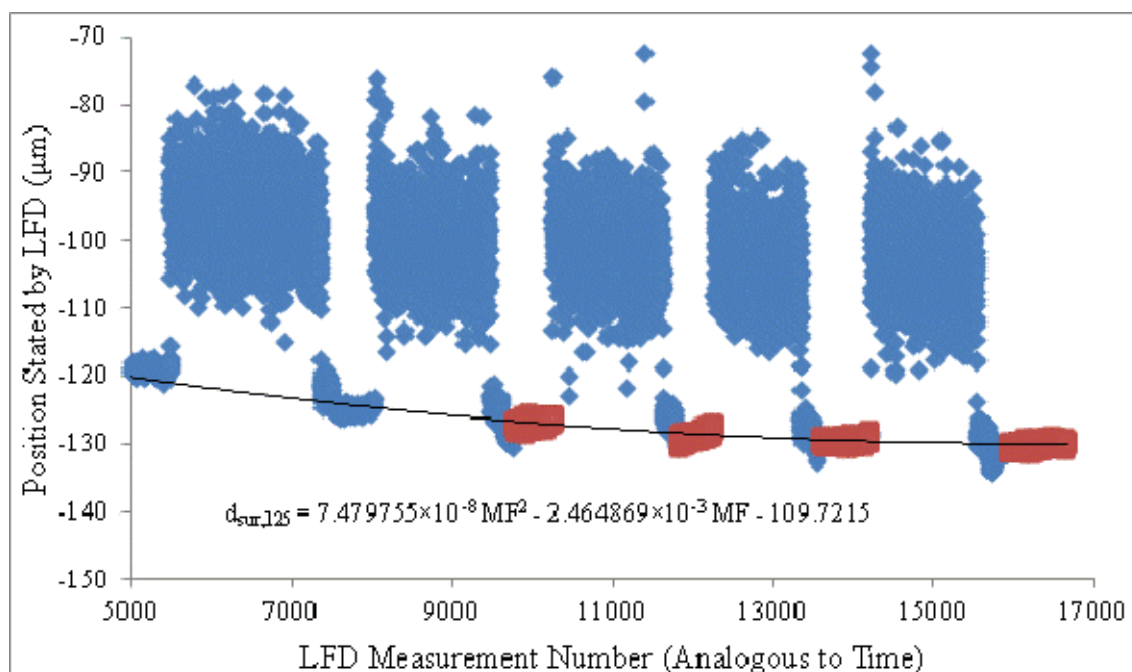


Figure B-33: Position of the Aluminum Substrate Stated by the LFD for Run 125

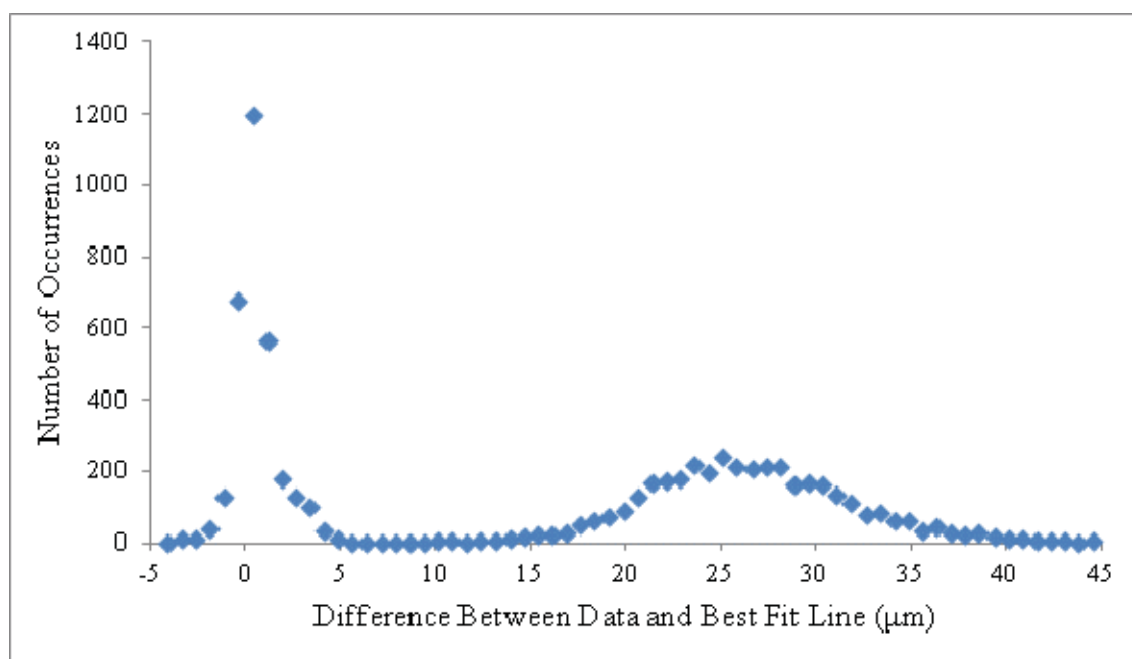


Figure B-34: LFD Histogram for Run 125

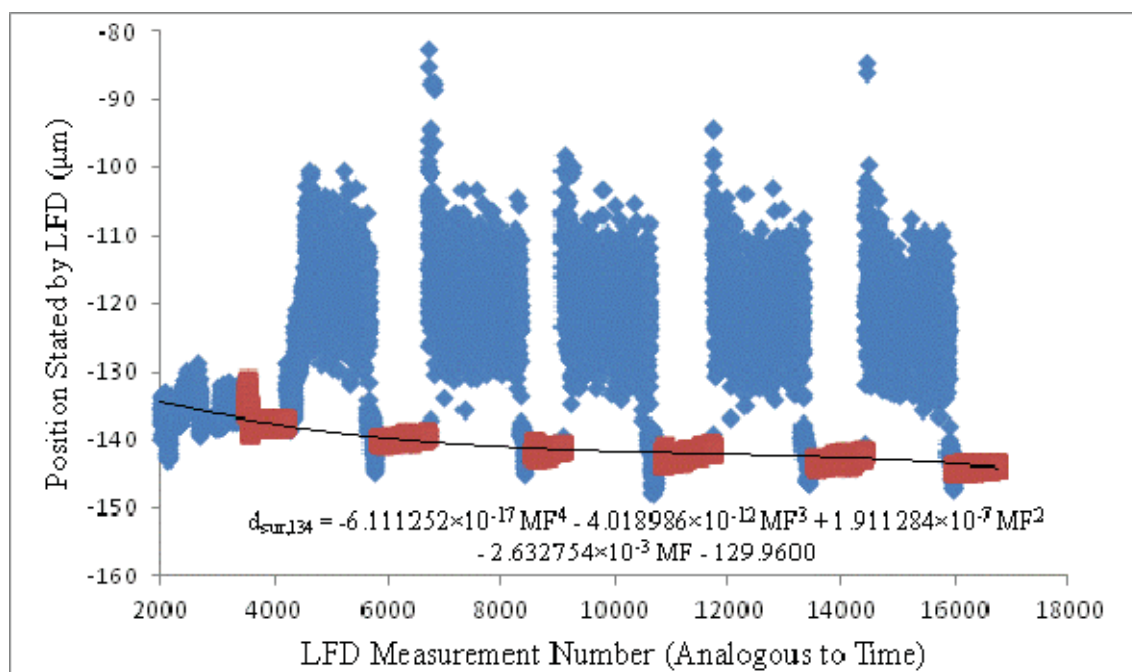


Figure B-35: Position of the Aluminum Substrate Stated by the LFD for Run 134

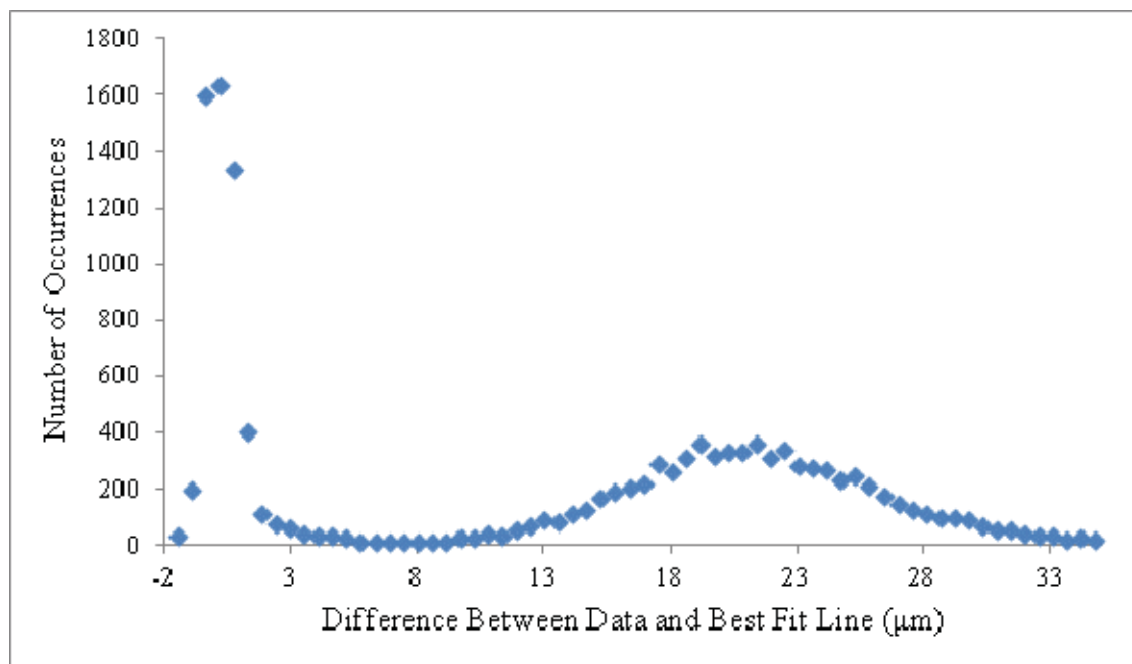


Figure B-36: LFD Histogram for Run 134

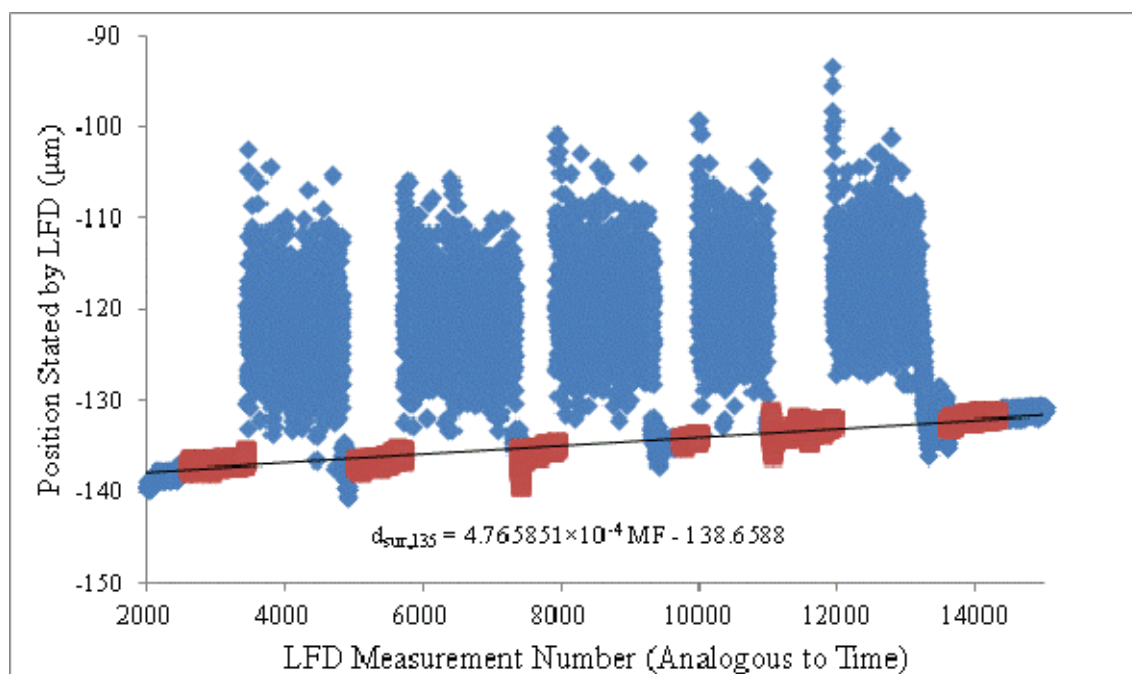


Figure B-37: Position of the Aluminum Substrate Stated by the LFD for Run 135

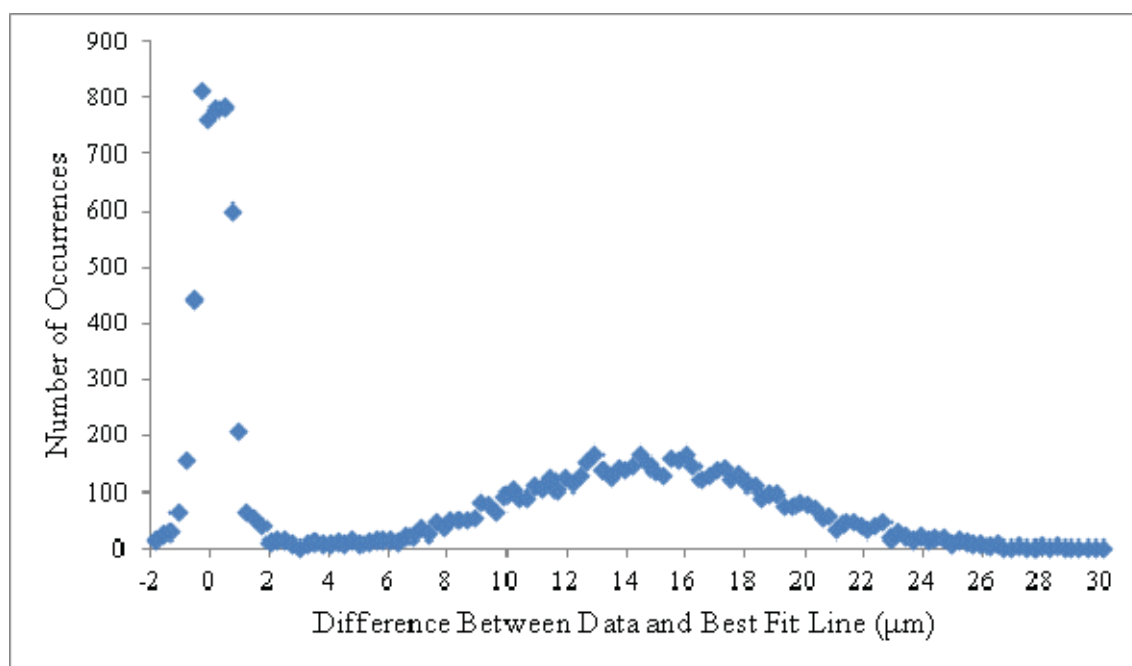


Figure B-38: LFD Histogram for Run 135

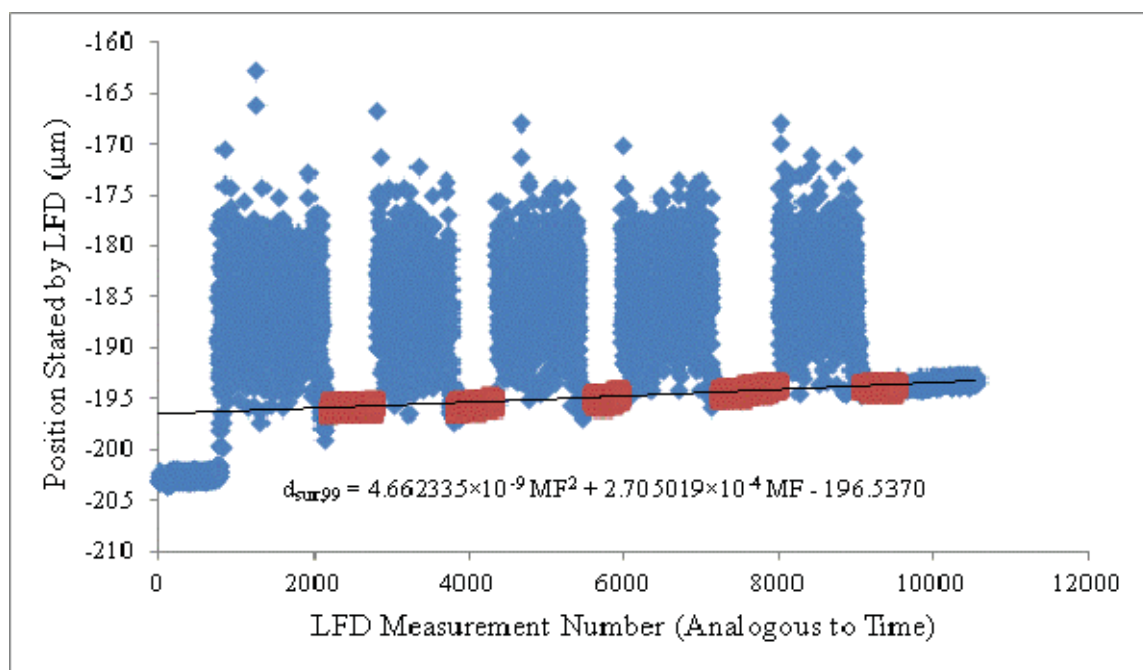


Figure B-39: Position of the Aluminum Substrate Stated by the LFD for Run 99

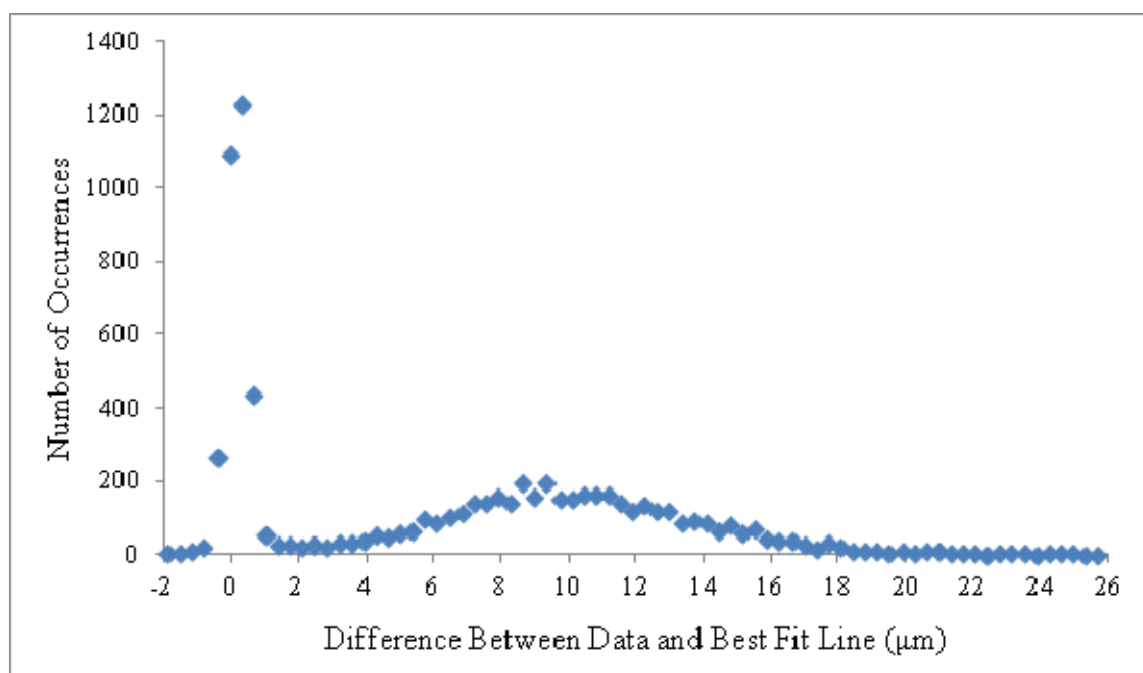


Figure B-40: LFD Histogram for Run 99

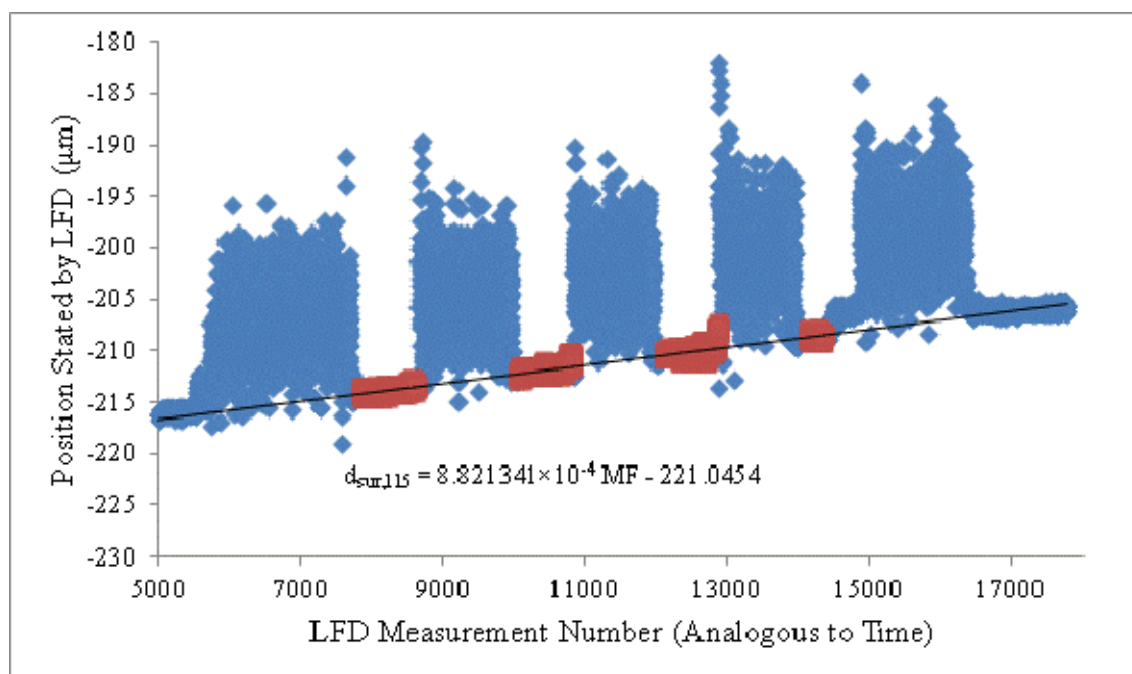


Figure B-41: Position of the Aluminum Substrate Stated by the LFD for Run 115

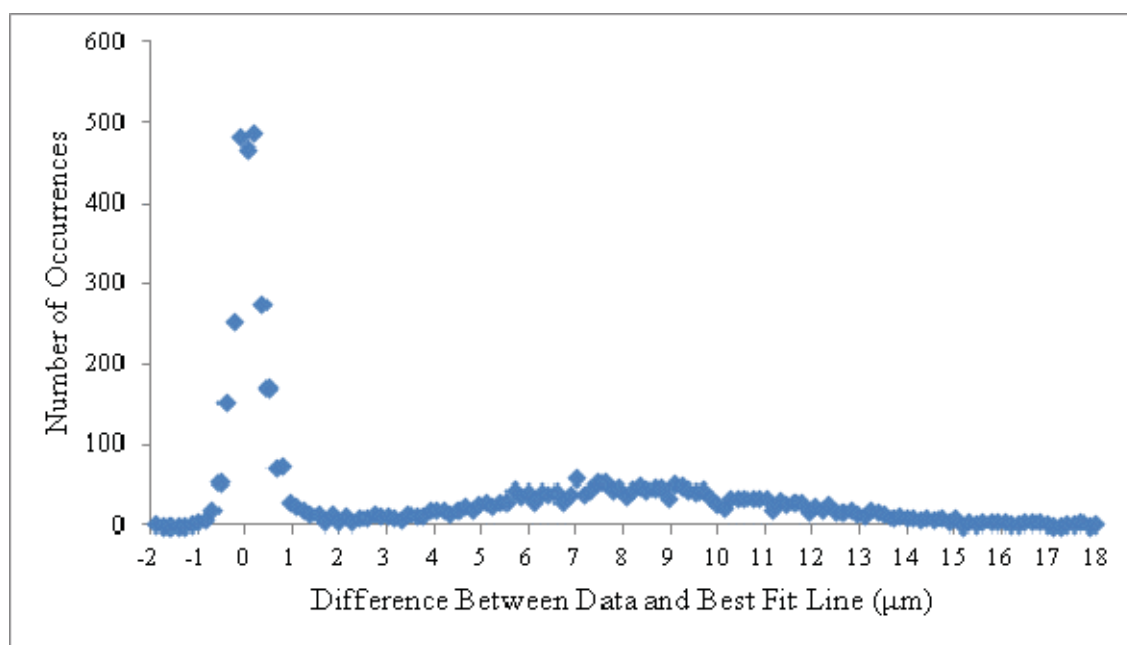


Figure B-42: LFD Histogram for Run 115

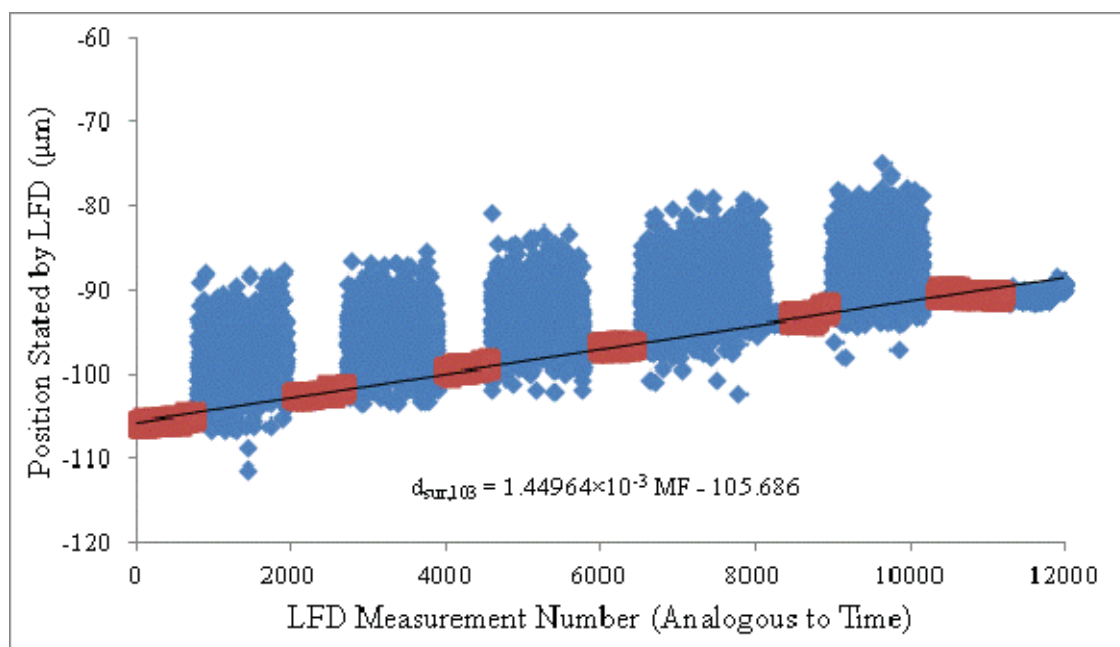


Figure B-43: Position of the Aluminum Substrate Stated by the LFD for Run 103

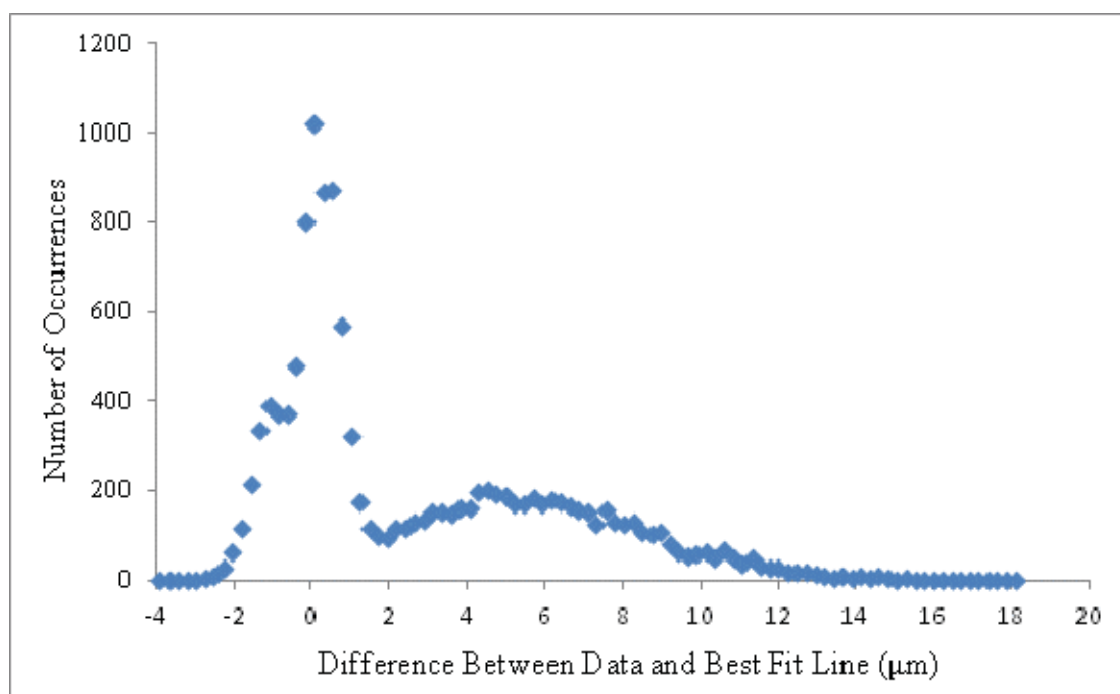


Figure B-44: LFD Histogram for Run 103

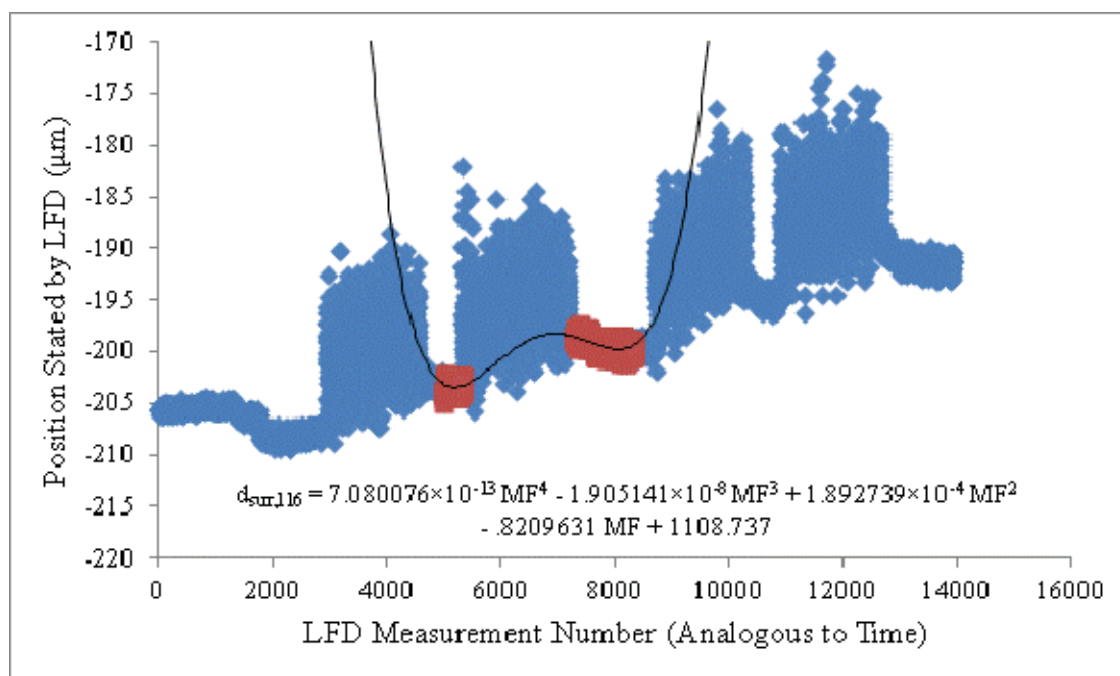


Figure B-45: Position of the Aluminum Substrate Stated by the LFD for Run 116

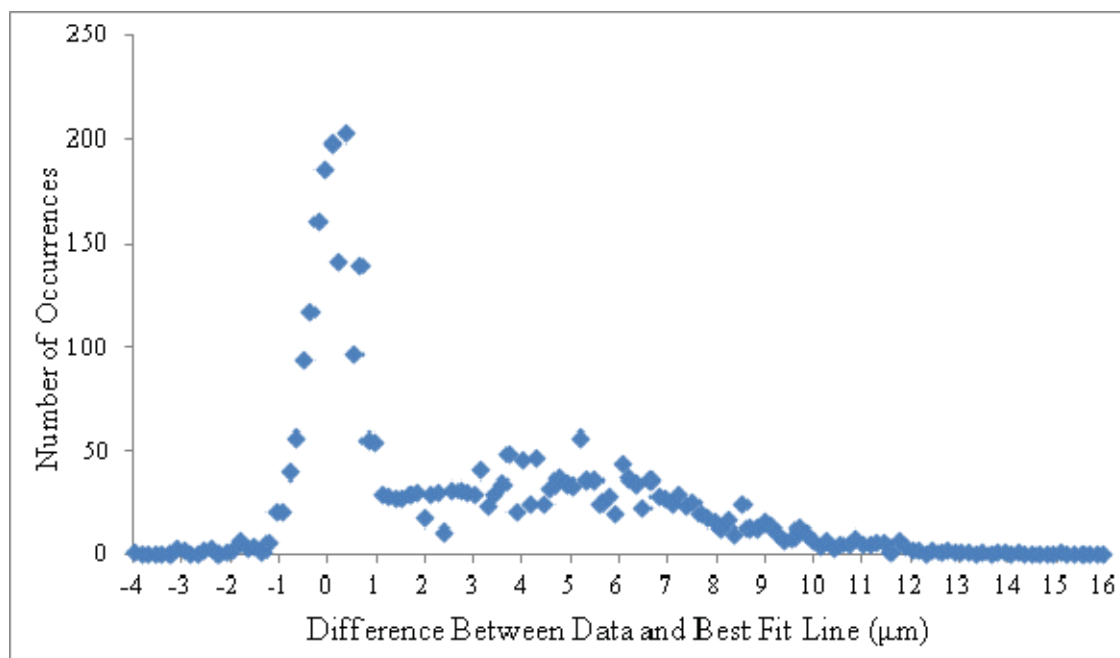


Figure B-46: LFD Histogram for Run 116

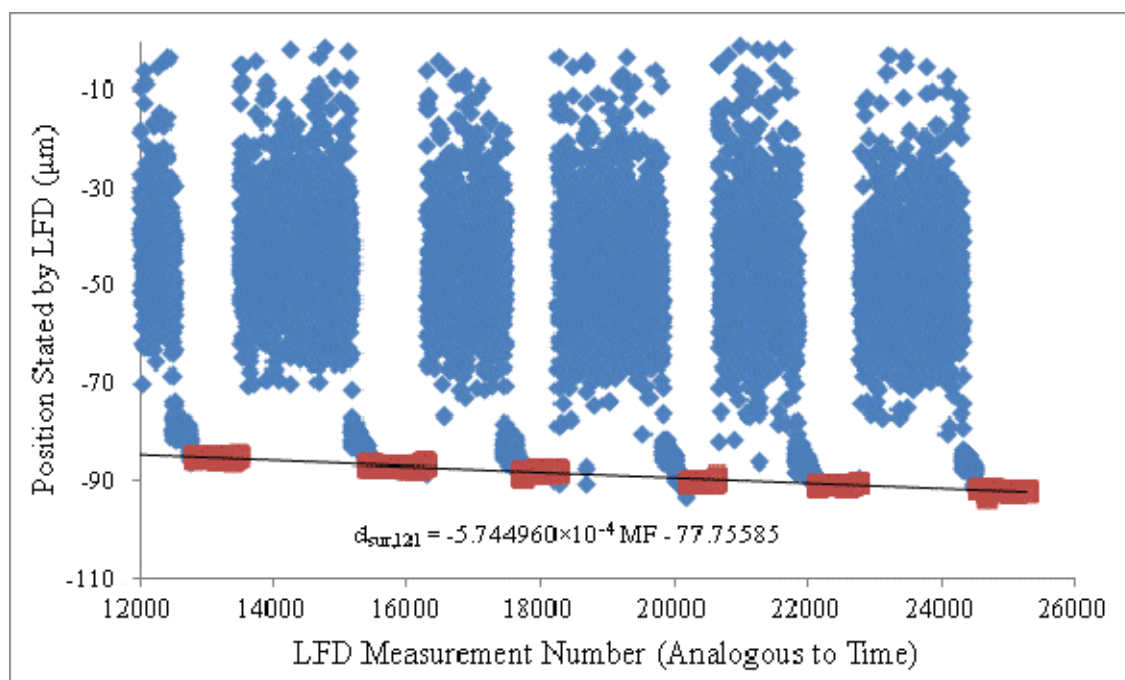


Figure B-47: Position of the Aluminum Substrate Stated by the LFD for Run 121

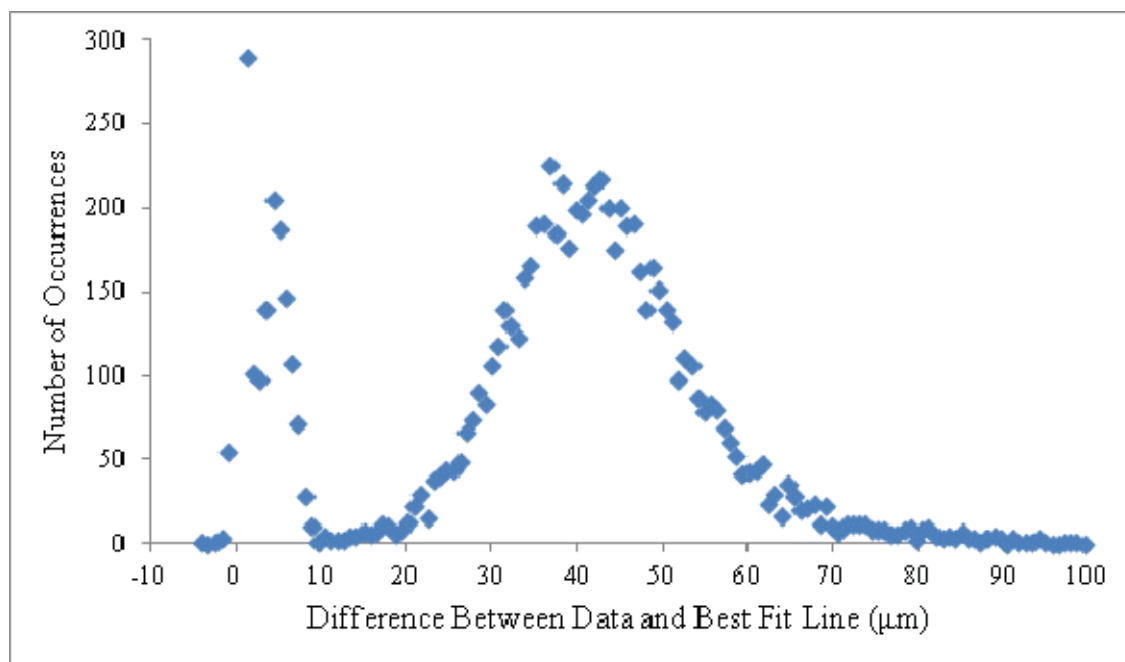


Figure B-48: LFD Histogram for Run 121

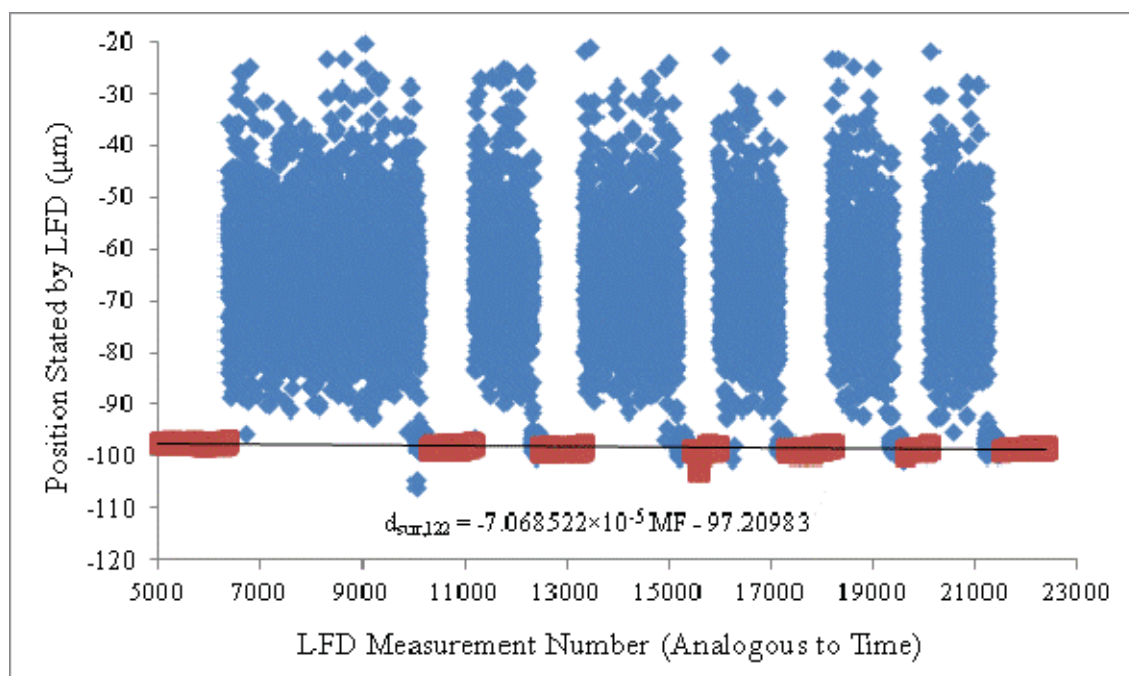


Figure B-49: Position of the Aluminum Substrate Stated by the LFD for Run 122

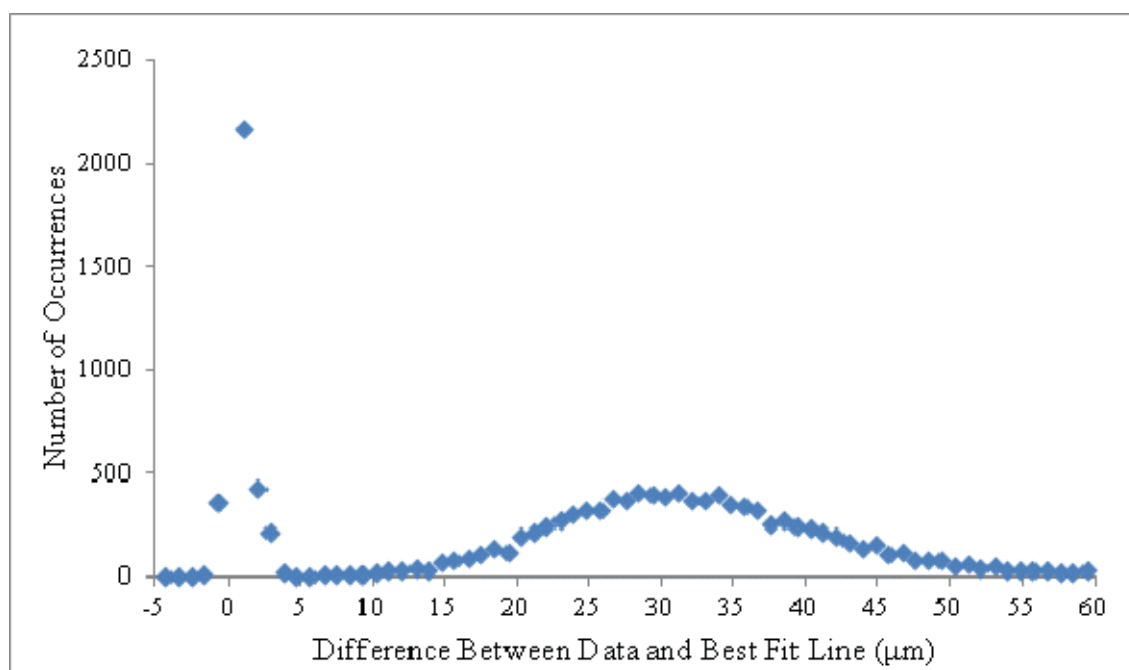


Figure B-50: LFD Histogram for Run 122

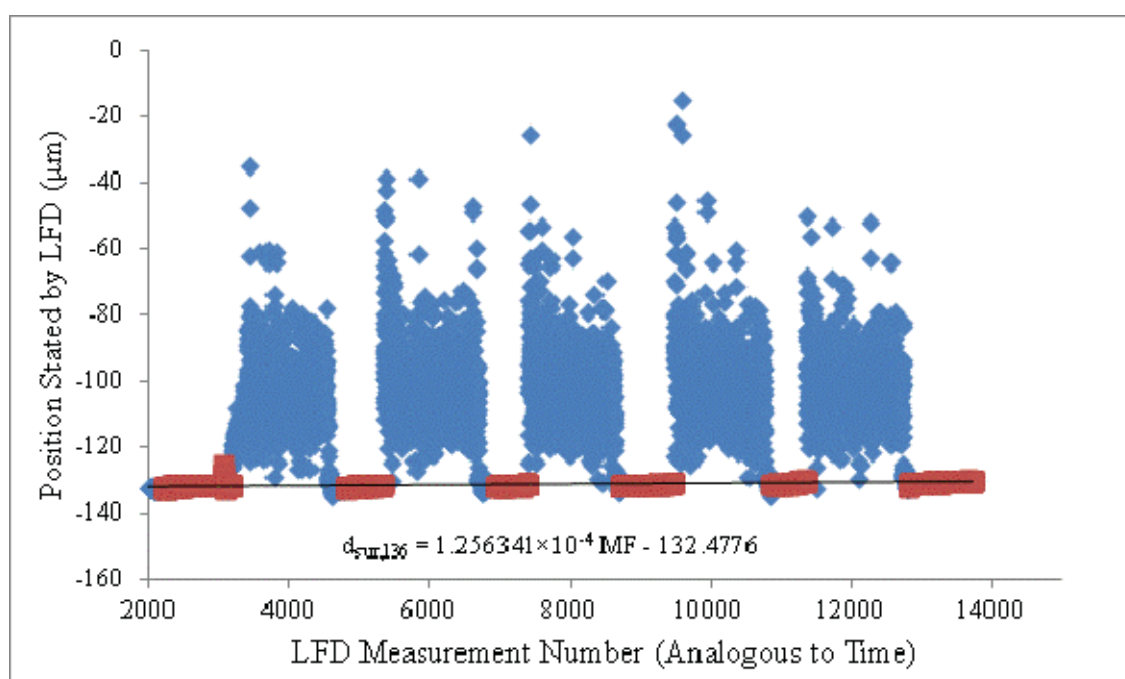


Figure B-51: Position of the Aluminum Substrate Stated by the LFD for Run 136

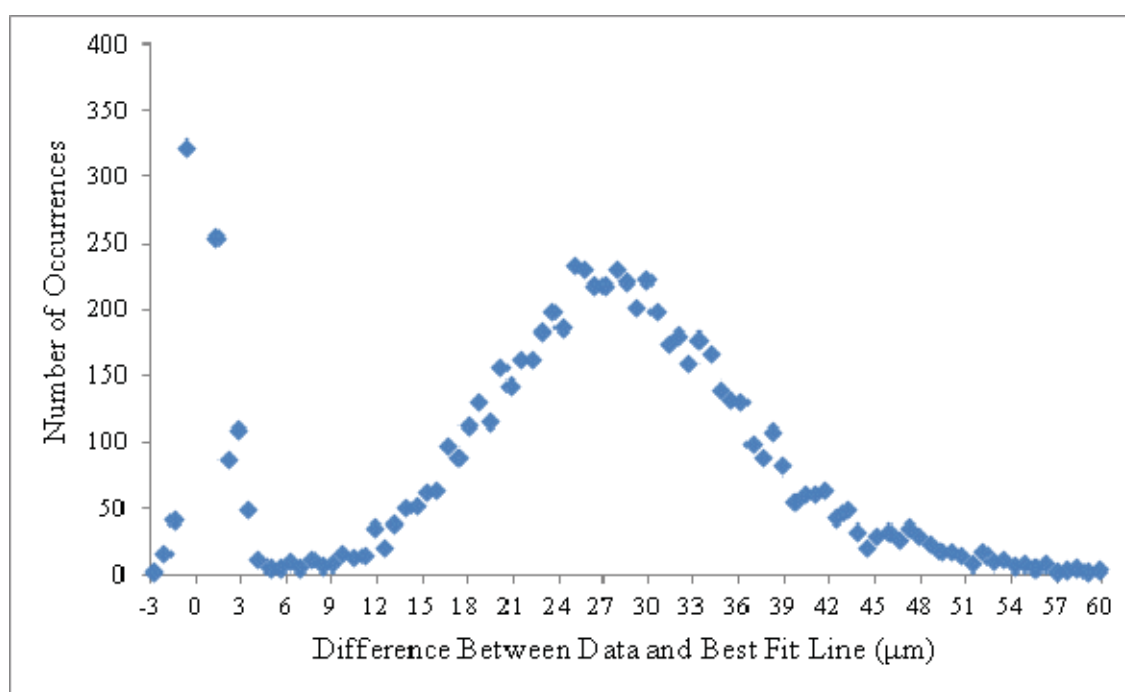


Figure B-52: LFD Histogram for Run 136

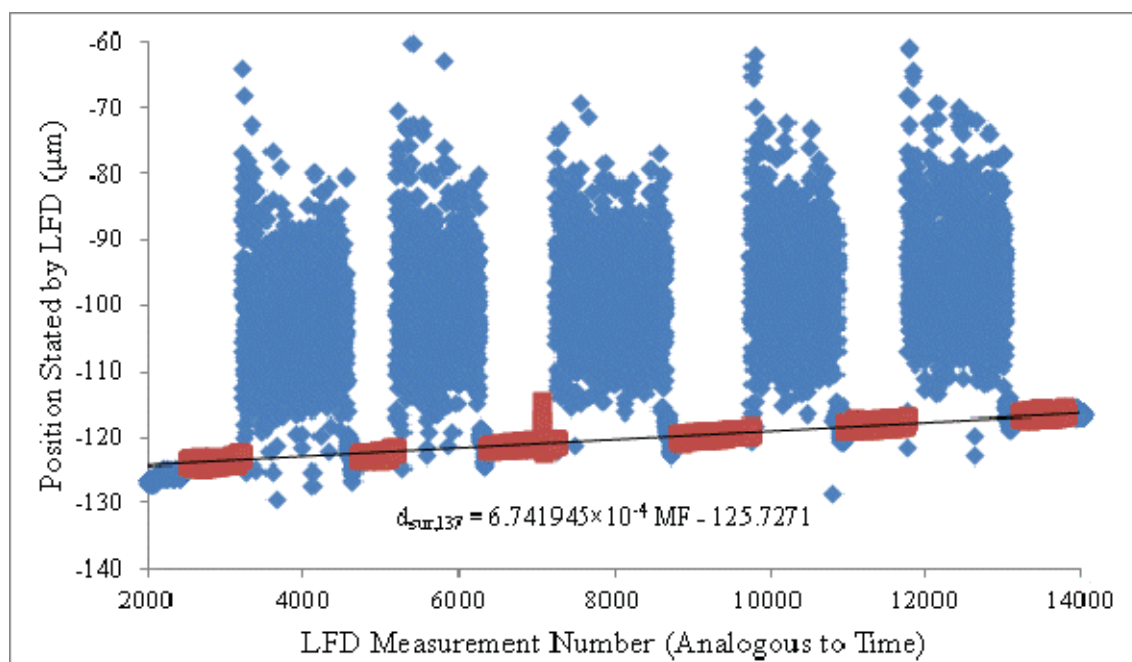


Figure B-53: Position of the Aluminum Substrate Stated by the LFD for Run 137

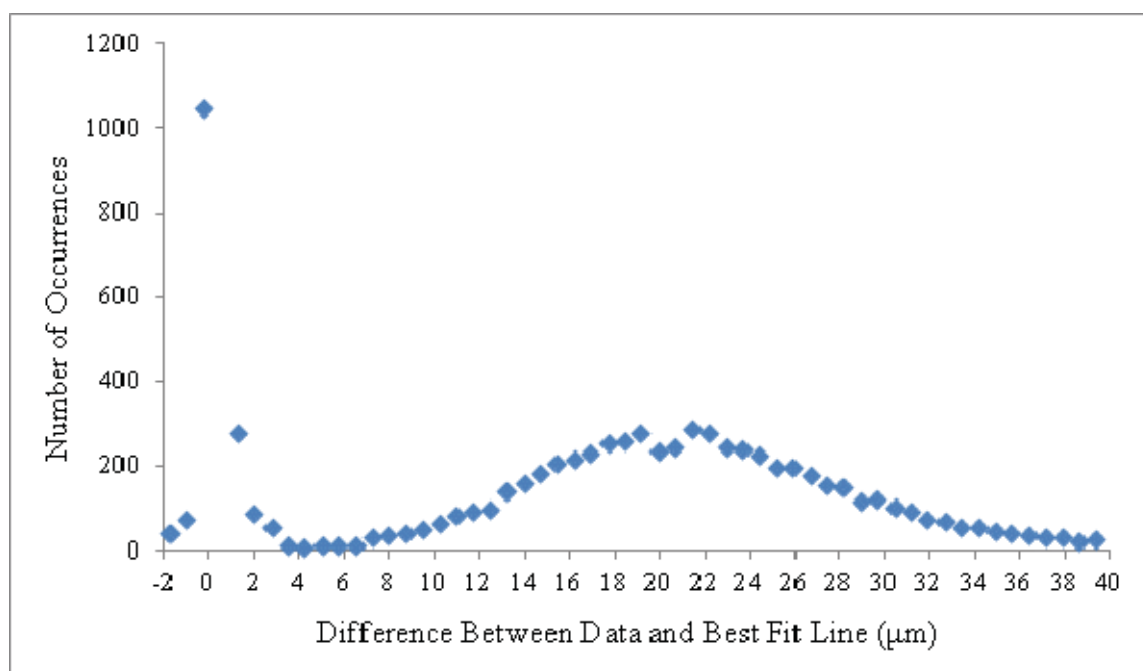


Figure B-54: LFD Histogram for Run 137

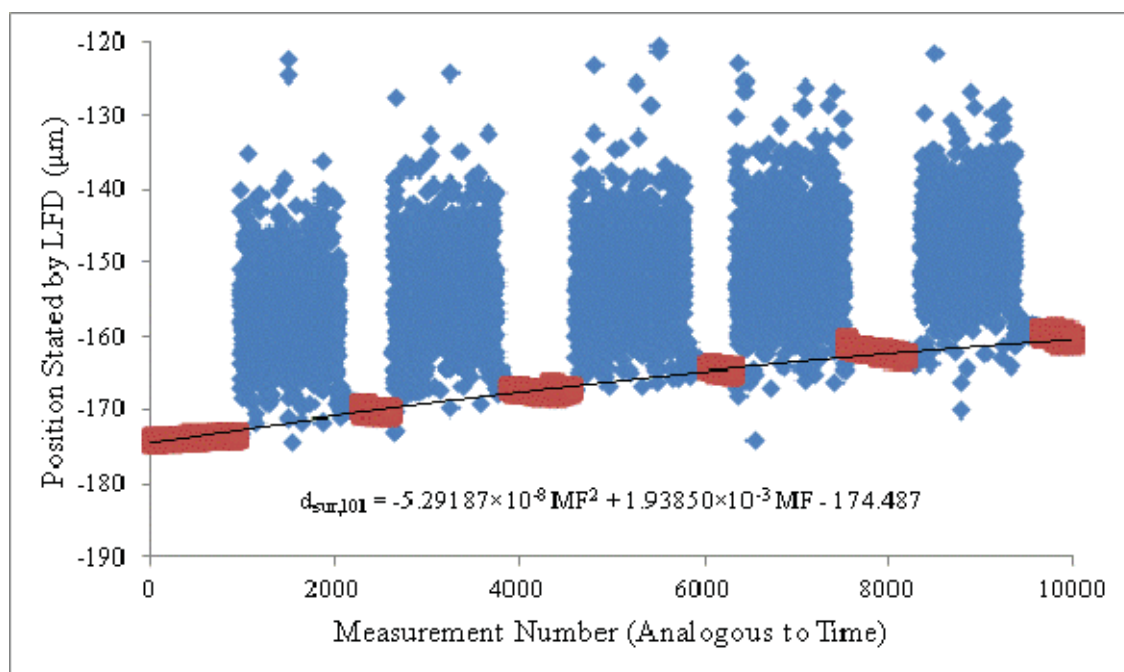


Figure B-55: Position of the Aluminum Substrate Stated by the LFD for Run 101

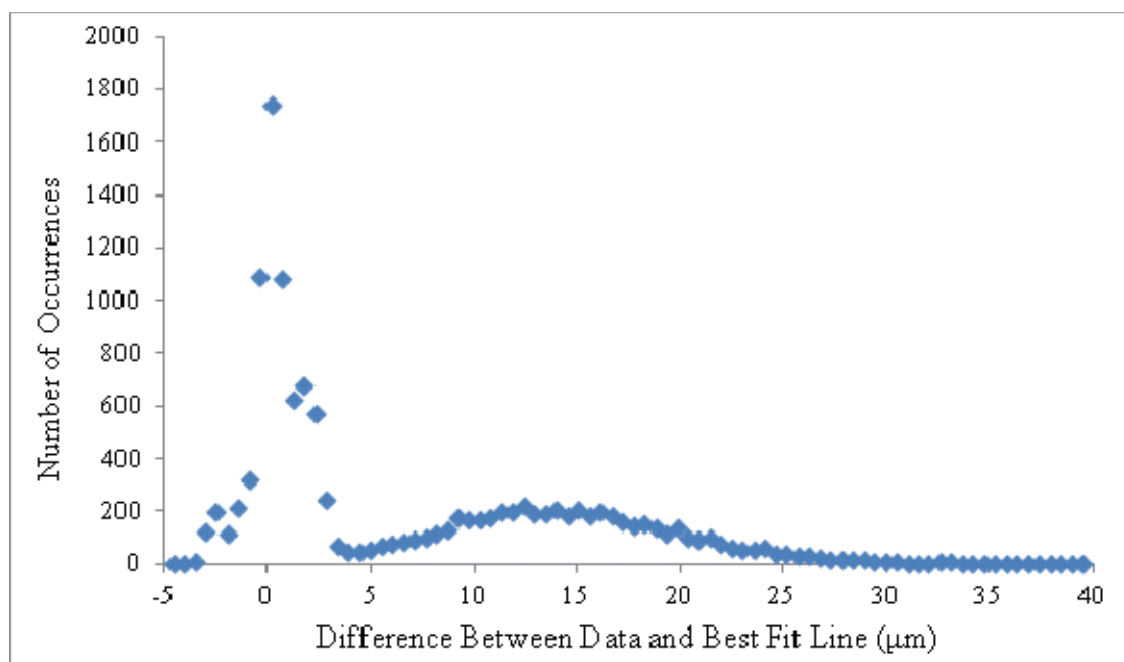


Figure B-56: LFD Histogram for Run 101

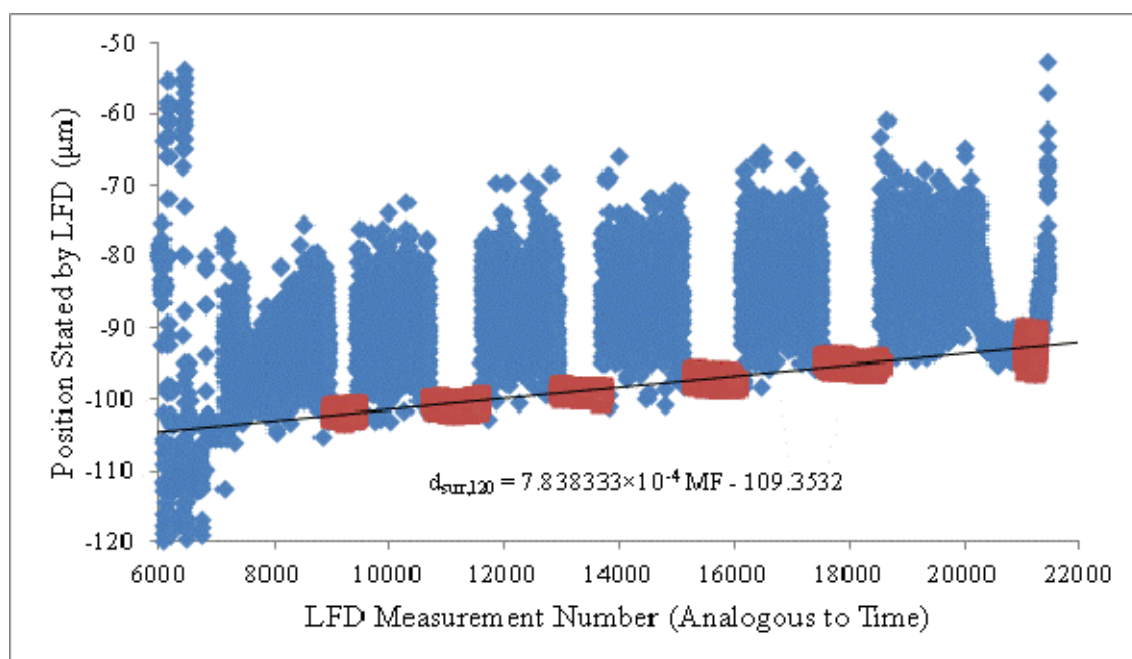


Figure B-57: Position of the Aluminum Substrate Stated by the LFD for Run 120

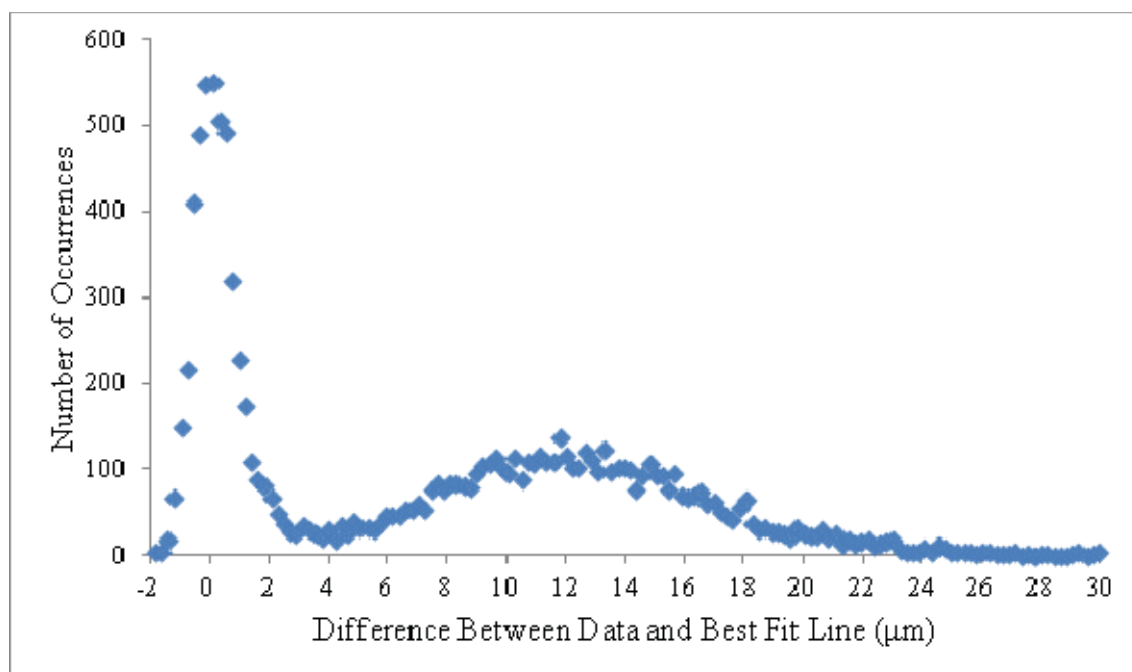


Figure B-58: LFD Histogram for Run 120

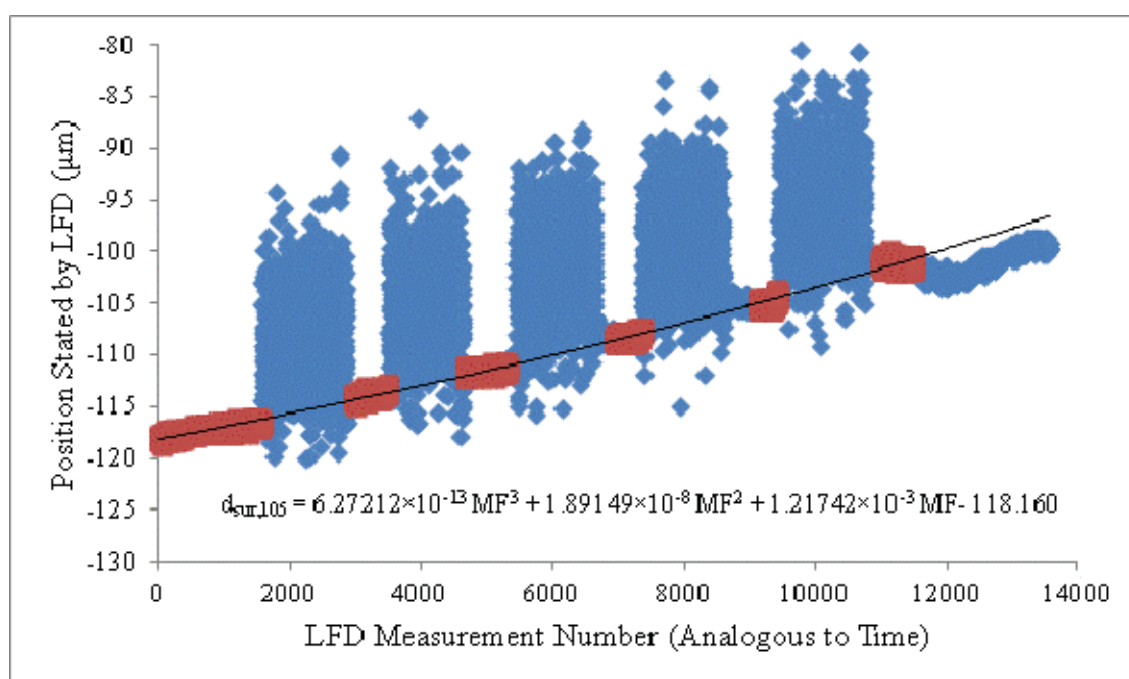


Figure B-59: Position of the Aluminum Substrate Stated by the LFD for Run 105

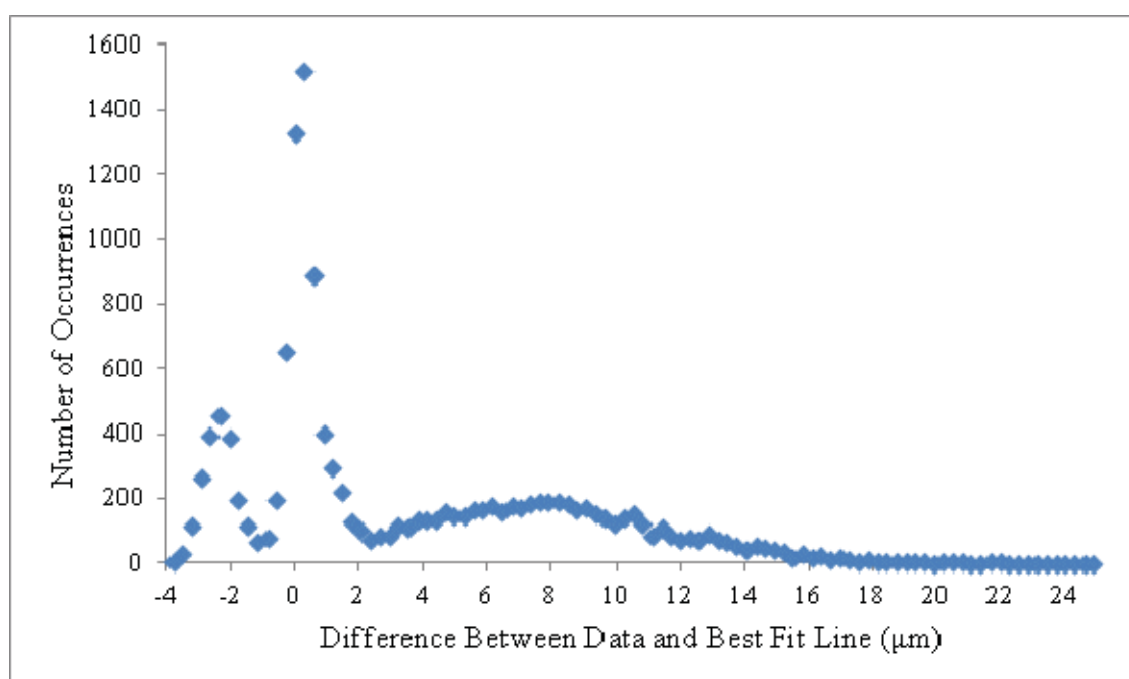


Figure B-60: LFD Histogram for Run 105

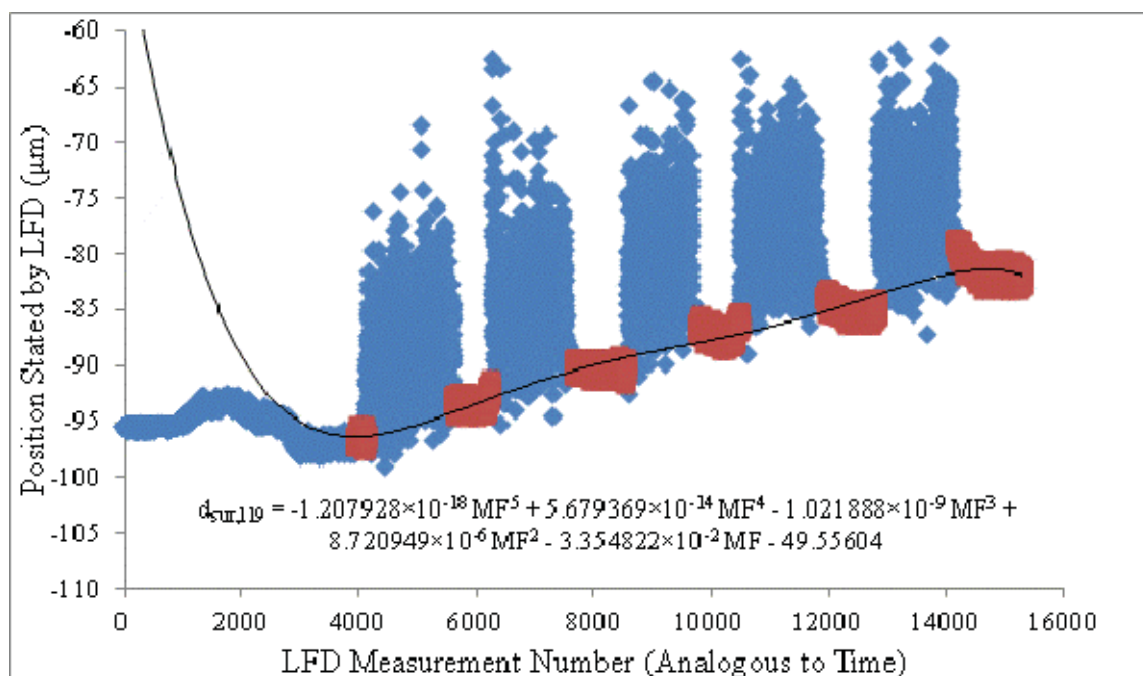


Figure B-61: Position of the Aluminum Substrate Stated by the LFD for Run 119

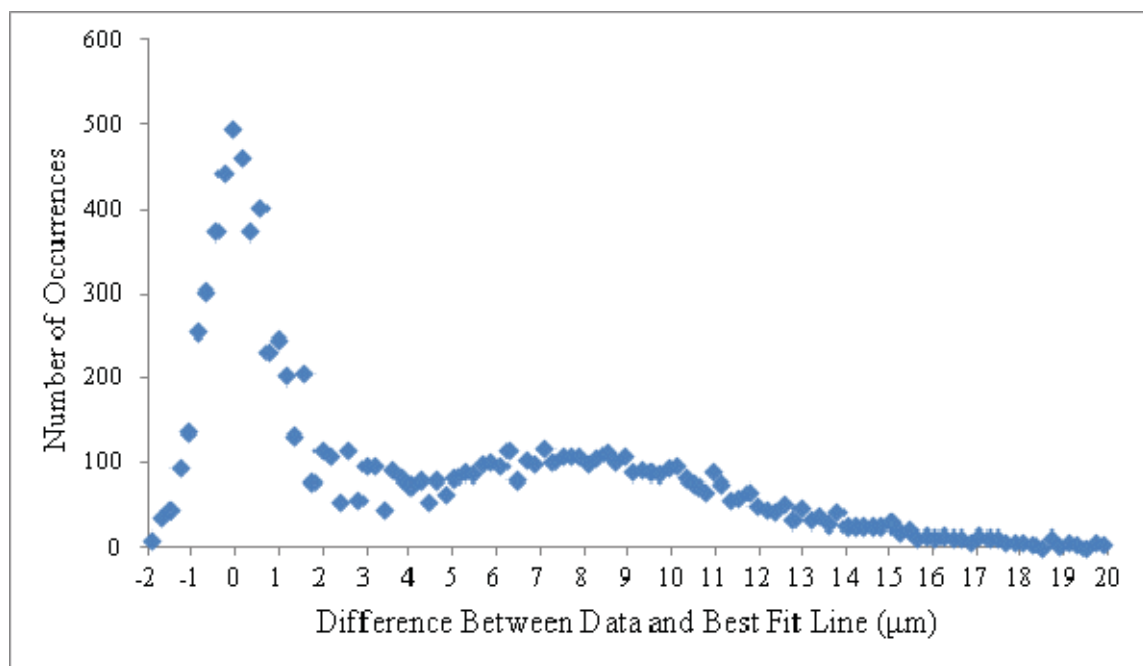


Figure B-62: LFD Histogram for Run 119

Appendix C: Derivation of Equation

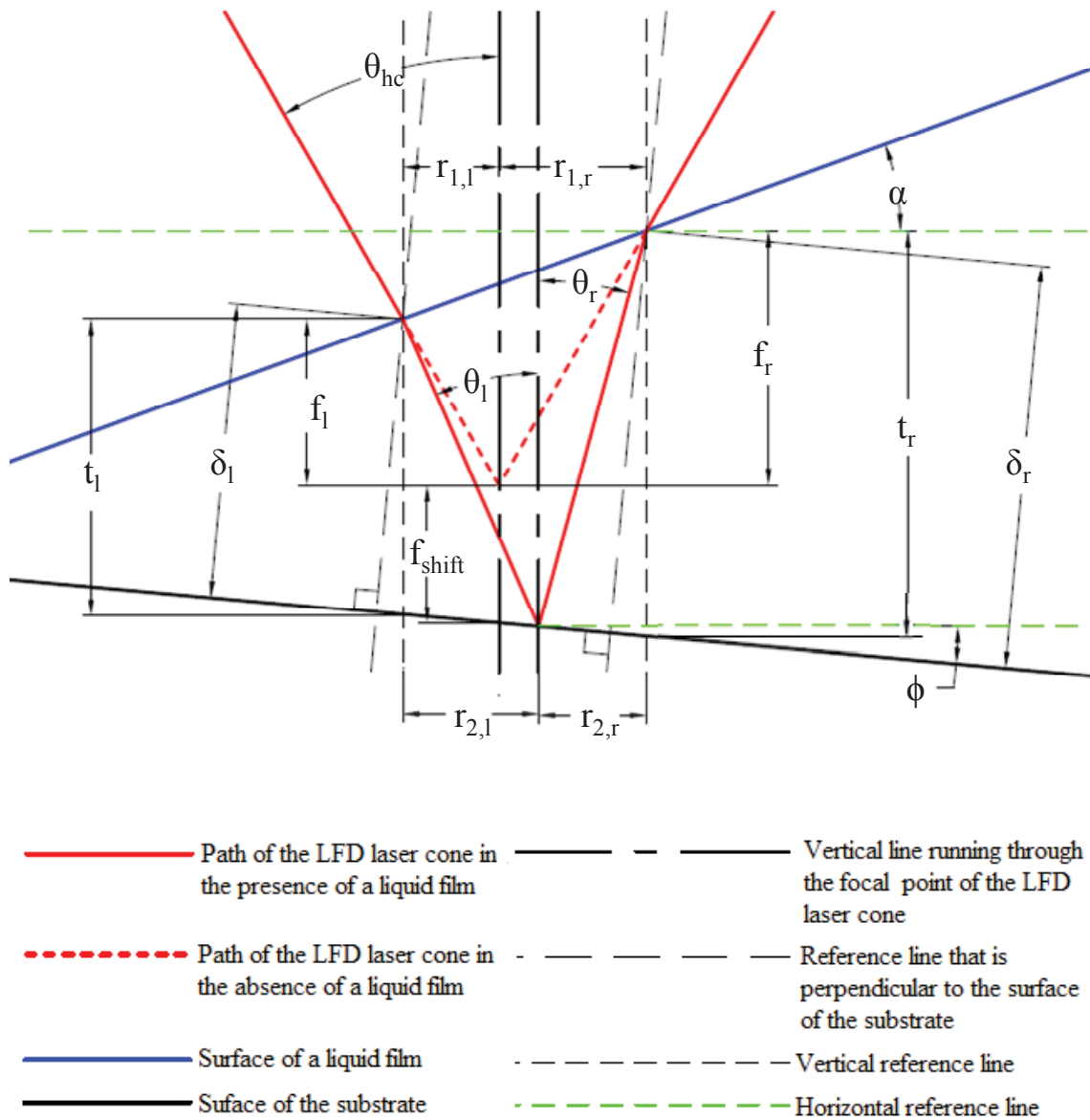


Figure C-1: Illustration of the LFD's Conical Laser Beam Passing Through the Surface of the Liquid Film and Reflecting off of the Aluminum Substrate

From geometry:

$$t_l = f_{shift} + f_l - r_{1l} \tan \phi \quad (eq\ C - 1)$$

$$t_l = f_{shift} + \frac{r_{1l}}{\tan \theta_{hc}} - r_{1l} \tan \phi \quad (eq\ C - 2)$$

Rearranging can combining equations C-1 and C-2:

$$r_{1l} = \frac{t_l \tan \theta_{hc} - f_{shift} \tan \theta_{hc}}{1 - \tan \theta_{hc} \tan \phi} \quad (eq\ C - 3)$$

$$r_{1l} = A(t_l - f_{shift}) \quad (eq\ C - 4)$$

Where (already defined in section 5.3.2:

$$A = \frac{\tan \theta_{hc}}{1 - \tan \theta_{hc} \tan \phi} \quad (eq\ 5 - 14)$$

From geometry:

$$t_l = f_{shift} + f_r - r_{1l} \tan \phi - r_{1l} \tan \alpha - r_{1r} \tan \alpha \quad (eq\ C - 5)$$

And:

$$\begin{aligned} t_l = f_{shift} + \frac{r_{1r}}{\tan \theta_{hc}} - \frac{t_l \tan \theta_{hc} \tan \phi - f_{shift} \tan \theta_{hc} \tan \phi}{1 - \tan \theta_{hc} \tan \phi} \\ - \frac{t_l \tan \theta_{hc} \tan \alpha - f_{shift} \tan \theta_{hc} \tan \alpha}{1 - \tan \theta_{hc} \tan \phi} - r_{1r} \tan \alpha \quad (eq\ C - 6) \end{aligned}$$

Rearranging:

$$r_{1r} = \frac{t_l \tan \theta_{hc} (1 + \tan \theta_{hc} \tan \alpha) - f_{shift} \tan \theta_{hc} (1 + \tan \theta_{hc} \tan \alpha)}{(1 - \tan \theta_{hc} \tan \phi)(1 - \tan \theta_{hc} \tan \alpha)} \quad (eq\ C - 7)$$

Rewriting as:

$$r_{1r} = B(t_l - f_{shift}) \quad (eq\ C - 8)$$

Where:

$$B = \frac{\tan \theta_{hc} (1 + \tan \alpha \tan \theta_{hc})}{(1 - \tan \theta_{hc} \tan \phi)(1 - \tan \theta_{hc} \tan \alpha)} \quad (eq\ 5 - 15)$$

From geometry:

$$t_l = \frac{r_{2l}}{\tan \theta_l} - r_{2l} \tan \phi \quad (eq\ C - 9)$$

Rearranging:

$$r_{2l} = \frac{t_l \tan \theta_l}{1 - \tan \theta_l \tan \phi} \quad (eq\ C - 10)$$

Therefore:

$$r_{2l} = C t_l \quad (eq\ C - 11)$$

Where:

$$C = \frac{\tan \theta_l}{1 - \tan \theta_l \tan \phi} \quad (eq\ 5 - 16)$$

From geometry:

$$t_l = \frac{r_{2r}}{\tan \theta_r} - r_{2l} \tan \phi - (r_{2r} + r_{2l}) \tan \alpha \quad (eq\ C - 12)$$

$$t_l = \frac{r_{2r}}{\tan \theta_r} - \frac{t_l \tan \theta_l \tan \phi}{1 - \tan \theta_l \tan \phi} - r_{2r} \tan \alpha - \frac{t_l \tan \theta_l \tan \alpha}{1 - \tan \theta_l \tan \phi} \quad (eq\ C - 13)$$

Rearranging:

$$r_{2r} = \frac{t_l \tan \theta_r (1 + \tan \theta_l \tan \alpha)}{(1 - \tan \theta_l \tan \phi)(1 - \tan \theta_r \tan \alpha)} \quad (eq\ C - 14)$$

Rewriting as:

$$r_{2r} = D t_l \quad (eq\ C - 15)$$

Where:

$$D = \frac{\tan \theta_r (1 + \tan \theta_l \tan \alpha)}{(1 - \tan \theta_l \tan \phi)(1 - \tan \theta_r \tan \alpha)} \quad (eq\ 5 - 17)$$

From geometry:

$$r_{1l} + r_{1r} = r_{2l} + r_{2r} \quad (eq\ C - 16)$$

Substituting equations C-4, C-8, C-11, and C-15:

$$A(t_l - f_{shift}) + B(t_l - f_{shift}) = C t_l + D t_l \quad (eq\ C - 17)$$

Rearranging gives:

$$\frac{t_l}{f_{shift}} = \frac{A + B}{A + B - C - D} \quad (eq\ C - 18)$$

From geometry:

$$t_r = f_r + f_{shift} + r_{1r} \tan \phi \quad (eq\ C - 19)$$

$$t_r = \frac{r_{1r}}{\tan \theta_{hc}} + f_{shift} + r_{1r} \tan \phi \quad (eq\ C - 20)$$

Rearranging gives:

$$r_{1r} = \frac{t_r \tan \theta_{hc} - f_{shift} \tan \theta_{hc}}{1 + \tan \theta_{hc} \tan \phi} \quad (eq\ C - 21)$$

Rewriting as:

$$r_{1r} = E(t_r - f_{shift}) \quad (eq\ C - 22)$$

Where:

$$E = \frac{\tan \theta_{hc}}{1 + \tan \theta_{hc} \tan \phi} \quad (eq\ 5 - 18)$$

From geometry:

$$t_r = f_l + f_{shift} + (r_{1r} + r_{1l}) \tan \alpha + r_{1r} \tan \phi \quad (eq\ C - 23)$$

$$\begin{aligned} t_r = \frac{r_{1l}}{\tan \theta_{hc}} + f_{shift} + \frac{t_r \tan \theta_{hc} \tan \alpha - f_{shift} \tan \theta_{hc} \tan \alpha}{1 + \tan \theta_{hc} \tan \phi} + r_{1l} \tan \alpha \\ + \frac{t_r \tan \theta_{hc} \tan \phi - f_{shift} \tan \theta_{hc} \tan \phi}{1 + \tan \theta_{hc} \tan \phi} \quad (eq\ C - 24) \end{aligned}$$

Rearranging:

$$r_{1l} = \frac{t_r \tan \theta_{hc} (1 - \tan \theta_{hc} \tan \alpha) - f_{shift} \tan \theta_{hc} (1 - \tan \theta_{hc} \tan \alpha)}{(1 + \tan \theta_{hc} \tan \phi)(1 + \tan \theta_{hc} \tan \alpha)} \quad (eq\ C - 25)$$

Rewriting as:

$$r_{1l} = F(t_r - f_{shift}) \quad (eq\ C - 26)$$

Where:

$$F = \frac{\tan \theta_{hc} (1 - \tan \alpha \tan \theta_{hc})}{(1 + \tan \theta_{hc} \tan \phi)(1 + \tan \theta_{hc} \tan \alpha)} \quad (eq\ 5 - 19)$$

From geometry:

$$t_r = \frac{r_{2r}}{\tan \theta_r} + r_{2r} \tan \phi \quad (eq\ C - 27)$$

Rearranging:

$$r_{2r} = \frac{t_r \tan \theta_r}{1 + \tan \theta_r \tan \phi} \quad (eq\ C - 28)$$

Rewriting as:

$$r_{2r} = G t_r \quad (eq\ C - 29)$$

Where:

$$G = \frac{\tan \theta_r}{1 + \tan \theta_r \tan \phi} \quad (eq\ 5 - 20)$$

From geometry:

$$t_r = \frac{r_{2l}}{\tan \theta_l} + (r_{2l} + r_{2r}) \tan \alpha + r_{2r} \tan \phi \quad (eq\ C - 30)$$

$$t_r = \frac{r_{2l}}{\tan \theta_l} + r_{2l} \tan \alpha + \frac{t_r \tan \theta_r \tan \alpha}{1 + \tan \theta_r \tan \phi} + \frac{t_r \tan \theta_r \tan \phi}{1 + \tan \theta_r \tan \phi} \quad (eq\ C - 31)$$

Rearranging:

$$r_{2l} = \frac{t_r \tan \theta_l (1 - \tan \theta_r \tan \alpha)}{(1 + \tan \theta_r \tan \phi)(1 + \tan \theta_l \tan \alpha)} \quad (eq\ C - 32)$$

Rewriting as:

$$r_{2l} = J t_r \quad (eq\ C - 33)$$

Where:

$$J = \frac{\tan \theta_l (1 - \tan \theta_r \tan \alpha)}{(1 + \tan \theta_r \tan \phi)(1 + \tan \theta_l \tan \alpha)} \quad (eq\ 5 - 21)$$

From geometry:

$$r_{1l} + r_{1r} = r_{2l} + r_{2r} \quad (eq\ C - 33)$$

Substituting equations C-22, C-26, C-29, and C-33 gives:

$$F(t_r - f_{shift}) + E(t_r - f_{shift}) = J t_r + G t_r \quad (eq\ C - 34)$$

Rearranging:

$$\frac{t_r}{f_{shift}} = \frac{E + F}{E + F - G - J} \quad (eq\ C - 35)$$

From geometry:

$$t_l = \frac{\delta_l}{\cos \emptyset} \quad (eq\ C - 36)$$

$$t_r = \frac{\delta_r}{\cos \emptyset} \quad (eq\ C - 37)$$

Substituting equations C-36 and C-37 and rearranging gives:

$$\frac{\delta_l}{f_{shift}} = \cos(\emptyset) \cdot \frac{A + B}{A + B - C - D} \quad (eq\ C - 38)$$

$$\frac{\delta_r}{f_{shift}} = \cos(\emptyset) \cdot \frac{E + F}{E + F - G - J} \quad (eq\ C - 39)$$

The average of δ_l and δ_r is:

$$\delta_{ave} = \frac{\delta_l + \delta_r}{2} \quad (eq\ C - 40)$$

Substituting equations C-38 and C-39 gives:

$$\frac{\delta_{ave}}{f_{shift}} = \frac{\cos(\emptyset)}{2} \cdot \left(\frac{A + B}{A + B - C - D} + \frac{E + F}{E + F - G - J} \right) \quad (eq\ 5 - 13)$$

Appendix D: Uncertainty in the Momentum Flux

The momentum flux was one of the primary independent variables in this experiment. This variable was not directly measured, and its error was estimated by equation E-9. The definition of momentum flux is:

$$MF = \rho V^2 \quad (E - 1)$$

Writing the average flow velocity as:

$$V = \frac{\dot{m}}{\rho A} \quad (E - 2)$$

Ideal gas law:

$$P = \rho RT \quad (E - 3)$$

Substituting and rearranging, the momentum flux in terms of the measured variables is:

$$MF = \frac{\dot{m}^2 RT}{PA^2} \quad (E - 4)$$

The partial derivatives with respect to each measured variable is:

$$\frac{\partial MF}{\partial \dot{m}} = \frac{2\dot{m}RT}{PA^2} \quad (E - 5)$$

$$\frac{\partial MF}{\partial T} = \frac{\dot{m}^2 R}{PA^2} \quad (E - 6)$$

$$\frac{\partial MF}{\partial P} = -\frac{\dot{m}^2 RT}{P^2 A^2} \quad (E - 7)$$

$$\frac{\partial MF}{\partial A} = -\frac{2\dot{m}^2 RT}{PA^3} \quad (E - 8)$$

Therefore, the uncertainty in the momentum flux due to the uncertainty in \dot{m} , T , P , and A can be calculated by:

$$\sigma_{MF} = \sqrt{\left(\frac{\partial MF}{\partial \dot{m}}\right)^2 \sigma_{\dot{m}}^2 + \left(\frac{\partial MF}{\partial T}\right)^2 \sigma_T^2 + \left(\frac{\partial MF}{\partial P}\right)^2 \sigma_P^2 + \left(\frac{\partial MF}{\partial A}\right)^2 \sigma_A^2} \quad (E - 9)$$

This equation was used to calculate the error in the momentum flux for all of the experiments. The experimental uncertainty in \dot{m} , T , P is already stated in table 4-1. The uncertainty in the cross-sectional area of the test article is $\pm .013$ mm.